CHARACTERIZATION OF NANOSCALE ELECTRONIC MATERIALS USING NOVEL METHODS FOR SCAN PROBE MICROSCOPY

BY

ERIC MICHAEL SEABRON

DISSERTATION

Submitted in partial fulfillment of the requirements
for the degree of Doctorate of Philosophy in Materials Science and Engineering
in the Graduate College of the
University of Illinois at Urbana-Champaign, 2017

Urbana, Illinois

Doctoral Committee:

Professor John Rogers, Chair and Director of Research
Professor Xuling Li, Chair
Professor William Wilson, Research Advisor, Harvard University
Professor John Abelson
Professor Paul Braun

ABSTRACT

Transistors have been improved to achieve higher performance by substantially scaling down the physical size of the devices. Currently, high performance Silicon based transistors have been shrunk to the nanoscale. To further improve the performance of transistors researchers are exploring the use of novel semiconductors with unique nanoscale morphologies. To create processes to utilize the properties of new materials, there has been significant effort to better understand how these material's electrical properties effect transistors in real devices. The primary challenge associated with electronic material characterization for process optimization is the difficulty of mapping electrical properties with a resolution high enough to spatially resolve nanoscale phenomena.

In this thesis we will explore several scan probe based microscopy techniques capable of mapping changes in electronic properties with sub-diffraction spatial resolution. Using novel methods for scan probe based microscopy, we combined electrical and morphology mapping to reveal structural driven electrical properties to provide insight into growth physics and electrical transport. We used novel methods for Electric Force Microscopy, Near Field Infrared Microscopy, and Microwave Impedance Microscopy (MIM) to map non-uniform doping and the free carrier distribution in the bulk Gallium Arsenide nanowires. Our results revealed cyclical doping inhomogeneity in regions with morphological defects; we used that information to create a physical model to predicts the impurity distribution along the nanowire. This enables us to better understand the physics behind in situ doping during the growth process.

In addition, we used of Microwave Impedance Microscopy to qualitatively characterize carbon nanotube (CNT) electrical properties. Using novel methods to maximize the signal and sensitivity of the microwave reflectivity response to the carbon nanotubes, we were able to

spatially map and distinctly identify the electronic character of individual carbon nanotubes in an array with 50nm resolution. Our results provide that MIM can be used to distinguish semiconducting, semi-metallic, and metallic carbon nanotubes by detecting their quantum capacitance, which is directly related to the density of states. We also explored Carbon Nanotube heterojunctions and metal-semiconductor interfaces; we believe that our results are direct evidence of electron-electron screening in 1-dimensional semiconductors.

Finally, we introduce a novel, intermittent-contact, approach to Microwave Impedance Microscopy that uses the native water layer, which exists on surfaces in ambient humidity conditions, to further improve sensitivity and resolution. In addition, this approach doesn't require any special sample preparation making 100% clean, which is preferred in an industrial laboratory setting. Our results prove that both tapping mode Atomic Force Microscopy and force curve mapping can be used with MIM to electronically characterize carbon nanotube arrays at the nanoscale. The Fast Force Curve mapping variant of MIM shows the most promise for acquiring accurate, high resolution, maps of CNT electronic character without altering the sample. It is worth noting that high resolution mapping of the electrical character of individual carbon nanotubes in a large array has never been achieved before this work.

To all those who weren't given the opportunities I had to succeed in life and academia

To my many academic mentors that always believed in me

To my wife Deveine Toney for supporting me through graduate school

To my daughter Farrah Seabron who inspired me to stay focused

To my mother who continuously challenged me to be better

To my family who encouraged me to be different

In loving memory of Cheyenne Farrar and Patricia Farrar

ACKNOWLEDGEMENTS

I would like to acknowledge all those who directly contributed or supported to this work.

Committee:

- Prof. John Rogers
- Prof. Xuling Li
- Prof. William Wilson
- Prof. John Abelson
- Prof. Paul Braun

Collaborators:

- Xu Xie
- Wonsik Choi
- Parsian Mohseni
- Slava Rotkin
- Scott MacLaren
- Julio Soares
- Ernie Sammann
- Tobias Gokus
- Keith Jones
- Ryan Fuierer
- William Sweets

Facility/Staff Support:

- Materials Research Laboratory at the University of Illinois Urbana-Champaign
- Oxford Instruments PLC – Asylum Research
- PrimeNano Inc
- NeaSpec Inc
- Northrup Grumman Corp

This work was funded by the Nation Science Foundation:
DMR: 1508140
CMMI GOALI: 1436133

TABLE OF CONTENTS

CHAPTER 1: Motivation - Nanoscale Electronic Materials and Devices ……………………………1

CHAPTER 2: Scan Probe Methods for Electronic Material Characterization …………………41

CHAPTER 3: Electrical Scan Probe Microscopy of Periodic Doping In Planar Gallium Arsenide Nanowires …………………………………………………………71

CHAPTER 4: Scan Probe Microwave Reflectivity Mapping of Nanoscale Electronic Phenomena on Aligned Carbon Nanotubes ……………………………………...110

CHAPTER 5: Tapping and Force Curve Scan Probe Methods for 100% Clean Microwave Reflectivity Mapping of Carbon Nanotubes …………………………………...157

CHAPTER 6: Summary and Future Work ...…………………………………………………..199

APPENDIX A: Procedure for Chemical Vapor Deposition Growth of Carbon Nanotubes …...206

APPENDIX B: Procedures for Microwave Impedance Microscopy Imaging……..…………..209

CHAPTER 1

MOTIVATION - NANOSCALE ELECTRONIC MATERIALS AND DEVICES

The primary goal of my doctoral dissertation is to analyze intriguing nanoscale electronic materials to reveal poorly understood physical phenomena which impact process development and device operation. The scope of this work spans the fundamental physical nature of novel electronic materials and tip-cantilever dynamics, to develop novel methodologies for material characterization using scan probe microscopy. We will also describe the physical interactions between the probe and material, using theoretical and qualitative models, to better interpret unique nanoscale phenomena we observe. This document will feature work done in collaboration with other groups (Professor John Rogers and Professor Xuling Li) including carbon nanotube purification, MoS_2 characterization, and GaAs nanowire growth.

1.1 Introduction to Electronic Devices

Computers and Radio Frequency electronics transcend our everyday lives. They are present in our computers, smart phones, cars, satellites, and modern medical equipment. These devices are made of the small, highly complex systems which are built to consume minimal power, have low rates of failure, and be incredibly robust. Fundamental to all electronics is the transistor which works by controlling current flow through a semiconducting material. The electronics industry has driven the size of transistors to the nanoscale to increase performance and efficiency; the smallest consumer level transistor approaching semiconducting channel sizes of less than 30nm according to IBM's production pipeline illustrated in figure 1.1 [1]. However, there is a fundamental limit to the efficiency gain from making transistors smaller using

conventional materials and techniques. To further improve transistor performance researchers are considering different kinds of semiconducting materials and nanoscale geometries to improve transistor performance. Some of the more promising nanoscale electronic materials include carbon nanotubes (1-dimensional) and III-V semiconducting nanowires (3-dimensional) will be analyzed using novel characterization methods in this work.

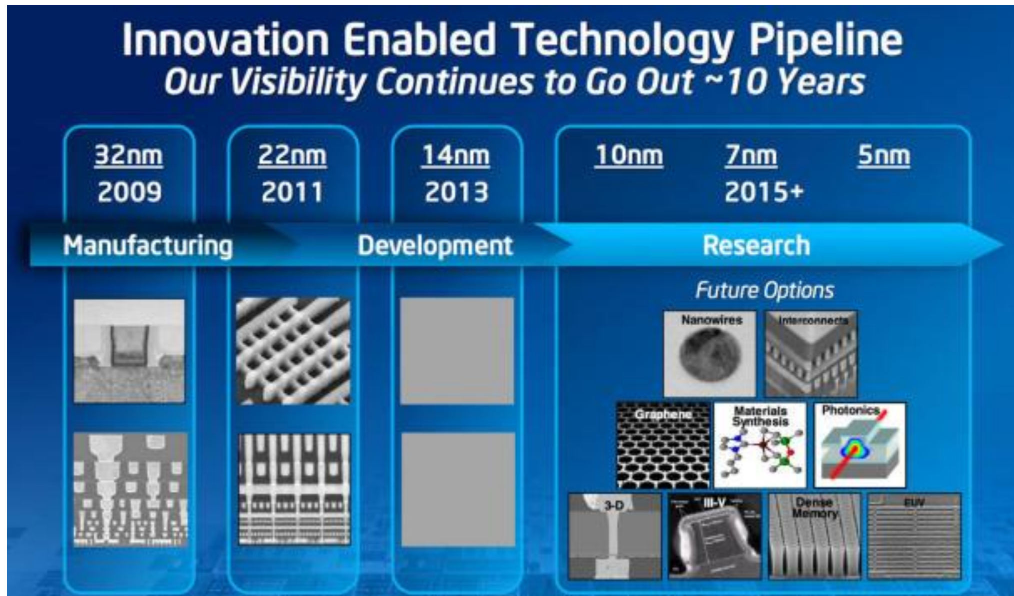

Figure 1.1: Illustration of the trend that the nanotechnology industry (IBM) is moving [1].

Consider a conventional transistor as seen in figure 1.2 where the red line represents current flow. The transconductance, g_m, is considered the primary figure of merit for potential transistor performance. The transconductance is related to the transistor's ON and OFF current; the current flow during the saturated "ON" state (I_{DS}^{ON}) from the drain to source and the current flow during the "OFF" state ($I_{leakage}^{OFF}$) [2]. If the leakage current is several orders of magnitude less than the saturated "ON" current, which is true for high performance transistors, the transconductance is strongly influenced by the "ON" current given in equation 1.2. The carrier mobility (μ) is a measure of how quickly a charge can move through a material in the presence of an electric field typically produced by a gate voltage. The carrier mobility is enhanced in

materials with smaller effective carrier mass at the conduction band-edge (m*). The contribution of N, the number of available free charge carriers, is also worth noting because it means that the transconductance may be enhanced by doping. The cutoff frequency, f_T, is another important figure of merit attributed to the transconductance for very high frequency RF transistors. It defines the maximum switching speed of the transistor without signal attenuation or significant loss in gain [3]. In a simple model, the maximum cutoff frequency is inversely proportional to the resistance of the transistor multiplied by the gate capacitance. The gain of the transistor is also correlated to the cut-off frequency, so having a high cutoff frequency is important for many applications of field effect transistor technology.

$$g_m = \frac{\partial I_{DS}}{\partial V_{gate}} = \frac{I_{DS}^{ON} - I_{leakage}^{OFF}}{V_{ON}} \quad (1.1)$$

$$I_{DS}^{ON} \sim R^{-1} = eN\mu * \frac{Cross\text{-}Area}{Length} \quad (1.2)$$

$$\mu = \frac{q\tau_{scatter}}{m^*} \quad (1.3)$$

$$f_T = \frac{g_m}{2\pi C_{gs}} \sim \frac{1}{RC} \text{ and } Gain \sim \frac{f_T}{f} \quad (1.4)$$

Resistance is caused by scattering events in which a mobile carrier either changes direction (elastic scattering) and/or loses energy (inelastic scattering) while moving through a material. Although the overall current path is measured as a linear path from source to drain denoted by the solid red line in figure 1.2, the actual carrier path is better illustrated by the randomly oriented dotted red line. Each scattering event has the potential to vastly slow the carrier's linear movement through the transistor which lowers the carrier mobility (equation 1.3). From equation 1.4, notice that the lower the resistance and capacitance, the higher the transconductance meaning the device can operate at a higher switching frequency and gain. This favors a device geometry with a short conduction channel, to reduce the number of carrier

scattering events along the conduction pathway, from source to drain. Narrow conduction channels are important for minimizing the drain-source and gate capacitance. This is the underlying premise behind the appeal of using nanoscale device geometries and using materials with higher carrier mobility for next generation devices.

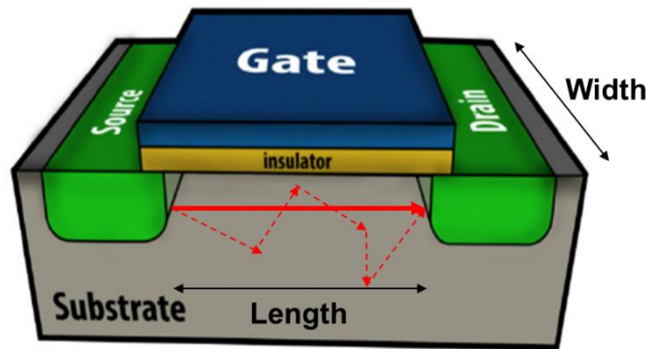

Figure 1.2: Simple illustration of a conventional transistor. The carrier pathway is shown as red arrows moving from source to drain.

The degradation of charge mobility is dominated by scattering processes. As the probability of scattering increases, the charge mobility decreases alluding to the importance of minimizing defect density. The primary types of scattering in solid state semiconductors are coulomb scattering from impurities in the conduction channel caused by intentional or unintended dopant ions, grain boundaries in the material which naturally form in crystals, and phonon-electron scattering that governs the material's intrinsic electron mobility which diminishes with increasing temperature.

The transconductance is adversely affected by the leakage current during the "OFF" state, this becomes problematic in short channel devices. Short channel effects are dependent on the semiconductor band-gap and the presence of defect states that aid the quantum tunneling of carriers across the conduction path. During transistor operation, even when the gate voltage is "OFF", there is an applied electric field across the drain-source which encourages current flow.

Typically, a transistor is “OFF” when the gate voltage is zero; we expect no current flow despite the drain-source voltage. This is because without the gate voltage the collective energy of the carriers in the active region is not enough to overcome the bandgap energy allowing for current flow. However, statistically there are some charge carriers with enough thermal energy to excite to the conduction band and travel across the conduction path without the aid of the gate voltage, this is the primary cause of leakage current during the “OFF” state. Short channel effects become increasingly important for devices with nanoscale conduction channel lengths. When transistors are designed with shorter channels to increase the “ON” current much less energy is needed for carriers to tunnel across the semiconducting channel.

1.2 Gallium Arsenide Nanowires Devices

Group III-V semiconductors are well known for their superior carrier mobility compared to conventionally used bulk Silicon. High mobility implies that the semiconducting material will have a higher intrinsic conductivity which leads to higher transistor performance [4]. Gallium Arsenide (GaAs) is a preferred III-V semiconductor because it not only has a higher carrier mobility than Silicon, but also has a larger bandgap energy as seen in figure 1.3. The bandgap energy determines the amount of energy needed for an electron in the valence band to excite to the conduction band to allow current flow. Short channel effects which diminish the transconductance are caused by moving charge carriers (current flow) during the “OFF” state of the transistor. A larger bandgap implies that more energy is needed to create current flow; this increases the gate voltage needed for sustain the “ON” state, but also decreases the chances of electrons tunneling through the active region during the “OFF” state. Hence, for transistors with nanoscale channel lengths GaAs has an advantage over other III-V semiconductors by both

improving the "ON" current and discouraging current leakage during the "OFF" state when compared to bulk Silicon.

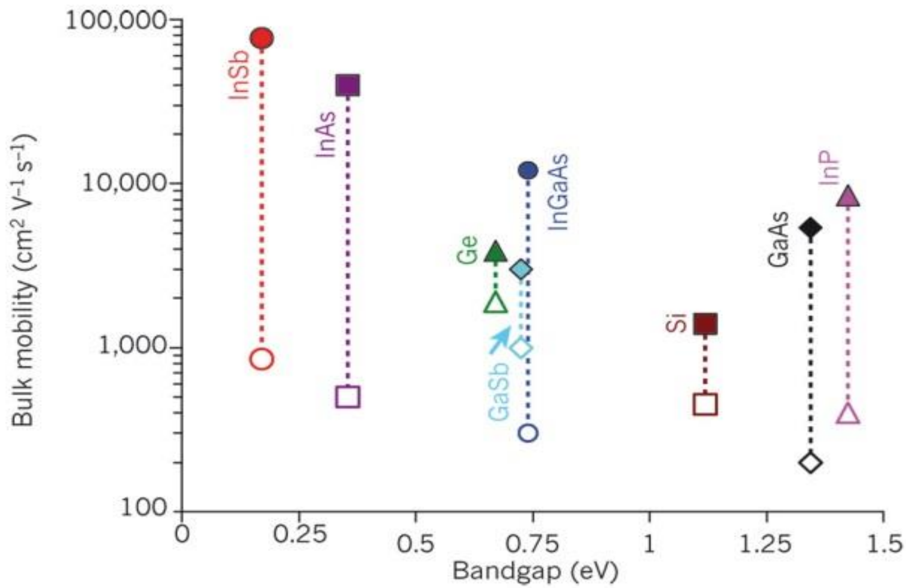

Figure 1.3: A graph of bandgap energy vs. charge mobility of electrons (filled) and holes (unfilled) for various bulk semiconductors [5].

In the nanowire (NW) geometry, the idea is to create a short length, narrow width channel to minimize capacitance and resistance, this is typically achieved using complex etching and pattern processing [6,7,8]. When growing nanowires, they naturally grow in an ideal physical morphology where the narrow width and short length can be controlled by their growth conditions. Conventionally vertically grown nanowires transistors were the commonly used in research, however they suffer from issues such as stack faults growth defects and complex processing for transistor design [9]. For the purposes of the experiments used in this thesis we will focus on novel planar GaAs NWs.

One of the biggest advantages of planar nanowires is that the crystal structure self-aligns relative to the growth substrate which can be seen in figure 1.4. This vastly improves the current carrying capability of a single device by using multiple nanowires in an array, this improves the

feasibility of using of planar nanowires in a large variety of high performance transistor geometries [10,11,12,13]. A sacrificial layer below the NW growth interface enables post-growth transfer of well-aligned planar NW onto foreign substrates to be utilized in various advanced devices [11]. The lateral geometry is also compatible with conventional planar processing which is ideal for utilizing conventional fabrication equipment and lithography techniques to create the source, drain, and gate electrodes. Furthermore, the growth mechanism also creates single crystalline GaAs free of stacking fault defects. This dramatically decreases the grain boundary scattering which increases the effective carrier mobility. According to the previous study done by Xiuling Li's group in University of Illinois, a planar NW was grown without any failures in crystallinity for over 6um in length, whereas vertical NW growth is only able to grow up to 500nm before the formation of stacking faults [14].

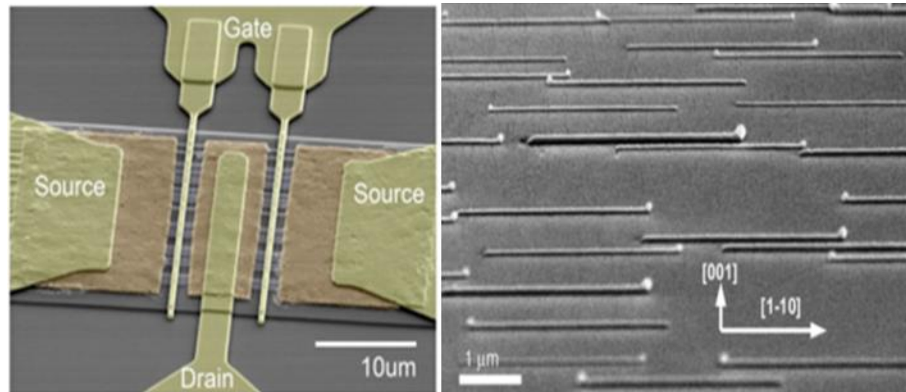

Figure 1.4: Scanning Electron Microscopy images of laterally aligned GaAs nanowires before (right) and after (left) device fabrication [11].

Metal Organic Chemical Vapor Deposition (MOCVD) was used to grow planar NWs. It enables in situ doping to nearly atomically abrupt PN junctions, which eliminates the need for complex doping processes. To control the spatial placement of the PN junction, a typical doping process requires several masks layers to lithographically pattern the p-type and n-type regions. This process not only takes more steps, but can result in a non-ideal spatial gradient of doping

across the metallurgical junction. Depending on the methodology, many forms of doping such as ion implantation can also cause additional physical defects that can lower conductivity. These processes affect the potential barrier of tunneling and may introduce defects states in the junction that could contribute to short channel effects. In contrast, in-situ doping doesn't require any additional processing after growth. The doping incorporation can switch from n-type to p-type during the NW growth and its placement along the nanowire can easily be controlled. MOCVD growth of planar nanowires creates a sharper doping profile than conventional methods without the issues of unwanted defects, crystalline mismatch, and complex lithography processing [15].

1.3 Planar GaAs NW Growth using MOCVD

Metal Organic Chemical Vapor Deposition, MOCVD, is a high temperature (400-600°C) growth process in which metal-organic precursors flow through the CVD reaction chamber in the gaseous phase until it chemically reacts to epitaxially grow a thin film. For the growth of GaAs nanowires a gold (Au) nanoparticle is used to catalyze the chemical reaction and facilitate nanowire growth via a Vapor-Liquid-Solid mechanism. At high temperatures, the gold nanoparticle behaves like a liquid and begins to wet the substrate, it absorbs the Gallium from the GaAs substrate which forms a gold-Gallium (Au-Ga) alloy nanoparticle. In the vapor stage of the reaction the metal-organic precursor containing Arsenic (As) atoms reacts with the Au/Ga nanoparticle, the Arsenic is absorbed by the Au-Ga nanoparticle. Once the As concentration inside the Au/Ga nanoparticle reaches saturation, GaAs precipitates out of the nanoparticle in its lowest free energy resulting in the growth of a monocrystalline nanowire. The diameter distribution of the resulting nanowires is correlated to the size distribution of the metal nanoparticles. The growth of the nanowire is limited by the presence of the precursor gas, so it's

length can be easily controlled by adjusting the growth time. Hence there is a pathway to control the physical dimensions of the nanowire without the need for lithographic techniques [14].

To control the planar growth and direction of the nanowire requires a specific crystal orientation of the substrate such that the free energy is minimized at the nanowire-substrate interface [14]. Growth temperature is an important parameter to promote planar growth, the wetting of the gold nanoparticle on the substrate, which is sensitive to temperature, can create enough adhesion force to discourage out of plane growth. GaAs NWs grown on (111) GaAs substrates prefer to grow out-of-plane creating vertical free standing NW structures (figure 1.5b) [16,17]. To encourage planar nanowires growth (100) GaAs substrates are used for MOCVD growth at a temperature of 465°C. The nanowires naturally grow very well aligned along a particular crystalline plane [18]. The different crystal orientations can be seen easily in figure 1.5a, where the TEM image shows the crystal formation near the gold nanoparticle [14]. Figure 1.5b illustrates how each crystal orientation has a preferred growth direction, the adhesion forces of the growth front determine which growth direction will be preferred. Figure 1.5c is an SEM image after cooling showing how the gold can wet differently on the substrate which may determine whether the nanowire grows in the planar direction. Since each growth direction is a low energy state, under non-ideal growth directions some nanowires will still grow out of plane as seen in figure 1.5d [17].

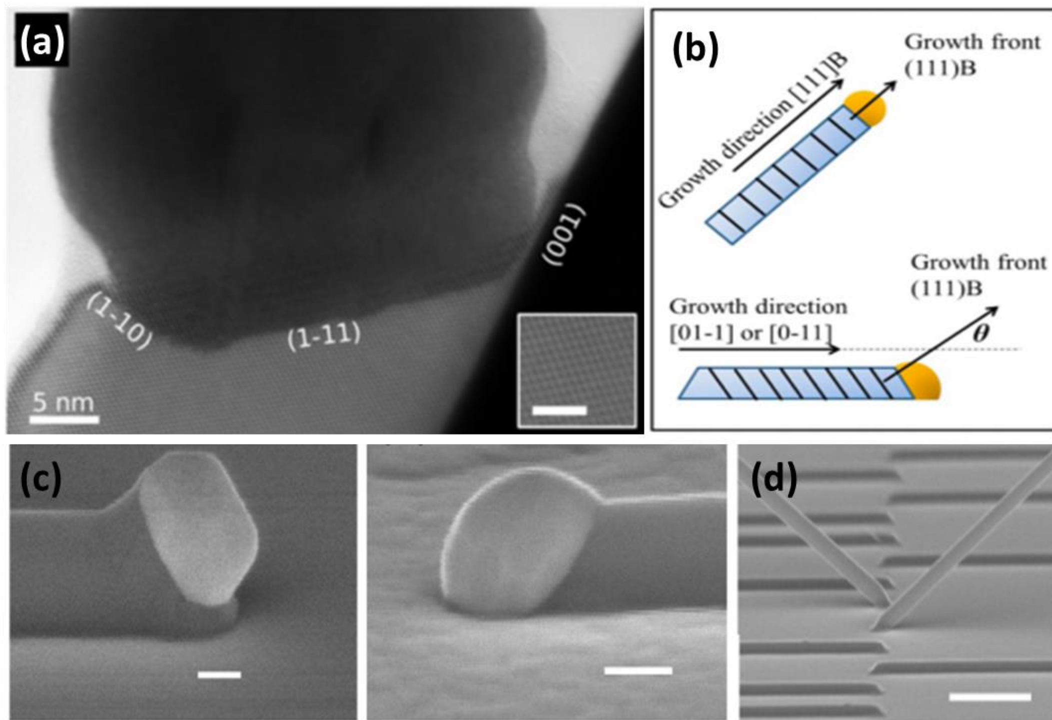

Figure 1.5: (a) TEM image of a GaAs nanowire's crystal lattice structure at the catalyst particle interface,14 (b) an illustration of the two most likely pathways for nanowire growth, (c) SEM images of planar nanowires showing how the wetting of the catalyst effects growth angle, (d) SEM images of nanowires growing in and out of plane [17].

The use of MOCVD to grow lateral nanowires offers a unique opportunity for in-situ doping. The incorporation of dopants such as silicon, carbon, or zinc to create n-type and p-type regions in the nanowire is done by simply flowing different organo-metallic precursors in vapor phase during growth [19]. In-situ zinc doping has been shown to be achievable by flowing the dopant gases in the CVD chamber during growth [19]. As seen in figure 1.6, the dopant gas can be turned on and off creating visible corrugation in the lattice. These corrugations are periodic which implies that there is added complexity to the super-saturation and precipitation of the dopants in the gold nanoparticle, the underlying physical mechanisms of this phenomena is not well understood [19].

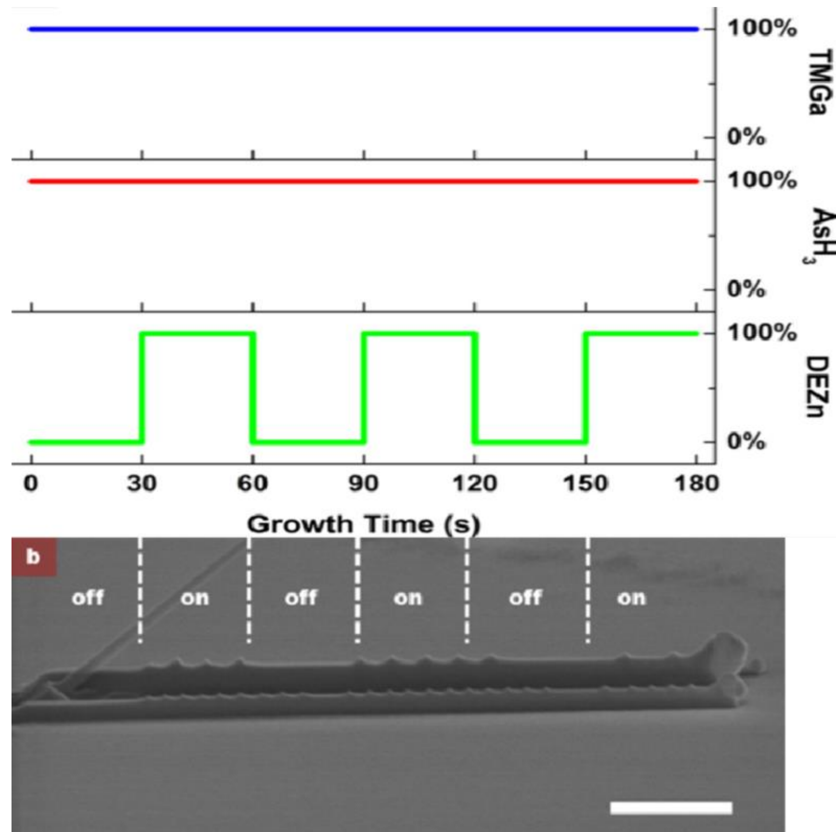

Figure 1.6: (a) Shows the periodic introduction of doping gases labeled as DEZn. (b) SEM image of Nanowire after growth. These figures are aligned in order to show how the introduction of doping gas affects the NW morphology [19].

1.4 The Physics of Carbon Nanotube based Devices

Carbon Nanotubes (CNT) have been a material of interest by the research community for next generation electronics since their discovery in 1991 [20]. The appeal of carbon nanotubes is their unique 1-dimensional quantum behavior that allows them to have a theoretical carrier mobility well over 2-orders of magnitude greater than any bulk material semiconductor at room temperature (100,000 cm^2/V-s for CNTs, 1400 cm^2/V-s for Silicon, 8500 cm^2/V-s for GaAs). CNTs in the semiconducting form are an excellent candidate for high performance, low power, RF field-effect transistors and nanoscale logic devices [21,22].

Carbon nanotubes are composed of a single atomic layer of carbon, a graphene sheet, rolled into a hollow cylinder [23]. The sp^2 C-C covalent bonds form the 1-dimensional nanotube structure. Their unique morphology is the key to its extraordinary transport properties, although the underlying physics is not fully understood. First, a honeycomb graphene lattice contains three Carbon atoms bonded to another as seen in figure 1.7 [24]. Each carbon atom has an unbonded electron that forms a pi-orbital which leads to a very high intrinsic carrier density in the honeycomb graphene lattice. Due to the symmetry of the DOS for this atomic configuration, both electrons and holes have the same effective mass; this allows for of their equal contribution to current flow unlike most semiconductors where electrons dominate conduction [25]. Second, it is believed that phonon-electron scattering, which typically limits the conductivity of single crystals in ambient temperature, is minimized by the CNT's 1-dimensional nature and strong carbon-carbon bonds [25]. One hypothesis is that there are notably fewer acoustic phonon states to facilitate low energy scattering because there are less degrees of freedom for crystal lattice vibrations in low dimensional materials. Optical phonon scattering is also minimized in CNTs because its monoatomic composition and strong C-C bonds which creates a relatively high activation energy for the creation of high energy optical phonons [25]. According to literature it is predicted that carbon nanotubes have an optical phonon energy of 0.15-0.2eV compared to 0.063eV for Silicon and 0.034eV for GaAs [25,26].

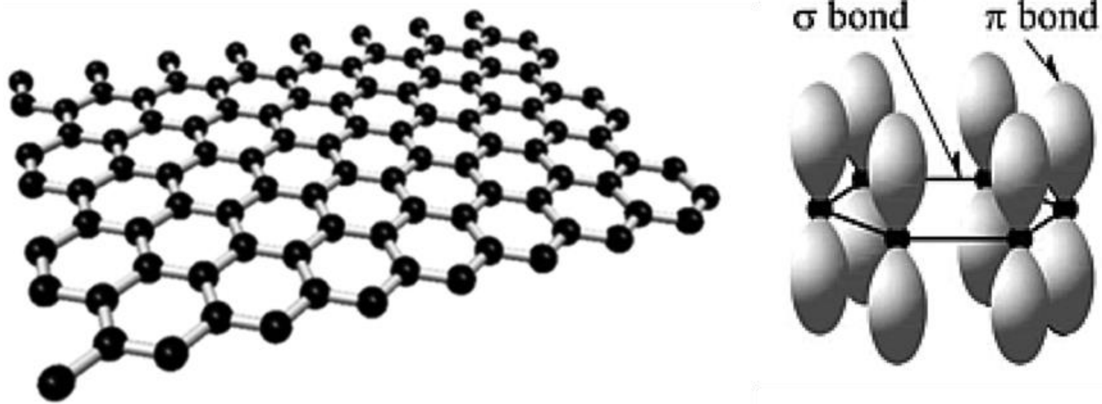

Figure 1.7: Illustration of a honeycomb sp2 graphene lattice (left) and the free bonds that produce mobile carriers states (right) [24].

A carbon nanotube's properties are defined by a chiral vector which describes the angle in which the graphene sheet is rolled and the tube diameter. Naturally carbon nanotubes come in a wide dispersion of chiralities which can have significant differences in electrical properties [27]. A chiral vector is the translation of the two unit vectors a_1 and a_2 by integer numbers m and n for a honeycomb (graphene) lattice: $C= ma_1+na_2$ (fig 1.8). The CNT bandgap energy and diameter, both of which effects the intrinsic carrier density, can be determined by the chirality vector. If |m-n| is an integer multiple of 3, then the nanotube will have a zero-energy bandgap will be a metal. For all the other (m,n) values the carbon nanotube has direct band-gap and will be a semiconductor. For large (m,n) values the diameter of the nanotube is larger and the bandgap energy is notably smaller. In some cases, the bandgap energy can be small enough that the thermal excitation of carriers can cause semiconducting CNTs to behave metallic at room temperature, these are called semi-metallic CNTs [27]. Figure 1.8 illustrates how the chiral vector can affect the CNT diameter and bandgap energy [28]. Since CNTs naturally occur with a wide dispersion of chiralities, there is a two-thirds probability of growing a semiconducting CNT and a one-third probability of growing a metallic CNT.

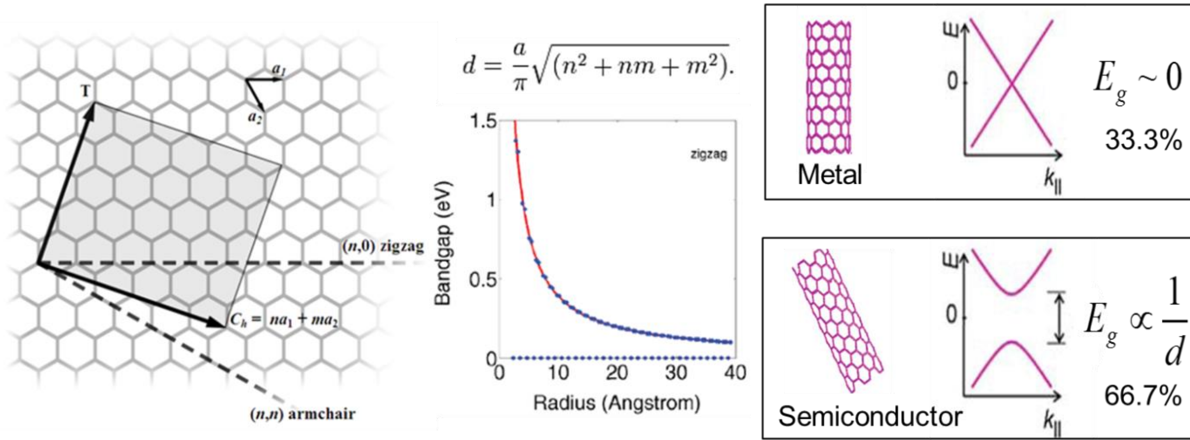

Figure 1.8: Analytical model used to determine how chirality effects the CNT properties. Lattice vector map showing how chirality corresponds to the graphene lattice (left), models used to correlate the chiral vector to CNT properties such as diameter (middle) and bandgap energy (right) [28].

Figure 1.9 illustrates a conventional Carbon Nanotube Field Effect Transistor (CNTFET) geometry. The ultimate goal is to create a CNTFET capable of ballistic transport, which occurs when charge carriers can travel across the semiconducting active region without a single scattering event. The mean-free-path, distance traveled by a carrier between scattering events, in a semiconducting CNT is greater than 1um under ideal conditions [25]. The mean-free-path and carrier mobility is particularly important for high frequency applications, where the cut-off frequency is limited by the resistance and capacitance of the device. The capacitance, particularly the drain source capacitance, can be greatly reduced to increase the cut-off frequency by increasing the channel length (equation 1.4). The channel length can be maximized without increasing the resistance provided that the channel length is less than the mean-free-path. For an ideal CNTFET with an active region length less than mean-free, <1um, the transconductance can be optimized such that the maximum cutoff frequency is greater than 1THz [29]. Ballistic transport has not yet been achieved at room temperature, but the potential of quasi-ballistic transport is the motive behind intense CNTFET research for next generation Radio Frequency

device applications [29]. CNTFETs have also have an advantage for low power applications since they typically have a low threshold voltage, which is gate bias needed to induce current during the "ON" state. The threshold voltage is related to the bandgap energy of the semiconductor which determines the energy needed to excite mobile charge carriers; CNTs have a smaller bandgap energy ~0.3-0.8eV compared to ~1.1eV for Silicon. Finally, CNTFETs are typically ambipolar which means they can work under forward and reverse bias without breakdown. This offers further device application flexibility compared to conventional FETs.

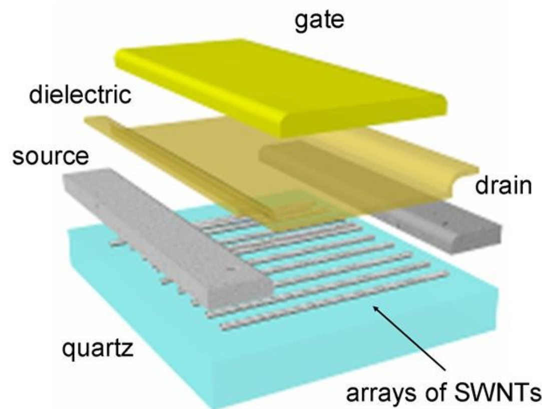

Figure 1.9: Simplified model of a top gated CNT Field Effect Transistor [30].

The primary difficulty of creating high performance CNTFETs is the inability to control the chirality dispersion. If even a few metallic nanotubes are present the conduction channel, the device be shorted leading to a high "OFF" state current and the drain-source capacitance will be much higher, both of which degrades the transconductance and the cutoff frequency. Even if all the metallic CNTs are removed, any variation in the diameters of the semiconducting CNTs will result in different threshold voltages for each nanotube. If higher gate threshold is used the smaller bandgap nanotubes will create hot electrons that increase optical phonon scattering; likewise, if a lower gate threshold is used than the larger bandgap semiconducting CNTs won't conduct current. Dispersion in nanotube electrical properties not only degrades the performance

of individual CNTFETs, but also limits process scalability due to an increased variance in switching dynamics of transistors on the wafer scale.

Material Parameters	Ideal RF Applications
Diameter	1.2-1.8nm
Purity	99.999% Semiconducting
Length	> Channel Length (~1um)
Alignment	All Parallel
Density	> 10 NT/um
Uniformity	Wafer Scale

Table 1.1: Table listing all the most important wafer scale material parameters that must be satisfied to achieve optimal CNTFETs for radio frequency applications [29].

Researchers have determined the ideal material parameters to create optimal CNTFETs for Radio Frequency applications [29]. So far achieving 100% purity, meaning all metallic CNTs in the array are removed, has been the most difficult to achieve. In the next section, we will review promising purification techniques including some original research. Despite the significant progress in achieving purified arrays of CNTs, there is still a need for reliable methods to characterize the CNT arrays with high enough resolution to get precise and accurate statistics on purity, doping, and defect density. Without proper characterization methods CNT processing optimization remains difficult to achieve. In this thesis, I will explore novel electronic characterization techniques to quantify CNT array purity and gain insight into electronic phenomena that may affect CNTFET processing and performance.

1.5 CNT Processing for Purification, Densification, and Alignment

A common method for selective chirality purification is density gradient ultracentrifugation (DGU). DGU works by separating bulk carbon nanotubes, grown using arc-discharge, based on their buoyant density using a high-speed centrifuge [31]. The hollow cylindrical geometry of single wall CNT means that the buoyant density of the nanotube is directly related to the surface-to-volume ratio which is directly correlated to the nanotube. Larger diameter nanotubes correspond to smaller buoyant density whereas smaller CNTs have higher density. Also, bundled and multi-walled CNTs have a notably higher density than individual single walled nanotubes allowing for the complete removal of unwanted CNT morphologies [31]. The density gradient is formed by dissolving short CNT in the proper aqueous solution [31]. After the centrifugation the CNTs settle at the point in gradient solution that correlates with its buoyant density; after which the fractionation process is used to separate the layers of the CNT based on density, or diameter. The effectiveness this method for chirality separation is evident in figure 1.10, which shows layers of different nanotube chiralities after the centrifuge process. This is a highly effective way of not only separating the semiconducting nanotubes from the metallic nanotubes, but also to obtain a narrow distribution of chirality which minimizes the issue of diameter dispersion.

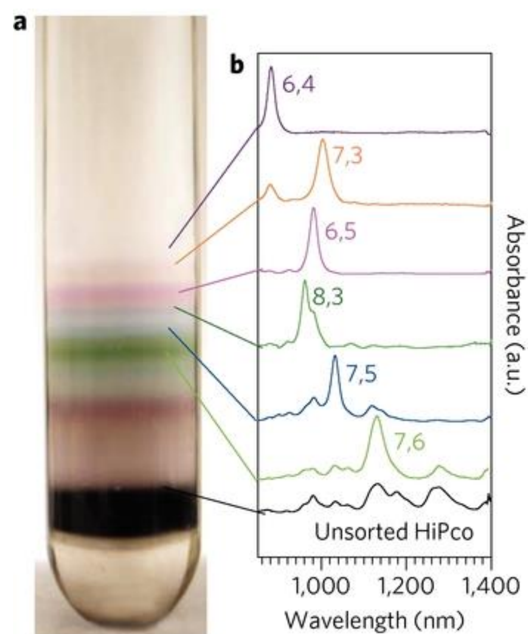

Figure 1.10: On the left is a picture of a vial of CNTs in solution after high density ultra-centrifuge. Notice that the colors, which are real, correspond to the differing nanotube diameters. On the right is an infrared absorbance spectrum showing the different chiral species in each layer [32].

However, there are several problems with this method that need to be addressed before it can be used for electronic device applications. First, the CNTs are hydrophobic so naturally they will conglomerate in clusters of bundled nanotubes, to mitigate this issue it is common practice to add surfactants to the aqueous solution to prevent clustering. The surfactant must be amphiphilic and be able to coat all CNTs individually and uniformly. Moreover, the surfactant coating must be reversible so that surfactant encapsulation can easily be removed after fractionation [31]. The commonly used surfactants are not easily removed without leaving residue that act as a contamination source during device fabrication. The second major drawback is that the nanotubes, which are already typically short (<10um), can be further broken up during the centrifugation process. This creates a distribution of nanotube lengths which implies that some of them will be too short to span the active region of the device. To achieve the maximum

device conductance, these short CNT sections need to be deposited and aligned on a suitable substrate which adds further processing complexity [33]. These issues with surfactant residue and alignment are observable in figure 1.11, where a centrifuge purified sample of aqueous CNTs was deposited on a quartz substrate.

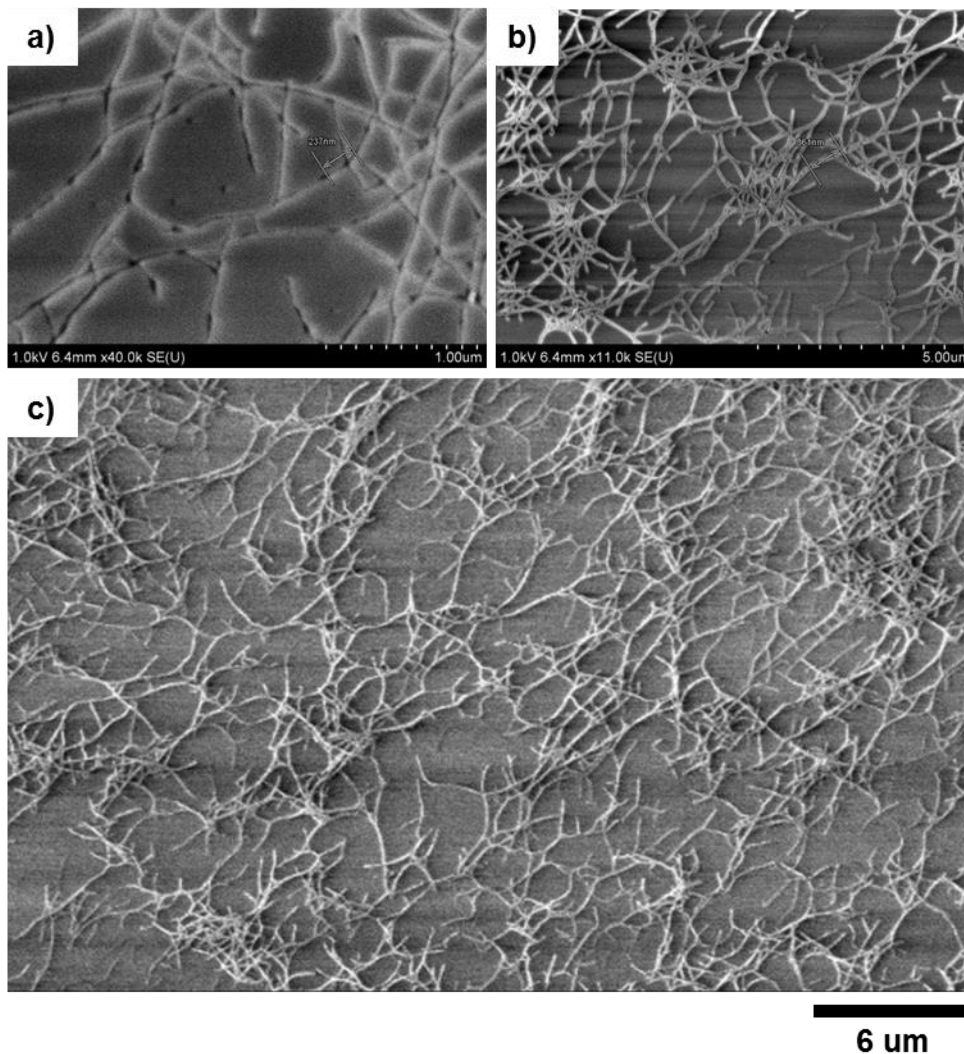

Figure 1.11: (a-c) Original Scanning Electron Microscopy (SEM) image of a typical sample of as deposited random networks of DGU purified CNTs. The remaining surfactant after deposition can be seen under high resolution.

In a random network of nanotubes, such as the ones produced from DGU purified CNTs, the CNTs electronically interact with each other and the desired near ballistic carrier transport in

individual SWNT is not observed. Growing aligned CNTs reduces intertubular interactions and the overall conduction path length across the active region which enhances the effective conductance of the CNT transistor [34]. Single crystalline quartz or sapphire can be used for substrate-directed aligned CNT growth when the substrate is cut at a specific orientation [35,36]. After annealing the cut substrate well defined step edges form, it is believed that the well-defined step edges create an anisotropic van der walls interaction that induces aligned CNT growth perpendicular to the step edges. The degree of alignment is directly related to the quality of the cut and annealing time of the quartz or sapphire crystal prior to the growth of CNTs [37].

Chemical vapor deposition (CVD) is the most common process for growing aligned CNTs [36]. An inert gas such as Argon passes through a liquid bubbler filled with a carbon source, typically a hydrocarbon such as ethanol or methanol, to create a vapor. In the CVD furnace a sample with strips of metal (typically Fe or Cu) on quartz is annealed. The high temperature drives off any oxygen creating pure (unoxidized) metal nanoparticles to catalyze the decomposition of the hydrocarbon. Patterning of the metal thin film allows for the control of the CNT array location. Similar to a Vapor-Liquid-Solid growth mechanism, the metal nanoparticle behaves like a liquid at the growth temperature, typically above 800°C. Once the carbon precursor gas is introduced at high temperature, the carbon is absorbed into the metal catalyst particle. Once the metal nanoparticle is saturated with carbon, the carbon precipitates out of the particle in its lowest free energy state in the form of carbon nanotubes [38]. The diameter of the CNT is correlated to the size and shape of the nanoparticle during growth. Smaller nanoparticles will yield smaller diameter CNTs as opposed to bigger nanoparticles; to minimize the diameter distribution of the CNTs, the metal nanoparticle size must be controlled. Ostwald ripening during the metal nanoparticle annealing is unavoidable and not well controlled, it can widen the

nanoparticle size distribution before CNT growth. Also, as the CNTs grows, the nanoparticle can change in size and/or shape which may cause a shift in CNT chirality mid-growth. The growth parameters that control the final size distribution of the metal nanoparticles after annealing is the metal type, starting thickness of a metal film, the surface energy of the substrate, the annealing time, and temperature. As the CNTs grow they prefer to align perpendicular to the step edges of the substrate and parallel to the flow direction of the gases [39]. To achieve a high degree of alignment, clean Y-cut quartz is used as a substrate and is placed in the CVD chamber such that the gas flows perpendicular to the step edges. If done correctly, long, nearly defect free, CNTs can be grown with a very high degree of alignment as seen in figure 1.12.

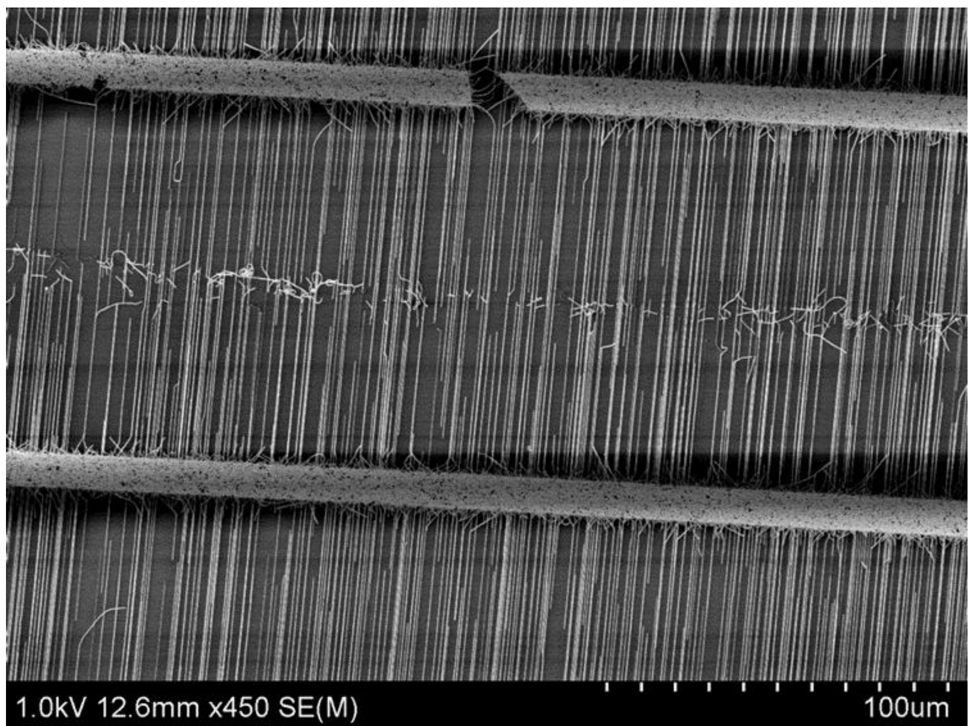

Figure 1.12: Scanning Electron Microscope image of an CVD grown aligned CNT array on quartz.

Aside from the issues with the presence of semiconducting and metallic nanotubes, one major issue with conventional CVD growth of Carbon Nanotubes on quartz is the density

limitation. It has been shown that it is difficult to grow arrays above a density of 5-7NT/um using this method. The primary reason is believed to be caused by misaligned CNT in the growth region and sporadic alignment of short NTs in the metal catalyst regions which appear as stripes of dense CNTs in figure 1.12. These nanotubes block the further growth of adjacent nanotubes which minimizes the potential growth density. In a research group at Duke, they mitigated this issue by using a cyclical etch-regrowth process to achieve aligned arrays above the desired 10NT/um [40]. The idea is to introduce water vapor and take away the carbon precursor for short times to etch away the short stray CNTs in the metal catalyst regions. The time used for the etch back is short enough to prevent notable etching of the long nanotubes, but long enough to get rid of the short stray nanotubes; the result of this etch back can be seen in figure 1.13a. After the etch-back the precursor was reintroduced to grow more nanotubes in places that were previously blocked by stray NTs leading to much higher nanotube densities on quartz [40].

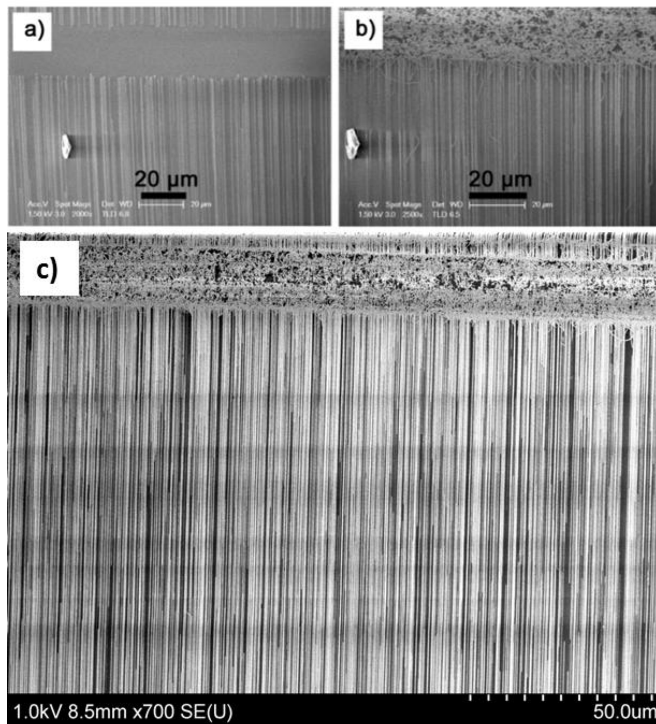

Figure 1.13: SEM images during different stages of the regrowth process: initial etch (a), first regrowth (b), and several regrowth cycle (c) [40].

One of the first methods of mitigating the effects of metallic carbon nanotubes from CNTFETs was selective electrical breakdown. The semiconducting NTs naturally do not conduct electricity as well as the metallic nanotubes when there is no gate voltage. Before the gate is added, a CNTFET behaves like a diode. When applying a large bias voltage across the diode most of the current will flow through the metallic CNTs. The metallic nanotubes will decompose at high current levels while semiconducting nanotubes remain intact [38]. One disadvantage of this simple method is that without a proper gate structure the semiconducting nanotubes may not stay in the "OFF" state after the metallic nanotubes have decomposed; current flow in the remaining semiconducting nanotubes may damage them. However, the major downfall of this technique is that the metallic nanotubes typically only decompose at a point leaving behind most the remaining metallic nanotube. Although the metal nanotubes no longer contribute to current flow, they still cause parasitic capacitances that diminishes FET performance. Plus, the decomposed section of the nanotube turns into amorphous carbon residue that coats the sample causing additional issues. The goal of the purification method proposed in the next section, called thermocapillary purification, is to get rid of the entire metal nanotube in a scalable way such that this is no longer an issue for device degradation.

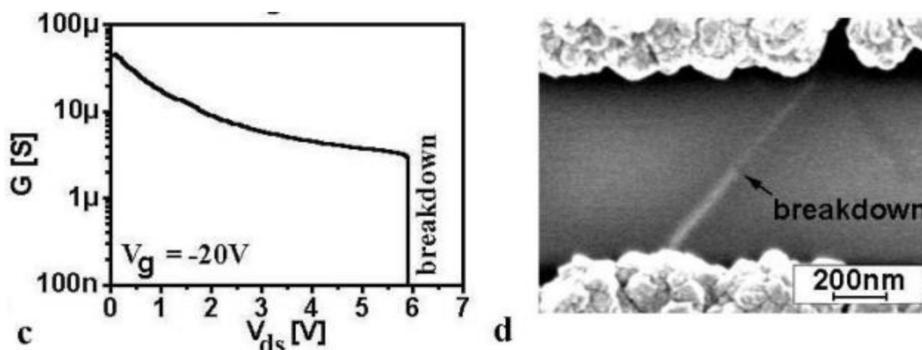

Figure 1.14: On the left is a plot of the conductance of a CNT diode with a metal nanotube across the terminals, notice the conductivity goes to zero after the metal nanotube breakdown. On the right is a SEM image of the diode, notice the breakdown only occurs at point [41].

1.6 Thermocapillary Purification of Aligned Arrays of Carbon Nanotubes

In collaboration with the Professor John Rogers, we developed a novel process to get rid of all the metallic nanotubes in an as-grown aligned CNT array to improve device performance. To do this we utilized the thermocapillary effect of a thermal resist layer deposited onto a nanotube array [42,43,44,45]. The idea is that the thermal resists dewetts to expose only nanotubes that have been selectively heated. An O_2 plasma etch is used to remove the exposed nanotubes while the other nanotubes remain protected by the thermal resist layer. An advantage of this method is that the entire metal NT is removed to eliminate any parasitic capacitance contributions. Also, the thermal resist layer should completely protect the semiconducting nanotubes during etching and can be easily removed. Since the powers needed to produce selective heating to initiate dewetting is notably less than the breakdown method, incidental damage to the semiconducting tubes from current flow is no longer an issue.

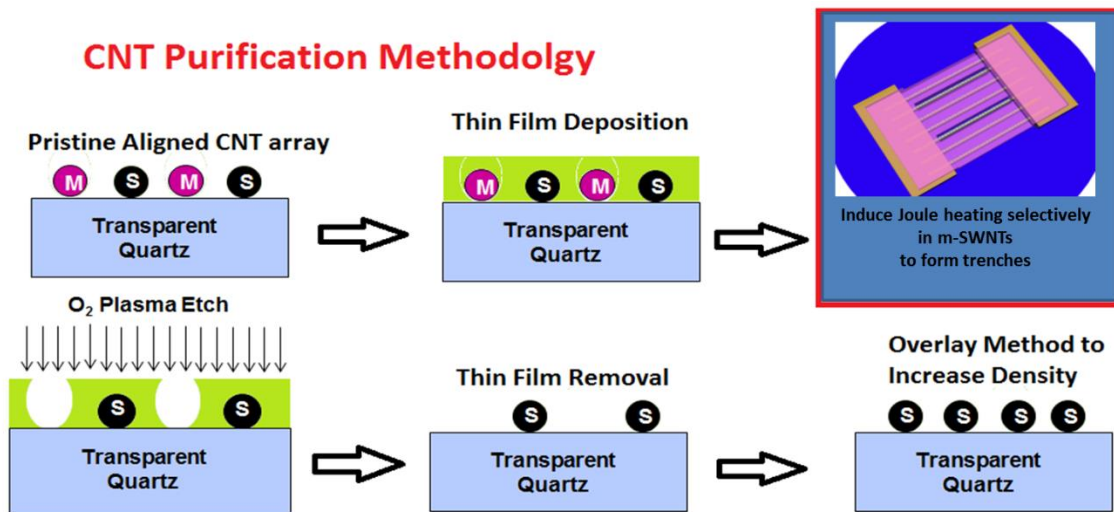

Figure 1.15: Illustration of the thermocapillary purification process.

An essential aspect of this process is the ability to create selective heating in the metal nanotubes. The other important aspect is to create narrow (width), deep (height) trenches to

expose only the metal nanotube and not nearby adjacent nanotubes. The theory for how to achieve this is summarize in figure 1.16, notice that the power density inside the nanotube is the primary experimental variable for creating the ideal trench; higher power yields better trenches [42]. However, since the thermal resist layer is temperature sensitive it is also important to control the background temperature and heat distribution to avoid exposing semiconducting CNTs and spontaneous dewetting.

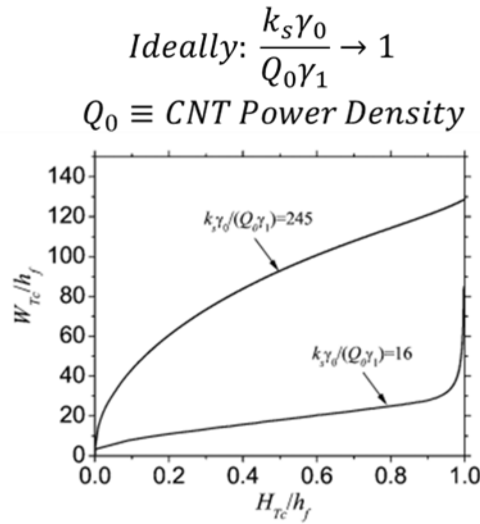

Figure 1.16: Analytical model showing how power density effects the trench geometry, each line represents the normalized depth (x-axis) and width (y-axis) for a trench at a set power density, for our small molecule thermal resist [42].

Under the optimal experimental conditions, background temperature and power density, a well-defined trench can be formed over a metallic nanotube [43]. An example of a good trench formed over a metal nanotube by applying a bias across metal contacts can be seen in the AFM images in figure 1.17.

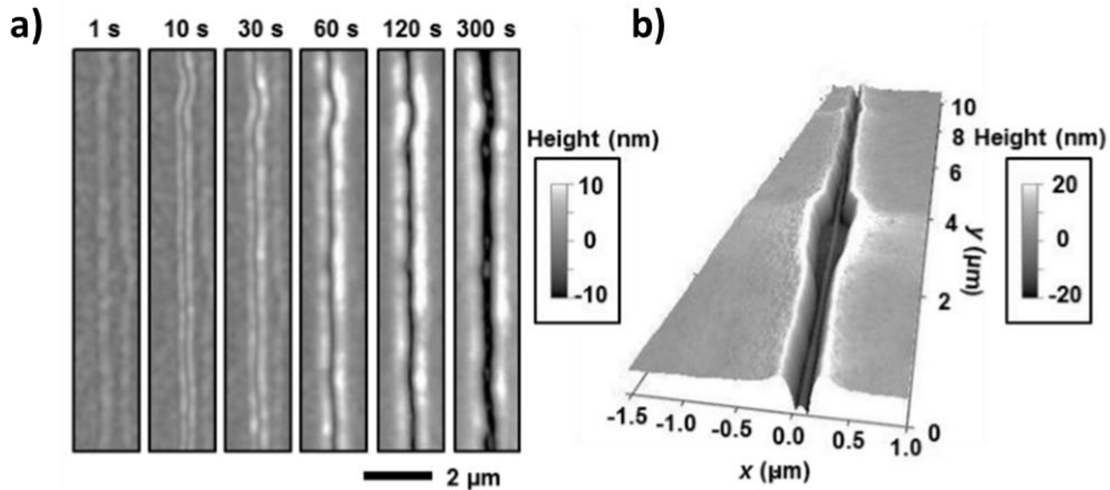

Figure 1.17: (a) consecutive AFM images of a trench formed over a metallic carbon nanotube over a period of time, (b) 3D AFM image of a trench to show the non-ideal size and shape of a typical trench [43].

One method of controlling the CNT power density is Joule heating by directly injecting current into a CNT diode [44]. A diode is patterned onto an aligned array of CNTs and a probe is used to apply a voltage drop across the device to drive a current across the CNTs. Similar to the electrical breakdown method, the current prefers to flow across the metal nanotubes only causing them to rapidly heat up. However, the thermal resist layer is very sensitive to temperature gradient, hence the semiconducting nanotubes must be turned off to prevent any current flow and subsequent heating. To do this without a gate electrode, the metal type used for the two-terminals should create a Schottky contact with the semiconducting nanotubes [45]. After extensive characterization it was found that Ti contacts work the best for selective heating and contact patterning. As seen in figure 1.18, the probes used in this technique can only process one device at a time; attempts at making more intricate patterns of devices for multiple device purification has been studied with limited success [44]. Difficulties arise from resistance in the contact network which can non-uniformly increase the background temperature and change the

experimental conditions. It was shown that the heat issue can be mitigated by operating under vacuum and applying a periodic voltage to improve temperature stability.

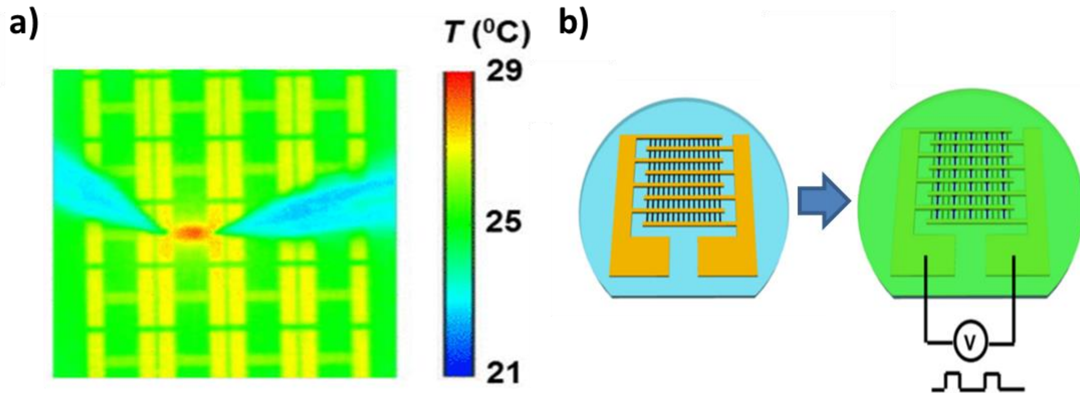

Figure 1.18: (a) Thermal IR imaging of probes and CNT device. (b) Illustration of a proposed experimental setup for creating larger arrays of purified CNTs, the green represents the thermal resist layer and the step function represents the periodic voltage across the device [44].

For a CNT purification method to have a high impact on CNT device fabrication there must be a pathway to make the technique scalable. To make the thermocapillary purification scalable we had to develop a variation of the technique that allows multiple device purification in one step without a lot of excess heat. This means that using probes is not a likely pathway, instead we developed a way to utilize microwave energy to couple directly to an array of CNT diodes. To do so we used a single mode microwave reactor that can control the background temperature. Once we illuminated a device under 300W of 2.45Ghz microwave power there was a notable trench that formed over the metal nanotubes which can be seen in figure 1.20 [45]. The CNT power density was much stronger near the contact by looking at the depth of the trench. The non-uniformity of the trench depth with distance away from the contact implies that there is a microwave near-field effect associated with driving current in the metallic CNTs [45]. We will utilize this near-field effect to optimize the microwave driven thermocapillary purification process.

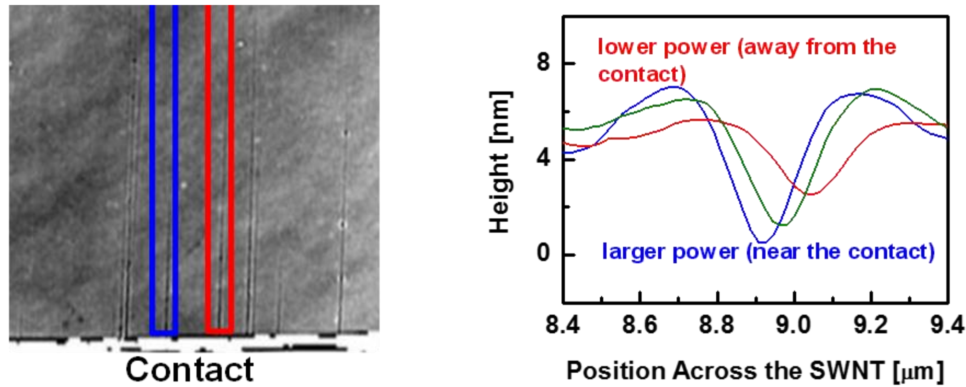

Figure 1.19: AFM data of a CNT-metal contact interface after microwave heating at 2.45GHz. Topology image (left) and line-cuts, parallel to contact, (right) of the trenches formed [45].

We were able to use microwave nearfields to drive the thermocapillary effect using dipole antenna arrays which couple to incident high frequency electric field. To optimize and map the effect of the antenna geometry on the microwave near-field, we utilized ANSYS High Frequency Simulation Software to model the electromagnetics using finite element analysis [45]. The simulations were conducted as a 3-dimensional steady state model with a single polarized microwave source propagating in the Z-direction as seen on figure 1.20a, the source is polarized parallel to the dipole length. In the actual experiment setup, the microwave reactor has multiple polarizing slits which act as a multiple polarized microwave sources. This FEA simulation maps the Electric Field strength across the sample if it were positioned normal to one slit. The color maps show a relatively uniform E-field enhancement perpendicular to the dipole gap and notable decrease as one moves further away from the metal contact. This distribution is repeated for any number of dipole array configurations and it agrees with the experimental observation in figure 1.19, the E-field strength quickly decrease the further away from the metal contact. For figures 1.20c-e, we used a parametric solver to plot the tradeoffs between the dipole geometry and E-field enhancement at the center of the gap. It was shown that the dipole gap size had the biggest impact on the near-field enhancement, so short gaps, <10um, showed the best results. The dipole

length and width shows a linear correlation to the enhancement and is the most important for maximizing the amount of active space for devices. It was shown that the width size had a much weaker slope, ~0.9 $V/V_{incident}$ (enhancement factor) per 100um, than the length size, ~2.4 $V/V_{incident}$ (enhancement factor) per 100um. This favors a wider dipole for optimal wafer device density, but higher aspect ratio, length/width, diode antennas will have a higher enhancement factor.

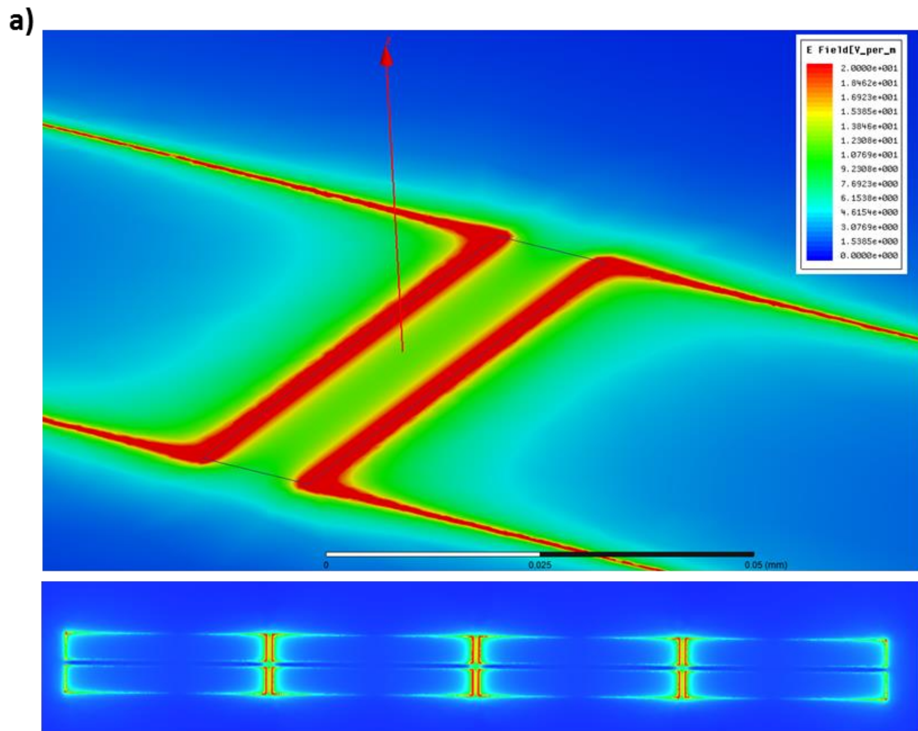

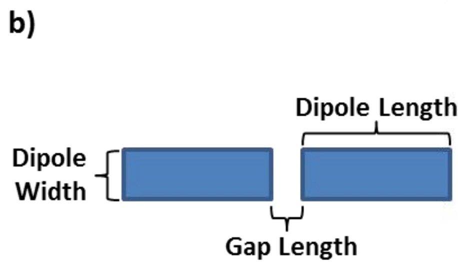

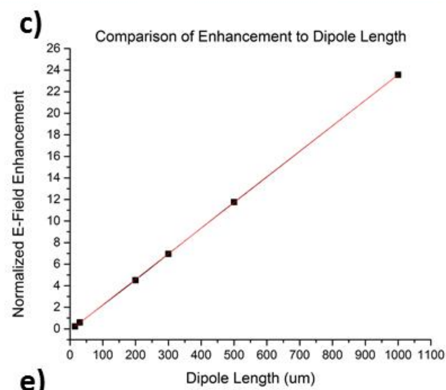

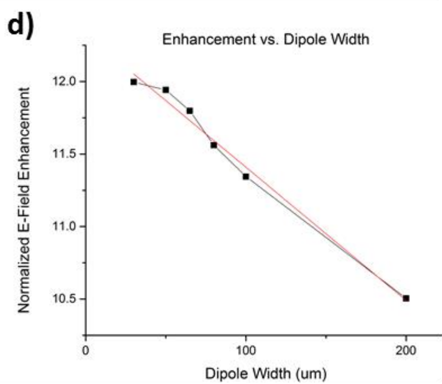

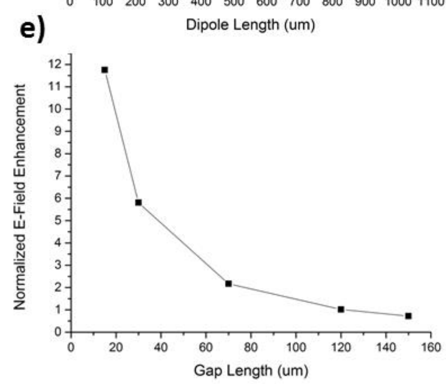

Figure 1.20: (a) Color Map of the normalized E-field enhancement (V/m) simulation data for various dipole configurations [45]. (b-e) Parametric data shows the tradeoff between characteristics of the geometric model (x-axis) and the E-field enhancement (y-axis).

Using the information regarding metal contact type acquired from the joule heating thermocapillary experiment and the electromagnetic simulations we successfully developed a process to create full trenches leading to purified devices. The microwave thermocapillary purification method works with arrays of wide area, narrow gap CNT diodes on the wafer scale [45]. To conclusively prove that this method has high selectivity and capable of achieving 100% purification, single nanotube devices were patterned with dipole contacts, probes were used to take the IV curves of several devices before purification to identify them as semiconducting or metallic. After exposing the entire sample with multiple devices in the microwave reactor an AFM was used to characterize the trench depths, there is a clear bimodal distribution of measured trench depths which correspond perfectly with the previously identified nanotube type (figure 1.21b). Wide array nanotube devices were purified and made into transistors to show the before and after effect of the purification method, the ON/OFF ratios were vastly improved on multiple devices simultaneously [45]. These successful experimental results strongly implies that there is real potential in this method for scalable CNT purification.

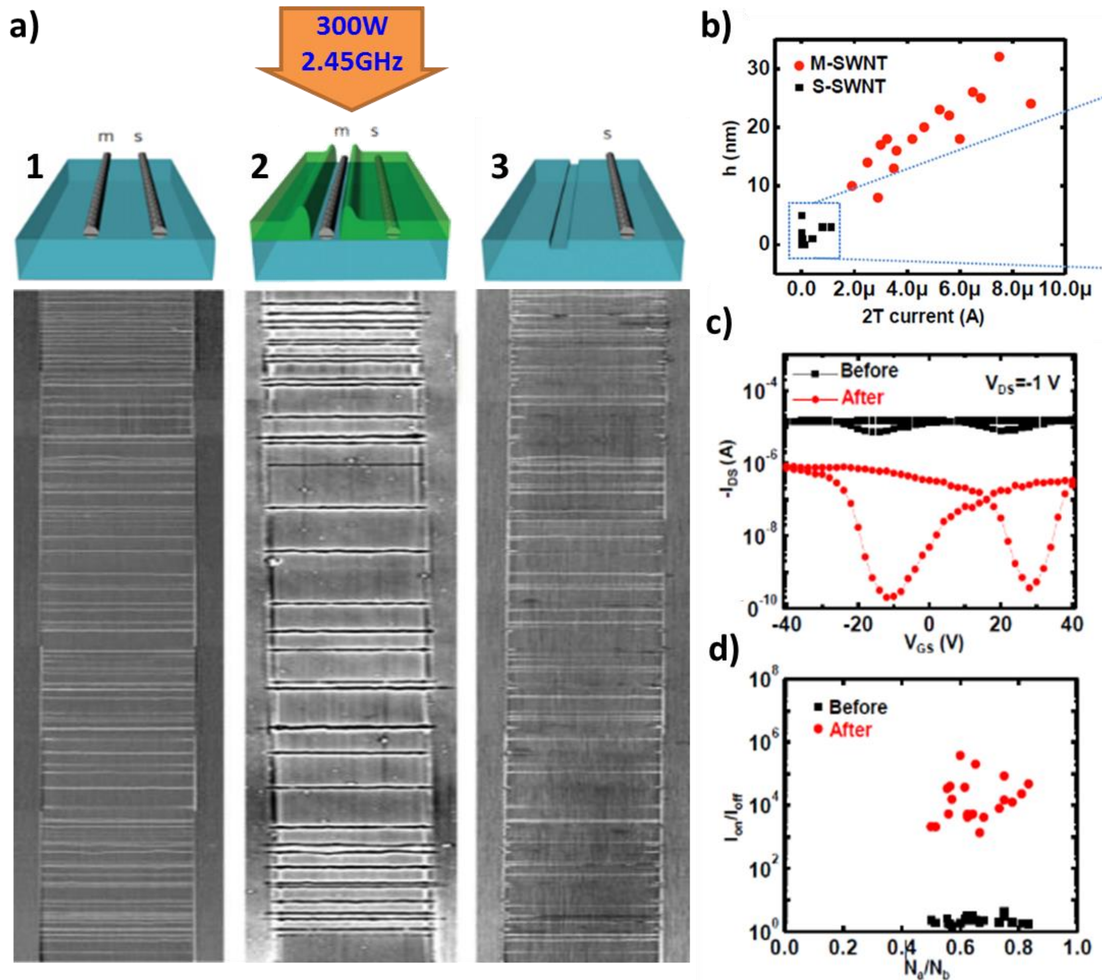

Figure 1.21: (a) illustration and AFM data corresponding to the steps of the purification process: CNT growth (left), trench formation (middle), and O_2 etch (right) to show the precision and accuracy of microwave trench formation. (b) Trench data and (c-d) IV statistics of several devices before and after thermocapillary purification [45].

For the thermocapillary method the main issue is the incidental damage of the remaining semiconducting nanotubes which diminishes the device's optimal performance. This occurs during the oxygen plasma etching phase of the process where the metallic nanotubes are supposed to be the only nanotubes that are etched away. The thermocapillary layer is only capable of protecting the nanotubes at a minimum thickness. Any nanotube that is close to a metallic nanotube can be damaged also if the trench is wide enough that it reduces the resist

layer thickness below the critical minimum thickness. The trench width limits the maximum metallic CNT density that this method can purify without damaging the semiconducting CNTs. A thinner resist layer can be used to keep the trench width narrow, but it increases the required selectivity to avoid the formation of shallow trenches over the semiconducting nanotubes which can also lead to tube damage [45]. In figure 1.22, a probabilistic model is used to determine the density limit for purification of as-grown CNT arrays depending on the ratio of metallic nanotubes in the array and the estimated average trench width. It is shown that working with nanotube arrays that are pre-enriched with more semiconducting nanotubes, greater than the naturally occurring 66%, can benefit from higher density limit. If the density is too high than the adjacent semiconducting NTs are too close to the metallic NTs to avoid being etched away which diminishes the post-purification density limiting the maximum current.

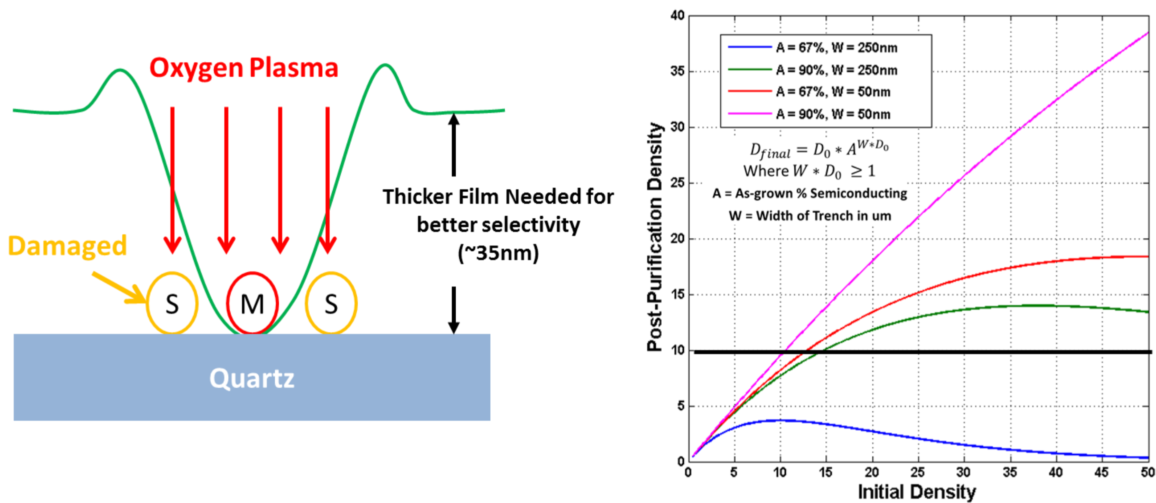

Figure 1.22: (left) Illustration of the sample geometry that causes damage to semiconducting nanotubes for high density samples. (right) Plot of the tradeoff between maximum post-purification density and initial as-grown density for different experimental conditions.

1.7 Summary of Motivation and Thesis Overview

The creation of in-situ doped planar GaAs nanowires is a notable advancement in nanoscale semiconductors for next generation transistors. However, the creation of corrugations and lateral doping in planar nanowires leaves some unanswered questions regarding the transport properties of these nanowires. What do these corrugations imply about the distribution of dopants and how does this affect the carrier transport and distribution across the nanowire? Understanding these questions are important to improving growth methods and understanding device performance. These questions also allude to a broader challenge to develop methods to characterize and spatially map electrical transport properties at the nanoscale. In this thesis, we will explore the use of novel scan probe characterization methods with nanoscale spatial resolution to helps us create a physical model to explain the electronic effects of this phenomena in planar GaAs NWs.

There have been attempts to use both highly enriched semiconducting CNT seeds and long arrays of purified aligned CNTs to make high performance CNTFETs. Until there is a process to create high density, aligned, >99% purified arrays of defect free single walled carbon nanotubes, next generation nanotube transistors will not perform at their desired optimal device performance. All the methods used to achieve these process goals require quantitative and phenomenological data on nanotube electronic character, semiconducting or metallic, before and after growth/purification at the individual tube level. In this thesis, we were able to achieve this using a novel scan probe technique called Microwave Impedance Microscopy, which revealed many interesting CNT electronic phenomena which provide insight into CNT growth and device physics.

Chapter 1 is used to define the motivation behind this work, which is to advance the development of next generation nanoscale electronic devices. It introduces the important aspects of devices and the nanoscale materials, notably GaAs NWs and CNTs, that make them. A detailed overview of planar GaAs nanowire growth and CNT purification are presented. This provides a basis for the challenges that can be solved and types of phenomena that can be revealed by developing novel methods for electronic material characterization at the nanoscale.

Chapter 2 is an overview of the scan probe techniques used to perform the electronic characterization at the nanoscale. The techniques reviewed include atomic force microscopy (AFM), electric force microscopy (EFM), scanning capacitance microscopy (SCM), microwave impedance microscopy (MIM), and scanning near-field optical microscopy (SNOM). A variation of these techniques, except SCM, are used for electronic material analysis throughout the thesis.

Chapter 3 describes a detailed analysis of dopant distributions in novel planar GaAs nanowires. Our goal is to detect morphology correlated perturbations in a map of the electron density and dopants acquired using MIM-AFM. The results were verified using SNOM and EFM and used to build a physical model to describe band bending in the doped regions of the planar nanowire.

Chapter 4 describes a novel application of MIM to map the electrical properties of SWCNTs with nanometer resolution. We developed new methods for MIM characterization to direct observe, for the first time, the morphologically correlated electronic response of interesting CNT phenomena such as bundles, semi-metals, intra-tubular junctions, and CNT-metal interfaces. We show that this method of CNT metrology has major advantages for purification inspection compared to tradition characterization techniques.

Chapter 5 is a study of MIM characterization of CNT using a non-contact scanning methodology. Challenges which limit the flexibility of the contact mode MIM-AFM inspection methods presented in Chapter 4, are explored with detail and overcome using tapping and force curve scanning geometries. An in depth experimental analysis of how the tip-cantilever affects observable signal is presented to show the advantages and issues with non-contact MIM. The successful characterization of CNTs electronic properties in a non-contact geometry shows more promise for high resolution capacitance mapping than conventional contact mode MIM methods.

Chapter 6 provides an overview of the work presented and goals achieved in the thesis. Here we will also introduce possible directions for future.

1.8 References

1 Shankland, Stephen. “Moore's Law: The rule that really matters in tech.” *CNET Sci-Tech News.* October, 2012. https://www.cnet.com/news/moores-law-the-rule-that-really-matters-in-tech/

2 Felix, P., and J.l. Pelloie. "General Calculation of MOSFET Transconductance in the Saturation Range: Electric-field-induced Improvement in the Strong-inversion Region." Solid-State Electronics: 463-71. Print.

3 Pozar, David M. Microwave Engineering: Chapter 10. *John Wiley & Sons*, 2009.

4 Duan, Xiangfeng, et al. "High-performance thin-film transistors using semiconductor nanowires and nanoribbons." Nature 425.6955 (2003): 274-278.

5 Pillarisetty, Ravi. "Academic and industry research progress in germanium nanodevices." Nature 479.7373 (2011): 324-328.

6 Nikoobakht, B.; Wang, X.; Herzing, A.; Shi, J. “Scalable Synthesis and Device Integration of Self-Registered One-Dimensional Zinc Oxide Nanostructures and Related Materials.” Chem. Soc. Rev. (2013): 42, 342-365.

7 Nikoobakht, B. “Toward Industrial-Scale Fabrication of Nanowire-Based Devices.” *Chem. Mater.* (2007): *19*, 5279-5284.

8 A. Razavieh, P. K. Mohseni, K. Jung, S. Mehrotra, S. Das, S. Suslov, X. Li, G. Klimeck, D. B. Janes, and J. Appenzeller, "Effect of Diameter Variation on Electrical Characteristics of Schottky Barrier Indium Arsenide Nanowire Field-Effect Transistors", ACS Nano 8(6), 6281-6287 (2014).

9 Riel, Heike, et al. "III–V compound semiconductor transistors—from planar to nanowire structures." MRS Bulletin 39.08 (2014): 668-677.

10 Stormer H. L. Gossard A. C. Dingle, R. and W. Wiegmann. Electron mobilities in modulation doped semiconductor heterojunction superlattices. Journal of Applied Physics, 33:666, 1978.

11 X. Miao, K. D. Chabak, C. Zhang, P. K. Mohseni, D. E. Walker Jr., and X. Li, "High Speed Planar GaAs Nanowire Arrays with fmax > 75 GHz by Wafer-Scale Bottom-up Growth," Nano Letters, (2014).

12 Fortuna, S. A.; Wen, J.; Chun, I. S.; Li, X. “Planar GaAs Nanowires on GaAs (100) Substrates: Self-Aligned, Nearly Twin-Defect Free, and Transfer-Printable.” Nano Lett. (2008): 8, 4421-4427.

13 Zhang, C.; Dowdy, R.; Li, X. "High Voltage Gain MESFET Amplifier Using Self-Aligned MOCVD Grown Planar GaAs Nanowires", Device Research Conference (DRC), 2013, 63-64.

14 S.A. Fortuna, J. Wen, I.S. Chun, and X. Li, "Planar GaAs Nanowires on GaAs (100) Substrates: Self-Aligned, Nearly Twin-Defect Free, and Transfer-Printable", Nano Letters 8 (12), 4421-4427 (2008).

15 Tsivion, D.; Schvartzman, M.; Popovitz-Biro, R.; von Huth, P.; Joselevich, E. "Guided Growth of Millimeter-Long Horizontal Nanowires with Controlled Orientations." Science (2011): 333, 1003-1007.

16 R. S. Dowdy, D. A. Walko, and X. Li, "Relationship between plannar GaAs nanowire growth direction and substrate orientation" Nanotechnology 24, 035304 (2013).

17 C. Zhang, X. Miao, P. K. Mohseni, W. Choi, and X. Li, "Site-Controlled Planar GaAs Nanowire Growth: Yield and Mechanism", Nano Letters, 14 (12), 6836 (2014)

18 S.A. Fortuna and X. Li, "Metal-catalyzed semiconductor nanowires: a review on the control of growth directions", Semicond. Sci. Technol. 25 (2010) 024005.

19 R. Dowdy, C. Zhang, P. K. Mohseni, S. A. Fortuna, J-G Wen, J. J. Coleman, and X. Li, "Perturbation of Au-assisted Planar GaAs Nanowire Growth by p-Type Dopant Impurities", Optical Materials Express Vol. 3, Issue 10, pp. 1687-1697 (2013).

20 Iijima, Sumio, and Toshinari Ichihashi. "Single-shell carbon nanotubes of 1-nm diameter." Nature 363.6430 (1993): 603-605.

21 Avouris, Phaedon. "Carbon nanotube electronics and optoelectronics." MRS Bulletin 29.6 (2004): 403-410.

22 Avouris, Ph, et al. "Carbon nanotube transistors and logic circuits." Physica B: Condensed Matter 323.1 (2002): 6-14.

23 Park, Ji-Young. "Band Structure and Electron Transport Physics of One-Dimensional SWNTs." Ed. Ali Javey and Jing Kong. Carbon Nanotube Electronics. New York: Springer, 2009.

24 Bourgeat-Lami, Elodie, Jenny Faucheu, and Amélie Noël. "Latex routes to graphene-based nanocomposites." Polymer Chemistry 6.30 (2015): 5323-5357.

25 Wong, H-S. Philip, and Deji Akinwande. Carbon nanotube and graphene device physics. Cambridge University Press, 2011.

26 Amirtharaj, Paul M., and David G. Seiler. "Optical properties of semiconductors." Handbook of Optics Volume II Devices Measurements and Properties Second Edition 158 (1994).

27 Dai, Hongjie, Ali Javey, Eric Pop, David Mann, Woong Kim, and Yuerui Lu. "Electrical Transport Properties And Field Effect Transistors Of Carbon Nanotubes." Nano: Brief Reports and Reviews 01.01 (2006): 1-13.

28 Anantram, M. P., and F. Leonard. "Physics of carbon nanotube electronic devices." Reports on progress in physics 69.3 (2006): 507.

29 Koswatta, Siyuranga O., et al. "Ultimate RF performance potential of carbon electronics." IEEE Transactions on Microwave Theory and Techniques 59.10 (2011): 2739-2750.

30 Kloeppel, James E. New kind of transistor radios show capability of nanotube technology." Illinois New Bureau: Physical Sciences. University of Illinois. Janurary 28, 2008.

31 Green, Alexander A., and Mark C. Hersam. "Ultracentrifugation of single-walled nanotubes." Materials Today 10.12 (2007): 59-60.

32 Ghosh, Saunab, Sergei M. Bachilo, and R. Bruce Weisman. "Advanced sorting of single-walled carbon nanotubes by nonlinear density-gradient ultracentrifugation." Nature nanotechnology 5.6 (2010): 443-450.

33 Schroter, Michael, Martin Claus, Paulius Sakalas, M. Haferlach, and Dawei Wang. "Carbon Nanotube FET Technology for Radio-Frequency Electronics: State-of-the-Art Overview." IEEE Journal of the Electron Devices Society 1.1 (2013): 9-20.

34 Kim, Sunkook. "Single-walled Carbon Nanotube Transistors." Ed. Faiz Rahman. Nanostructures in Electronics and Photonics. Singapore: Pan Stanford Pub., 2008.

35 Kocabas, C.; Hur, S. -H.; Gaur, A.; Meitl, M. A.; Shim M.; Rogers, J. A. "Guided growth of large-scale, horizontally aligned arrays of single-walled carbon nanotubes and their use in thin-film transistors." Small (2005), 1, 1110 1116.

36 Ding, L.; Yuan, D.; Liu J. "Growth of high-density parallel arrays of long single-walled carbon nanotubes on quartz substrates." J. Am. Chem. Soc. (2008), 130, 5428 5429.

37 Xiao, Jianliang, et al. "Alignment controlled growth of single-walled carbon nanotubes on quartz substrates." Nano letters 9.12 (2009): 4311-4319.

38 Hofmann, Marlo, Sreekar Bhaviripudi, and Jing Kong. "Direct Synthesis and Integration of SWNT Devices." Ed. Ali Javey and Jing Kong. Carbon Nanotube Electronics. New York: Springer, 2009.

39 Jeon, Seokwoo, et al. "Growth of serpentine carbon nanotubes on quartz substrates and their electrical properties." Nano Research 1.5 (2008): 427-433.

40 Li, Jinghua, et al. "Growth of high-density-aligned and semiconducting-enriched single-walled carbon nanotubes: decoupling the conflict between density and selectivity." ACS Nano 8.1 (2013): 554-562.

41 Seidel, R. V., et al. "Bias dependence and electrical breakdown of small diameter single-walled carbon nanotubes." Journal of applied physics 96.11 (2004): 6694-6699.

42 J. Song, C. Lu, C. Zhang, S.H. Jin, Y. Li, S.N. Dunham, X. Xie, F. Du, Y. Huang, and J.A. Rogers, "Modeling of Thermocapillary flow to purify single-walled Carbon Nanotubes," RSC Advances 4, (2014): 42454-42461.

43 Jin, Sung Hun, et al. "Using nanoscale thermocapillary flows to create arrays of purely semiconducting single-walled carbon nanotubes." Nature nanotechnology 8.5 (2013): 347-355.

44 Xie, Xu, et al. "Direct current injection and thermocapillary flow for purification of aligned arrays of single-walled carbon nanotubes." Journal of Applied Physics 117.13 (2015): 134303.

45 Xie, Xu, et al. "Microwave purification of large-area horizontally aligned arrays of single-walled carbon nanotubes." Nature communications 5 (2014): 5332.

CHAPTER 2

SCAN PROBE METHODS FOR ELECTRONIC MATERIAL CHARACTERIZATION

With the advent of the nanotechnology era there is a need for novel semiconducting materials that possess desirable thermal and electrical properties in the quantum regime. Although nanoscale materials, such as the ones mentioned in Chapter 1, have shown promise for next generation solid-state devices, creating devices that perform at a level that can compete with current technology has proven difficult. The challenge of controlling and optimizing the processes needed to create high performance devices at the wafer scale is exasperated by experimental obstacles related to electronic materials characterization at the nanoscale. Various approaches to spatially characterize electronic materials using scan probe microscopy are introduced in this section.

2.1 Introduction

A traditional method for measuring electronic properties is to fabricate a device and derive the material's transport properties. Device fabrication is used to determine the extrinsic characteristics of a simple device made of novel nanoscale materials. For example, taking the diode I-V curve response can provide insight into the transconductance of a material. The biggest shortcoming of this method is the inability to separate the impact of device geometry and processing conditions from the intrinsic material properties in the measured data. Since there is no spatial information, there is no simple way to visualize local issues, such as nanoscale defects, that can affect the overall device performance.

Exploring and developing new scan probe microscopy techniques for nanoscale electronic materials characterization is the primary objective of my doctoral research. Scan probe microscopy covers a broad range of methods and has proven to be very useful for nanomaterial characterization. This is due to its tip limited resolution limit which can probe very small features (10-100nm). The primary methods for scan probe characterization of electronic materials that we will be explore in this work fall into three categories: Electric-force AFM, Capacitance AFM, and Optical Near-field AFM. Each method requires a unique physical model for each material system. These physical models are meant to be qualitative guidelines for how we expect the observed signals to respond to the electronic attributes that we are trying to detect. The physical models are idealized such that they only incorporate the phenomenon that is most relevant to the desired observable signal which excludes artifacts and small signal contributions. To further validate the scan probe image data other methods can be used to verify topology and electronic character such as electron microscopy, device fabrication, and complementary scan probe techniques. The physical model is used to interpret the measured observables to create a complete understanding of the electronic properties of a nanoscale material system. For novel material systems, the observations are compared directly with other published theory and experimental data of similarly characterized material systems to ensure that the analysis is consistent and accurate.

2.2 Atomic Force Microscopy

Atomic Force Microscopy is a form of imaging that can spatially map atomic scale forces. The forces are detected by a tip attached to a cantilever probe, this localizes the detection area for each pixel in the image [1]. The XY spatial map is formed by taking nanometer steps

with piezo scanner. Under ideal experimental conditions, the spatial resolution of any AFM technique is limited by the width of the tip apex, typically <100nm. The tip is either very close or touching the sample so that it can feel the van der walls forces on the surface. All short-range forces, including Van der Waals and electrostatic forces, are detected by a change in the bending mechanics of the tip-cantilever. Conventionally AFM is used to map the sub-nanometer variations in surface topography by detecting the Van der Waals forces [1]. The versatility of this technique allows for the simultaneous detection of other nanoscale forces along with surface topology which is useful for measuring structurally correlated electrical properties.

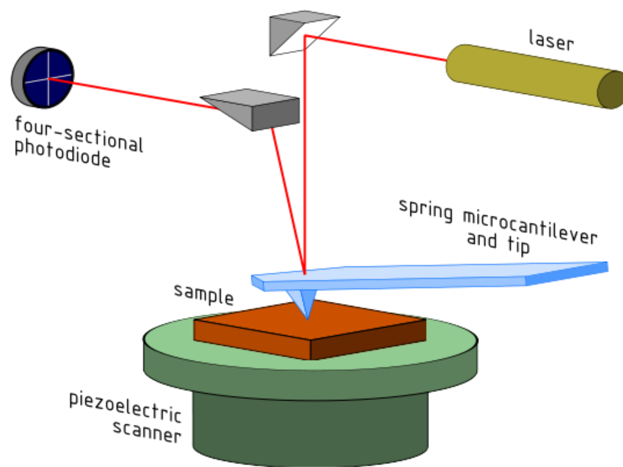

Figure 2.1: Simple model of an Atomic Force Microscopy configuration where the movement of the cantilever is recorded by the laser and laser diode.

When using a sharp tip (<25nm) in a stable ambient environment, it is possible to achieve an accurate topology resolution of less than a nanometer. One method for obtaining this resolution is tapping mode AFM. For our setup, this is done by driving a sinusoidal tip-cantilever oscillation using Z-piezo coupled to the probe and detecting spatial changes in the tip's oscillation amplitude and phase to map topology. Depending on the length and stiffness of the cantilever, each tip has a unique free amplitude oscillation at a frequency in range of ~10kHz-1MHz. The oscillation produces additional higher frequency harmonic oscillations from the

different bending motions of cantilever. The lateral oscillation, Z-direction, at the first harmonic, equal to the piezo drive frequency, contains the most information regarding the surface topology [1]. When the probe is lowered to the surface the tip begins tapping on the surface, the cantilever oscillation information is recorded by a laser beam that reflects off the backside of the cantilever onto a spatially sensitive, high-resolution photo-detector. The photodetector signal is correlated to the Z-piezo drive signal of the cantilever *via* a lock-in amplifier. When the tip is in good condition (clean), the amplitude and phase of the tip oscillation can be mathematically converted into nanometers with high accuracy. When the Van der Waals forces interact with the tip, the attractive forces dominate when lightly tapping the surface; when the tip can't get any closer to the surface the repulsive forces dominate [1]. Hence, operating in the repulsive force tapping regime produces the most accurate topology map. Measuring and understanding the details of the tapping dynamics is important to avoid artifacts when working with scan probe techniques.

AFM can be an important tool for the characterization of electronic materials at the nanoscale. The ability to image surface topology with sub-nanometer resolution allows for the mapping of roughness, crystal defects, and grain boundaries in thin films and low dimensional materials. This can provide insight into the origin of electron scattering and device defects. In collaboration with Prof Xuling Li's group, we utilized AFM to image the morphology of epitaxially grown monolayer MoS_2 to help optimize growth conditions. Single atomic layer MoS_2 is a 2-dimensional semiconductor with favorable physical and electronic properties. We know that grain boundary scattering degrades the transport properties and the grain boundary size can be controlled by growth conditions. Figure 2.2a and b are the topology and tapping phase images of a single monolayer MoS_2 crystal. The topology image shows the beginning stages of multi-layer growth in the center of the MoS_2 and the crystalline step-edges of the

substrate underneath it. The phase image reveals symmetrical grain boundaries formed from two single triangular crystals growing in the opposite orientation; notice these grain boundaries are barely visible in the topology image. Figure 2.2c is a topology image of a continuous layer of monolayer MoS_2; it reveals at the risen grain boundaries that are typically less than 1.5nm tall and a monolayer of MoS_2 is 0.6 nm tall. Fully developed multilayer MoS_2 nanocrystals appear as a series of small triangular planes inside larger triangular planes. The resolution is good enough that someone could count the number of atomic layers and grains in the MoS_2 crystal. We can use AFM to measure the defect density and average grain size under different growth conditions to optimize the production of single crystal, defect free, monolayer MoS_2. The ability to detect these unique physical morphologies in nanoscale electronic materials such as monolayer MoS_2 using AFM is paramount for next generation devices.

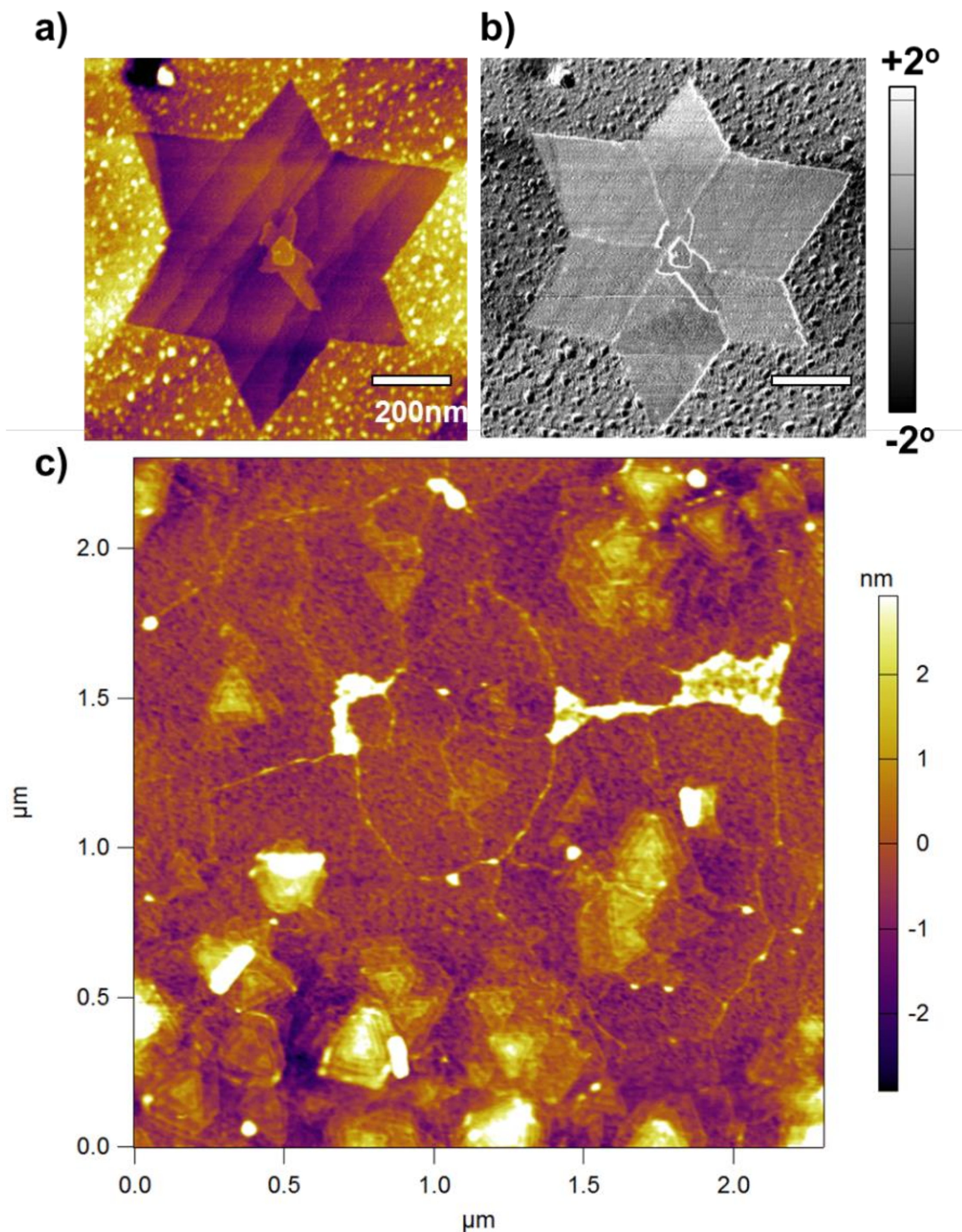

Figure 2.2: AFM topology (a) and phase (b) maps of a single atomic layer flake of MoS_2. (c) AFM topology map of a continuously grown monolayer MoS_2, the grain boundaries between single crystals are visible and examples of multi-layer MoS_2 can be seen toward the bottom of the image.

2.3 Electric Force Microscopy

Electric Force Microscopy (EFM) is a scan probe technique that uses a conductive AFM tip to detect short-range electrostatic forces to map surface potential and capacitance. For this method the observable deflection signal, is driven by a sinusoidal tip bias, is sensitive to a complex function of Van der Waals and coulomb forces [2,3]. EFM is typically operated in a dual pass liftmode in which the electrical data is recorded when the tip is a finite distance away from the sample surface so that the tip isn't touching the sample. This is important detail since the contribution of Van der Waals forces fall off much faster than the electric forces with increasing tip-surface separation [4]. In the first pass, a tapping scan maps the surface topology without tip bias; in the second pass a non-contact scan maps the Coulomb forces driven by a modulated tip bias at a fixed tip-sample Z offset (20-200nm) without a piezoelectric driven mechanical oscillation. This ensures that any spatial changes deflection in the second pass of the EFM scan can only be caused by the electrostatically coupling to sample surface. The electrostatic forces (F) which are detected by the cantilever deflection is given by:

$$F = \frac{1}{2}(\Delta V)^2 \frac{\partial C(z)}{\partial z} \qquad (2.1)$$

Where $\Delta V = V_{tip} - V_{surf}$ and C(z) is the tip-sample capacitance as a function of tip-sample separation, z. A tip bias, which contains a DC and AC component, is used to drive the electrostatic forces. The amplitude of the tip bias, V_{DC} and V_{AC}, and the frequency of the AC component, ω, determines the tip bias voltage, V_{tip}, according to equation 2.2.

$$V_{tip} = V_{DC} + V_{AC}\sin(\omega t) \qquad (2.2)$$

The total force detected by the tip is a summation of several force contributions that occur at different harmonic frequencies accord to the following three equations:

$$F_{DC} = \frac{1}{2}\left[(V_{DC} - V_{surf})^2 + \frac{{V_{AC}}^2}{2}\right]\frac{\partial C(z)}{\partial z} \qquad (2.3)$$

$$F_{1\omega} = \frac{1}{2}(V_{DC} - V_{surf})V_{AC}\frac{\partial C(z)}{\partial z}\sin(\omega t) \quad (2.4)$$

$$F_{2\omega} = \frac{1}{4}V_{AC}\frac{\partial C(z)}{\partial z}\cos(2\omega t) \quad (2.5)$$

For Kelvin Probe Microscopy (KPFM), a variant of EFM, both the tip-sample capacitance and the surface potential can be measured by demodulating at the first and second harmonic of the drive frequency [5,6]. The surface potential is measured using a feedback loop to adjust V_{DC} such that the first force harmonic, $F_{1\omega}$, is equal to zero. This implies that a numeric map of the relative magnitude of V_{DC} is equal to a map of the surface potential [5]. To obtain quantitative data for the surface potential map, the capacitance gradient ($\frac{\partial C(z)}{\partial z}$) and the AC drive voltage (V_{AC}) contributions can be nullified by mapping $\frac{|F_{1\omega}|}{|F_{2\omega}|}$ [6]. Literature studies have successfully measured surface potential with very high SNR using KPFM on semiconducting nanowires. The contrast is enhanced by adding metal contacts to inject charges into the nanowire. In the study shown in figure 2.3, the surface potential maps the effects of scattering on surface potential revealing location of strong scattering defects along the conduction path [7].

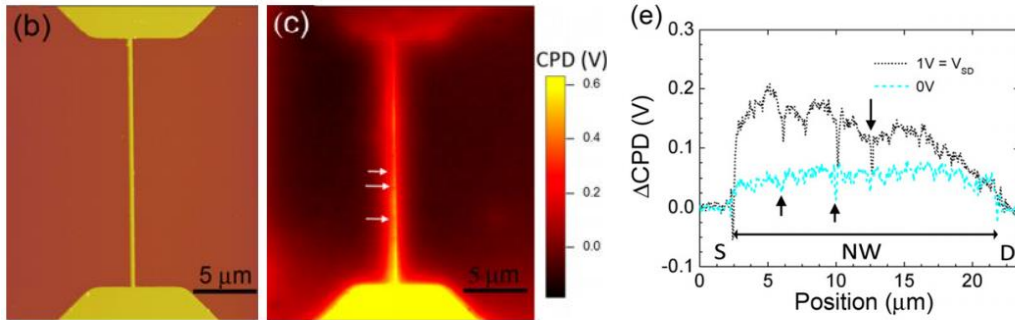

Figure 2.3: Shows an AFM image and KPFM image (top-left) of a p-doped Si Nanowire sample with ohmic contacts. On the bottom line cuts were taken of the KPM image to reveal regions of high electron scattering implying the presence of structural defects (top-right) [7].

When dealing with homogenous nanoscale electronic materials, sometimes EFM has a weak sensitivity of subtle changes in coulomb forces on the sample surface. The measured

capacitance gradient is a summation of the cantilever, sidewall, and stray capacitances in parallel with the desired tip capacitance. To avoid topography artifacts in the electrical data, the EFM must be acquired with a Z offset where the electric forces between the tip apex and sample surface are weak. The unwanted cantilever, sidewall, and stray capacitance contributions are consistently large due to the large geometry of the probe and cantilever compared to the tip apex; the capacitance contribution from the tip apex falls off much quicker with increasing Z-offset than the large geometry capacitance contributions. In addition, the resolution is reduced with larger Z offsets since the effective area of the tip-sample capacitance coupling gets larger with bigger Z offsets. This can be understood by considering that the XY spatial components have a smaller effect on the effective tip-sample distance, $r^2 = z^2 + x^2 + y^2$, which drastically effects the tip capacitance, $C_{tip} = \sum_{(X,Y)} C(r)$, when z is large. Common sources of capacitance noise that effect the SNR of the surface potential data are contamination, oxide layers, trapped surface charges, and moisture [8,9,10]. The presence of multiple noise sources and the inability to separate the coulomb data from the surface potential data due to weak SNR in the force channels makes accurate, precise, high resolution KPFM very difficult to achieve for some nanoscale electronic systems.

In our experiments, we found that operating EFM to maximize the overall sensitivity to electrical forces can be done to resolve high resolution images of tip-sample capacitance on weakly interacting surfaces. The conductive AFM tip is most sensitive to weak forces at its mechanically resonant cantilever frequency, ω_{tip}; this is how tapping mode AFM detects weak Van der Waals forces to create topology maps. The tip-sample capacitance gradient, $\frac{\partial C(z)}{\partial z}$, is most sensitive to spatial changes in coulomb forces at the its resonant cantilever frequency (100kHz – 1MHz) [11]. Typically, in conventional KPFM modulation schemes, the $F_{2\omega}$ channel,

which is linearly correlated to the capacitance gradient, has a weaker SNR than the $F_{1\omega}$ channel since it is off tip resonance. We found that by driving the tip bias at half the resonant tip-cantilever frequency, $\omega_{tip}/2$, the observable in the $F_{2\omega}$ channel, which is only sensitive to $\frac{\partial C(z)}{\partial z}$, has a much higher sensitivity to weak forces since it occurs at the resonant frequency, $2\omega = \omega_{tip}$. This method is a non-destructive technique for the precise qualitative mapping of surface capacitance with very high sensitivity without the need of a strong tip bias and feedback loops. Despite the promise EFM shows for the characterization of nanoscale electronic materials, its sensitivity to capacitance in the non-contact operating mode, at longer distances $z > 20$nm, implies that geometric capacitance coupling will dominate the signal. For nanoscale electronic materials such as carbon nanotubes, the electronic or quantum capacitance contains more detailed information on intrinsic electrical properties than the geometric capacitance, which is only sensitive to the frequency dependent permittivity. This limitation is shown in figure 2.4, where an AFM and EFM image of a carbon nanotube array is shown. CNTs which have a notably weak capacitance signal show strong contrast using our dual-pass EFM method driven at half the resonant tip-cantilever frequency. However, the EFM resolution is not tip-limited and its sensitivity to intrinsic electronic properties isn't strong enough to pick up the difference between semiconducting and metallic CNTs. Although it's sensitivity and resolution have limitations, for our experiments the ability to confidently map coulomb forces without the influence of topology makes EFM and KPFM a great complimentary tool for checking observations made with more sensitive scan probe capacitance measurements for topology driven artifacts.

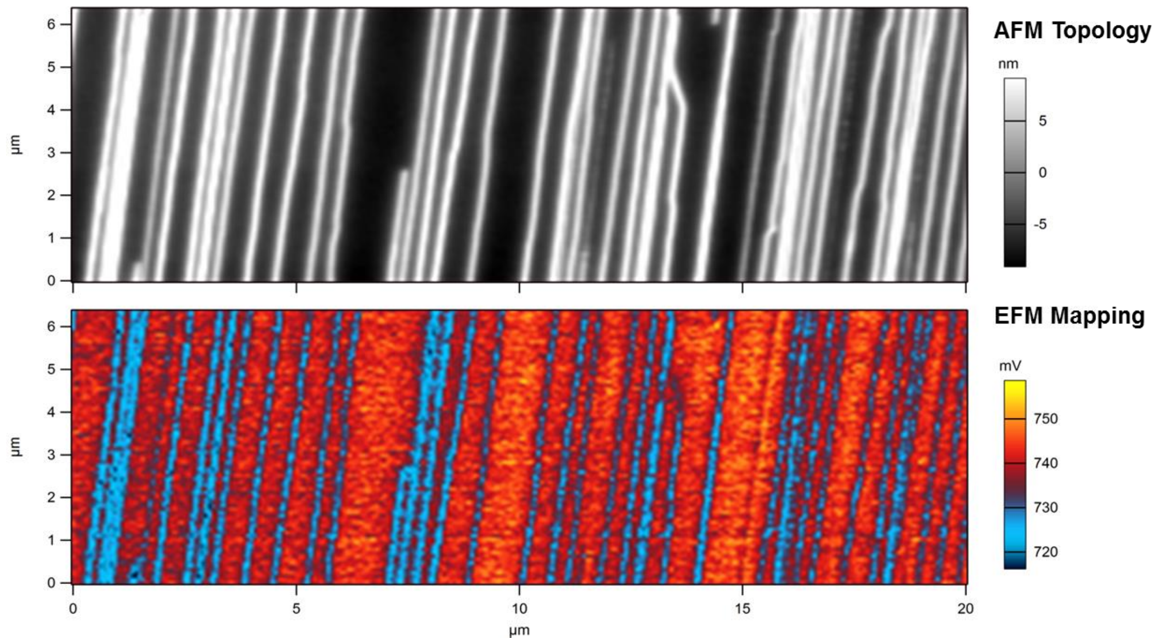

Figure 2.4: AFM topology (top) and EFM map (bottom) of an as-grown array of aligned SWNTs. Areas of blue show a strong deflection EFM signal, however there is no clear contrast selectivity.

2.4 Scanning Capacitance Microscopy

Scanning Capacitance Microscopy (SCM) is a contact mode scan-probe technique that utilizes a capacitance sensor connected to the probe to detect spatial changes in the sample's electronic capacitance, which can be correlated to the spatial distribution of doping and static charge beneath the tip [12]. Scanning Capacitance Microscopy detects the electronic properties in a material by forming a capacitor geometry that behaves like a parallel plate capacitor, where the sample is the dielectric medium and the conducting plates are the tip and a ground plane under the sample. A capacitance sensor, which can be made from a LCR resonator, is implemented in series with the tip and sample to detect spatial variations in capacitance [12]. An AC tip bias, typically <10MHz, drives a oscillating capacitance signal which is demodulated *via* a lock-in amplifier to obtain dC/dV phase and amplitude data [12]. The capacitance signal is measured across the entire thickness of the sample from the tip to a ground plane on the backside

of the sample. For SCM the signal observable, dC/dV, defined as the slope of the C-V curve, comes from driving carriers in and out of the conduction band using the tip potential. The amplitude of the dC/dV signal can be correlated to the doping concentration and the built-in potential and regions of space charge can be mapped by applying DC bias to offset the flat-band voltage shift in the C-V curve [13,14]. The C-V curve response to doping and built-in charge this is illustrated in figure 2.5.

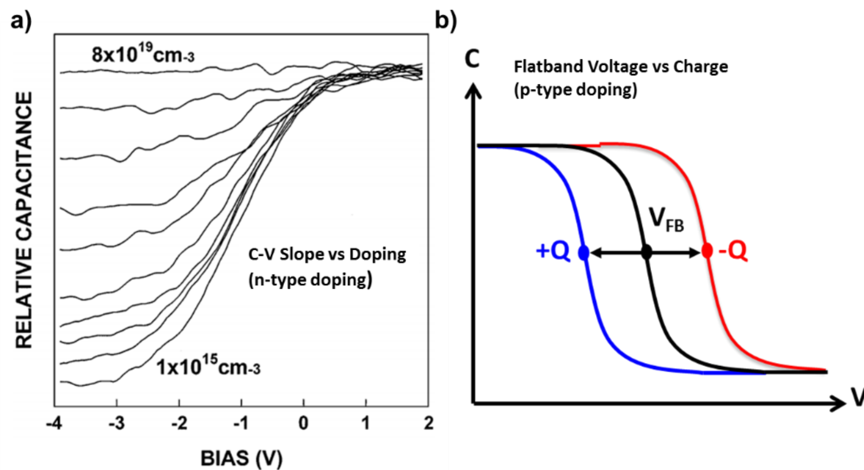

Figure 2.5: (a) Experimental data for the Capacitance – Voltage response of a semiconductor with differing levels of doping, the higher dope semiconductor had a smaller C-V response. (b) Illustration of how the C-V curve responds to built-in charge, it laterally shifts the entire curve along the Voltage axis (x-axis). [12,13,14]

For some materials a very high tip potential is needed to achieve maximum sensitivity (~aF) to changes in capacitance. However, this can modify the depletion width near interfaces, including the tip-sample interface, and can shift the local Fermi energy level making intrinsic measurements difficult. Observable capacitance contrast can result from spatial changes in layer thickness, dielectric constant variations, built-in charge, and charge density. SCM is effective at measuring local changes in doping concentration in bulk electronic material systems [12]. A capacitance-voltage (C-V) map is easy to acquire on bulk electronic materials due to the comparatively large sample volume to generate a stable, average sample response. The

usefulness of SCM for mapping nanoscale bulk devices can be seen in figure 2.6, where different DC offsets reveal the space charge region for a PN junction on a sRAM sample [15]. However, increasing the tip potential to increase sensitivity is not always an option when trying to obtain insight into the material's intrinsic properties. This is because high tip potentials can inject charges and cause dielectric breakdown which can permanently change the sample's local electronic properties. The small volumetric cross section of low dimensional materials means its will have a small, sometimes negligible, influence on the measured average dielectric constant across the sample. Instead other variations in the capacitor's dielectric medium, sample volume, such as roughness, trapped charges, and internal E-fields would act as noise, even if a higher tip potential used to increase sensitivity. For SCM, the lack of sensitivity to surface capacitance at low tip biases limits its feasibility for the characterization of low dimensional materials.

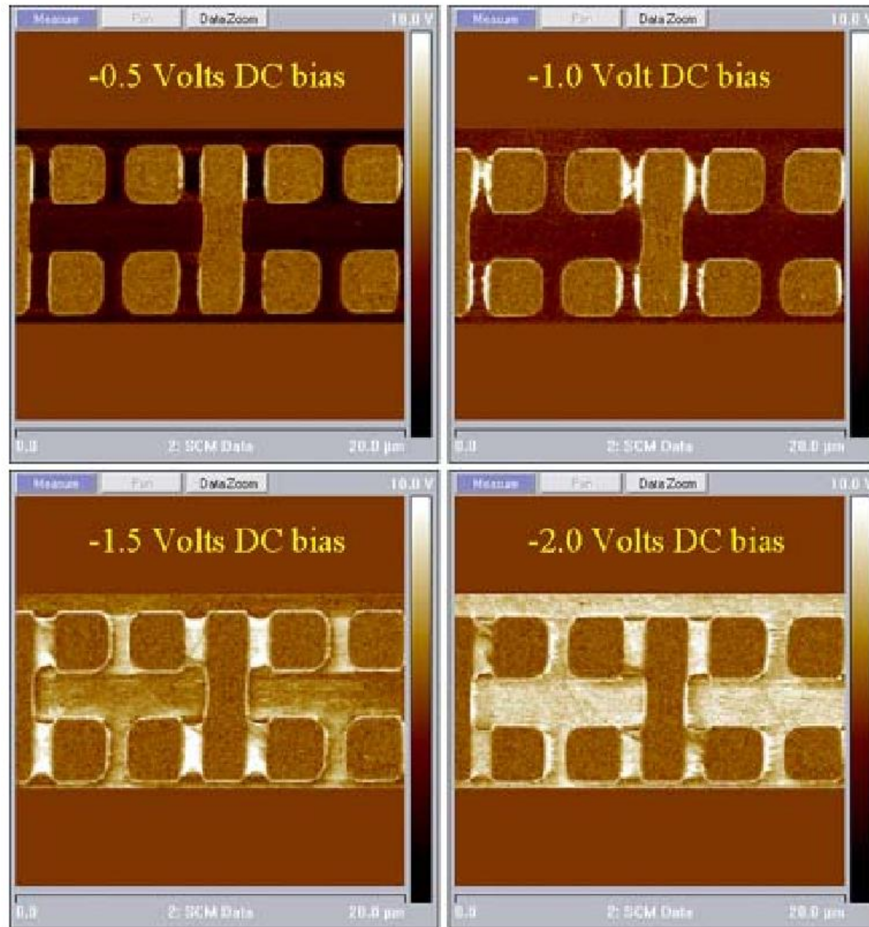

Figure 2.6: SCM data of an SRAM sample with different DC tip offsets. The squares are p-type with n-type in-between. The space charge region is shown are areas of high signal shown as white color contrast between the square regions. [15]

2.5 Microwave Impedance Microscopy

Microwave Impedance Microscopy (MIM), is an electrical probe cantilever based scan-probe technique that maps changes in surface impedance using microwave reflectivity [16,17,18,19,20]. The probe has a built-in RF transmission line that extends down the cantilever and to the tip apex. Since the tip apex is much smaller than the microwave wavelength, it has a large impedance and it creates a strong near-field. This means that when properly calibrated almost all the microwave power should be reflected at the tip, $\Gamma \rightarrow 1$, the only way for the tip to dissipate or transmit energy is through near-field coupling between the tip and sample surface.

The observable is a spatial map of the deviation from total reflection, Γ(x,y), with tip limited resolution. Contrast originates from spatial variations in the tip-sample impedance which is sensitive to the resistive and capacitive properties of the dielectric sample volume coupled to the tip [21].

In a simple transmission line model, the microwave field interaction from the end of the tip can be characterized by the reflection coefficient:

$$\Gamma = \Gamma_r + i\,\Gamma_i = \frac{Z_{sample} - Z_{int}}{Z_{sample} + Z_{int}} \qquad (2.6)$$

where Γ_r is the in-phase voltage reflection and Γ_i is the out-of-phase component, Z_{sample} is the impedance of the sample surface coupled to the near-field, Z_{int} refers to "internal circuit", from the probe which is well matched to the 50 Ohm system electronics using a matching network. In general, Z_{int} is much smaller than Z_{sample}; the sample impedance is necessarily high, >>50Ω, due to the nanoscale volume of the near-field which is limited by the RF penetration depth and the size of the tip apex. This implies that the observable signal will be close to total reflection, after proper calibration; using this assumption one can expand equation 2.6 using a Taylor series expansion [22]. In equation 2.7 the observable is given by:

$$\Gamma(x, y) = 1 - Z_{int}\left[2Z_{sample}^{-1} + 2Z_{sample}^{-2} + \cdots\right] \sim Z_{sample}^{-1}(x, y) \quad (2.7)$$

Notice that the higher order terms have a negligible effect on the reflectivity because the sample impedance is so high. The measured real and imaginary parts of the reflection correspond to the resistive and capacitive components of the sample impedance. The resistive component is originates from RF power leakage through the tip-sample interaction, in some experimental geometries it is sensitive to changes in surface conductivity. The real part of the reflection couples strongly to metallic structures that absorb RF power and/or extend the RF transmission line to radiate more power. The imaginary part of the reflection is sensitive to the capacitance

component of the sample impedance, which is highly sensitive to coulomb interactions unique to the tip-sample geometry. Developing an analytical and physical model for tip-sample interaction is essential for the analysis of MIM data. In most cases, we can assume no significant tunneling through the tip for non-metals, unless there is direct conductive pathway to ground. Sensitivity to surface conductivity is possible, but in our model we neglect the dissipative term, $Re[Z_{sample}] = R_s$, in equation 2.8; we assume only the capacitive coupling contributes significantly. Hence, the observable RF reflectivity will be dominated by and linearly proportional to the sample capacitance, C_s. The sample impedance given by equation 2.8, it is a good start for interpreting the MIM data after calibration, discussed later in the chapter 2.

$$Z_{sample} = R_s - \frac{i}{\omega C_s} \rightarrow \Gamma_i(x,y) \sim C_{tip-sample}(x,y) \qquad (2.8)$$

MIM has a high sensitivity (~aF) to subtle changes in electrical properties and a low surface penetration depth when operating at low RF power, which limits the detection range of the microwave “near-field” to just below the tip apex. The two primary origins of contrast are changing permittivity and electron density on the surface. This contrasts with Scanning Capacitance Microscopy (SCM) which directly probes changes in capacitance across the entire sample thickness using a high voltage sinusoidal tip potential [23]. The major advantage of MIM for nanoscale electronic material characterization is the low penetration depth of the near-field which makes this technique is most sensitive to the electronic properties near the sample surface. This is important for maximizing the signal contributions of nanoscale materials relative to their bulk substrates. MIM also uses lower power than SCM since the tip-sample capacitance coupling to the microwave near-field is much shorter range; in contrast, high power is needed for SCM to capacitively couple across the sample thickness. Capacitance coupling at microwave frequencies is unique because it is not a sensitive to all coulomb forces, only mobile charges that are fast

enough to react to the high frequency oscillation without damping couple strongly to the microwave signal. In other words, free mobile charge carriers can couple strongly, however, bounded charge carriers couple according to the material's frequency dependent dielectric constant and static charges don't couple at all. This implies that typical electronic material characteristics such as dopant density, ionized defects, and built-in charge cannot be measured directly. Only the mobile carrier density distribution resulting from morphological and electronic phenomena can be revealed.

The MIM-AFM system used for this research is composed of an Asylum MFP3D AFM, PrimeNano MIM electronics, a tip holder connected to a matching network via a coaxial cable, and a specialized MIM tip. MIM is conventionally done in contact mode where the tip remains in direct contact with the sample for the entire scan period. A matching network allows for the transmission of a low power RF signal, (-10dB at 3 GHz) to the apex of the tip by connecting the probe to RF reflectometer electronics which converts the microwave reflection at the tip into data. The signal is reflected from the sample-tip interface and coupled into an RF Mixer which resolves the in-phase reflection, Γ_r, and the out-of-phase reflection, Γ_i in data channels that are isolated and mapped independently. The RF electronics returns the in-phase and out-phase components of the reflection in the form of arbitrary voltage changes in the I and Q channel as seen in figure 2.7. The AFM controller spatially records the I and Q values along with the AFM topography data. The desire reflection information is from the apex of the tip, but there is an impedance change between the tip and measured frame of reference from differing path lengths of the incident and reflected signals and impedance mismatch between the matching network and the tip. This shift in the frame of reference leads to a phase mismatch between the I and Q

channel and the desired S11 reflection observable. A calibration must be done in order to isolate the real and imaginary parts of the reflection signal.

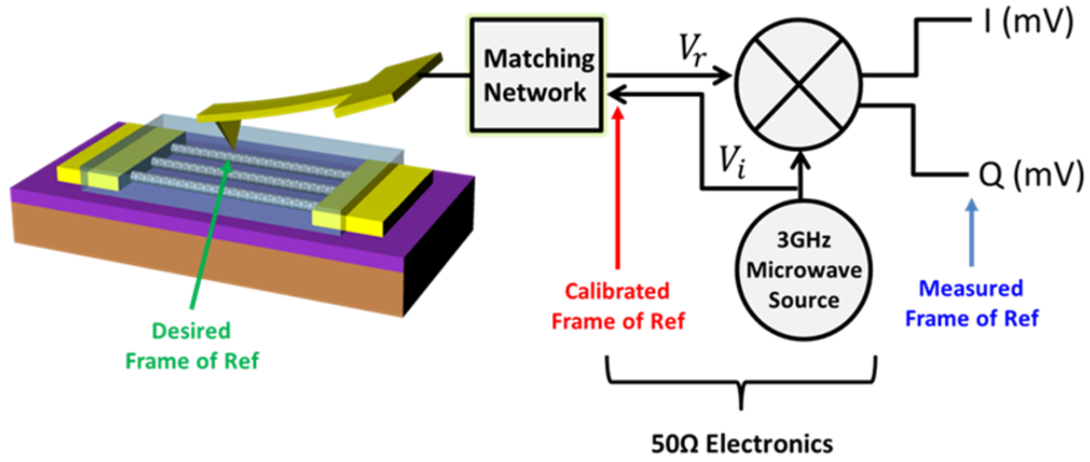

$$S_{11} = \frac{V_r}{V_i} \sim \Gamma = \Gamma_r + i\,\Gamma_i = \frac{Z_{ext} - Z_{int}}{Z_{ext} + Z_{int}}$$

Figure 2.7: Simplified Diagram Showing the signal pathway in MIM.

MIM is a qualitative technique that can only measure spatial changes in signal so normalizing and optimizing the observable contrast using a calibration standard is essential. The calibration is done by imaging a sample with areas of different capacitive properties and similar carrier mobility or conductivity, such as Alumina (Al_2O_3) dots on SiO_2 which are both insulators with differing dielectric constants. Since the contrast is only caused by capacitance changes, the mixer's phase offset can be tuned until all the signal is in either the I or Q channel, the orientation of the capacitance channel, imag(Γ), can be assigned to the acquired data. After proper calibration both the resistive and capacitive channels are isolated and can be mapped spatially and displayed independently providing different information about the sample. The calibration standard is also an important way to benchmark the SNR of the experimental setup.

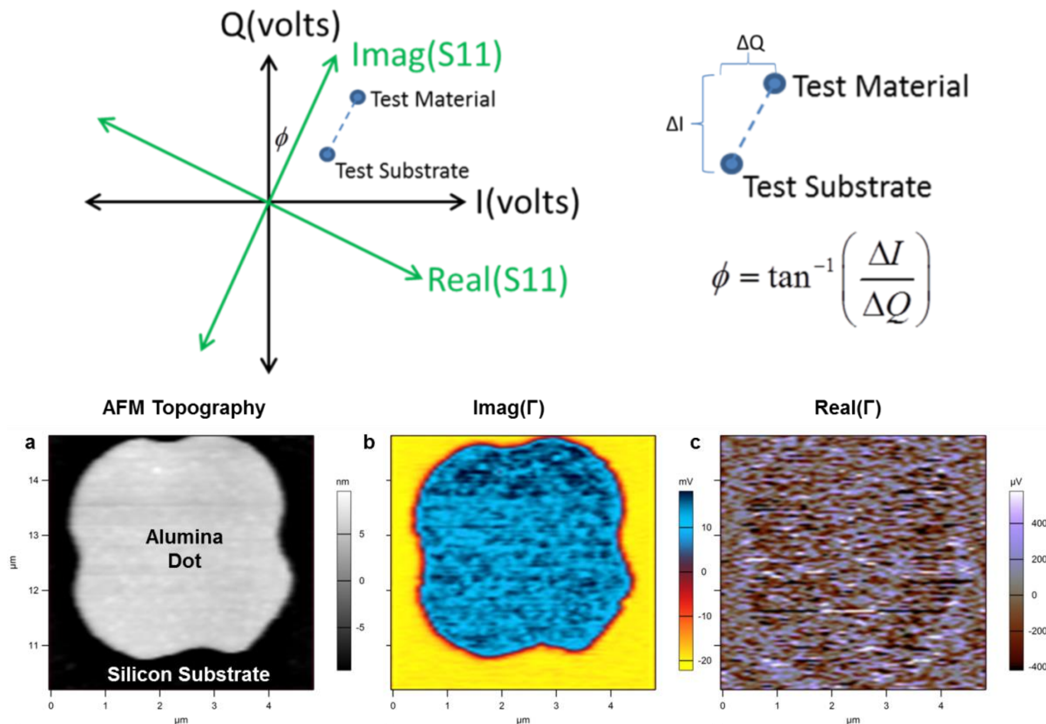

Figure 2.8: Diagram showing the basic concept behind using a calibration sample to correct for shifts in the frame of reference.

There are two primary noise contributions that limit the SNR the environmental drift and the quality of the probe connection to the matching network. Environmental signal drift, or background capacitance, is noise contribution from changing local temperature and humidity; this can be mitigated by using a stable experimental setup with proper shielding and by taking small, quicker images. However, this form of noise creates a dynamic background signal and effects the extrinsic properties of the sample-tip interaction, which limits the ability to obtain quantitative data in ambient conditions. As seen in figure 2.9, there is a physical coaxial connection that extends from the tip to a contact pad which couples to the tip holder matching network. The presence of parasitic capacitances and resistances along the delicate transmission path, such as dirt on the contact pad or damage to the probe's shielding layer, can attenuate the RF signal which diminishes the SNR.

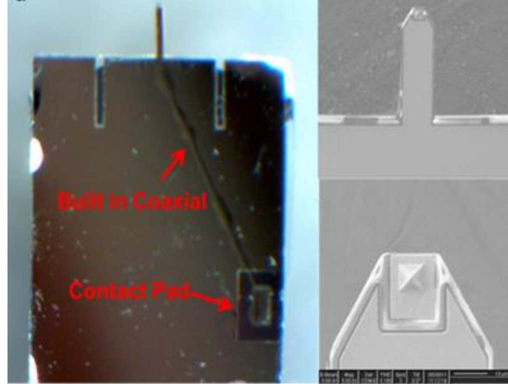

Figure 2.9: Image of MIM-AFM setup. Probe showing the tip connected to a contact pad via a built-in coaxial. SEM images of tip of a MIM-AFM probe.

The MIM tip behaves like a RF nanoantenna, there is an inverse tradeoff between tip sharpness and S/N [24]. In figure 2.10, simulations clearly show that the microwave reflection sensitivity increases with larger tip apexes [25]. Simply increasing the RF power would increase both the signal and the noise floor, so for very sharp tips there is a tradeoff between SNR and spatial resolution. This emphasizes the importance of developing higher quality coaxial probes, more sensitive RF detection electronics, and novel imaging schemes to improve the resolution and sensitivity of MIM.

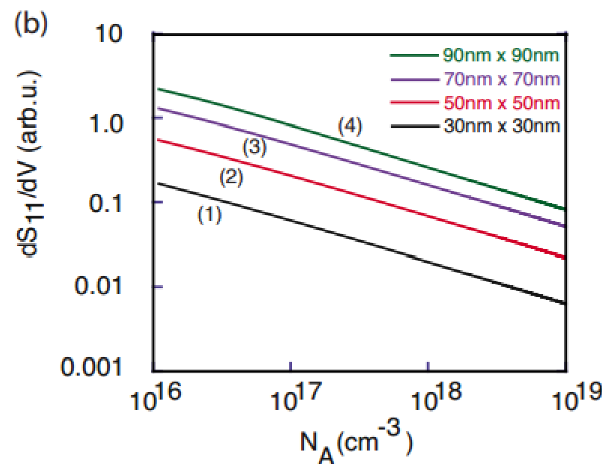

Figure 2.10: Simulation data showing the reflection dependence on tip size. Notice that the y-axis is plotted in log form implying that there is significantly more contrast (signal difference) available for moderately larger tips [25].

The desired observable capacitance data can be in either the I or Q data channels with a positive or negative linear correlation to the imaginary reflection data, since it is possible for the mixer to be exactly 180 degrees out of phase. The orientation of the reflection channel can be accounted for by considering that the alumina has a higher dielectric constant, 9.7, compared to SiO2, 3.9, so it will have a higher capacitance. Recording the calibration sample image is a reliable way of ensuring adequate SNR and proper phase calibration. In figure 2.11, a high quality MIM-AFM image of the calibration sample shows the potential to map capacitance with high sensitivity electronic properties on the sample surface.

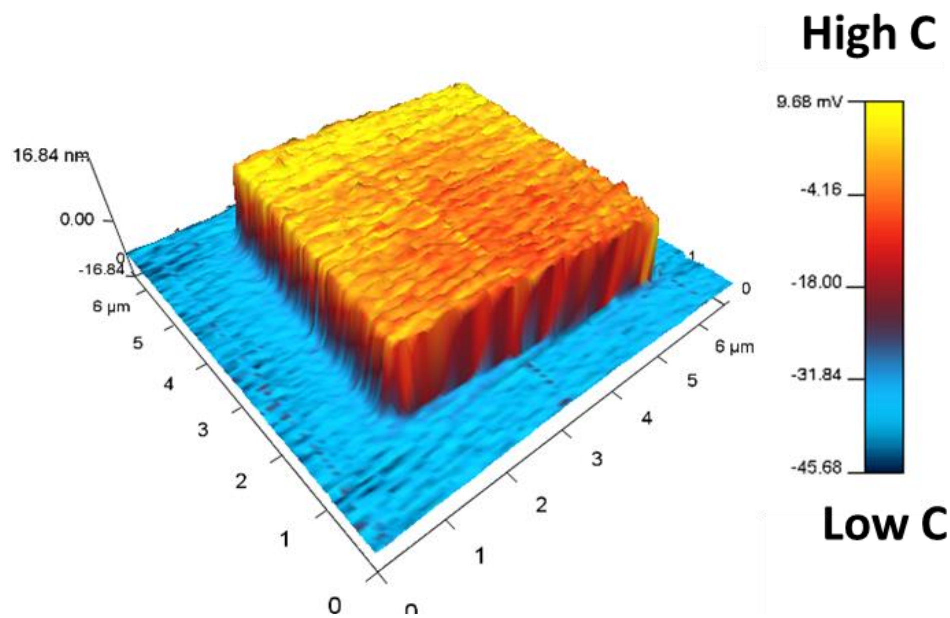

Figure 2.11: 3D capacitance/topography overlay of Alumina Dot used for Calibration.

2.6 Optical Near-Field AFM

Optical Spectroscopy is a common way to measure material composition by detecting spatial changes in optical behavior resulting from chemical and structural variation on the sample. The fundamental drawback of optical spectroscopy is the diffraction limited resolution

which limits the ability to acquire detailed data maps of nanoscale materials. Recent developments in spectroscopy utilize the tip limited resolution of AFM to overcome the diffraction limited resolution of optical spectroscopy. This scan probe approach to optical spectroscopy is called scanning near-field optical microscopy (SNOM). The idea is to couple the incident laser light to a very sharp AFM tip to induce an optical near-field with an enhanced electric field directly below the tip apex. This method can vastly improve the resolution of optical spectroscopy beyond the diffract limit by spatially mapping the signal response to the tip location. Since the measured signal is dominated by the light-matter interaction directly under the tip, the resulting map of the optical response will have tip limited resolution.

The tip enhanced near-field is a result of the incident laser's interaction with surface plasmons on a metal AFM tip. For SNOM imaging, polarized, coherent laser light interacts with the free electrons on the surface of a metal tip with a sub-diffraction radius of curvature. The incident optical E-field couples to free electrons on the tip's surface inducing carrier motion like an oscillating dipole. These moving charges, called surface plasmons (SP), have a physical oscillation wavelength determined by the wavelength of the incident light and the dielectric constants of the tip, surrounding fluid (air), and sample. For SP's, the kinetic energy from electron motion is converted to electrostatic potential energy when the charge carrier approaches its maximum displacement from equilibrium. The SP's the potential energy is stored as a dipole resulting in spatial variations in charge density; the highest charge density occurs around the electrostatic potential energy maxima at the oscillation nodes spaced a wavelength apart [26]. The SP dipole creates a local E-field outside of the metal surface at the same frequency as the incident light. When the surface plasmon is localized to an area smaller than its natural oscillation wavelength the moving charges are forced into a smaller area, such as the tip apex or

the edges of a metal nanoparticle, as all the kinetic energy is converted to electrostatic potential at the spatially confined edges. This increases the local charge density and electrostatic potential in the spatially confined region compared to an infinite metal surface; the strength of the resulting quasi-static E-field can be determined by taking the spatial gradient of the electrostatic potential. Since the spatially confined edges have the highest electrostatic potential (volts) and it quickly falls off at the center of the SP, where the kinetic energy at its maximum, and in regions with a larger surface, the potential gradient (E-field) is largest in the regions with the most spatial confinement [26,27]. This implies that the strength of the resulting SP E-field (V/m) can be greatly enhanced on the sharpest edge of a non-symmetrical metal surface such as the sharp tip apex when the polarization of the incident light is properly oriented relative to the tip geometry [27]. Light emitted by the SP E-field, known as a surface plasmon- polariton, should be the same as the incident light except with a notable short-range, near-field enhancement. The apex of a metal AFM tip for our experiments is ~25nm which is much smaller than the wavelength of the incident optical laser light in the infrared. This enhances the amount of signal available from the light-sample interaction due to the higher light intensity directly under the tip. Also, it ensures that most of the detected signal is coming from the sample surface coupled to the near-field just below the tip apex, the contribution of the far-field signal is greatly reduced which improves SNR. When the photodiode detects the backscatter from the light-sample interaction, it can be spatially correlated to the tip position which implies that the spectroscopy data has tip limited resolution. In figure 2.12, an optical simulation shows the enhancement effect of a polarized optical E-field incident on a sharp gold tip.

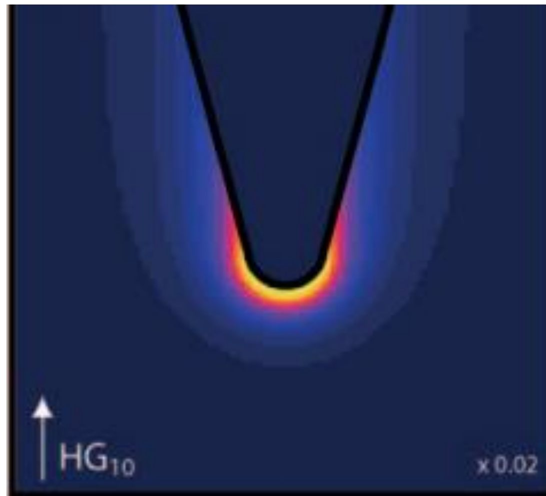

Figure 2.12: This image is a finite element simulation of a sharp gold tip in a polarized E-field, the polarization direction is noted in the lower left corner [28].

The size and geometry of a tip has a large effect on the tip-enhancement effect, hence non-uniformities in tip size and shape may have a notable effect on the precision of the spectroscopy data. Irregularities in tip shape can occur within one batch of tips and subject to changing geometry during an AFM scan from tip broadening and contamination. For our experiments, we utilize a mid-IR laser source which has a major advantage for mitigating tip geometry issues. The near-field effects from the tip sharpness is less sensitive to the tip's geometry in the mid-IR because the wavelength of the incident light, >1um, is so much larger than the dimensions near the tip apex making the near-field coupling non-resonant in nature [29]. As a result, the near-field enhancement of the incident E-field isn't a strong function of light frequency in the infrared compared to visible light. Although the tip's overall sharpness at the apex is important for near-field enhancement in the mid-IR, the changing tip geometry shouldn't have a large effect on the strength of the near-field. Despite this advantage, there is still enough variance in the tip geometry from one tip to another such that a standard calibration sample is needed to normalize the spectroscopy signal according to the Near-Field optical enhancement spectrum to acquire accurate data.

For our experiments, we will use SNOM with a mid-IR laser source to map spatial changes in dielectric constant and free carrier density. The observable contrast originates from the change in local reflectivity, R, detected as the backscattered signal at the resonant frequency of the plasmonic free-carrier oscillations in the mid-IR [30,31]. The reflectance observable has a nonlinear response to the sample's index of refraction, Z, which is correlated to the local dielectric properties according to equation 2.9 [32]. For materials with a high carrier density, such as doped semiconductors and metals, the dielectric constant at infrared frequencies is linearly correlated to the local free carrier concentration, n, according equation 2.10 which was derived using the Drude Model [32]. Modifications to the dielectric constant in the mid-IR spectrum are a result of light absorption from the polarization of bulk-plasmons at the plasma resonant frequency [32]. This implies that an inhomogeneous distribution of free carriers, or nearly free carriers in the case of doping, will result in an observable spatially contrast when mapping reflectivity in the mid-IR spectrum.

$$R = \left|\frac{1-Z}{1+Z}\right|^2 \sim \left|\frac{1-\sqrt{\varepsilon\mu}}{1+\sqrt{\varepsilon\mu}}\right|^2 \qquad (2.9)$$

$$\varepsilon(\omega_{IR}) = \varepsilon_\infty\left(1-\frac{\omega_{plasma}{}^2}{\omega_{IR}{}^2 + i\omega_{IR}\gamma}\right) \sim \frac{n}{\omega_{IR}{}^2 + i\frac{\omega_{IR}}{\mu}} \qquad (2.10)$$

We were able to improve the sensitivity of SNOM using a sophisticated interferometer to isolate backscatter signal from the near-field interaction from the unwanted far-field signal. The total observable signal has a large contribution from the far-field backscatter, originating from the diffraction limited laser spot which is much bigger than the tip, and the near-field backscatter, originating from the localized light-matter interaction beneath the tip. The contribution of the near-field signal is maximized when the tip is touching the surface and drops rapidly as the tip-sample distance increases. When operating in tapping mode, the near-field

signal is modulated at the resonant tapping frequency of the AFM cantilever [31]. A heterodyning modulation scheme is used to isolate and eliminate the far-field signal contribution to improve sensitivity and SNR. The mirror's position in the interferometer is modulated to create modulated phase interference. The power of the incident laser is modulated at the mirror frequency by oscillating between constructive and destructive interference. Both the near-field and far-field signals are modulated at the mirror frequency, but only the near-field signal is modulated at the tip frequency. After demodulating the measured backscatter signal, several sub-bands in the frequency domain arise which correspond to $f_{backscatter}(n,m) = n*f_{cantilever} \pm m*f_{mirror}$, where n and m are integer modes [31]. The sub-bands where n>1 will be dominated by the near-field signal with the additional contribution from the far-field signal being the same for all m values. Taking the signal difference between $f_{backscatter}(2,1)$ and $f_{backscatter}(2,2)$ eliminates the remaining contribution of the far-field signal which greatly improves the resolution, SNR, and sensitivity of the SNOM technique [33].

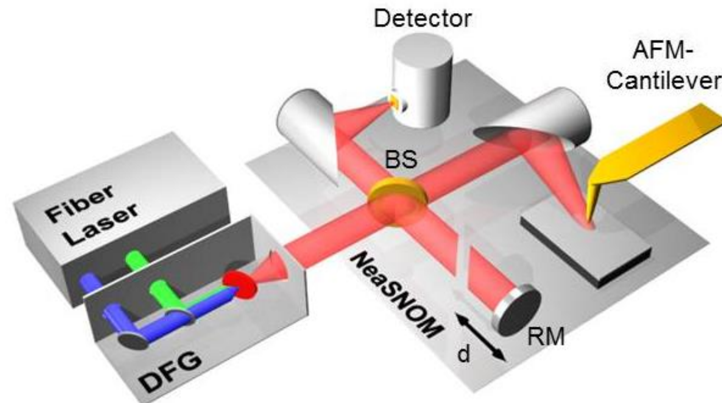

Figure 2.13: This shows a simple schematic of the SNOM system used in this research [34].

Previous experimental studies in literature allude to the success of mapping electronic character on semiconducting nanowires using SNOM in the mid-IR and utilizing a heterodyne

modulation scheme [35]. In figure 2.14 the dopant profile of a ZnO nanowire shows contrast between the Sulfur doped region in-between two undoped regions [36]. The potential for using SNOM-IR to map electronic structure is evident and appealing.

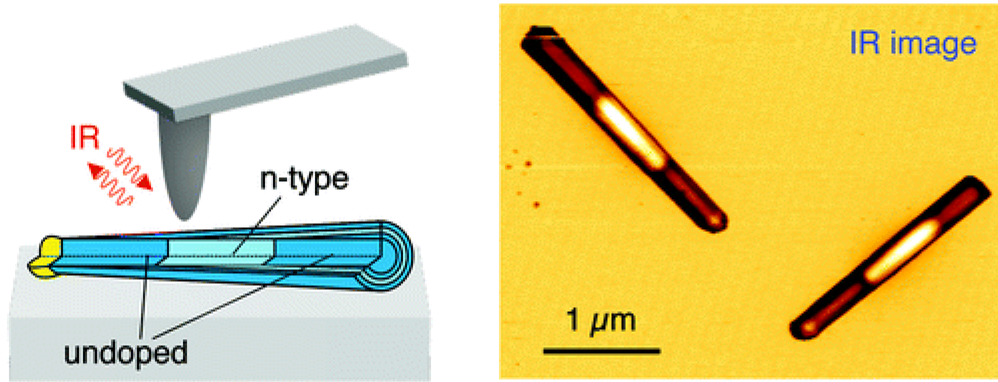

Figure 2.14: Simple schematic showing the SNOM-IR measurement technique on doped ZnO nanowires (left). High resolution SNOM-IR image of doped ZnO nanowire clearly showing doping contrast [30,29].

2.7 References

1 Sarioglu A.F., Solgaard O., Bhushan B. (eds). Chapter 1: Time-Resolved Tapping-Mode Atomic Force Microscopy. *Scanning Probe Microscopy in Nanoscience and Nanotechnology*. Springer, Berlin, Heidelberg (2011). DOI: 10.1007/978-3-642-10497-8_1

2 Ziegler, D., & Stemmer, A. “Force gradient sensitive detection in lift-mode Kelvin probe force microscopy.” *Nanotechnology,* (2011) 075501-075501.

3 Avila, A., & Bhushan, B. “Electrical Measurement Techniques in Atomic Force Microscopy.” *Critical Reviews in Solid State and Materials Sciences,* (2010) 38-51.

4 Bhushan, Bharat, and Anton V. Goldade. "Measurements and analysis of surface potential change during wear of single-crystal silicon (100) at ultralow loads using Kelvin probe microscopy." *Applied surface science* 157.4 (2000): 373-381.

5 Kikukawa, Atsushi, Sumio Hosaka, and Ryo Imura. "Silicon pn junction imaging and characterizations using sensitivity enhanced Kelvin probe force microscopy." *Applied Physics Letters* 66.25 (1995): 3510-3512.

6 Müller, F., et al. "Applications of scanning electrical force microscopy." *Microelectronics Reliability* 37.10 (1997): 1631-1634.

7 Bae, S. S., et al. "Characterizing defects and transport in Si nanowire devices using Kelvin probe force microscopy." *Nanotechnology* 23.40 (2012): 405706.

8 Jacobs, H. O., H. F. Knapp, and A. R. O. S. I. Stemmer. "Practical aspects of Kelvin probe force microscopy." *Review of Scientific Instruments* 70.3 (1999): 1756-1760.

9 Sugimura, Hiroyuki, et al. "Potential shielding by the surface water layer in Kelvin probe force microscopy." *Applied physics letters* 80.8 (2002): 1459-1461.

10 Garcia-Martin, Antonio, and Ricardo Garcia. "Formation of nanoscale liquid menisci in electric fields." *Applied physics letters* 88.12 (2006): 123115.

11 Müller, F., et al. "Applications of scanning electrical force microscopy." *Microelectronics Reliability* 37.10-11 (1997): 1631-1634.

12 Williams, C. C. "Two-dimensional dopant profiling by scanning capacitance microscopy." *Annual review of materials science* 29.1 (1999): 471-504.

13 Brotherton, S. D. "Introduction." *Introduction to Thin Film Transistors*. Springer International Publishing, 2013. 1-5. Chapter 2, pages 17-28.

14 Edwards, Hal, et al. "pn-junction delineation in Si devices using scanning capacitance spectroscopy." *Journal of Applied Physics* 87.3 (2000): 1485-1495.

15 Unpublished Application Note decribing the Bruker SCM (SRAM) test sample. Bruker Nano Inc. December 4, 2012. http://www.brukerafmprobes.com/Images/SCMSAMPLE%20App%20Note.pdf

16 Lai, K.; Kundhikanjana, W.; Kelly, M.; Shen, Z. X. Modeling and Characterization of a Cantilever based Near-Field Scanning Microwave Impedance Microscope. *Rev Sci Instrum* 2008, *79,* 063703.

17 Yang, Y. L.; Lai, K. J.; Tang, Q. C.; Kundhikanjana, W.; Kelly, M.; Shen, Z. X.; Li, X. X. A Shielded Cantilever-Tip Microwave Probe for Micro/Nano Surface Imaging of Conductive Properties. *Proc IEEE Micr Elect* (2011), 79-82.

18 Lai, K.; Kundhikanjana, W.; Peng, H.; Cui, Y.; Kelly, M. A.; Shen, Z. X. Tapping Mode Microwave Impedance Microscopy. *Rev Sci Instrum* (2009), 80 (4), 043707.

19 Lai, K.; Kundhikanjana, W.; Kelly, M. A.; Shen, Z. X. Calibration of Shielded Microwave Probes using Bulk Dielectrics. *Appl Phys Lett* (2008), 93 (12), 123105.

20 Lai, K.; Ji, M. B.; Leindecker, N.; Kelly, M. A.; Shen, Z. X. Atomic-Force-Microscope-Compatible Near-Field Scanning Microwave Microscope with Separated Excitation and Sensing Probes. *Rev Sci Instrum* (2007), 78 (6), 063702.

21 Steinhauer, D. E., et al. "Quantitative imaging of dielectric permittivity and tunability with a near-field scanning microwave microscope." *Review of Scientific Instruments* 71.7 (2000): 2751-2758.

22 Seabron, Eric, et al. "Scanning probe microwave reflectivity of aligned single-walled carbon nanotubes: Imaging of electronic structure and quantum behavior at the nanoscale." *ACS nano* 10.1 (2015): Supplemental section.

23 Anlage, S. M.; Vlahacos, C. P.; Dutta, S.; Wellstood, F. E. Scanning Microwave Microscopy of Active Superconducting Microwave Devices. *IEEE T Appl Supercon* (1997), *7*, 3686-3689.

24 Smoliner, J., et al. "Scanning microwave microscopy/spectroscopy on metal-oxide-semiconductor systems." *Journal of Applied Physics* 108.6 (2010): 064315.

25 Wu, S. J.; Kienberger, F.; Tanbakuchi, H. Scanning Microwave Microscopy: Advances in Quantitative Capacitance and Carrier Density Measurements at the Nanometer Scale. *Wor Sci Ser Nano* (2013), *7*, 481-512.

26 Smith, David R. “Plasmonics Enhancement.” *Meta Group Novel Electromagnetic Media.* Duke University Pratt School of Engineering, 2017. http://people.ee.duke.edu/~drsmith/plasmonics/enhancement.htm

27 Hartschuh, Achim. "Tip- enhanced near- field optical microscopy." *Angewandte Chemie International Edition* 47.43 (2008): 8178-8191.

28 Bouhelier, Alexandre, and Lukas Novotny. "Near-field optical excitation and detection of surface plasmons." *Surface Plasmon Nanophotonics*. Springer Netherlands, (2007). 139-153.

29 Bründermann, Erik, and Martina Havenith. "SNIM: Scanning near-field infrared microscopy." *Annual Reports Section" C"(Physical Chemistry)* 104 (2008): 235-255.

30 Stiegler, J. M., et al. "Correlative infrared–electron nanoscopy reveals the local structure–conductivity relationship in zinc oxide nanowires." *Nature communications* 3 (2012): 1131.

31 Stiegler, J. M. "Infrared Spectroscopic Near-Field Microscopy of Nanoparticles and semiconducting nanowires. PhD thesis at the University of Pais Vasco (2012)

32 Atkin, Joanna M., et al. "Nano-optical imaging and spectroscopy of order, phases, and domains in complex solids." Advances in Physics 61.6 (2012): 745-842.

33 N. Ocelic, A. Huber, and R. Hillenbrand. Pseudoheterodyne detection for background-free near-field spectroscopy. Applied Physics Letters, 89(10): 101124 (2006)

34 F. Huth, A. Govyadinov, S. Amarie, W. Nuansing, F. Keilmann, R. Hillenbrand, "Nano-FTIR-Nanoscale chemical mapping by local infrared fingerprint". Nanoletters 12, (2012): 3973

35 Huber, Andreas J., et al. "Simultaneous IR Material Recognition and Conductivity Mapping by Nanoscale Near- Field Microscopy." Advanced Materials 19.17 (2007): 2209-2212.

36 Stiegler, J. M., et al. "Nanoscale free-carrier profiling of individual semiconductor nanowires by infrared near-field nanoscopy." *Nano letters* 10.4 (2010): 1387-1392.

CHAPTER 3

ELECTRICAL SCAN PROBE MICROSCOPY OF PERIODIC DOPING IN PLANAR GALLIUM ARSENIDE NANOWIRES

Significant portions of this chapter were published as "Direct electrical probing of periodic modulation of zinc-dopant distributions in planar gallium arsenide nanowires." Seabron, E., Choi, W., Mohseni, P.K., Kim, J.D., Gokus, T., Cernescu, A., Pochet, P., Johnson, H.T., Wilson, W.L. and Li, X., ACS Nano 11.2 (2017): 1530-1539. Reproduced with permission from the journal. The scan probe characterization and physical model analysis for the interpretation of the results were the primary contribution by the author. Other results presented in this chapter, including the GaAs nanowire growth and Density Function Theory, were the outcomes of close collaborations and joint work with collaborators.

3.1 Introduction

The potential use of nanowire (NW) structures as active components in a multitude of emerging devices is by now well explored [1-8]. The unique sub-set of planar NWs, assembled with lateral alignment along the substrate surface, is gaining considerable research interest due to its excellent material quality and planar processing compatibility [9-13].

Planar NWs, or NWs grown *via* the selective lateral epitaxy (SLE) approach, are catalyzed by metal nanoparticles according to the vapor-liquid-solid (VLS) or vapor-solid (VS) mechanism [10-13]. One obvious benefit of this technique is the ability to fully exploit conventional planar fabrication technology to realize NW based devices [14,15]. For this study, the most notable advantage of this growth mode is the unique ability to form lateral junctions

including p-n junctions and heterojunctions *in-situ* as the NW growth proceeds in-plane along a given crystal orientation. The simplicity through which lateral doping profiles can be defined spatially during planar NW growth can be applied to various electronic device including FETs, photodetectors, solar cells, and LEDs [1-8]. Examples of device applications in nanoelectronics that employ the SLE growth technique include, metal-semiconductor field-effect transistors (MESFETs) and metal-oxide semiconductor field-effect transistors (MOSFETs) with single GaAs NW channels, GaAs NW array-based high electron mobility transistors (HEMTs) with record-setting DC and RF performance, simple circuits such as amplifiers, and gate-all-around (GAA) MOSFETs utilizing heteroepitaxially-grown planar InAs NWs on GaAs substrates [5,13,16,17,18]. The challenge is analyzing the electronic profile with high sensitivity and resolution for process optimization and device physics. Accurate control over the formation of specific dopant distribution profiles requires the use of precise and non-destructive methods for the characterization the profiles.

Several methods exist for the determination of dopant distribution profiles in semiconductor NW, including secondary ion mass spectrometry (SIMS) and three-dimensional (3-D) near-atomic-scale spatial resolution *via* atom-probe tomography (APT) [19-26]. These methods have the advantage of quantitatively determining the chemical concentration of the dopant impurities. However, they are also destructive in nature and don’t provide any insight into device morphology and transport properties. Non-destructive electrical scan probe techniques, have been explored for the qualitative study of various electronic nanomaterials including nanowires [27-37]. Novel methods must be explored to overcome inherent issues that limit sensitivity to very small electronic perturbations at the surface such as doping distributions [27–37].

Microwave Impedance Microscopy (MIM), which uses a specialized co-axial cantilever to transmit a low power (~10 dB) localized microwave signal to the tip, has the potential to achieve unprecedented high sensitivity without risking modifying the intrinsic properties of the samples. It has been demonstrated as a powerful non-destructive method for the measurement of carrier concentrations [38,39]. Infrared scanning near-field optical microscopy (SNOM-IR) technique can spatially map IR absorption, the light is focused on the sample *via* a tip induced near-field effect allowing for sub-diffraction tip-limited resolution [40]. Drude absorption dominates the mid-IR absorption in highly doped semiconductors and metals, based on the model the observable contrast is dominated by changes in mid-IR absorption directly related to the free carrier concentration distribution introduced by the dopants [41–43]. This method has shown promise in providing dopant profile measurements on NW and nanotube structures [39]. Electric field microscopy is a non-contact technique that is sensitive to any coulomb forces that strongly contribute to the tip-sample interaction. It has the advantage of absolutely decoupling the topology data from the electrical mapping data while still simultaneously getting both information and requires a relatively simply experimental setup and widely available conductive AFM probes.

In this chapter, we will exploit these two state-of-the-art nanoscale resolution techniques, sMIM and SNOM-IR, to investigate the effects of the distribution of Si (n-type) and Zn (p-type) impurity dopants on the carrier concentration within the individual SLE-grown multi-junction GaAs NWs. We implement a tip voltage modulated variant of MIM called MIM2 to directly probe for spatial changes in impurity dopant concentration. By directly correlating the AFM topography, MIM, MIM2, and SNOM-IR mapping of corrugated p-type sections, we show the preferential incorporation of Zn-impurities at the location of twin planes valleys formed within

the corrugated segments. We developed an analytical and physical model of the twinned planes based on the TEM analysis and DFT modeling, which shows favorable binding energetics of Zn dopants at twin planes compared with undoped twins, supporting the physical observation of corrugated sections in twinned planar GaAs NWs upon heavy p-type doping. The model completely agrees with the observed trends in the electrical-topographical mapping data, which is verified using EFM analysis as a control for topography and electrical data cross-talk.

3.2 Electron Microscopy Analysis

Post-growth inspection was performed using an SEM, to observe physical defects on the nanowire surface, and TEM to look for possible crystal defects inside the nanowire. Here we want a high resolution image of how doping effects the nanowire's crystal structure. To do so we modulated the doping incorporation during the MOCVD growth and imaged the nanowire after growth. Figure 1 shows a multi-p-n junction planar GaAs NW and the corresponding flow modulation used during growth. Figure 3.1a shows a top-view SEM image of the entire NW (~18 μm long and 250 nm in diameter), with 8 distinctly doped n- or p- segments (as labeled) and the Au seed particle at the tip of the NW on the far right, and the corresponding switching (on/off) of the MOCVD growth precursors during the multiple junction formation. The periodically corrugated structure in the p-type segments is clearly visible in the SEM image due to an increased yield of secondary electrons from the terraced surfaces in these regions. Figure 3.1bc show higher magnification, 45° tilted-views of the third p-n junction (counted from base to tip, from Si- to Zn-doped) segment and the Zn-doped segment near the NW tip, respectively. Periodically corrugated morphology is only observed on the Zn-doped segments, whereas the Si-doped region shows a smooth morphology (left-hand side of image in Figure 3.1b. The formation

of periodic structural perturbations caused by p-type Zn and C impurities in GaAs planar NWs has been reported before; for details regarding the crystal structure, the effect of seed particle size on twin periodicity, and evidence of dopant incorporation *via* electrical device characterization, the readers should reference [44]. As shown in the TEM image in Figure 3.1d, the corrugation corresponds to the occurrence of twin planes (indicated by black arrows), which sit between the protrusions (red arrows) in the periodic surface topography. Accurate physical measurements of crystal morphology are used to construct the physical model to interpret electrical mapping data and to formulate an analytical model. This is essential to answering the long-standing research question of doping uniformity and its relationship with twin plane defects in planar, in-situ doped NWs.

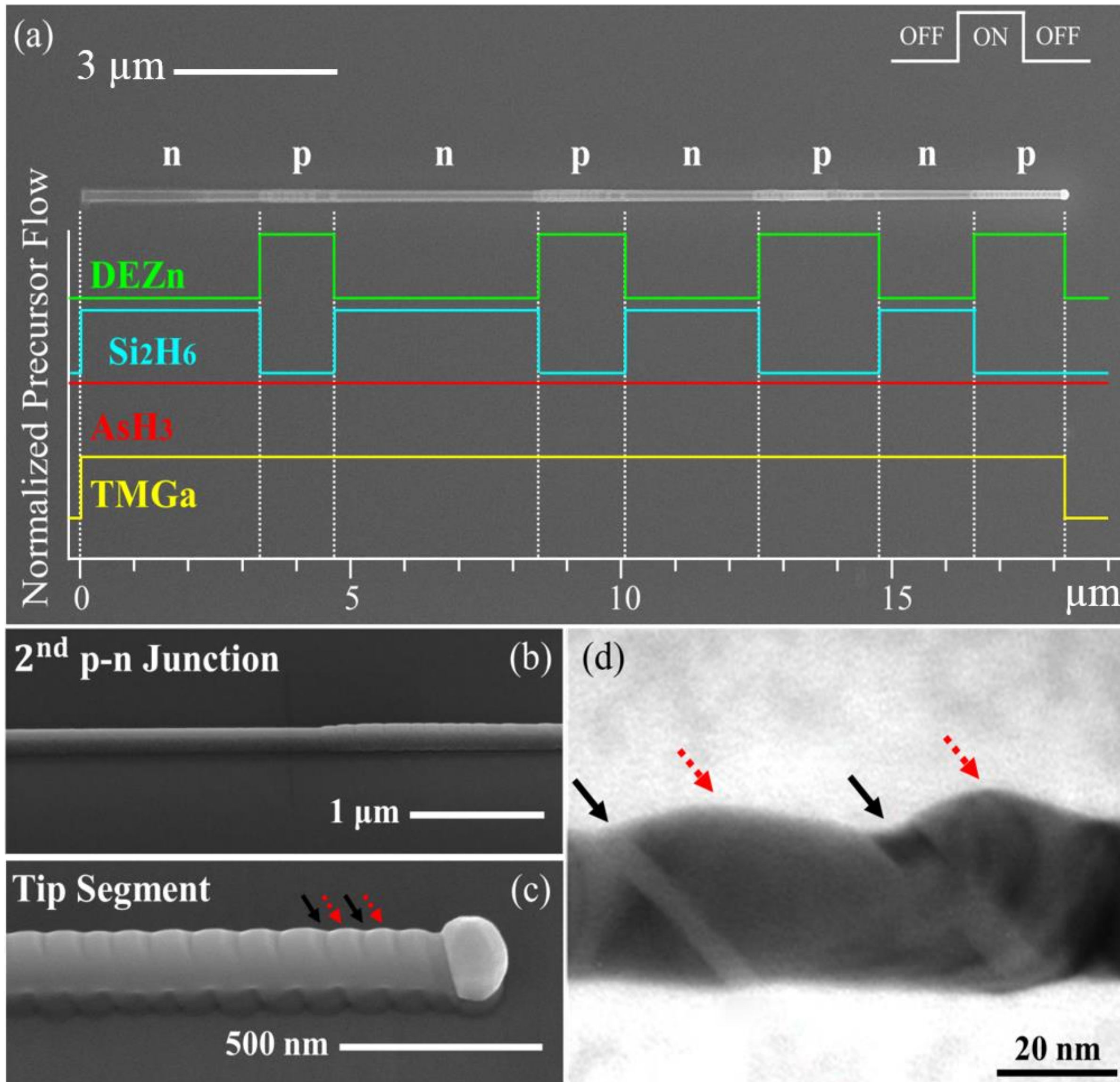

Figure 3.1. Growth scheme and structure of a planar GaAs nanowire with multiple lateral p-n junctions. (a) Top-view SEM image of a planar multi-junction GaAs NW containing alternative n- and p-doped segments, as labelled above the NW. Normalized MOCVD precursor flow rates are superimposed for TMGa (black), AsH_3 (red), Si_2H_6 (blue), and DEZn (green). (b) and (c) show 45° tilted-view images of the 2nd axial n-p junction and the p-type segment before the tip of the same NW, where the corrugated faceting morphology of the p-layer is clearly visible. (d) TEM image (adapted with permission) showing the twin planes (black arrows) between the ridges (red dashed arrows) in a Zn-doped planar GaAs NW segment.

3.3 Microwave Impedance Microscopy (MIM) Analysis

All our purposes all MIM analysis was done on as-grown planar GaAs NW samples in a contact mode scanning geometry. For MIM-AFM experiments the microwave signal propagates from the source (-10dB, 2.7-3.3GHz) to the apex of the coaxial tip where a portion of the signal is reflected back according to the sample impedance. The observable contrast is the imaginary part of the microwave reflection signal is proportional to the tip-sample capacitance (Chapter 2). For nanoscale 3-dimensional (bulk) semiconductors the measured capacitance comes from charge stored in the metal-semiconductor junction formed in the contact mode geometry [38]. For a contact mode scanning microwave impedance microscopy (MIM) measurement, the metal tip directly contacts with the semiconductor surface (GaAs nanowire) to form metal-semiconductor (M-S) junction as illustrated at figure 3.2. By applying bias between tip and metal plane, M-S junction capacitance (C_{surf}) is stored via a depletion of charge at the interface between metal tip and semiconductor NW. C_{surf} can be calculated as:

$$C_{surf} = \frac{\varepsilon_S}{\lambda_D} = \sqrt{\frac{q\varepsilon_S n^*}{V_t}} \sim n^{\frac{1}{2}} \qquad (3.1)$$

Where ε_s, λ_D, n^*, V_t, and n are permittivity of semiconductor, Debye screening length under the tip (not to be confused with Debye length from homojunction), carrier concentration of charges involved in screening, thermal voltage, and free carrier concentration respectively. We can assume that the observable MIM capacitance is sensitive to the spatial changes in free carrier concentration near the NW surface. It is worth emphasizing that mobile carriers, electrons and holes, in the presence of a strong electric field creates a dipole which may spatially confine them enough such that do not behave like free carriers (n). Spatially confined mobile carriers should not couple as strongly to the microwave E-field as truly free carriers because their resonant

oscillation dynamics are dampened by the static dipole contribution. For equation 3.1, this is an important distinction when interpreting which carriers will be involved in screening (n*); these considerations will directly affect the observable surface capacitance.

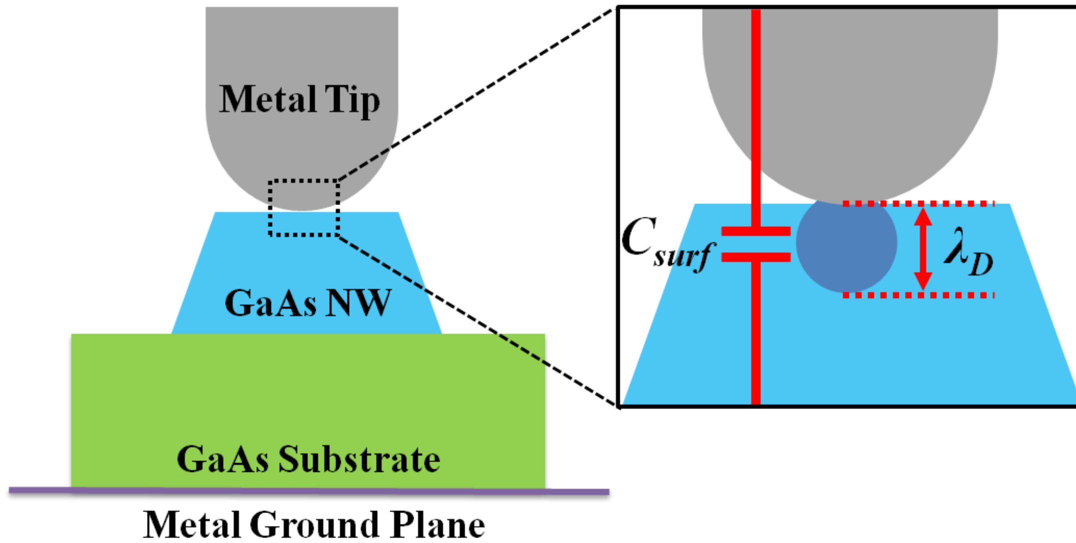

Figure 3.2: Simplified schematic of the contact mode sMIM. Metal tip is directly contacting with the surface of sample (GaAs NW) to detect M-S junction capacitance (C_{surf}). The magnified geometry of the M-S junction is shown in box. The depletion region (remarked as darker color) is formed in GaAs NW at the bottom of the metal tip along with Debye length (λ_D) to form C_{surf}.

A major advantage of MIM-AFM measurements is the ability to directly correlate accurate topology and free carrier distribution which can reveal morphology driven electronic phenomena. Figure 3.3 shows a free carrier concentration color map overlayed on to a 3D topology image of a single PN junction NW. The data was purposefully taken with a broad MIM tip to maximize the capacitance SNR at the cost of resolution. The image shows small areas of high capacitance in the valleys of the corrugated region surrounded by larger regions of low capacitance. Linecuts taken parallel to the NW axis was taken to align the relative MIM capacitance signal and AFM topology data to reveal morphology correlated trends. The capacitance peak is particularly strong and easily distinguishable at the interface where the ridges

begin to form. Similar observations of morphology correlated electronic structure is repeated throughout the analysis of this chapter.

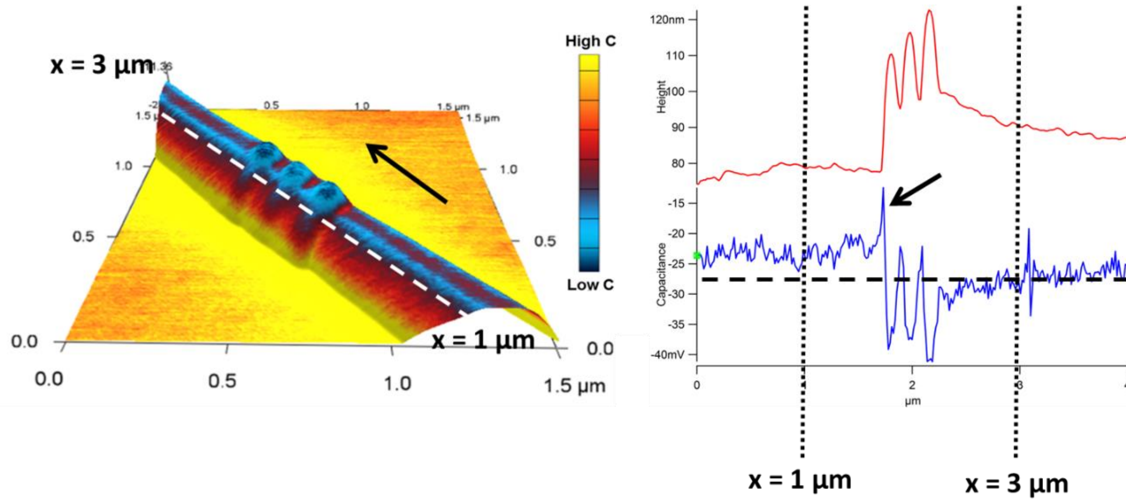

Figure 3.3: (left) Color Map of MIM capacitance overlayed on a 3D AFM image, the arrow points to the direction of nanowire growth. (right) Linecuts taken parallel to the white dotted line to correlate MIM and topology data.

Figure 3.4a shows an AFM topography map of an 8-segmented, multi-p-n junction planar GaAs NW (the SEM of the same NW was shown in Figure 3.1a), where the in-plane dimension is in units of micron (µm) and the height (shown as color contrast) is in units of nanometers (nm). The taller regions (orange-tone) are the p-type segments because of the twinned structure and the purple-toned regions represent the n-type segments. In all Figure 3.4 panels, the dotted arrows point to the NW tip (growth front where the Au particle is located). Figure 3.4bc show 2D color maps of the topography and the corresponding capacitance, respectively, of the corrugated p-doped segment in the region outlined by a dashed line box in figure 3.4a. The taller corrugated twins appear as regions of higher brightness, with a height difference of approximately 25 nm. Notice that the areas with the lowest capacitance (darker blue tone) are precisely located in the distinct corrugation peak regions. The high capacitance detected at the edge of the NW come from the geometrical artifact of MIM and existence of highly Zn-doped

GaAs parasitic thin film under the NW (discussed in more detail later in chapter). The correlation between topography and capacitance can be better viewed in figure 3.4d, line scans of the topography and capacitance (imaginary reflectance or MIM-Im) as a function of position along the NW axis, where the variation in AFM height (top, red curve) and the capacitance (bottom, blue curve) are plotted. The vertical black dotted lines serve as guides to mark the one-to-one correlation of the tallest region of the corrugated p-segment with the valley of capacitance signal, while the solid black arrows denote notable capacitance increase beyond the baseline in the twinned notched regions between the corrugations in the p-type segments. Note that there is also a local maximum in the valley of capacitance (center of the vertical lines). These observations provide for the first time spatially resolved evidence at the nanometer scale that the distribution of carriers (holes) in the Zn-doped GaAs NWs is not uniform electrically, and indicate that there is an accumulation of free carriers at the twin-plane defects regions and a depletion of free carriers at the corrugation peaks.

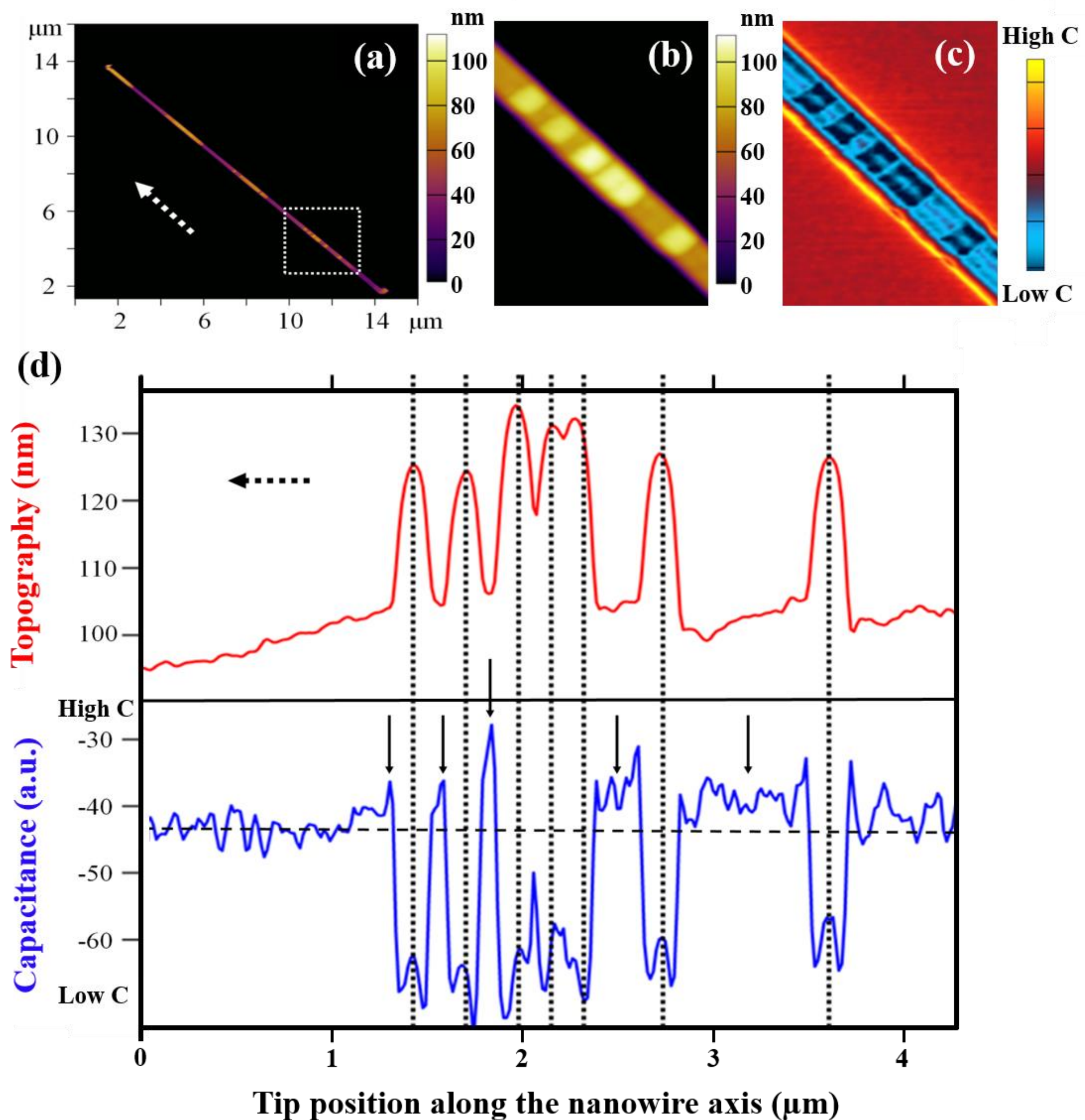

Figure 3.4: MIM imaging and line-scans of the Zn-doped segment of a p-n junction NW. (a) AFM topography image of the full NW, the white box represents the region of interest. (b) Topography and (c) MIM capacitance images. (d) Height (red) and capacitance (blue) linescans obtained along the length of the NW segments shown in (b), (c). Dotted, vertical lines mark the center of the visible corrugation peaks. The dashed horizontal line shows the base line capacitance level. Solid black arrows indicated the regions of Zn accumulation (p+ regions) corresponding to the location of twin-planes in the p-type segments of the planar NWs. All dotted arrows point in the growth direction of the NW.

In the MIM2 measurement, the Fermi energy level at the surface is influenced by the tip bias modulated at a fixed frequency (~90 kHz); the tip bias has a fully offset sine wave form that oscillates between 0 and V_{tip} [39]. The experimental geometry for measuring the differential capacitance *via* MIM2 is similar to that of Scanning Capacitance Microscopy (SCM) where the tip-semiconductor interface forms a gating structure that when biased can cause population inversion or depletion directly underneath the tip. The simple interpretation of the capacitance signal is that it mimics semiconductor C-V curves which has been shown, in previous experiments with SCM, to have weaker voltage dependence at higher doping concentrations [45–47]. Since we are measuring a differential signal the average slope of the C-V curve from V = 0 to V_{tip} gives rise to the observed MIM2 signal. By applying the tip bias, it is possible to compensate for the internal fields in a carrier depletion region; the charge stored in the region from ionized dopants and excess charge carriers manifests as a flat-band voltage shift in the C-V curves such that a stronger bias is needed to achieve a notable change in the population of free carriers (*i.e.* population inversion or accumulation) [48,49]. We hypothesize that both the overall dopant concentration and the presence of internal E-fields (space charge) will impact the MIM2 response. In figure 3.5, there are three spatial profiles of capacitance images (overlaid with topography) obtained from the same single junction NW on the Zn doped side of the p-n junction under conventional MIM (grounded tip) and MIM2 with a V_{tip} of -3V and -9V, respectively. Figure 3.5d shows the corresponding line scans, including AFM topography, as labeled. Note that shown in figure 3.5bc are the differential capacitance under the corresponding bias where the dark blue color indicates near zero response to the modulated tip voltage, while green to yellow color shows increasing sensitivity to the modulated voltage. At V_{tip} = -3V (figure 3.5b), the modulated tip bias shows minimum effect on the measured capacitance everywhere except a

small area in the center of the lower doped flatband region, while at V_{tip} = -9V (figure 3.5c), dramatic localized changes in capacitance can be seen everywhere except the highly doped p+ region. For instance, L1 (the valley in the periodic topography corrugation as indicated by arrows in figure 3.5), is characterized by the clear increase in MIM capacitance and a lack of MIM2 response observed; while L2 (the center of the peak region in the periodic topography) shows a localized maximum in the MIM capacitance and a strong peak in MIM2 especially under the higher modular tip bias (V_{tip} = -9V).

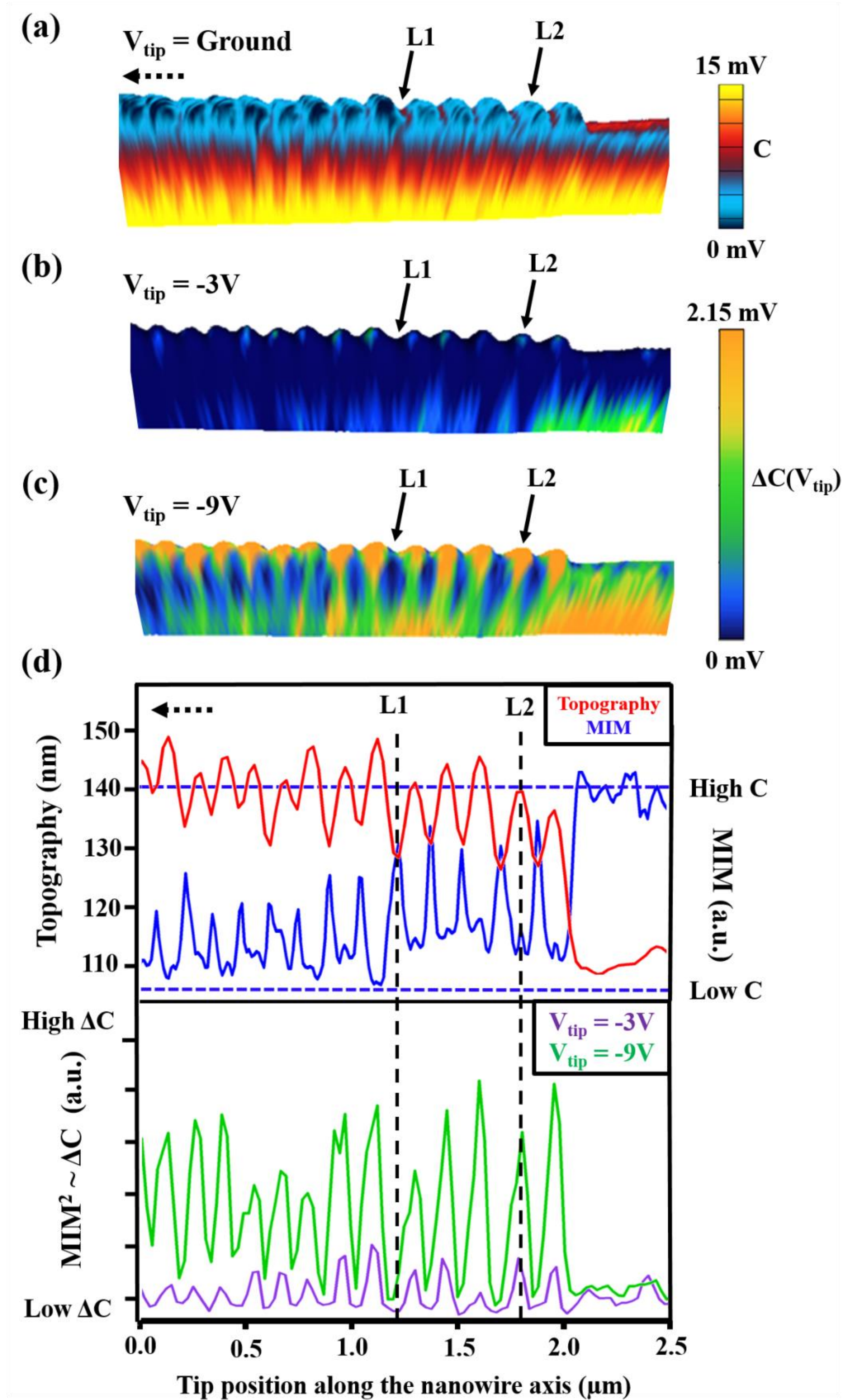

Figure 3.5: Conventional MIM and Tip Voltage Modulated MIM (MIM2) of the Zn doped segment of a single-p-n junction planar GaAs NW.

Figure 3.5 (cont.): (a,b,c) Overlay of data represented in color onto a 3D view of NW topography. Dotted arrows in figure (a) and (b) indicate the growth direction of NW. (a) Contact mode MIM color scheme. All MIM2 data was taken with a tip modulation in sine wave form varying between 0 and V_{tip} at 90kHz; they both have the same color scale where areas with zero response are dark blue and higher sensitivity to the modulated voltage are shown in yellow. (b) MIM2 data taken at V_{tip} = -3V (c) MIM2 data taken at V_{tip} = -9V. (d) Plot of several line cuts down the axis of the NW corresponding to the topography (top, left axis, red), MIM trend (middle, right axis, blue), and MIM2 numerical data offset to zero (bottom, left axis, green and purple). Arrows and vertical lines mark interesting phenomena that consistent across all the data forms: L1 is a potential well formed from the highly Zn doped p+ region in the notches and L2 is the flat band region that exists at the center of the peaks.

3.4 Infrared Scanning Near-field Optical Microscopy (SNOM-IR) Analysis

Infrared near-field maps of individual NWs were acquired by utilizing a SNOM microscope with a tunable continuous-wave CO_2-laser (Access laser) at a frequency of 884 cm^{-1} was focused on metal coated AFM tip with an apex radius of approximately 20 nm. Our setup was able to simultaneously acquire the topology and absorption amplitude and phase maps of the NWs using a heterodyne modulation scheme to isolate only the near-field components under the tip, the details of the optical signal processing technique can be found in chapter 2 [40]. According to the Drude model, the optical absorption in the mid-IR is proportional to the free carrier concentration (refer to chapter 2). Our observed contrast is the surface's free carrier distribution making mid-IR SNOM characterization a complementary method to MIM for electronic property mapping [43].

For comparison, optical amplitude and phase images generated *via* SNOM-IR mapping along the same segment of the NW of interest are shown in figure 3.6. In the SNOM images, we observe an increase (decrease) in local intensity of optical amplitude (optical phase) in regions adjacent to the three notches, indicative of a rise in scattering as expected from an excess of free charge carriers consistent with a simple Drude absorption model [43]. Thus, the MIM and

SNOM results are consistent and point to preferential localization of Zn dopant impurities along the twin planes in the p-type NW segments. The analysis of linescans obtained from SNOM experiments performed under an 884 cm^{-1} excitation frequency. Figure 3.6ace show topography, optical amplitude, and optical phase images, respectively, of the same multi-n-p planar GaAs NW. The black solid line in (a), highlighted by the white border, marks the location where the corresponding topography, amplitude, phase profiles where obtained, as shown in (b), (d), and (e). In direct agreement with sMIM results, increased scattering from free charge carriers is qualitatively represented by maxima in the optical amplitude profile, and by minima in the optical phase profile, which both coincide with the location of twin-planes (regions between notches, observed as minima) in the topography linescan. It is worth noting that the qualitative trends of the SNOM data match very well with that of the sMIM data in figure 3.4, which highlights the power of SNOM as a complementary technique and the validity of our previous MIM observations.

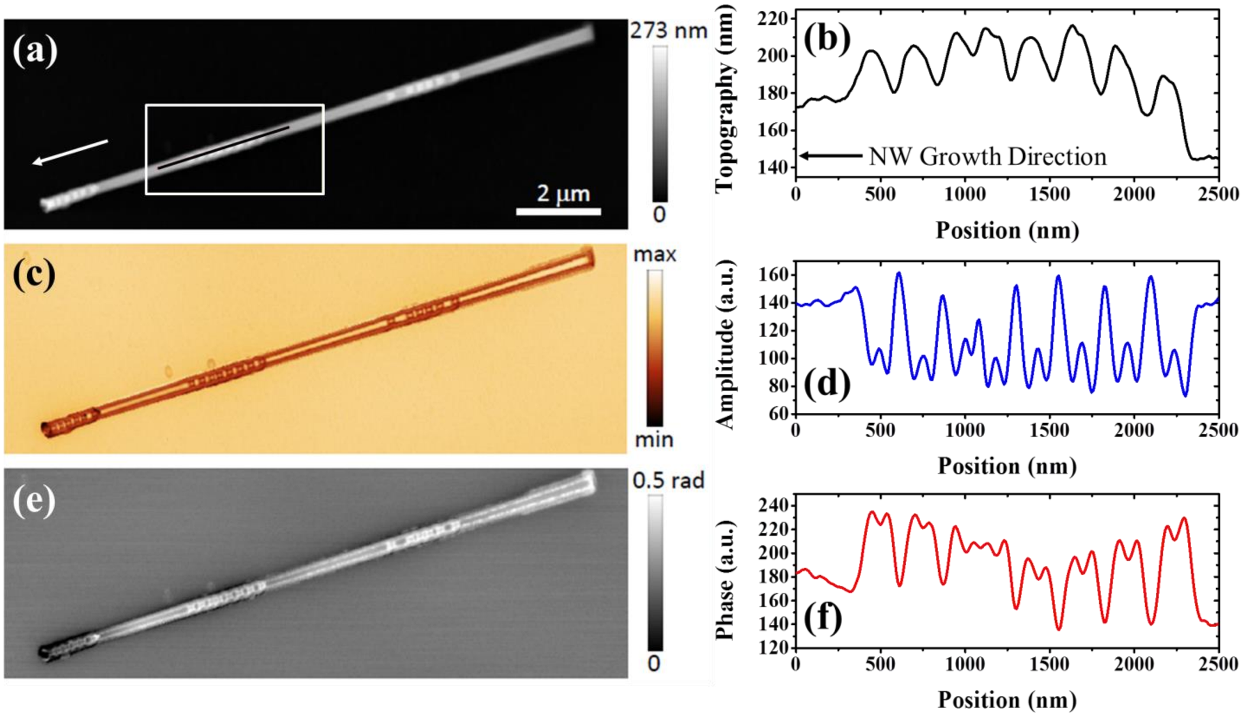

Figure 3.6: SNOM-IR mapping of multiple p-n planar GaAs NW at an IR laser frequency of 884 cm^{-1} (11.31 μm wavelength). (a) AFM topography scan and (b) corresponding axial linescan. (c) Near-field amplitude image (S_4), directly correlated to the free carrier concentration, and (d) corresponding axial linescan. (e)Near-field phase image and (f) corresponding axial linescan. All linescans were obtained along the black line, highlighted by the white border, in (a). The white and black arrows in (a) and (b) indicate the NW growth direction, respectively.

3.5 Physical Model

Based on the sMIM and SNOM profiles along the Zn-doped p-type NW segments, it can be presumed that the corrugated Zn-doped GaAs NW segment is composed of a series of p – p+ (peak–notch) homojunctions, as illustrated in Figure 4(a) in both side-view (x-z) and top-down view (x-y). The areas of greater hole concentration in the twinned notches are denoted as the p^+ region and the lower hole concentration in the non-twinned raised areas are the p region. The dimensions of the p+ region (twin plane) and p region (non-twin plane) are assumed to be 4 nm and 246 nm, respectively, by correlating sMIM capacitance and near-field amplitude linescan

results with AFM topography, SEM, and TEM measurements from multiple NWs. Assuming an average Zn doping concentration of 1.67×10^{18} cm^{-3} in the NW (nominal experimental values based on planar control samples) and a volume fraction of 1.6% (4 nm/246 nm) for the p^+ region, we estimate the doping concentration in the p region to be ~7×10^{16} cm^{-3} if the p^+ region is to be 1×10^{20} cm^{-3}, the threshold value for twin generation based on the DFT modeling. (see methods). Note that all values assumed here are approximations and only used for qualitative trend analysis (refer to methods). Using these values of doping concentrations, the valence potential and electrical field spatial profiles along the NW axis can be calculated. The theory and MATLAB script for the a 1-dimensional theoretical model for the expected band bending along the backbone of a NW described by our analysis is shown with detail in the methods section.

In the physical model, we will create a simple 1-dimensional plot of the bandbending along the corrugated non-uniformly doped regions of the nanowire. It will consist of a p-doped and p+ doped homojunction described by theoretical and experimental data. We will use MATLAB to perform the numerical simulation, the details of the original equation can be found in literature [61,62]. We first start by defining our universal constants: $\mathcal{E} = 11$ is the dielectric constant of GaAs, $V_T = 0.026$ is the thermal voltage at ambient temperatures, and q is the elementary unit charge. The estimated doping concentrations for the p and p+ side of the homojunction are obtained from the DFT analysis and bulk experimental results. The doping values used in the model are $N_p = 7 \times 10^{16}$, on the p side, and $N_{pp} = 1 \times 10^{20}$, on the p+ side. The function for the built-in potential and Debye screening length constant both of which are functions of the doping concentration [61]:

$$V_{bi} = V_T \ln\left(\frac{Np}{Npp}\right) \qquad (3.2)$$

$$L_{Dp} = 1E6 * \sqrt{\frac{\varepsilon\varepsilon_0 V_T}{N_p q}} \qquad (3.3)$$

$$L_{Dpp} = 1E6 * \sqrt{\frac{\varepsilon\varepsilon_0 V_T}{N_{pp} q}} \quad (3.4)$$

The spatial dimensions of the NW doping sections obtained through TEM analysis is numerically plotted as a function of x along the NW homojunction (nm). According to the data for every 250nm there is a highly doped p+ side approximately 4nm long. The functions used for the relative band potential across the p and p+ region is shown below [62]. The electric field and charge density can be plotted by taking the first and second derivative, accordingly, of the potential function with respect to the x-axis.

$$\Phi_p(x) = V_{bi} * \frac{L_{Dp}}{L_{Dp}+L_{Dpp}} * e^{-x/L_{Dp}} \quad (3.5)$$

$$\Phi_{pp}(x) = V_{bi} * \left(1 - \frac{L_{Dpp}}{L_{Dp}+L_{Dpp}}\right) * e^{-x/L_{Dpp}} \quad (3.6)$$

$$E(x) \sim \frac{\partial \Phi}{\partial x} \ and \ \rho(x) \sim \frac{\partial E}{\partial x} \quad (3.7)$$

$$\rho(x) \sim \frac{\partial^2 \Phi}{\partial x^2} \quad (3.8)$$

The profile can be divided into three regions, I – III, as indicated in figure 3.7b by the arrows. Region I represents the peak potential region centered at the p+ notch, which drives hole diffusion downhill from p+ to p region, leaving behind ionized acceptors in the p+ region near the p+-p interface. This forms an accumulation layer of holes in the p region near the junction. However, due to the carrier continuity of the homojunction, the p^+ region is not fully depleted, so a larger number of free carriers remain in the charge neutral region of the p^+ side. This agrees with the observations of high sMIM capacitance and high SNOM amplitude signals in the notch regions. In Region II holes are localized by the strong internal fields, forming a space charge region, which suppresses their contribution to coulomb screening at the sample surface just below the tip. Considering that holes in this region cannot be treated like truly free carriers, the

surface capacitance in Region II should be reduced. The steep decline in the MIM capacitance signal observed exactly at the onset of the topographical corrugation peak (figure 3.5d) is consistent with the presence of this space charge region. Region III is the quasi-flatband region in the lower doped p-region where the holes do not experience strong localizing E-fields; hence, they behave like free carriers. This model explains the small but distinct spike in capacitance exactly in the middle of the deep capacitance valley (figure 3.5d), which is spatially correlated with the center of the topological corrugation peak region. Figure 3.7c is an expanded view of Region I (p^+ notch) to highlight the flat band region in the center of the potential well, where the charge neutrality means the holes are also free carriers, except with a much higher concentration than in Region III. This agrees completely with the observed capacitance peaks indicated by the black arrows in Figure 3.5d.

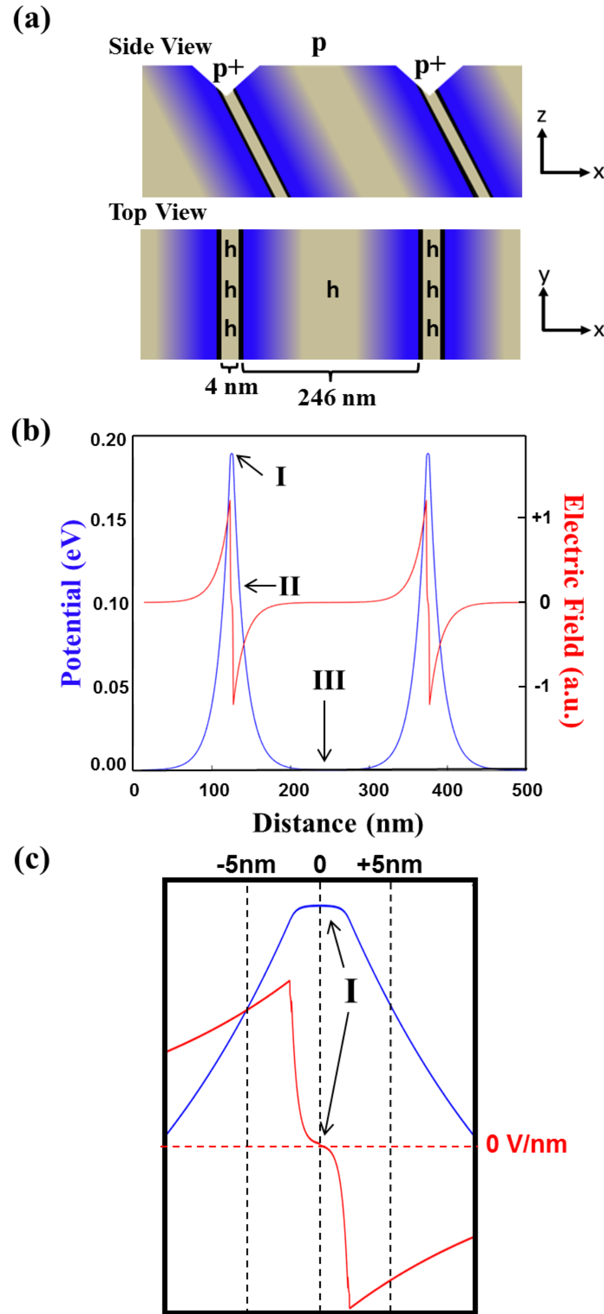

Figure 3.7: Physical model of the p region with twin-planes. (a) An illustration of the physical geometry along the NW corrugations used for numerical calculation. The blue regions represent areas of band bending or space regions where holes don't behave like truly free carriers. (b) A plot of the numerical calculation of the potential (blue, left axis) and E-field (red, right axis) as a function of x according to the figure 2a. Three regions are identified as I, II, III represent the highly doped (p+) hole potential well, space charge region with high E-fields, and the lower doped (p) flat band region. (c) An expanded view of region I in figure 2b where a hole potential well is shown as an area of flat band and zero E-field centered x = 0.

The physical model presented above can further be supported by bias-modulated microwave impedance microscopy (MIM2) measurements. Based on the physical model in figure 3.8, we expect the space charge region (p-side of Region II) and the flatband region (center of the p-region, Region III) to show a strong response to high tip bias (-9V) since they have a smaller dopant concentration. In region III there is a flatband in the lesser p-doped region allowing for free carriers respond strongly to the microwave signal, this is clearly shown in figure 3.8. The redistribution of the free electrons by the internal E-field is the likely cause of the local maxima in the SNOM-IR and MIM contrast. The presence of internal E-fields in the space charge region (Region II) would cause a voltage shift in the C-V response which suppresses the differential capacitance signal at low tip bias (-3V). On the other hand, the capacitance in the middle of a highly doped p+ region (Region I) would be minimally affected by the tip bias because of the higher dopant concentration and strong local E-fields that interact with the charge carriers, preventing the free carriers from locally redistributing to compensate for the modular tip bias. The MIM and MIM2 observations are completely consistent with the physical model of spatial distribution of carriers in the NW presented in figure 3.7 and 3.8.

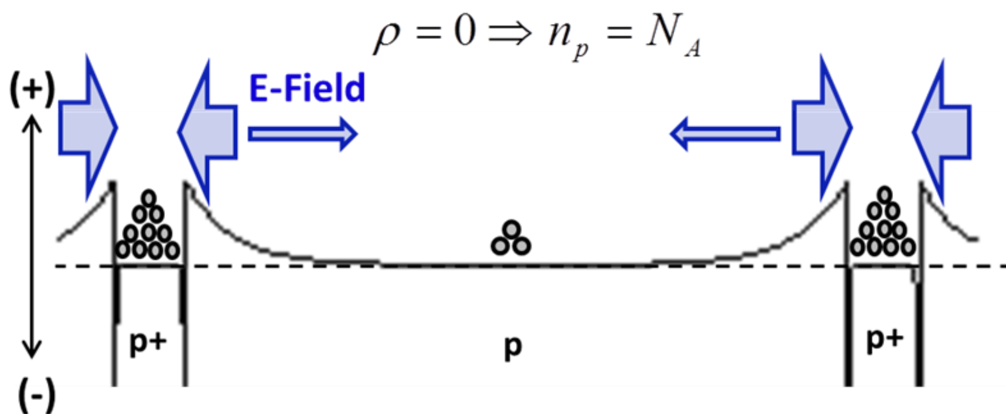

Figure 3.8: Physical model illustrating how the internal electric field across of the homojunction redistributes the free carriers.

3.6 Electrostatic Force Microscopy (EFM) Analysis

High capacitance at the side walls of the NW was also detected at the dual pass electrostatic force microscopy (EFM) measurement (figure 3.9), which eliminates any topology crosstalk lead to geometric capacitance artifacts (refer to Chapter 2). This indicates that the detection of capacitance contrast along the interfacial line between the NW and the substrate is a real detection of changing electronic properties. For the dual pass EFM, a single pass is used to acquire a topography scan and a second pass with a Z-offset (typically 50nm) retraces the original pass in non-contact mode while applying a modulated bias signal to the tip. The forces induced on the tip are dominated by electrostatic forces at the tip apex, which induces a deflection signal that is demodulated at the excitation frequency. Any contributions to the deflection signal based on topology coupling such as van der walls forces or surface geometric capacitance coupling to the tip side wall, discussed in detail in the methods section, would be attenuated from the Z-offset and further suppressed by the demodulation scheme.

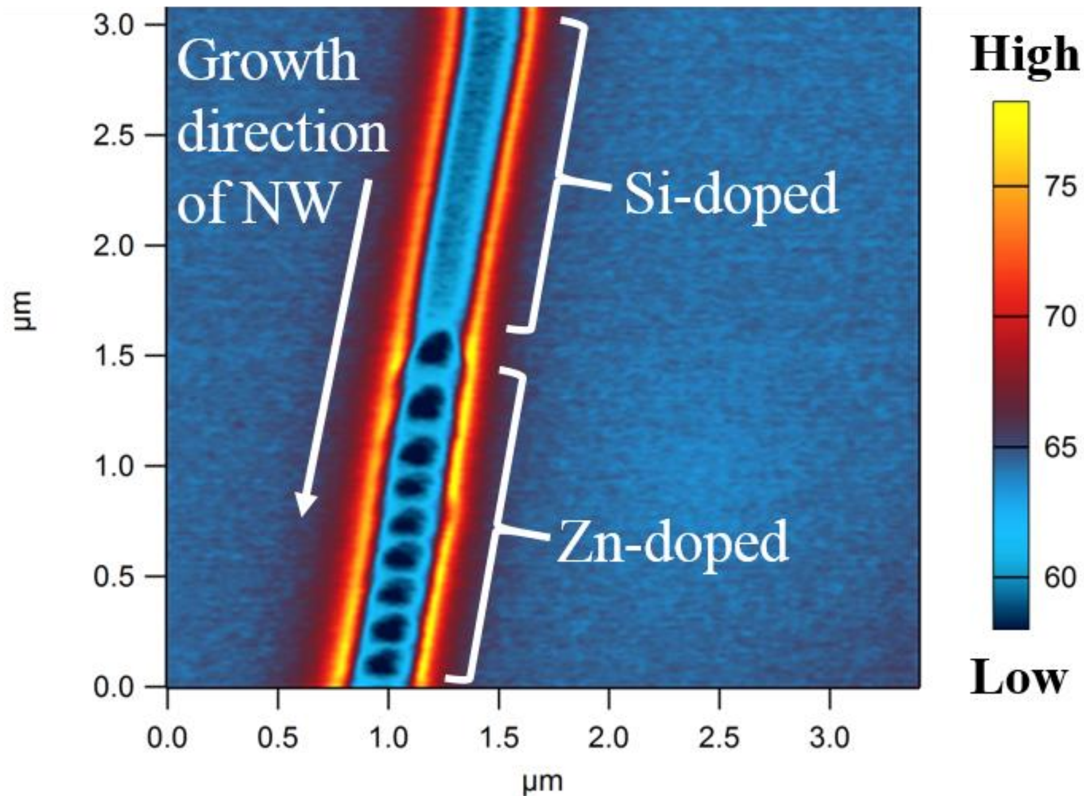

Figure 3.9: Surface potential changing along the GaAs NW measured *via* dual pass EFM measurement. The detection of significant potential changes at the edge of the NW by dual pass EFM indicates that the free carriers exist at the interface between the GaAs NW and the substrate. The contrast difference between the edge of the Si-doped segment and the Zn-doped segment is assumed to be caused by the difference in thickness of the parasitic thin film under the NW between the two segments. (the thickness of highly Zn-doped parasitic film direct under the NW is increasing along the NW growth direction).

The detection of high capacitance signal at the interface between the NW and the substrate, which was detected by MIM, SNOM-IR, and EFM can only be explained by the existence of highly Zn-doped GaAs. A parasitic thin film under the NW has been studied by APT measurement on a similar multiple p-n junction planar GaAs NW structure which could cause a shift in capacitance [26]. As multi p-n junction GaAs NW is grown continuously inside the chamber, highly Zn-doped thin film is grown on the substrate during each step of p-type NW growth process. Therefore, the parasitic thin film inevitably exists under the segments of the GaAs NW that were grown after the growth of p-type segments, and the film under the NW

cannot be eliminated after the chemical etching process (Figure 3.10). During the growth of a multiple p-n junction GaAs NW, the parasitic highly Zn-doped thin film is grown on the substrate accumulatively during each step of p-type NW growth process and the thickness continuously to build up as the NW length extends, as illustrated in Figure 3.10. This explains why the interface capacitance along the Zn-doped NW segment is higher than that of Si-doped segment in previously shown electrical maps (p-type NW was grown after the growth of n-type segment). The edge effect observed is localized so it should not affect the analysis of the periodic dopant distribution observed at the top surface of the NWs.

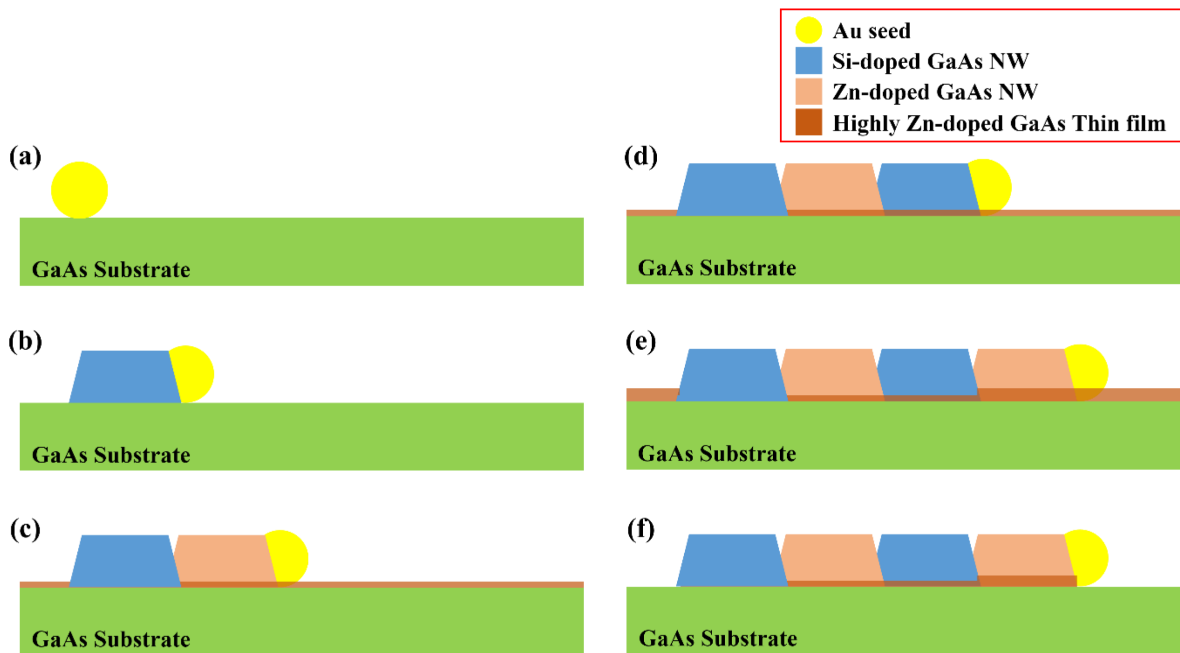

Figure 3.10: Growth of n-p-n-p multiple junction GaAs NW. (a) Au seed metal is deposited on GaAs substrate. (b) – (e) n-p-n-p GaAs NW is grown. Highly-Zn doped GaAs parasitic thin film is deposited on the substrate while growing p-type GaAs NW segments. The thickness of the parasitic thin film increases along with the number of Zn-doped NW segments. (f) Parasitic thin film exists at the interface between the GaAs NW and the substrate, even after the post-chemical etching process.

3.7 Conclusions

A spatial correlation between impurity species and defects in NWs has been reported previously in several studies. Hemesath *et al.* showed direct evidence of impurity Au atoms and their preferential incorporation along the grain boundaries of Si NWs having <110> growth directions [50]. Prominent twinning was also observed during growth of one-dimensional, Sb-doped ZnO nanostructures [51]. In fact, it was later shown that Sb-doping can lead to a kinking of the ZnO NW morphology at the site of twin planes [52]. Furthermore, dramatic changes in crystal structure were shown to result during Zn doping of both twinned superlattice InP and kinked, polytypic GaN NWs [53,54]. Lastly, we note that Chen *et al.* have reported on the localization of seed particle impurities, during In/Sb alloy-assisted growth, at twin plane defects in Si NWs [55]. It was proposed in their study that uniform incorporation of impurity species precedes their preferential segregation at the site of twin planes, and that the likelihood for localization at a defect site is proportional to the segregation energy of the impurity species.

In summary, utilizing the state-of-the-art, non-destructive, tip-based scanning microscopy techniques, MIM, MIM2, and IR-SNOM, we have probed the dopant distribution profile in multi-junction planar GaAs NWs grown by Au-seeded SLE mechanism. By the one-to-one correlation of the topography, electrical carrier distribution, and dopant impurities scattering profiles, we have, for the first time, provided unambiguous evidence that Zn dopants are preferentially accumulated at the twin-plane boundaries. We attribute this phenomenon to an energy driven mechanism where having Zn impurities residing in the twin planes lowers the twin formation energy, as confirmed by DFT calculations.

3.8 Methods

TEM Imaging

Post-growth inspection was performed using a Hitachi S-4800 field-emission scanning electron microscopy (SEM) system, JEOL 2010 LaB6 transmission electron microscope (TEM) and the locations of individual NWs of interest were marked and mapped using an FEI Helios NanoLab 600i focused ion beam (FIB) system for subsequent correlation of MIM and SNOM data.

MIM Imaging

All MIM experiments were performed using PrimeNano Inc, Microwave detection electronics, tip holders, and custom coaxial tips, in conjunction with an Asylum MFP3D Atomic Force Microscope. All AFM-MIM analysis was done on as-grown samples in a contact mode scanning geometry. For this setup, the microwave signal propagates from the source (-10dB, 2.7-3.3GHz) to the apex of the coaxial tip where a portion of the signal reflected back according to the sample impedance. The imaginary part of the microwave reflectivity was isolated using a capacitive standard calibration sample, alumina (Al_2O_3) dots on silicon, making the technique sensitive to small changes in surface capacitance (Chapter 2). The MIM-Im signal is proportional to the tip-sample capacitance resulting from charge stored in the metal-semiconductor junction formed in the contact mode geometry [38]. Other contributions to the capacitance signal such as thermal drift from internal electronics and environmental stray capacitance creates an arbitrary baseline signal that must be normalized using a linear flatten filter; this makes the technique qualitative in nature.

SNOM Imaging

Mid-Infrared absorption maps of individual NWs were acquired by utilizing a commercially available SNOM microscope (neaSNOM, neaspec GmbH). Here the output of a continuous-wave tunable CO_2-laser (Access laser) at a frequency of 884 cm^{-1} was focused *via* a parabolic mirror on to a Pt/Ir coated Si-AFM tip (Arrow NCPT, Nanoworld) with an apex radius of ~20 nm. While scanning, the sample below the AFM tip, we detect and analyze the tip-scattered light using a Michelson interferometer to obtain simultaneous optical amplitude and phase maps of the NWs (Chapter 2). To eliminate far-field background scattering, the AFM is operated in dynamic mode where the tip oscillated at an amplitude of about 40-50 nm at a frequency ~ 250 kHz allowing interferometric heterodyne detection of the apertureless nearfield signal. The optical detector signal is demodulated at higher harmonics of the tip oscillation frequency yielding background-free SNOM-IR amplitude and phase signals.

Nanowire Growth

Nanowire growth was led by Wonsik Choi as apart of Professor Xuling Li's group at the University of Illinois – Urbana Champaign Electrical Engineering Department. The information in this subsection was preformed and described by Wonsik Choi. Sample preparation for NW growth was initiated by surface cleaning of semi-insulating (SI) GaAs (100) substrates with resistivity of (1.8×10^{18}) Ω·cm in a diluted solution of hydrochloric acid and deionized water (volumetric dilution ratio of 1:1) for the removal of surface oxide layers and residual organic contaminants. Next, monodispersed Au colloids (BBI solutions) with 250 nm diameters were drop-cast onto the GaAs surface, and samples were loaded in a horizontal-flow configuration 200/4 AIXTRON MOCVD reactor for SLE-NW synthesis. Prior to the onset of growth, a surface

oxide desorption step at 650 °C was implemented for a period of 10 minutes under an arsine (AsH_3) flow of 50 sccm. The supply of TMGa, AsH_3, Si_2H_6, and DEZn, precursor gasses provided group-III, group-V, n-type dopant, and p-type dopant growth species, respectively, under a constant hydrogen (H_2) carrier gas flow of 5 L/min. Planar NW growth was carried out at a temperature of 460 °C for a total duration 160 seconds at a reactor pressure of 950 mBar. During growth, the supply of Si_2H_6 and DEZn were alternated 8 times, with dopant precursor flows monotonically increasing in each sequentially grown segment, resulting in the lateral assembly of 4 n-p (also, 3 p-n) junctions along the axial growth direction. Based on calibrations of GaAs (100) thin films, Si concentrations in the alternating n-type segments are estimated as 1.63×10^{17}, 4.47×10^{17}, 4.71×10^{18}, 9.45×10^{18} cm^{-3}, while Zn concentrations in the alternating p-type segments are estimated to be 1.67×10^{18}, 3.33×10^{18}, 5.33×10^{18}, 6.00×10^{18} cm^{-3}, from NW base to tip. Growth was terminated after the formation of the final p-type segment through the cessation of TMGa and DEZn supply, and the samples were cooled under a constant AsH_3 flow. After removal for the growth reactor, the samples were subjected to a short (5 seconds) etching process in a solution of H_2SO_4 : H_2O_2 : H_2O (1 : 8 : 340) for the removal of a 20 nm parasitic thin film on the sample surface, which was formed in tandem with NW growth, both on the NW sidewalls and in the exposed substrate surfaces between NWs. We note that this post-epitaxy etching process does not adversely influence the morphology or structure of the laterally-grown NWs, nor does it modify the distribution of dopants therein.

Density Functional Theory (DFT)

DFT analysis was led by Professor Harley Johnson's group in collaboration with Professor Xuling Li's group at the University of Illinois – Urbana Champaign Electrical

Engineering Department. The information in this subsection was described by Wonsik Choi and Xuling Li. Using the BigDFT electronic structure code the effect of Zn dopant atoms on the formation energy of these twins is analyzed [56,57]. We construct an orthorhombic, periodic 432-atom unit cell, approximately 2.1 nm by 2.4 nm by 2.0 nm, containing a pair of GaAs twins. The calculation parameters are chosen in accordance with those reported previously for similar semiconductor materials: the exchange-correlation energy is handled *via* the generalized gradient approximation (GGA) with HGH pseudopotential and a Brillouin zone integration at the Γ point [58]. The structural relaxations use the FIRE algorithm with an energy convergence criterion of 3 meV/Å. The energy of the twin boundary in undoped GaAs is found to be 2.05 eV/$Å^2$, which is in good agreement with previous experimental measurements, and relatively low among III-V semiconductors [59]. As shown in Table 3.1, the formation energy of the same boundary in GaAs doped with 1% Zn or 10^{20} cm^{-3}, in the A-type (B-type) polarity, is reduced by roughly 3% (2%). One arrives at these numbers by comparing the energy of the twin in the doped case with the energy of GaAs, without a twin, at the same Zn concentration.

The thermodynamic chemical potential is defined in terms of the Zn-As pair, and defined by the energy difference between a pure GaAs system and the GaAs system with 1% Zn that contains one Zn-As pair substituting for a Ga-As pair. When a twin is present, and the Zn substitution is at the twin boundary, there is further energy reduction with additional Zn concentration. As shown in Table 3.1, this holds beyond the average concentration level of 1%, or approximately 10^{20} cm^{-3}. The energy reduction, in fact, has a stronger-than-linear dependence on Zn concentration. This result can be considered as the thermodynamic measure of the defect formation energy reduction due to Zn, when substitutional Zn is taken as a reference for Zn.

While the calculation results suggest that there is a non-negligible binding (or energy reduction due to spatial proximity) between the Zn dopants and a GaAs twin, one must also consider the relationship between the overall spatial distribution of Zn and the relatively distantly spaced twins found in the planar GaAs NWs. Since twinning is experimentally observed only when the nominal doping concentration is above the 10^{18} cm^{-3} range, Zn is only likely to promote twinning by reducing the twin formation energy if there is a sufficient spatial non-uniformity in the Zn distribution, so that locally the Zn concentrations can approach the 10^{19}-10^{20} cm^{-3} level considered in the computational study [44]. Indeed, previous experimental evidence suggests that there is a many-body effect by which Zn dopant atoms in GaAs segregate due to an attractive interaction [60]. In the present case, if a modest segregation effect shifts the average Zn concentration of 10^{18} to a local concentration that is an order of magnitude higher, as seen by Ebert *et al.*, the strong twin formation energy reduction seen in the present calculations would provide a clear explanation of the experimentally observed twins [60]. Thus, the Zn-induced twinning in GaAs may be driven by a two-step mechanism, as shown by the results of the calculations: first the Zn impurities segregate due to a negative binding energy (calculated to be 82meV in our unit cell containing three Zn atoms, Table 3.1); and, second, the twin forms due to an additional energy reduction of the twin in the presence of the Zn-enriched plane (calculated to be 77meV for three Zn atoms, Table 3.1). Overall, in this case, the twin formation is reduced by about 15% with respect to the undoped case. The three Zn atom case, considered here as an example to illustrate the role of the Zn planar concentration, corresponds to a Zn planar density of 0.59 nm^{-2} (or 5.9x 10^{13} cm^{-2}). It is also interesting to note that the effect becomes significantly stronger at slightly higher Zn concentrations; in the six Zn atom case, for example, the total energy reduction reaches 50%, most of which is due to the in-plane binding of the Zn dopant

atoms. Given such a mechanism, the twin is expected to appear when a threshold planar concentration is achieved, making the twin periodicity dependent on both Zn concentration and NW diameter in a complex manner deriving from the VLS process parameters [44].

	1 Zn	2 Zn	3 Zn	6 Zn
Bulk conc. (cm^{-3})	1.0×10^{20}	2.0×10^{20}	3.0×10^{20}	5.9×10^{20}
Planar conc. (nm^{-2})	2.0×10^{-1}	3.9×10^{-1}	5.9×10^{-1}	11.8×10^{-1}
$E_{In\text{-}plane\ binding}$ (meV)	0	-27	- 82	-464
$E_{Twin\ binding}$ (A/B) (meV)	- 32 / - 25	-51 / -37	- 77 / -55	- 82 / NC
$E_{Total\ binding}$ (A/B) (meV)	- 32 / - 25	-78 / -64	-159 / - 137	- 525 / NC
Max E reduction (%)	3	7	15	50

Table 3.1: DFT calculation results. Bulk concentrations are in cm^{-3}, planar concentrations are in nm^{-2}, Binding energies are in meV and reductions are in %. (A/B) denotes the (111)A or (111)B face of GaAs; and the twins are oriented along (111)B. NC: not calculated. The addition of Zn reduces the formation energy of the twin boundary through (i) a binding energy between Zn atoms, and (ii) a binding energy between the Zn and the twin.

Geometric Capacitance Artifacts

Due to the finite radius of tip apex and conical or pyramidic shape of tip, the geometric artifact capacitance is possibly convoluted between the probe tip and 3D-structured NW sample [63-65]. As shown in Figure 3.11a, two different kinds of capacitances can be measured through the metal AFM tip: one is the capacitance detected between the apex of the half sphere of the tip and the sample (C_{apex}), and the other is the capacitance measured from the interaction between the truncated cone of the tip and the sample (C_{cone}) [64]. When the tip is scanning the flat surface of the sample, most of the capacitance is detected at the cone, C_{cone}, and apex, C_{apex}, of the tip

can be ignored. However, when the tip is scanning the edge of sample where the height of the sample is taller than the radius of the half sphere of the tip apex, the side wall of the sample can be strongly coupled with the truncated cone of the tip, so the artifact capacitance can be detected. One important thing that should be considered is that the capacitances measured at the corrugated Zn-doped NW are dominated by C_{apex} because the height difference between the ridge and twin plane in the segment is smaller than the tip's radius (50nm) (figure 3.11b).

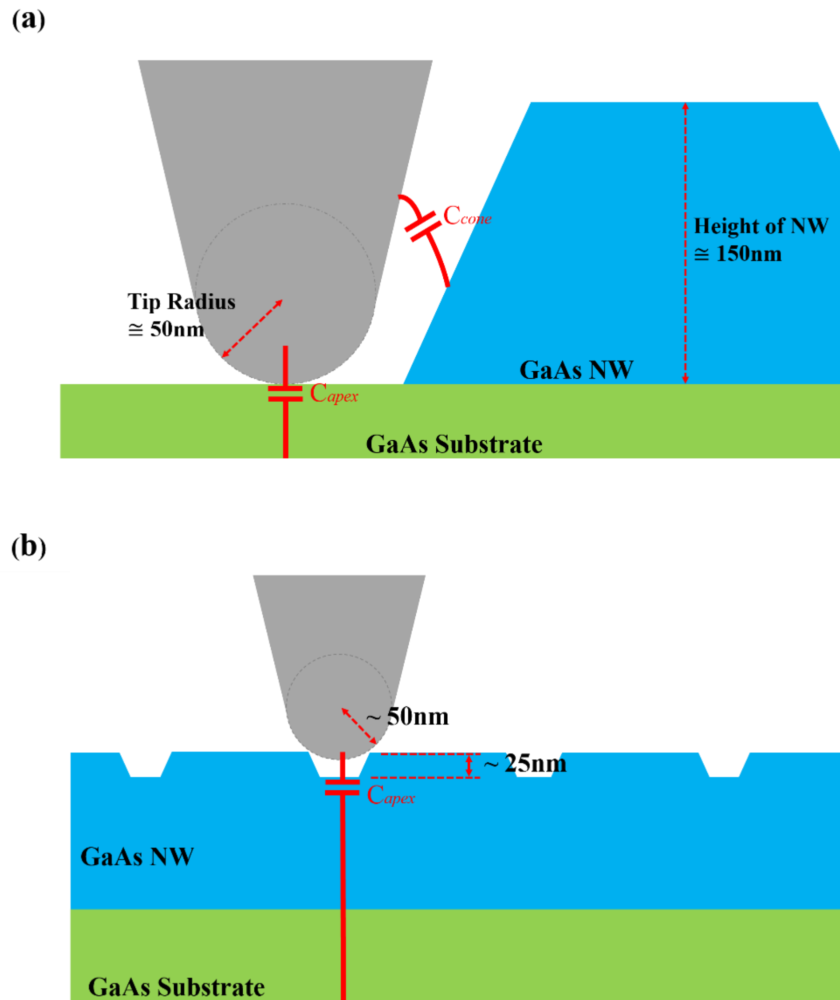

Figure 3.11: Schematic of mutual capacitances between the metal tip and the GaAs NW. (a) When the tip scans the edge of the NW, sidewall coupling occurs from capacitive coupling (C_{cone}) of the tip's cone to the sample. The tip radius and the height of the GaAs NW are 50nm and 150nm, respectively. (b) When the topographic height differences on the NW are smaller the radius of the sphere of the tip, the sidewall coupling capacitance is subtle.

3.9 References

1. Eaton, S. W.; Fu, A.; Wong, A. B.; Ning, C.-Z.; Yang, P. Semiconductor Nanowire Lasers. Nat. Rev. Mater. 2016, 1, 16028.

2. Saxena, D.; Wang, F.; Gao, Q.; Mokkapati, S.; Tan, H. H.; Jagadish, C. Mode Profiling of Semiconductor Nanowire Lasers. Nano Lett. 2015, 15, 5342-5348.

3. Zhang, C.; Li, X. III-V Nanowire Transistors for Low-Power Logic Applications: A Review and Outlook. IEEE Trans. Electron Devices 2016, 63, 223-234.

4. Schmid, H.; Borg, M.; Moselund, K.; Gignac, L.; Breslin, C. M.; Bruley, J.; Cutaia, D.; Riel, H. Template-Assisted Selective Epitaxy of III–V Nanoscale Devices for Co-Planar Heterogeneous Integration with Si. Appl. Phys. Lett. 2015, 106, 233101.

5. Miao, X.; Chabak, K.; Zhang, C.; K. Mohseni, P.; Walker, D.; Li, X. High-Speed Planar GaAs Nanowire Arrays with fmax > 75 GHz by Wafer-Scale Bottom-up Growth. Nano Lett. 2015, 15, 2780-2786.

6. Svensson, J.; Dey, A. W.; Jacobsson, D.; Wernersson, L.-E. III–V Nanowire Complementary Metal–Oxide Semiconductor Transistors Monolithically Integrated on Si. Nano Lett. 2015, 15, 7898-7904.

7. LaPierre, R. R.; Chia, A. C. E.; Gibson, S. J.; Haapamaki, C. M.; Boulanger, J.; Yee, R.; Kuyanov, P.; Zhang, J.; Tajik, N.; Jewell, N.; Rahman, K. M. A. III–V Nanowire Photovoltaics: Review of Design for High Efficiency. Phys. Status Solidi RRL 2013, 7, 815-830.

8. Åberg, I.; Vescovi, G.; Asoli, D.; Naseem, U.; Gilboy, J. P.; Sundvall, C.; Dahlgren, A.; Svensson, K. E.; Anttu, N.; Björk, M. T.; Samuelson, L. A GaAs Nanowire Array Solar Cell With 15.3% Efficiency at 1 Sun. IEEE J. Photovolt. 2016, 6, 185-190.

9. Nikoobakht, B.; Wang, X.; Herzing, A.; Shi, J. Scalable Synthesis and Device Integration of Self-Registered One-Dimensional Zinc Oxide Nanostructures and Related Materials. Chem. Soc. Rev. 2013, 42, 342-365.

10. Nikoobakht, B. Toward Industrial-Scale Fabrication of Nanowire-Based Devices. Chem. Mater. 2007, 19, 5279-5284.

11. Tsivion, D.; Joselevich, E. Guided Growth of Epitaxially Coherent GaN Nanowires on Sic. Nano Lett. 2013, 13, 5491-5496.

12. Fortuna, S. A.; Wen, J.; Chun, I. S.; Li, X. Planar GaAs Nanowires on GaAs (100) Substrates: Self-Aligned, Nearly Twin-Defect Free, and Transfer-Printable. Nano Lett. 2008, 8, 4421-4427.

13. Zhang, C.; Dowdy, R.; Li, X. High Voltage Gain MESFET Amplifier Using Self-Aligned MOCVD Grown Planar GaAs Nanowires, Device Research Conference (DRC), 2013, 63-64.

14. Zhang, C.; Miao, X.; Mohseni, P. K.; Choi, W.; Li, X. Site-Controlled VLS Growth of Planar Nanowires: Yield and Mechanism. Nano Lett. 2014, 14, 6836-6841.

15. Tsivion, D.; Schvartzman, M.; Popovitz-Biro, R.; von Huth, P.; Joselevich, E. Guided Growth of Millimeter-Long Horizontal Nanowires with Controlled Orientations. Science 2011, 333003-1007.

16. Fortuna, S. A.; Li, X. In GaAs FET with a High Mobility Self-Assembled Planar Nanowire Channel on a (100) Substrate. Device Research Conference (DRC) 2009, 19-20.

17. Zhang, C.; Li, X. Planar GaAs nanowire tri-gate MOSFETs by vapor–liquid–solid growth. Solid-State Electron. 2014, 93, 40-42.

18. Zhang, C.; Choi, W.; Mohseni, P. K.; Li, X. InAs Planar Nanowire Gate-All-Around MOSFETs on GaAs Substrates by Selective Lateral Epitaxy. IEEE Electron Device Lett. 2015, 36, 663-665.

19. Chia, A. C. E.; Boulanger, J. P.; LaPierre, R. R. Unlocking Doping and Compositional Profiles of Nanowire Ensembles Using SIMS. Nanotechnology 2013, 24, 045701.

20. Roussel, M.; Chen, W.; Talbot, E.; Lardé, R.; Cadel, E.; Gourbilleau, F.; Grandidier, B.; Stiévenard, D.; Pareige, P. Atomic Scale Investigation of Silicon Nanowires and Nanoclusters. Nanoscale Res. Lett. 2011, 6, 1-6.

21. Perea, D. E.; Hemesath, E. R.; Schwalbach, E. J.; Lensch-Falk, J. L.; Voorhees, P. W.; Lauhon, L. J. Direct Measurement of Dopant Distribution in an Individual Vapour-Liquid-Solid Nanowire. Nat. Nanotechnol. 2009, 4, 315-319.

22. Moutanabbir, O.; Isheim, D.; Blumtritt, H.; Senz, S.; Pippel, E.; Seidman, D. N. Colossal Injection of Catalyst Atoms into Silicon Nanowires. Nature 2013, 496, 78-82.

23. Xu, T.; Nys, J. P.; Grandidier, B.; Stiévenard, D.; Coffinier, Y.; Boukherroub, R.; Larde, R.; Cadel, E.; Pareige, P. Growth of Si Nanowires on Micropillars for the Study of Their Dopant Distribution by Atom Probe Tomography. J. Vac. Sci. Technol., B 2008, 26, 1960-1963.

24. Du, S.; Burgess, T.; Gault, B.; Gao, Q.; Bao, P.; Li, L.; Cui, X.; Kong Yeoh, W.; Liu, H.; Yao, L.; Ceguerra, A. V.; Hoe Tan, H.; Jagadish, C.; Ringer, S. P.; Zheng, R. Quantitative Dopant Distributions in GaAs Nanowires Using Atom Probe Tomography. Ultramicroscopy 2013, 132, 186-192.

25. Agrawal, R.; Bernal, R. A.; Isheim, D.; Espinosa, H. D. Characterizing Atomic Composition and Dopant Distribution in Wide Band Gap Semiconductor Nanowires Using Laser-Assisted Atom Probe Tomography. J. Phys. Chem. C 2011, 115, 17688-17694.

26. Qu, J.; Choi, W.; Katal Mohseni, P.; Li, X.; Zhang, Y.; Chen, H.; Ringer, S.; Zheng, R. Direct Observation of Dopants Distribution and Diffusion in Gaas Planar Nanowires with Atom Probe Tomography. ACS Appl. Mater. Interfaces 2016, 8, 26244-26250.

27. Koren, E.; Rosenwaks, Y.; Allen, J. E.; Hemesath, E. R.; Lauhon, L. J. Nonuniform Doping Distribution Along Silicon Nanowires Measured by Kelvin Probe Force Microscopy and Scanning Photocurrent Microscopy. Appl. Phys. Lett. 2009, 95, 092105.

28. Koren, E.; Hyun, J. K.; Givan, U.; Hemesath, E. R.; Lauhon, L. J.; Rosenwaks, Y. Obtaining Uniform Dopant Distributions in VLS-Grown Si Nanowires. Nano Lett. 2011, 11, 183-187.

29. Kikukawa, A.; Hosaka, S.; Imura, R. Silicon PN Junction Imaging and Characterizations Using Sensitivity Enhanced Kelvin Probe Force Microscopy. Appl. Phys. Lett. 1995, 66, 3510-3512.

30. Allen, J. E.; Perea, D. E.; Hemesath, E. R.; Lauhon, L. J. Nonuniform Nanowire Doping Profiles Revealed by Quantitative Scanning Photocurrent Microscopy. Adv. Mater. 2009, 21, 3067-3072.

31. Kelzenberg, M. D.; Turner-Evans, D. B.; Kayes, B. M.; Filler, M. A.; Putnam, M. C.; Lewis, N. S.; Atwater, H. A. Photovoltaic Measurements in Single-Nanowire Silicon Solar Cells. Nano Lett. 2008, 8, 710-714.

32. Gu, Y.; Romankiewicz, J. P.; David, J. K.; Lensch, J. L.; Lauhon, L. J.; Kwak, E.-S.; Odom, T. W. Local Photocurrent Mapping as a Probe of Contact Effects and Charge Carrier Transport in Semiconductor Nanowire Devices. J. Vac. Sci. Technol., B 2006, 24, 2172-2177.

33. Gu, Y.; Kwak, E.-S.; Lensch, J. L.; Allen, J. E.; Odom, T. W.; Lauhon, L. J. Near-Field Scanning Photocurrent Microscopy of a Nanowire Photodetector. Appl. Phys. Lett. 2005, 87, 043111.

34. Angela, C. N.; Thalita, C.; Klaus, O. V.; João, H. C.; Mônica, A. C. Evidence of Space Charge Regions within Semiconductor Nanowires from Kelvin Probe Force Microscopy. Nanotechnology 2009, 20, 465705.

35. Ono, S.; Takeuchi, M.; Takahashi, T. Current and Potential Characterization on InAs Nanowires by Contact-Mode Atomic Force Microscopy and Kelvin Probe Force Microscopy. Ultramicroscopy 2002, 91, 127-132.

36. Vinaji, S.; Lochthofen, A.; Mertin, W.; Regolin, I.; Gutsche, C.; Prost, W.; Tegude, F. J.; Bacher, G. Material and Doping Transitions in Single GaAs-Based Nanowires Probed by Kelvin Probe Force Microscopy. Nanotechnology 2009, 20, 385702.

37. Sommerhalter, C.; Matthes, T. W.; Glatzel, T.; Jäger-Waldau, A.; Lux-Steiner, M. C. High-Sensitivity Quantitative Kelvin Probe Microscopy by Noncontact Ultra-High-Vacuum Atomic Force Microscopy. Appl. Phys. Lett. 1999, 75, 286-288.

38. Kundhikanjana, W.; Yang, Y.; Tanga, Q.; Zhang, K.; Lai, K.; Ma, Y.; Kelly, M. A.; Li, X. X.; Shen, Z. X. Unexpected Surface Implanted Layer in Static Random Access Memory Devices Observed by Microwave Impedance Microscope. Semicond. Sci. Technol. 2013, 28, 025010.

39. Seabron, E.; MacLaren, S.; Xie, X.; Rotkin, S. V.; Rogers, J. A.; Wilson, W. L. Scanning Probe Microwave Reflectivity of Aligned Single-Walled Carbon Nanotubes: Imaging of Electronic Structure and Quantum Behavior at the Nanoscale. ACS Nano 2016, 10, 360-368.

40. Atkin, J. M.; Berweger, S.; Jones, A. C.; Raschke, M. B. Nano-Optical Imaging and Spectroscopy of Order, Phases, and Domains in Complex Solids. Adv. Phys. 2012, 61, 745-842.

41. Huber, A. J.; Wittborn, J.; Hillenbrand, R. Infrared Spectroscopic Near-Field Mapping of Single Nanotransistors. Nanotechnology 2010, 21, 235702.

42. Keilmann, F.; Huber, A. J.; Hillenbrand, R. Nanoscale Conductivity Contrast by Scattering-Type Near-Field Optical Microscopy in the Visible, Infrared and THz Domains. J. Infrared, Millimeter, Terahertz Waves 2009, 30, 1255-1268..

43. Stiegler, J. M.; Huber, A. J.; Diedenhofen, S. L.; Gómez Rivas, J.; Algra, R. E.; Bakkers, E. P. A. M.; Hillenbrand, R. Nanoscale Free-Carrier Profiling of Individual Semiconductor Nanowires by Infrared Near-Field Nanoscopy. Nano Lett. 2010, 10, 1387-1392.

44. Dowdy, R. S.; Zhang, C.; Mohseni, P. K.; Fortuna, S. A.; Wen, J.-G.; Coleman, J. J.; Li, X. Perturbation of Au-Assisted Planar GaAs Nanowire Growth by P-Type Dopant Impurities. Opt.Mater. Express 2013, 3, 1687-1697.

45. Buh, G. H.; Kopanski, J. J.; Marchiando, J. F.; Birdwell, A. G.; Kuk, Y. Factors Influencing the Capacitance–Voltage Characteristics Measured by the Scanning Capacitance Microscope. J. Appl. Phys. 2003, 94, 2680-2685.

46. Williams, C. C. Two-Dimensional Dopant Profiling by Scanning Capacitance Microscopy. Annu. Rev. Mater. Sci. 1999, 29, 471-504.

47. Abraham, D. W.; Williams, C.; Slinkman, J.; Wickramasinghe, H. K. Lateral Dopant Profiling in Semiconductors by Force Microscopy Using Capacitive Detection. J. Vac. Sci. Technol., B 1991, 9, 703-706.

48. Brotherton, S. D., Introduction. In Introduction to Thin Film Transistors, Springer: 2013; pp 1-5.

49. Edwards, H.; Ukraintsev, V. A.; San Martin, R.; Johnson, F. S.; Menz, P.; Walsh, S.; Ashburn, S.; Wills, K. S.; Harvey, K.; Chang, M.-C. PN-Junction Delineation in Si Devices Using Scanning Capacitance Spectroscopy. J. Appl. Phys. 2000, 87, 1485-1495.

50. Hemesath, E. R.; Schreiber, D. K.; Gulsoy, E. B.; Kisielowski, C. F.; Petford-Long, A. K.; Voorhees, P. W.; Lauhon, L. J. Catalyst Incorporation at Defects during Nanowire Growth. Nano Lett. 2012, 12, 167-171.

51. Yang, Y.; Qi, J.; Liao, Q.; Zhang, Y.; Tang, L.; Qin, Z. Synthesis and Characterization of Sb-Doped ZnO Nanobelts with Single-Side Zigzag Boundaries. J. Phys. Chem. C 2008, 112, 17916-17919.

52. Su, L.; Xiaozhong, Z.; Lihuan, Z.; Min, G. Twinning-Induced Kinking of Sb-Doped ZnO Nanowires. Nanotechnology 2010, 21, 435602.

53. Algra, R. E.; Verheijen, M. A.; Borgstrom, M. T.; Feiner, L.-F.; Immink, G.; van Enckevort, W. J. P.; Vlieg, E.; Bakkers, E. P. A. M. Twinning Superlattices in Indium Phosphide Nanowires. Nature 2008, 456, 369-372.

54. Yang, B.; Liu, B.; Wang, Y.; Zhuang, H.; Liu, Q.; Yuan, F.; Jiang, X. Zn-Dopant Dependent Defect Evolution in GaN Nanowires. Nanoscale 2015, 7, 16237-16245.

55. Chen, W.; Yu, L.; Misra, S.; Fan, Z.; Pareige, P.; Patriarche, G.; Bouchoule, S.; Cabarrocas, P. R. I. Incorporation and Redistribution of Impurities into Silicon nanowires during Metal-Particle-Assisted Growth. Nat. Commun. 2014, 5.

56. Genovese, L.; Neelov, A.; Goedecker, S.; Deutsch, T.; Ghasemi, S. A.; Willand, A.; Caliste, D.; Zilberberg, O.; Rayson, M.; Bergman, A.; Schneider, R. Daubechies Wavelets as a Basis Set for Density Functional Pseudopotential Calculations. J. Chem. Phys. 2008, 129, 014109.

57. Mohr, S.; Ratcliff, L. E.; Boulanger, P.; Genovese, L.; Caliste, D.; Deutsch, T.; Goedecker, S. Daubechies Wavelets for Linear Scaling Density Functional Theory. J. Chem. Phys. 2014, 140, 204110.

58. Cherkashin, N.; Darras, F. X.; Pochet, P.; Reboh, S.; Ratel-Ramond, N.; Claverie, A. Modelling of Point Defect Complex Formation and its Application to H+ Ion Implanted Silicon. Acta Mater. 2015, 99, 187-195.

59. Takeuchi, S.; Suzuki, K. Stacking Fault Energies of Tetrahedrally Coordinated Crystals. Phys. Status Solidi A 1999, 171, 99-103.

60. Ebert, P.; Zhang, T.; Kluge, F.; Simon, M.; Zhang, Z.; Urban, K. Importance of Many-Body Effects in the Clustering of Charged Zn Dopant Atoms in GaAs. Phys. Rev. Lett. 1999, 83, 757-760.

61. Van Zeghbroeck, Bart. "Principles of Semiconductor Devices (Chapter 3)." Colarado University (2011). http://ecee.colorado.edu/~bart/book/book/chapter3/pdf/ch3_8.pdf

62. Neudeck, Gerold W. The PN junction diode. Vol. 2. Addison-Wesley, 1983.

63. Rachel, A. O., Advances in AFMfm for the Electrical Characterization of Semiconductors. Rep. Prog. Phys.Reports on Progress in Physics 2008, 71, 076501.

64. Karbassi, A.; Ruf, D.; Bettermann, A. D.; Paulson, C. A.; van der Weide, D. W.; Tanbakuchi, H.; Stancliff, R., Quantitative Scanning near-Field Microwave Microscopy for Thin Film Dielectric Constant Measurement. Rev. Sci. Instrum.Review of Scientific Instruments 2008, 79, 094706.

65. Hudlet, S.; Saint Jean, M.; Guthmann, C.; Berger, J., Evaluation of the Capacitive Force between an Atomic Force Microscopy Tip and a Metallic Surface. Eur. Phys. J. B The European Physical Journal B - Condensed Matter and Complex Systems 1998, 2, 5-10

CHAPTER 4

SCAN PROBE MICROWAVE REFLECTIVITY MAPPING OF NANOSCALE ELECTRONIC PHENOMENA ON ALIGNED CARBON NANOTUBES

Significant portions of this chapter were published as "Scanning probe microwave reflectivity of aligned single-walled carbon nanotubes: Imaging of electronic structure and quantum behavior at the nanoscale." Seabron, E., MacLaren, S., Xie, X., Rotkin, S.V., Rogers, J.A. and Wilson, W.L., ACS nano 10.1 (2015): 360-368. Reproduced with permission from the journal. The experimental work and image analysis were the primary contribution by the author. Some of the theoretical work presented in this chapter, including the mathematical treatment of the observed signal, were the outcomes of close collaborations and joint work with collaborators.

4.1 Introduction

Single-walled carbon nanotubes (SWNTs) are unique nanomaterials with "quasi" one-dimensional structure driven electronic properties [1,2,3]. Their intriguing transport behavior makes them an excellent candidate materials for next generation device technologies including high performance, low power, RF field-effect transistors, and nanoscale logic devices [4,5,6]. Dense, horizontally aligned arrays of high purity, (99.999%) semiconducting nanotubes are the best development platform for many of these next generation device applications [7,8,9,10,11]. While growth and device processing methods have progressed steadily, materials inspection and metrology techniques are still limited [10,12,13,14,15,16,17,18,19,20,21]. There are very few nondestructive methods for electronic characterization of nanotubes at the nanoscale. Recently an array of innovative, reflective near-field microwave imaging modalities have been introduced

[22,23,24,25,26]. These techniques complement scanning tunneling microscopy and spectroscopy techniques developed, but with greater ease of use [27,28,29,30]. One versatile variant, Microwave Impedance Microscopy (MIM), is a high resolution structured cantilever based scan-probe technique, where a fixed low power RF frequency applied to a specialized tailored waveguide tip coupled to sensitive RF circuitry, is used to spatially map material impedance with a high sensitivity and signal-to-noise ratio (SNR) at resolutions (~50nm), mostly limited by the tip size [18,25,31,32,33,34]. MIM has a very high sensitivity (~aF) and low surface penetration depth at low RF power limiting its detection range to the changes in capacitance present in the microwave "near-field" just below the tip apex. This is in contrast to, for example, Scanning Capacitance microscopy which detects changes in capacitance as a result of an oscillating potential across the entire sample thickness which limits its sensitivity, even while operating at microwave frequencies a notably higher power RF source is needed to achieve nanoscale impedance sensitivity [35,36]. It is worth noting that low dimensional materials such as SWNTs tend to give a much lower capacitance signal than bulk samples due to their atomically limited sample volume, hence high sensitivity under low RF power conditions is a vital feature of MIM's experimental success with nanoscale materials. Herein we report the application of MIM to the assessment of the electronic properties of SWNTs grown in horizontally aligned arrays via CVD on quartz substrates. We present a model that shows that for nanotubes, under proper conditions, changes in reflectivity, (which also depends on tube conductance), can be dominated by the effects due to geometric and quantum capacitance [37]. Given the latter are determined by details of the SWNT symmetry, structure, free carrier concentration, and doping level, the technique is a direct probe of SWNT electronic structure.

We use MIM to map the electronic behavior of CVD grown, horizontally aligned SWNT arrays demonstrating metallic and semiconducting species can be easily and unambiguously identified. Moreover, using a voltage modulated variant of the technique, Microwave Impedance Modulation Microscopy (MIM^2), we image details of a wide variety of nanotube electronic phenomena ranging from the formation of complex intra-tube nanostructure heterojunctions to intricate doping behavior. Nanoscale microwave reflectance offers an extremely versatile nondestructive tool for nanotube characterization. We believe that as an inspection technique, this approach can have tremendous impact, allowing optimization of processing strategies including the development and optimization of scalable enriched growth, post-growth purification, and enabling detailed analysis of contact phenomena. Moreover this set of imaging modes, discussed henceforth, will allow us to shed the light on the quantum material properties of these 1-dimensional structures.

4.2 Measuring the Quantum Capacitance of SWNTs

In general, it is well known that the imaging microwave reflectance offers a unique window into the electronic response of materials, directly probing their conductance and permittivity [25,34,38]. A properly "tuned" microwave probe has minimal signal reflectivity, but when coupled to an external materials system, the impedance mismatch offers a sensitive probe of that material's macroscopic electronic character. Near-field imaging enables microwave reflectivity measurements at the nanoscale. Here the microwave voltage (or current) reflectivity, Γ, is the detected measure of the microwave tip-sample impedance mismatch. One specific technique example is Microwave Impedance Microscopy (MIM). This cantilever based scan-probe technique maps spatial changes in impedance revealing electronic characteristics with

~50nm spatial resolution [25,34,39,40]. The relationship between the experimental observable, Γ(x,y), and the sample's local impedance is as follows:

$$\Gamma = \Gamma_r + i\,\Gamma_i = \frac{Z_{sample} - Z_{int}}{Z_{sample} + Z_{int}} \sim Z_{sample}^{-1} \qquad (4.1)$$

here Z_{int} is a transmission line impedance of the system electronics (including the nanofabricated, built-in tip coaxial line) and Z_{sample} is an effective impedance of the sample.

Figure 4.1 shows a generalized, simple schematic of a MIM scan head and its electronics path. The shielded cantilever probe is a high performance transmission line fabricated and integrated into a specialized AFM tip [33,41]. A matching network allows for the transmission of a low power RF signal, (~ -10dB at 3 GHz) to the apex of the tip. The signal reflected from the sample-tip interface is coupled back into an RF Mixer which resolves the in-phase voltage reflection, Γ_r, and the out-of-phase signal component, Γ_i. After proper calibration, both the resistive and capacitive channels are isolated, mapped spatially and displayed independently. It is worth emphasizing that MIM is a relative technique which measures small spatial changes in reflection Γ(x,y). When applying this technique specifically to nanoscale low dimensional electronic materials, the physics of the tip – sample interaction offers an intriguing experimental opportunity. According to Chapter 2, the imaginary part of the microwave reflection is proportional to the tip-sample capacitance which in this case is the nanotube capacitance. The measured SWNT capacitance is related to the Density of States (DOS), which reflects the specifics of 1D quasi-electrostatic screening of a tip-induced charge density in the tube [42].

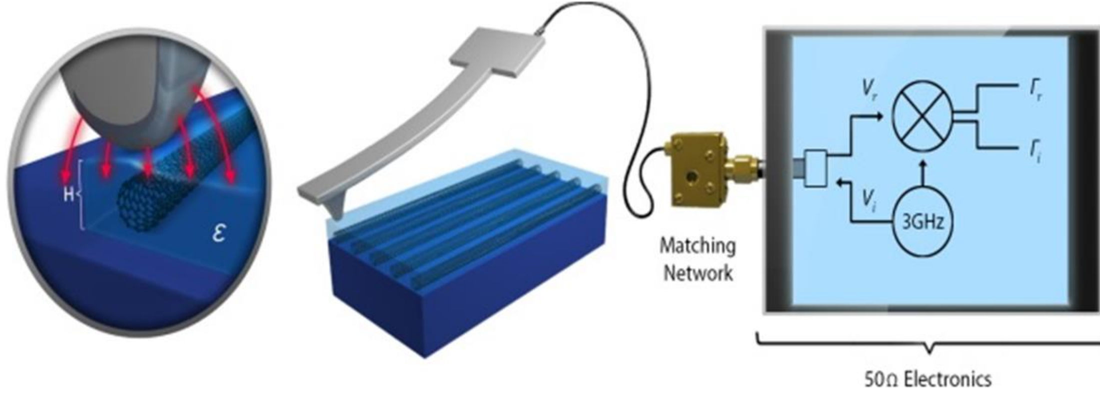

Figure 4.1: Simplified Schematic of the near-field microwave reflection geometry utilized. The high frequency microwave field, propagated to the nanofabricated cantilever tip (which acts as an open transmission line), excites a displacement current in the nanotube. This local response impacts the reflectivity of the microwave field detected at the matching network. The mixing electronics (shown in the box) allows optimization of the signal with direct independent detection of the real and imaginary parts of the signal. For signal optimization, a dielectric layer of thickness **H** and permittivity **Ɛ** is applied to the sample to control the geometric capacitance contribution.

The capacitive coupling to the quartz substrate acts as a uniform background signal, hence it is valid to assume $Z_{sample} \approx Z_{NT}$, where only the capacitive coupling contributes significantly. The carbon nanotube impedance is purely reactive as shown in equation 4.2.

$$Z_{NT} \approx \frac{1}{i\,\omega\, C_{NT} L_{NT}} \qquad (4.2)$$

The dielectric coating or air gap as show in figure 4.1 between the tip and the sample creates a large sample resistance and the substrate isolates the sample surface from a ground plane. In this configuration the tip acts like a gate electrode, the effects of the carbon nanotube quantum capacitance, directly related to the DOS, on the gate electrode response is evident throughout literature [43,44,45]. These examples agree with the predicted observable microwave reflectivity response described by equations 4.1-4.7. To proceed further we need to specify the SWNT term in equation 4.3. Total (proportional to the SWNT length) capacitance for a metallic SWNT should be written as:

$$C_{NT}^{-1} = \frac{1}{L_{NT}}(C_g^{-1} + C_Q^{-1}) \qquad (4.3)$$

here L_{NT} is the NT length (not to be confused with the inductance). The geometric capacitance per unit NT length is given by:

$$C_g = \frac{\varepsilon_i}{2\, ln\frac{2H}{R_{NT}}} \qquad (4.4)$$

where R_{NT} is the SWNT radius, *H* is the thickness of the dielectric medium or tip-nanotube separation distance, and ε_i is the average dielectric permittivity under the tip. The SWNT quantum capacitance is given by the nanotube DOS and can be written in terms of the quantum of conductance and the Fermi velocity for a metallic tube [46,47]:

$$C_Q = \frac{4G_0}{v_F}, \qquad (4.5)$$

here G_0 is the quantum of conductance and v_F is the Fermi velocity.

For our samples the length of the majority nanotubes, ~10um, are much longer than the tip diameter, ~50nm, which implies that variations in their individual tube length will have an insignificant impact on the signal. By combining equation 4.1 with equations 4.2 and 4.3, reveals that the reflection has the following relation to the nanotube capacitance:

$$\Gamma \sim \frac{1}{C_g^{-1} + C_Q^{-1}} \qquad (4.6)$$

Assuming Dirac dispersion relation for the SWNT electrons, the DOS of a semiconductor SWNT is given by:

$$g(E) = C_Q \frac{E}{\sqrt{E^2 - \Delta^2}} \qquad (4.7)$$

here, 2Δ is the s-SWNT bandgap. From this expression we obtain the metallic NT condition given as $g(E) \xrightarrow{\Delta=0} C_Q$, implying that there are plenty of free carriers and a flat DOS. It is easy to see from equation 4.7 that in the intrinsic semiconducting NT condition the fermi energy, E, is

inside the bandgap so there are very few free carriers implying no capacitance contrast, $g(E < \Delta) = 0 \rightarrow C_Q = 0$. The relationship between the fermi energy normalized to the bandgap, E/Δ, and the relative quantum capacitance is plotted in figure 4.2. Notice that the for semiconducting NTs (blue curve) the quantum capacitance is zero inside the bandgap as predicted [48].

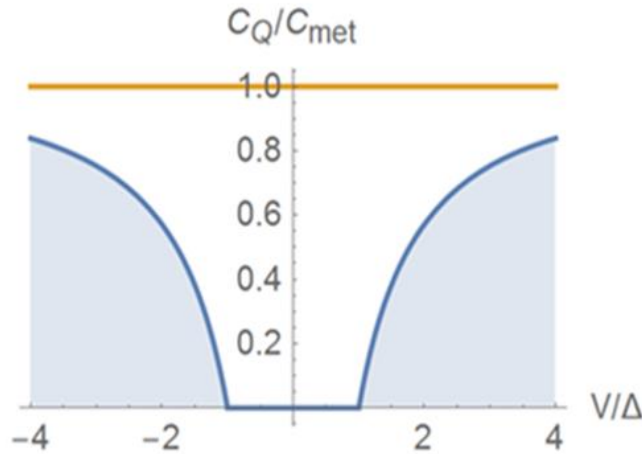

Figure 4.2: Quantum capacitance term for S-SWNT normalized to the metal C_Q vs. applied tip voltage in units of $\Delta = E_g/2$ [48].

Notice that the geometric capacitance, C_g, is not dependent on the NT properties, whereas C_Q, is directly correlated to the intrinsic NT electrical properties. Also, equation 4.6 shows that for arrays of NTs the observable reflectivity sensitivity to quantum capacitance can be enhanced under the proper experimental conditions where $C_g >> C_Q$. This presents a new opportunity to probe the elusive intrinsic properties of carbon nanotubes to map their electron identity at nanoscale. We found that you can control this condition by overlaying a high-k dielectric coating on top of the sample, essentially changing the permittivity of the capacitance medium from air, $\varepsilon_{air} = 1$, to a higher value. We mapped the impact of a dielectric over layer on the predicted percent difference between the total capacitance and the desired quantum capacitance of a metallic NT in figure 4.3, the lower the number the more favorable the experimental condition. The geometric capacitance, C_g, contribution can be manipulated by controlling thickness and

dielectric constant of the dielectric medium between the tip and sample. Using atomic layer deposition or e-beam sputtering to coat a few nm layer of a high-k metal oxide such as TiO_2, Al_2O_3, MgO, or HfO_2 maximizes the sensitivity to the nanotube's intrinsic electronic properties hidden within the quantum capacitance.

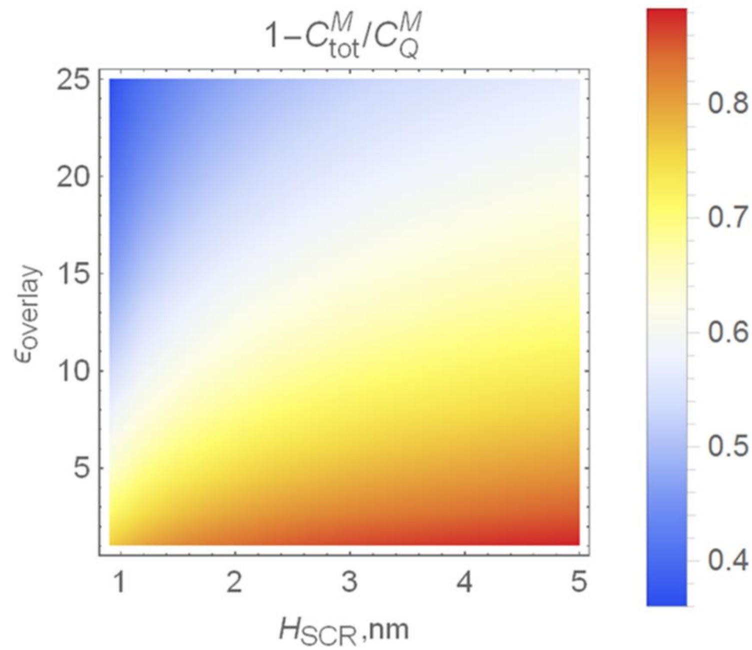

Figure 4.3: Fractional contribution of the quantum capacitance to the total capacitance as a function of dielectric layer thickness and dielectric constant.

We found that the Magnesium Oxide overlayer offers two distinct values: first, its high dielectric constant (Ɛ=9.7) decreases the contribution from C_g, greatly enhancing the dynamic range of the image. Second and more importantly, a MgO deposited layer can be easily and completely removed with a simple mild aqueous acid rinse, making this technique versatile and completely non-destructive as seen in figure 4.4. After MgO removal, the nanotubes can be further processed into devices. For deposited MgO, the layer can be completely removed allowing for further processing of the device under test. Figure 4.4 shows a XPS analysis of the

surface of a tested device. The loss of the Mg peaks in the spectra confirms the complete removal of the dielectric layer.

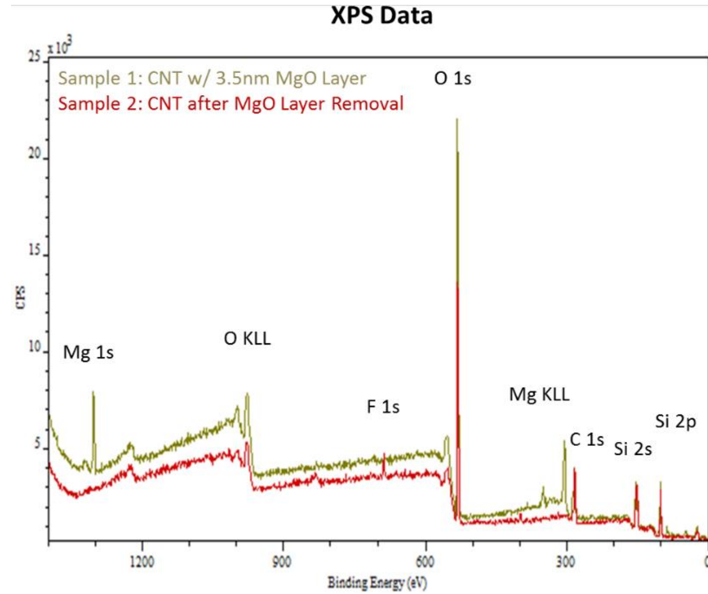

Figure 4.4: XPS analysis of a test structure before and after removal of a simple 3.5nm MgO dielectric layer.

Figure 4.5 presents the data taken in this quantum capacitance sensitive regime. We have overlain the 3D AFM topography rendering with a color map revealing the spatially dependent $\Gamma_i(x,y)$, capacitance coupling. The C_{NT} measured is a function of the effective carrier density. Given metallic tubes have a large number of free carriers at the Fermi level and a flat DOS, we expect a high capacitance for metallic species in an MIM image. Semiconducting tubes, (which, if intrinsic, should have a near zero free carrier density in the gap), should exhibit low capacitance. Figure 4.5 shows MIM images of individual aligned nanotube arrays on quartz with an MgO overlayer (top) or a SiO_2 overlayer (bottom). In both images, we detect a modest number of high capacitance nanotubes (40% of the 198 NTs in the field of view), consistent with the number of metallic nanotubes expected (~33%). As expected the contrast variance observed

is strongly dependent on the properties of the overlayer. For the SiO_2 overlayer there is a large variance in signal is detected. This variation can be driven by its lower Ɛ and the RMS roughness of the sample's dielectric layer, (~0.2nm), impacting on the C_g contribution. The choice of SiO_2 with its modest dielectric constant (Ɛ=3.9), results in a substantial contribution from C_g to the overall signal. There was a dramatic improvement in contrast uniformity observed in the image for the MgO layer compared to SiO2 despite having a comparable RMS roughness to SiO_2 (~0.2nm). Moreover, a SiO_2 overlayer, like most metal oxides, cannot be easily removed once its deposited, limiting the potential of this overlayer material for device process inspection. When using the MgO and metal oxides with comparable permittivity, the sensitivity and SNR of the capacitance channel are quite high, suggesting the potential of using MIM for identifying metallic and semi-metallic SWNTs with high precision. One current limitation is the spatial resolution, ~25-50nm (limited by available tips; note we are also exploring tip modification as an alternative pathway to improve resolution and SNR). This sets a limit of inspection to samples with SWNT densities <~20 NTs/um. Important here is topography and capacitance image data are acquired simultaneously allowing for detailed nanoscale mapping of the correlations between nanotube diameter and electronic properties without the addition of contacts.

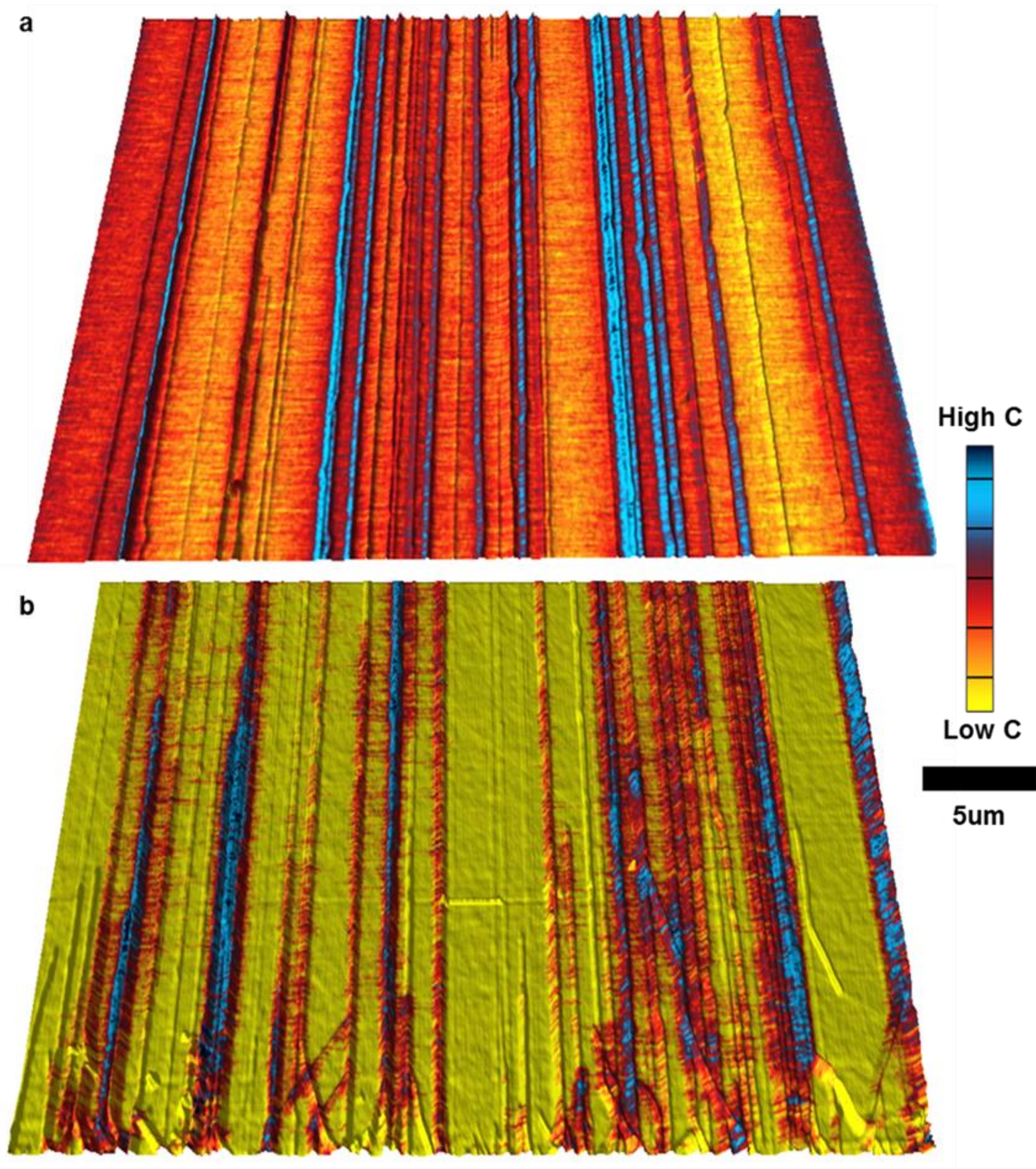

Figure 4.5: MIM imaging of SWNT array. (a,b) MIM capacitance images overlaid on top of AFM 3D surface topography of an array of CVD grown aligned SWNTs on quartz substrates. Each sample has a 3.5nm dielectric layer of (a) MgO and (b) SiO_2. The impact of the increased ε for MgO is apparent, resulting in improved contrast and uniformity.

4.3 CNT Metrology Experiments Proof of Concept

To confirm that the high capacitance nanotubes are metallic, two different methods were used for independent direct electronic property identification. The first was thermocapillary trench formation which is an extremely selective technique, capable of identifying 100% of the metallic nanotubes in arrays [49]. During this process, described in detail in chapter 2, the nanotube array is coated with a thin layer of thermal resist after which the metallic SWNTs are selectively heated. For the initial proof of concept experiment (figure 4.6) we used the microwave heating of CNT diodes using Ti contact for the best selectivity (chapter 2). Trenches develop in the resist deposited on the array above the individual metallic nanotubes *via* selective de-wetting of the resist. This trench formation can be easily detected with AFM. The position of the trenches allows us to identify, explicitly, the metallic and semi-metallic, heavily doped narrow bandgap, NTs in the array.

In figure 4.6 we show use of this approach to confirm the identifications suggested by MIM. Shown is a single SWNT array (>70 SWNTs), imaged using SEM, AFM, and MIM. The SEM shows all nanotubes in the array. In the MIM image, the intense blue lines demarcate the locations of high capacitance, i.e., the metallic and semi-metallic tube positions. A comparison of MIM trace with the AFM image revealing trench formation shows that MIM can predict the trench locations, which coincides with the presence of metallic NTs, with extremely high accuracy (>95%). Figure 4.6 also shows line cuts of the AFM measured trench topography (blue) and the MIM capacitance response (red) on the same sample, taken after complete removal of thermal resist and deposition of the dielectric overlayer. The line cuts exhibit the extraordinary high dynamic range of the MIM technique, not only showing that it readily

predicts that high capacitance tubes form deep trenches (as expected for metallic nanotubes), but also shows the relative depth of the trenches is strongly correlated to the capacitance detected.

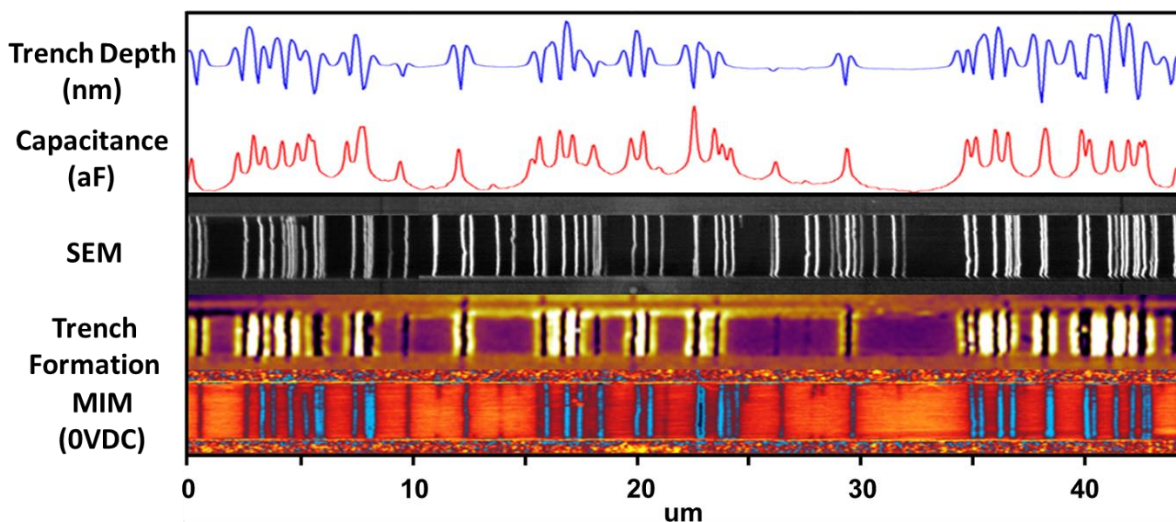

Figure 4.6: Electronic character identification using thermocapillary trench formation. (top) A SEM image of a nanotube array sample showing all nanotubes, below is an AFM image of thermocapillary trenches formed in the same sample, (the trench locations allow direct identification of the metallic SWNTs), and finally a MIM image of the same sample, (after complete removal of the thermal resist and addition of the dielectric overlayer). Direct comparison of the MIM image to the AFM image clearly illustrates that the high capacitance nanotubes (i.e., metallic nanotubes) are forming the trenches. (bottom) Line cuts of the AFM trench depth topography (blue), directly compared to the magnitude of capacitance signal (red).

A definitive way to correlate MIM response to CNT electronic identity is a single NT device analysis using both thermocapillary trench formation and IV curves for independent electronic property identification. When we initiate thermocapillary action in the thermal resist by applying a small bias across the Ti contacts the metallic SWNTs are "selectively" heated causing a trench to form [50]. Figure 4.7 shows the results the proof of concept experiment using CNT diodes, individual SEM (top), AFM (middle), MIM (bottom), images, as well as nanotube device transfer properties (I/V character) are shown. The center AFM image in each case shows the trench formation (or lack thereof) after resist deposition and thermocapillary flow. This direct correlation of I/V performance with trench formation clearly shows which device has a metallic

and semiconducting nanotube. The MIM can definitively detect and identify the nanotube electronic character of each device.

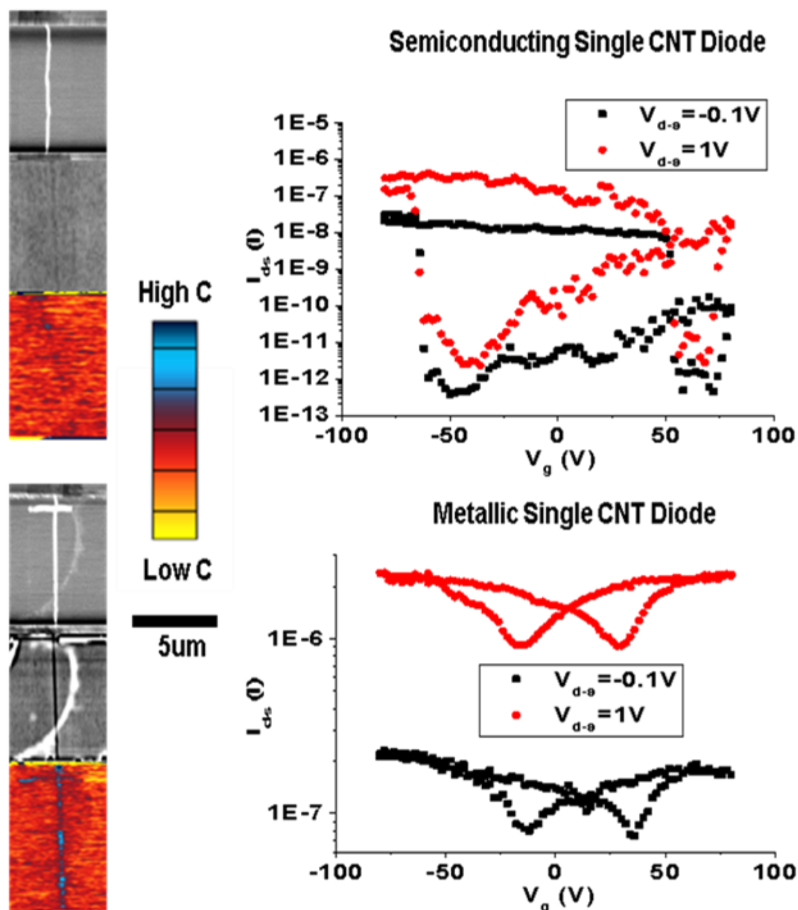

Figure 4.7: Electronic character identification using thermocapillary trench formation (Top). A study of single nanotubes is shown, each with an image panel (SEM/AFM/MIM) and an I/V curve for the tube in a simple device (Middle). An SEM image of a nanotube array sample, an AFM image of thermocapillary trenches formed in that same sample, (the trench locations allow identification of the metallic SWNTs) and an MIM image of the sample.

Another approach used to validate of the electronic property assignments from MIM is Raman spectroscopy [51]. In figure 4.9, we compare directly MIM inspection to Raman characterization; Raman spectroscopy is a widely used technique to identify SWNT chirality by detecting the frequency shift in backscatter from a monochromatic visible light source giving information on the phonon excitation-relaxation pathways [49,50,52,53]. Each chirality has a

unique resonant vibrational energy corresponding to the radial breathing phonon mode. If the energy relaxation produces a photon-phonon pair, the energy of the scattered photon will be the same as incident light minus the resonant vibrational energy [54]. This shift in energy relative to the incident light is the Raman shift use for the spectroscopy measurements. Kataura plots, created by Hiromichi Kataura, plots the CNT chiralities relative to their bandgap energy, first transition energy for metal nanotubes, and the Raman shift, based on the RBM [51,55]. A sample Kataura plot is shown in figure 4.8, which helps to guide the interpretation of Raman spectroscopy data for CNTs. When the lines representing the incident laser crosses near a NT chirality, denoted by the circle marks (red = metal, black = semiconducting), a peak in the Raman shift data corresponding to the y-axis is expected to appear for that NT chirality.

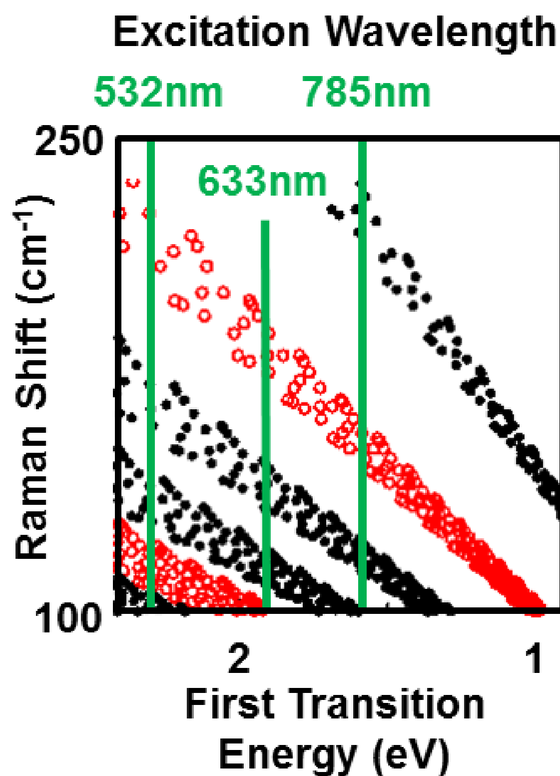

Figure 4.8: Analytical Kataura plot showing the Raman shift for different NT chiralities, with the red and black circles corresponding to the metallic and semiconducting CNTs respectively [56].

The semiconducting nanotubes, marked (S), were identified by their distinct Raman peaks (see also supplemental materials). As expected, in figure 4.9, the MIM shows very low capacitance for all of NTs identified as semiconducting nanotubes by the Raman Spectroscopy. The location of the metal nanotubes is readily apparent in the MIM line cut data with very high SNR. Although, the Raman data successfully identified several semiconducting nanotubes, there isn't a way to ensure the nanotubes that didn't show distinct peaks are metallic without used a different laser source. Notice the artificial peaks that are produced from the sapphire substrate on the right side of figure 4.9; a quartz substrate can't be used because of interfering Raman peaks from the quartz. The acquisition of the Raman data limits specific substrates and requires a complex optical setup for optimal SNR. Many of the NT Raman shift peaks are expected to be very close in frequency making them difficult to distinguish with limited spectral resolution, hence the interpretation of the data requires an in depth understanding of how Raman spectroscopy works which can be time consuming. The MIM has several clear advantages over conventionally used Raman spectroscopy, most notably its superior tip limited resolution compared to the diffraction limited resolution of most Raman setups.

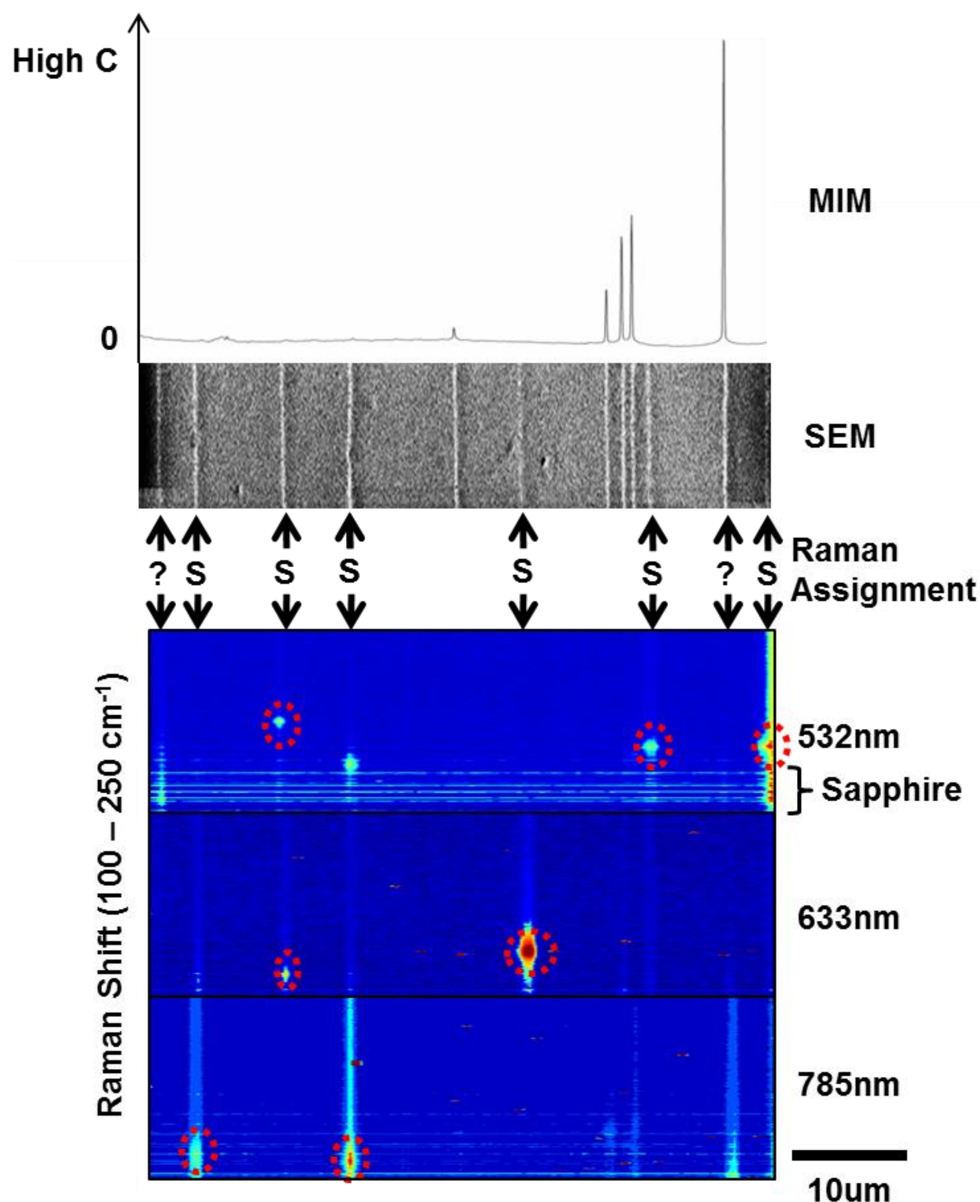

Figure 4.9: Raman Spectroscopy vs MIM analysis. (Top) A line cut of the MIM capacitance signal of a nanotube array. (Middle) A SEM image of the sparse SWNT sample showing all 12 nanotube locations. (Bottom) Confocal Raman images of the identified semiconducting SWNTs (marked S), under 532nm, 633nm, 785nm incident excitation wavelength (the array was transferred to a sapphire substrate for imaging.) The SWNTs marked with question marks have peaks that share similar responses to the metallic nanotubes making their assignment ambiguous. The unmarked NTs do not show strong Raman signal and may be considered metallic.

4.4 Ambiguity in CNT Electronic Character

Inspection for metallicity using MIM is sensitive enough to detect subtle changes in the NT capacitance very high resolution. However, the quantitative classification of the nanotube electronic character types as either semiconducting or metallic is not as simple as counting NTs for contrast. As seen in figure 4.10, there is a wide range of capacitance variation across nanotube implying that the identity classification is not as simple as counting MIM contrast. There are two observations that elude to some ambiguity with electronic type classification: there are some nanotubes show a weakly metallic MIM contrast and the ratio of measured semiconducting NTs are consistently less than the expected ratio of 2/3.

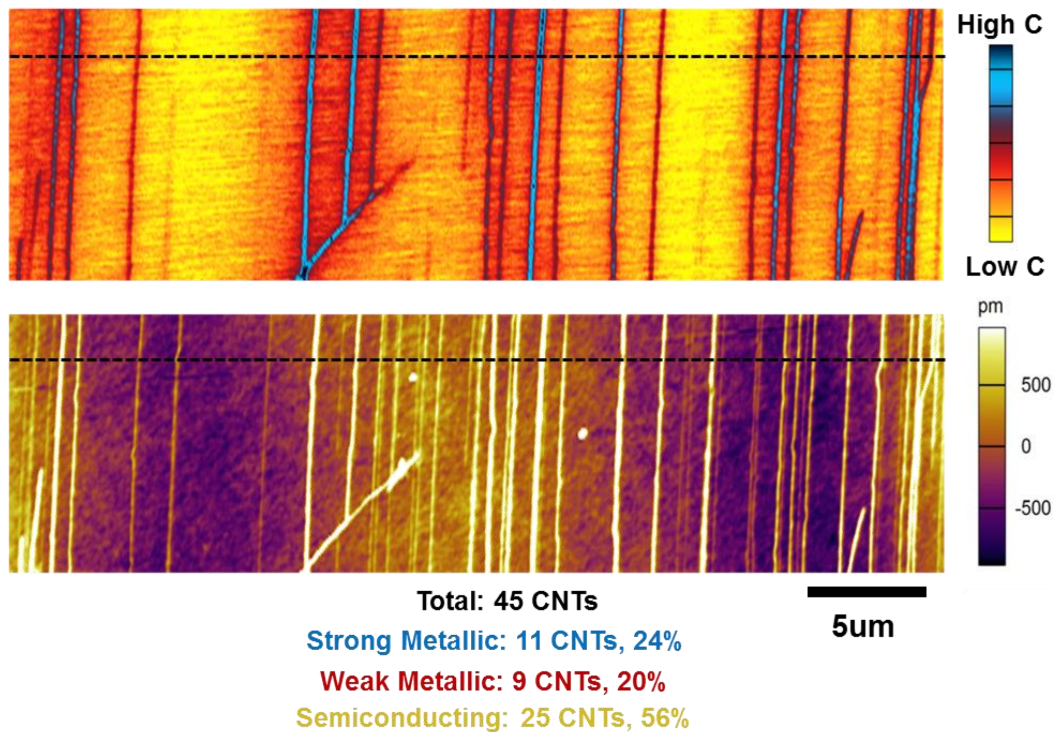

Figure 4.10: MIM capacitance (top) and AFM topology (bottom) images of an aligned CNT array. The CNT identity counting statistics for this sample taken along the black dotted line is shown below the images.

One source of this ambiguity comes from measuring extrinsic properties of nanotubes. When a semiconducting CNT has a notably small bandgap energy, doping can cause it to behave similarly to metal NTs, in these cases we consider the CNT to be a semi-metal. Semiconducting carbon nanotubes are easily p-doped from the environment, this can shift its fermi energy resulting in semi-metallic properties. Observed characteristic changes in nanotube devices when exposed to ambient oxygen are excellent examples of this type of phenomena, which is difficult to detect in individual nanotubes at the nanoscale [57,58]. The creation of semi-metallic nanotubes from environmental doping and the depletion of free carrier from defects sites are a possible explanation of the wide distribution of MIM capacitance seen experimentally. In figure 4.11, yellow arrows point to areas of inhomogeneous MIM capacitance along a nanotube, based on the intermediate nature of the observed high capacitance it is believed that it is the result of non-uniform doping and defect sites.

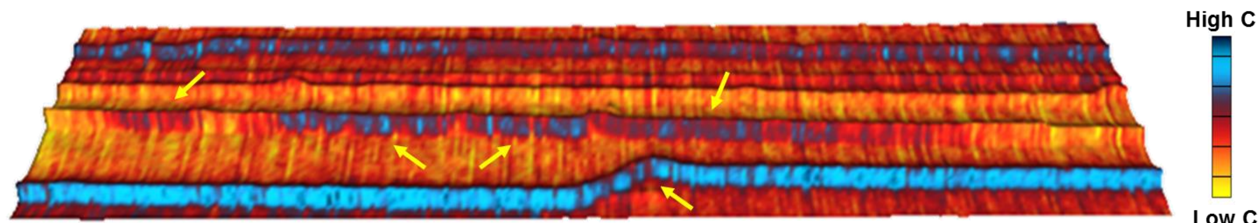

Figure 4.11: MIM capacitance color map overlayed on 3D AFM topology to reveal areas along the NTs with non-uniform contrast (yellow arrows).

In figure 4.12, we illustrate how complex nanotube structures can be explored with MIM to reveal additional source of identity ambiguity. The MIM color map overlay on 3D topology clearly shows of semiconductor-semiconductor and metal-semiconductor SWNT bundles. Shown is a single isolated s-SWNT/m-SWNT bundle (left) and a s-SWNT/s-SWNT bundle (right) of nanotubes with differing bandgap. The observed AFM topology data of a larger nanotube made of multiple small nanotubes confirms the presence of a NT bundle. Notice that

bundles containing a metallic nanotube appear like a metallic nanotube after bundling. The addition of a non-metallic CNT to the bundle had no measurable effect on the measured capacitance, whereas, the semiconducting bundle doesn't show any contrast. The width of a typical NT is less than 2nm, which is far below the tip limited resolution of most AFM tips, hence bundles containing only a few NTs are indistinguishable from taller SWNT in the topology data.

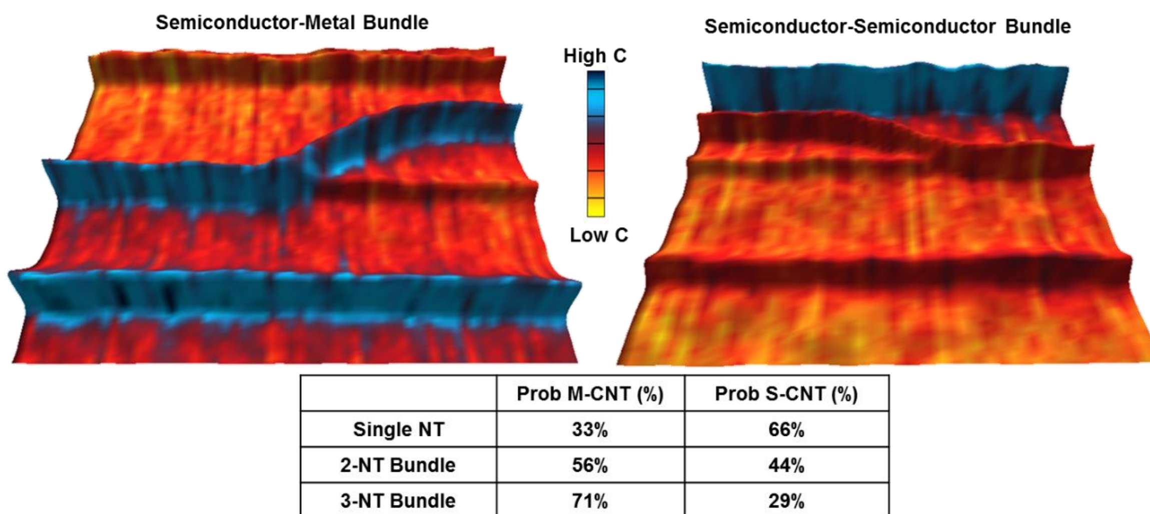

	Prob M-CNT (%)	Prob S-CNT (%)
Single NT	33%	66%
2-NT Bundle	56%	44%
3-NT Bundle	71%	29%

Figure 4.12: MIM images illustrating the observed signal for SWNT bundle formation. For the s-SWNT/m-SWNT bundle (left) the bundled structure has high carrier density, the s-SWNT/s-SWNT bundle has no free carriers.

A simple statistical analysis shows how bundles with 2 SWNTs have a 5/9 probability of showing metallic nature. If a sample has a notable concentration of NT bundles in its array, then the distribution of NT showing metallic behavior would be higher than the expect 1/3 probability. The effect of bundles on CNT identity statistics is evident in a hysterogram of MIM capacitance, seen in figure 4.13. Notice that the SWNTs showing semimetal metallic character have a distribution that favors larger diameter nanotubes than the intrinsic semiconducting nanotube distribution. By dividing the data into two groups, diameter <2nm, which is mostly to

contain single walled NT, and diameter >2nm, which is mostly to contain bundles, it is shown that the NT statistics with less bundles better reflect the predicted capacitance distribution.

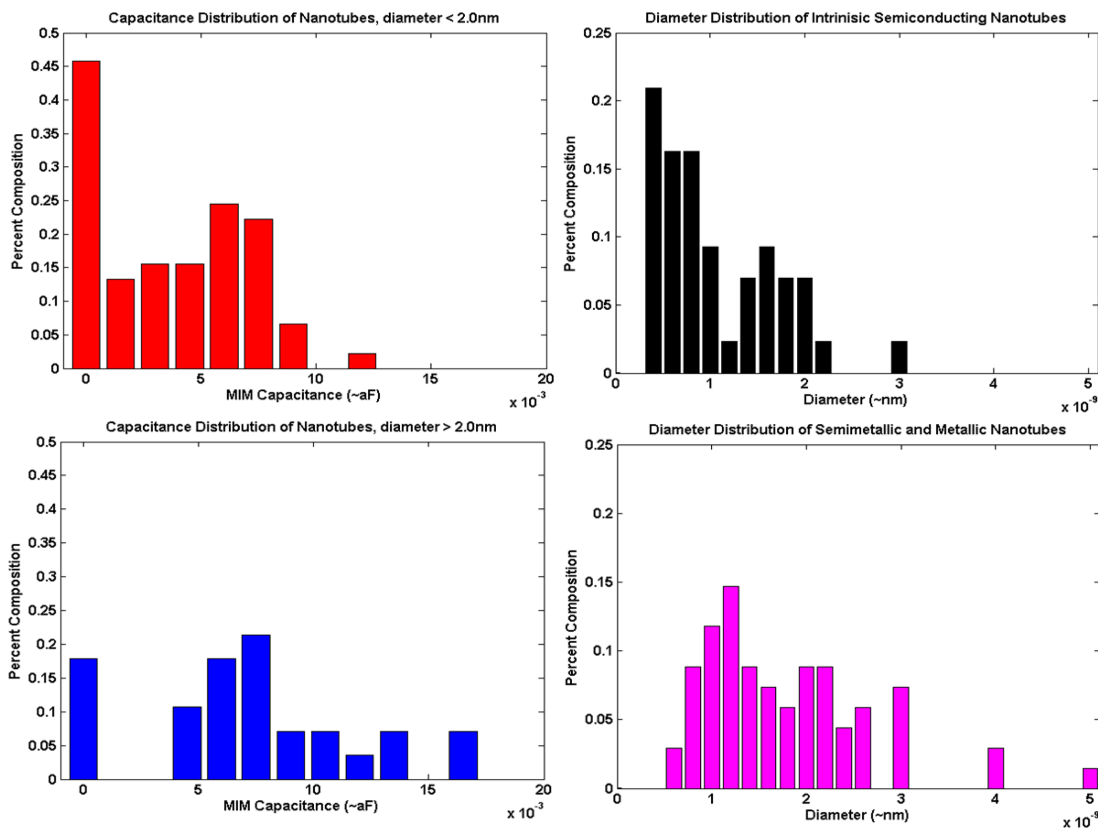

Figure 4.13: SWNT MIM capacitance and diameter distribution for the arrays studied. Notice that bundled nanotubes are also included in this data which will affect the capacitance vs diameter distribution.

Both the presence of nanotube bundles and semi-metallic nanotubes can cause identification ambiguity that can skew the CNT identification statistics. Knowing what to look for when analyzing the MIM data is important for interpreting the CNT electronic identity. In this chapter, we will further explore the use of novel variants of MIM to gain additional insight into the intrinsic properties of the nanotube which will mitigate CNT identification errors.

4.5 Voltage Modulated MIM

The quantum capacitance is related to the density of states as a function of the fermi level (equation 4.7). Referring to figure 4.2 (same as figure 4.15a), in metallic nanotubes the fermi level lies within the flat DOS region, the capacitance is independent of the Fermi energy position. Semiconducting nanotubes have zero carriers in the bandgap, however, carriers are excited when the fermi energy is above the bandgap. This suggests one can use a potential on the tip to shift the nanotube's Fermi level, a DC voltage applied to the tip, V, should influence the nanotube capacitance as predicted. In figure 4.14, the tip voltage (y-axis) is varied to experimentally probe the voltage dependent quantum capacitance for an array of NTs shown as a 3D topology image at the bottom of the image. As predicted the data revealed a trend that fully agrees with the DOS analytical model; only metallic NTs, which can be seen clearly in the MIM data at zero bias, remained the same capacitance throughout the bias sweep. Many of the semiconducting nanotubes, which didn't show contrast at zero bias, was able to turn on at higher tip voltages. Notice that not all the semiconducting nanotubes turned on at the same DC bias, this is due to differing bandgap energies of each semiconducting nanotube.

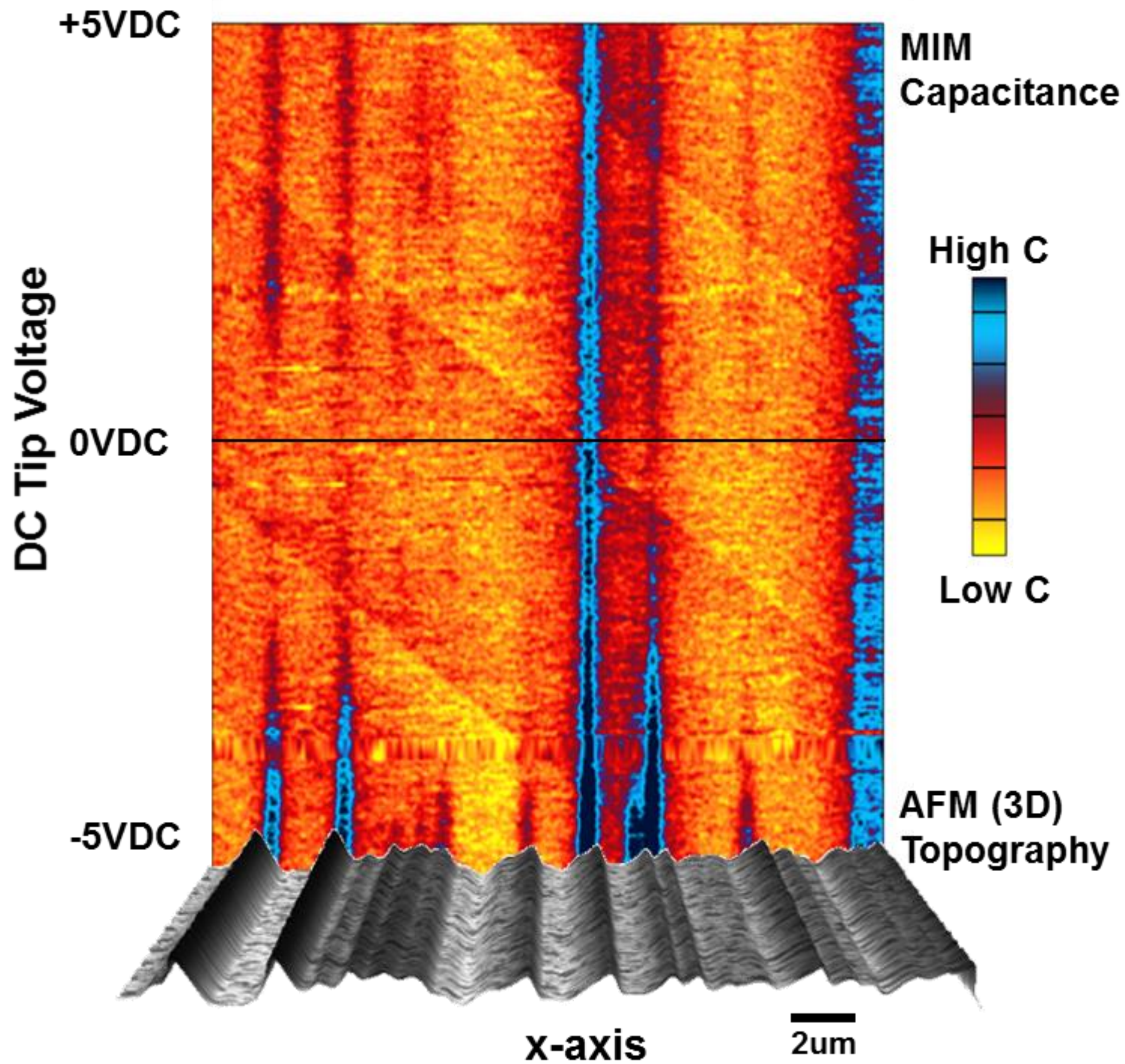

Figure 4.14: MIM-DC mapping shows the changing capacitance coupling with varying DC bias applied to the tip.

In figure 4.15a, the capacitance varies rapidly with local Fermi level at the bandgap energy near the 1D singularities of the DOS. Developing a strategy for measuring the local band bending profile enables the study of nanotube electronic properties with much more detail. Consider now the response to a low-frequency applied voltage. The tip voltage modulation will result in a variation in Γ_i, which is observed using a lock-in amplifier. The detected modulated

MIM (MIM2) signal is proportional to the voltage derivative of the reflection function which is related to the nanotube capacitance according to equation 4.8:

$$\frac{\partial \Gamma_i}{\partial V} \sim \frac{\partial C_{NT}}{\partial V} \qquad (4.8)$$

The geometric capacitance component is not voltage dependent so it does not produce any signal, while the quantum term may. For m-SWNT the conduction band dispersion is flat resulting in a zero derivative unless the voltage modulation amplitude is so large that the Fermi level reaches next subband. For an s-SWNT, signatures of the band edges where the quantum capacitance should rapidly change with voltage are observed if the modulation amplitude drives the fermi energy above the bandgap. Important here is the detailed character of the nanotubes electronic structure can be revealed by the derivative signal. The signatures for semi-metallic or doped semiconducting behavior can be mapped readily by noting the voltage response.

The conventionally used dC/dV modulation is a small amplitude, ~100mV, sine wave with a DC offset, -5V to 5V [59]. In general, the lock-in signal from conventional dC/dV SMM is sensitive to the slope of the band, the signal comes from the averaged capacitance change over the small AC voltage swing. The DC bias is used to sweep the fermi energy of the sample to map the voltage dependence of the dC/dV signal. Increasing the AC voltage swing can substantially increase the SNR; however, it causes the signal to deviate from the true slope of the band profile due to voltage averaging [59]. MIM2 uses a variant the dC/dV method that is more sensitive to the bandgap of semiconductors than the slope of the band profile. For MIM2 we used a fully offset sine wave as an AC bias, where the voltage swings between 0V and some other voltage value VAC, in the range (- 5 V,5 V). For MIM2 on semiconductors the signal should saturate when the VAC tip voltage is such that the Fermi Energy is greater than or equal to the band edge. In figure 4.15b, the measured lock-in signal for MIM2 can be represented as the voltage

derivative of the quantum capacitance function in figure 4.15a, it resembles the SWNT band profile.

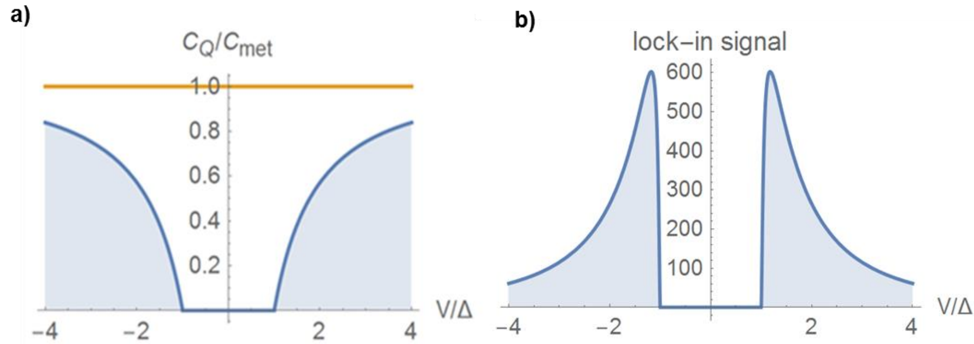

Figure 4.15: (a) Quantum capacitance term for S-SWNT normalized to the metal C_Q vs. applied tip voltage in units of $\Delta = E_g/2$. (b) Lock-in signal for S-SWNT vs. tip voltage in units of Δ, calculated using sup equation [48,60].

An analytical illustration of the expected tip potential interaction with the CNT DOS and band bending profile is shown in figure 4.16. A large MIM2 signal is predicted for small bandgap NTs which may have a semi-metallic electronic character and for space charge regions from band bending. In conventional dC/dV the relative differential capacitance signal maybe small if the fixed DC offset isn't enough or too much such that the Fermi energy falls is not sufficiently close to the bandedge [59]. For MIM^2 the carrier concentration dependence on the Fermi-level, being controlled by a tip voltage with fixed AC amplitude, is more pronounced due to the large tip voltage swings which can cause semi-metallic nanotubes to change from semiconducting to metallic within a single AC period. A comparison of the different modulation schemes, illustrated in figure 4.16, shows how the capacitance response from a larger AC swing will have a stronger SNR and the bandedge can be detected by the turn on voltage, VAC, needed to produce strong MIM2 signal.

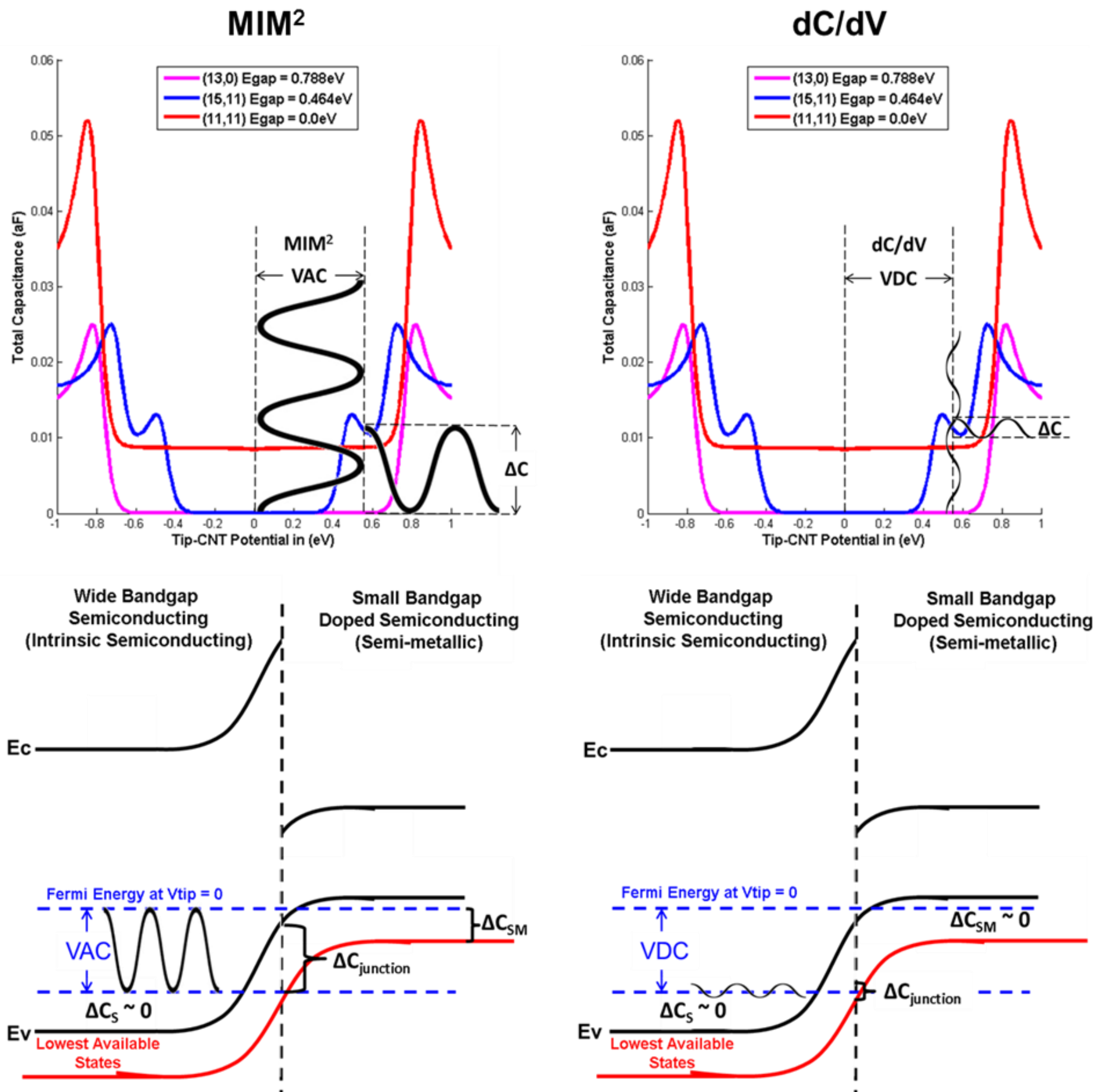

Figure 4.16: Model for different modulation schemes for MIM; MIM2 (left) and dC/dV MIM (right). The upper figures show how the voltage swing should yield differential capacitance for different Carbon Nanotube band profiles. It shows how MIM2 is particularly sensitive to bandgap; it predicts that the wider bandgap nanotube (pink) and the metallic nanotube (red) should show no capacitance change, no signal, whereas the narrow bandgap (blue) shows an appreciable capacitance change. The lower models are simplified band diagrams for a semiconducting-semimetal junction assuming that there is a finite number of hole states that is available to the detected capacitance. These figures show how when doing differential capacitance imaging at a fixed tip voltage, MIM2 can offer more information regarding bandgap and band bending.

We can further exploit this C_{NT} dependence as an alternative imaging modality, specifically sensing the dC_{NT}/dV derivative with lock-in amplification [61,62]. We implemented MIM2 using a low frequency (90 kHz) offset amplitude modulation (0V to V_{max}), the differential capacitance signal is demodulated using a lock-in amplifier. Higher AC bias frequencies improve the SNR by allowing for more averaging per pixel by the lock-in amplifier; ideally the maximum modulated frequency would be limited by the excited carrier's relaxation lifetime. In this case the limiting factor is the impedance detection response time of the RF electronics which is limited to ~100kHz. We expect the semiconducting nanotubes will show a differential capacitance signal (dC/dV) at a much higher VAC voltage than the semi-metallic nanotubes, and with larger bandgap (small diameter) semiconducting nanotubes and the metallic nanotubes requiring higher bias amplitudes to get to the "capacitive dispersive" regime and may not show any signal at all.

Figure 5a shows MIM, MIM2, and AFM data collected on the same array. The MIM2 map is plotted as a series of line scans of varying V_{max}. The detected MIM2 map is quite revealing. As predicted, only semiconducting (blue arrows) and semi-metallic (red arrows) SWNTs, identified by their weak or non-existent MIM signal and diameters typically 1-2nm, show a strong MIM2 signal. While small diameter, large bandgap semiconducting (pink arrows) and metallic (black arrows) SWNTs (black arrows) show faint or no MIM2 signal (indicating small dC_{NT}/dV). Clear signatures of the DOS singularities begin to appear at V_{max} (~3.5-4V) for some semi-metallic SWNTs (red arrows) which typically have larger diameters (>2nm) implying small bandgaps. The data suggest that MIM2 has the potential to reveal more intricate detail of the materials electronic behavior than MIM alone. In figure 4.17b the line cuts show we can map features related to the extrinsic band structure enabling exploration of the nanotube quantum

physics and more accurate NT character identification. For example, in this graph the vertical offset of each line cut is based on the zero bias MIM signal, for the NT types that show MIM2 signal there is a clear difference in the MIM signal to distinguish the semiconducting nanotubes from the semi-metallic. We know that the semi-metallic nanotube is intrinsically semiconducting since they exhibit DOS dispersion at reasonably low tip biases, note that the peaks in the MIM2 data occur at the similar tip potentials implying that they are related to the bandedge for similar chiral types. After comparing an analytical 1D DOS trace with the experimental data from MIM2 voltage sweep, we hypothesize that the small bandgap contributes to the susceptibility of the formation of semi-metallic NTs; however, environmental doping, defects, and fermi pinning accounts for the fermi level shift needed for narrow bandgap s-CNT to behave like semi-metals.

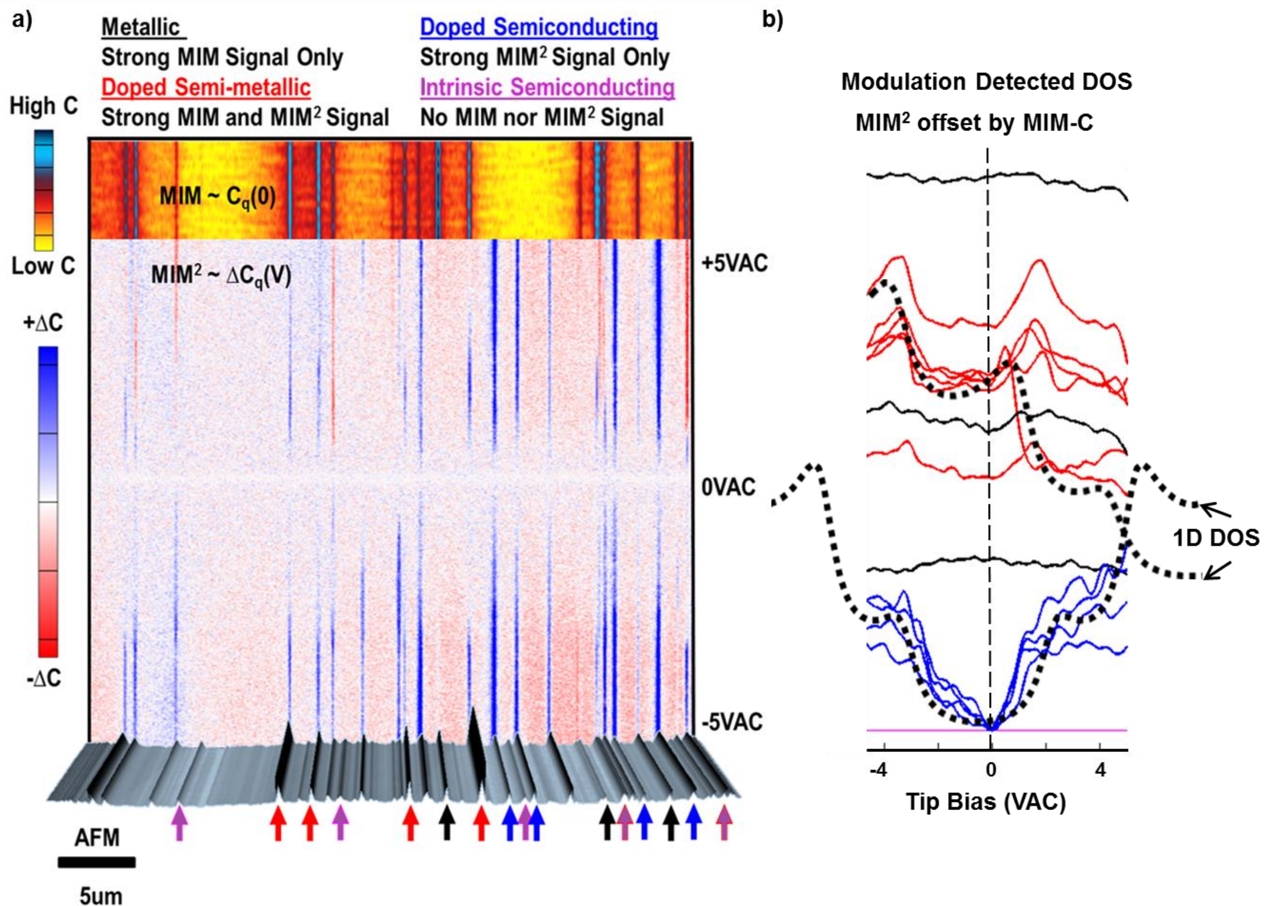

Figure 4.17: MIM2 Voltage Sweep Map: (a) MIM-DC mapping shows the changing capacitance coupling with varying DC bias applied to the tip. (b) MIM (at 0V, top edge), MIM2, and AFM topography scans (bottom edge) of the same SWNT array, illustrating the complementary nanoscale data obtainable with each technique. The capacitive signatures observed have been categorized for the four electronic nanotube types: those exhibiting strong MIM signal only, (black); strong MIM2 signal only (blue), both strong MIM and MIM2 signal, (red), and no signal with either technique, (pink). The suggested designations correspond as follows: (black) metallic, (blue) lightly doped semiconducting, (red) heavily doped semiconducting/semi-metallic, and (pink) intrinsic semiconducting nanotubes, respectively. The colored arrows below the AFM topography image identify the specific nanotube electronic behavior designation at each map location. (c) MIM2 line cuts. The voltage dependence of the modulation follows the dispersion curvature of the 1D nanotube DOS.

We emphasize that both the system detection geometry and signal processing strategies can be optimized to make the measurement more quantitative. In principle, the nanotube bandgap, Fermi level position, and potentially the whole DOS can be directly experimentally

determined in a non-destructive manner. Importantly, this technique appears to offer data similar to sophisticated Scanning Tunneling Spectroscopy and Microscopy (STS/STM) measurements, but with no special sample preparation or contact fabrication, and under ambient conditions [63,64,65,66]. The two techniques obtain the data inherently different: STS uses a large probe bias to create a tunneling current that can be quantitatively correlated to the spatial overlap between the state of the electron in the tip and in the sample, whereas MIM2 uses a tip bias to shift the local Fermi energy of the sample to populate higher energy states, this increases the local carrier density and thus the capacitance coupling. Here no current path is needed to detect the change in carrier density since the MIM setup measures local changes in the open circuit impedance. Although STS has a substantially better resolution (<1nm) due to very sharp dependence of tunneling current on topography and its spectral data are quantifiable, the MIM2 appears more attractive for sample inspection for wide area array of aligned CNTs since it allows for shortened image acquisition times, comparatively minimal setup complexity, avoids the need for a non-insulating substrate (aligned CNTs are typically grown on quartz), and offers a wide imaging field of view.

4.6 MIM and MIM2 of CNT interfaces

Direct correlation of MIM and MIM2 data with the nanotube array physical topography gives these techniques the versatility to explore not only spatial variations in carrier concentration (MIM), but also spatially map areas of band-bending and structurally dependent electronic perturbation. This is particularly useful for studying in detail how electronic behavior evolves due to nanotube-nanotube structural variations and intra-tubular interactions. For example, the signatures of both carbon nanotube bundling (figure 4.12) and intra-tubular

heterojunction formation (figure 4.18) have been observed. Carbon Nanotubes are known to exhibit intra-tubular junctions which are caused by chirality changes during growth, often leading to differences in doping, and/or defect induced nanotube unzipping [57,58,67,68]. This phenomenon manifests itself in the AFM topography as a sudden change in nanotube diameter (a height discontinuity), and may also be observed as a difference in MIM capacitance as figure 4.18a demonstrates. Additional analytical potential of MIM2 is evident in a comparison of features of individual nanotubes in figures 4.18ab. Here MIM and MIM2 scans were taken on the same region of a nanotube array with the specific behavior of two nanotubes highlighted.

Scanning along the nanotube T1, AFM shows a 1.25nm to 2.4nm height change, which is nearly doubling of the tube diameter. The MIM image suggests a transition between two modestly doped semiconductor segments, with the smaller diameter, wider bandgap, tube behaving near intrinsic and the larger diameter, smaller bandgap, tube behaving like a semi-metal. The MIM2 image (figure 4.18b) suggests the situation is more complex. The MIM2 signal, with a fully offset -2VAC voltage applied to the tip, reveals that the larger diameter, smaller bandgap, NT has a non-flat band dispersion, indicative of semi-metallic behavior; while the smaller diameter, wider bandgap, nanotube shows no band dispersion as expected for a semiconductor tube. It also reveals a bright region of a very high dC/dV, consistent with formation of a region of rapidly varying DOS near the intra-tubular discontinuity. This observation is consistent with the formation of a semiconductor-semiconductor CNT heterojunction with a quasi-atomically abrupt Schottky barrier and the corresponding screening length of the space charge. If the free carrier density of the semiconductor section is notably lower (nearly intrinsic), then the Debye screening length will be larger on the semiconducting side from the lack of carriers to facilitate electron-electron screening. This phenomena is

observed in image tube T1, where the bandbending, detected as strong MIM2 signal, extends over 1.2um from the interface into the small diameter semiconducting nanotube. Notice that the observed Debye length, which is well above the 50nm resolution limit, is larger than expected using bulk calculations for a doped homojunction; we believe that this is rare experimental evidence of the 1-Dimensional electron-electron screening. For the tube T2 in figure 4.18, MIM shows a SWNT junction where both tubes appear to be metallic. MIM2 suggest a subtly different interpretation, allowing for greater detail. It reveals that the large diameter SWNT (2.25nm) is actually a semi-metal (or semiconducting) nanotube that has formed an atomic interface with a metallic SWNT of a smaller diameter (1.3nm). The metallic nanotube is confirmed by the complete lack of MIM2 signal and the high MIM signal is which would be unusual for a small diameter (wide bandgap) semiconducting nanotube, even if it were highly doped. Refer to the larger diameter section of tube T2 which has formed an intra-tubular semiconductor-metal interface; here we observe another example of the unusual behavior of Debye screening in CNTs. The carrier density of the semi-metallic (or semiconducting) section is the same as the metallic nanotube implying that carrier diffusion has induced space charge at the interface. We believe that in CNTs the Debye screening length is much larger than expected because 1-dimensional quantum confinement extends the range of coulomb interactions in the material, which lowers the effectiveness of electron-electron screening. The strong MIM2 contrast from Debye screening can obscure the MIM2 response to band dispersion in semi-metallic NTs, making it difficult to accurately identify doped NTs near interfaces, as seen from tube T2. Notice that all the metallic and intrinsic semiconductor tubes in figure 4.18b show very little or no MIM2 signal which agrees with our results from figure 4.17. Only the larger diameter SWNT segments along T1 and T2 show the strong MIM2 signal, which reaffirms the theory that large

diameter, smaller bandgap, semiconducting CNT are more likely to behave semi-metallic when environmentally doped.

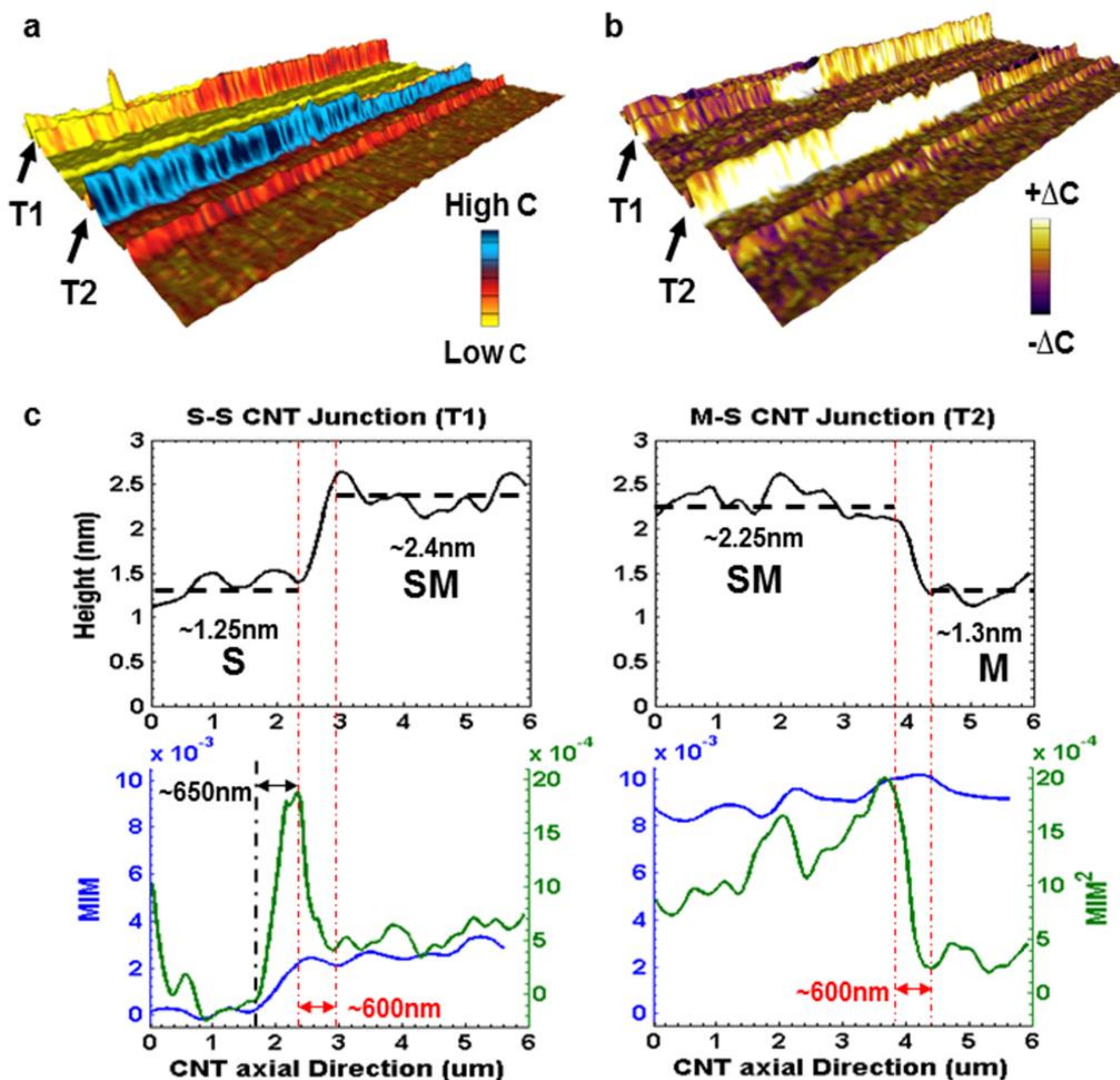

Figure 4.18: Observations of electronic structure in intra-tubular junctions. (a,b) Maps of intra-tubular junctions; a tube T1 shows an apparent doped semiconducting/semiconducting SWNT junction; a tube T2 shows a metallic/metallic nanotube junction, imaged with MIM and MIM2. Metallic SWNTs have high capacitance, with lower capacitance for the semiconducting SWNTs. (c) Line cuts for the topography, MIM and MIM2 signals, labeled for the widths of the inter-tubular junctions.

The contrast seen in figure 4.18 is driven by the formation of Schottky and ohmic junctions between s-CNTs and materials of differing work functions. A space-charge region forms at the junction, the internal electric fields in this region induces bandbending that extends a finite distance from the interface, we consider this the Debye screening length [69]. The mobile carriers drift to compensate for the internal electric fields formed in the space charge region. When the mobile charges move to adjust to the local space charge, they screen the coulomb forces from the nearby electrons that are further away from the interface [69]. The electron-electron screening is the underlying quantum phenomena that determines the Debye length and consequentially the size of the space charge region. We believe that this phenomenon behaves differently in low dimensional materials such as CNT than in bulk materials. Although the carrier density is very high on the surface of CNTs, the absolute volumetric carrier population of an intrinsic s-CNT is several orders of magnitude lower than a bulk semiconductor with a similar bandgap energy [58,59]. Moreover, in a simple 1-dimensionally confined system charges are screened by its neighboring carriers along the 1-dimensional conduction path instead of interacting with a spherical volume of mobile carriers. It is our hypothesis that since fewer carriers can participate in short-range coulomb screening in a 1-dimensinal system, the coulomb interaction between these charges have an extended range compared to bulk materials. Understanding the physics of electron-electron screening in a 1-dimensional system is important for the analysis and development of next generation devices with better transport properties. To experimentally map this phenomena in a device geometry requires the analysis of semiconducting CNT – bulk metal interfaces. The work function of individual SWNT has a range, 4.1eV – 5.3eV, that depends on this diameter and chiral type [70]. We predict long-range

bandbending at the SWNT-metal interface as described in figure 4.19. The Debye length can be measured with 50nm resolution to obtain empirical data on 1D electron-electron screening.

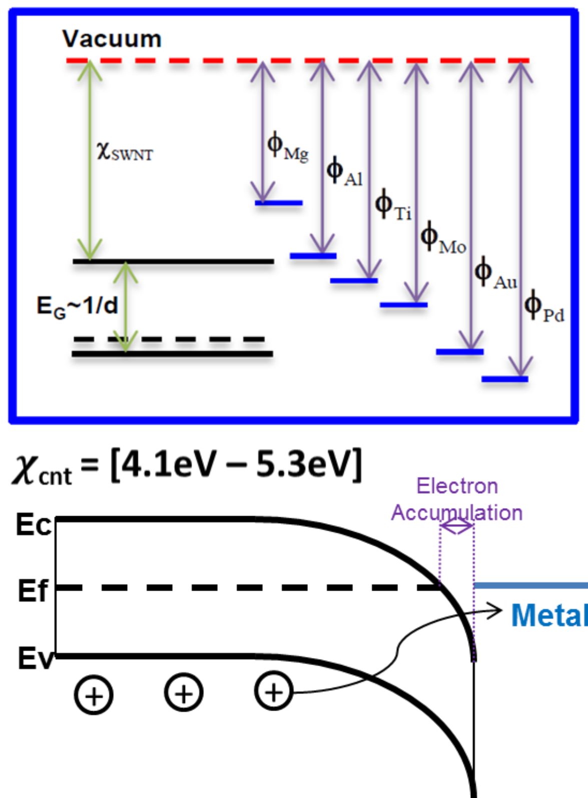

Figure 4.19: Illustration of the relative band potentials of a semiconducting CNT – metal interface before (top) and after (bottom) thermal equilibrium.

Figure 4.20 shows the ability of MIM2 to map the Debye screening length across the nanotube-metal interface. The topology, MIM capacitance, MIM conductance, and MIM2 map of the same CNT array interface is shown, the MIM2 was done with a modest -2VAC tip bias. Notice that the same NTs that showed contrast in the MIM capacitance data are not the ones that shows contrast in the MIM2 data. The NT identified as metallic in the MIM capacitance channel and the metal contact themselves showed little or no signal in the MIM2 channel as expected since they have a flat capacitance dispersion. However, all the semiconducting and semi-metallic NTs show a distinctive high signal at the metal interface indicative of the space charge region.

Notice that the MIM2 response drops dramatically after ~1.0-1.5um for most nanotubes, but the sensitivity to the Debye length extends almost the entire length of the tube. Our observations imply that there is both rapid bandbending from space charge at the metal interface and long-range coulomb interactions, possibly from weak electron-electron screening predicted in our hypothesis.

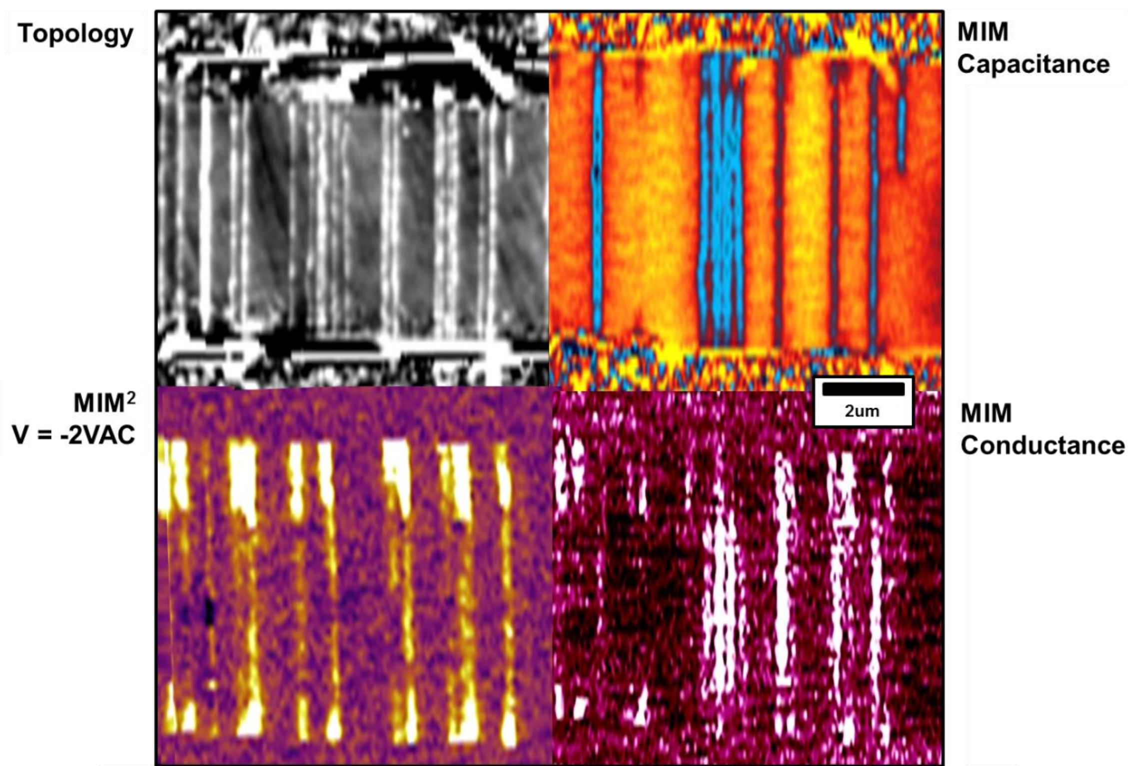

Figure 4.20: AFM topology (upper-left), MIM2 (bottom-left), MIM Capacitance and Conductance maps of a CNT-Ti interface with a 10um gap between the contacts.

The effects of the metal work function on the electrical behavior of carbon nanotubes is important for many CNT applications. For example, the success of thermocapillary purification relies on using metal contacts with a proper work function to increase the selectivity of trench formation (refer to Chapter 1). Typically for CNT devices, the metal work function should be chosen to create an ohmic barrier with the least amount of resistance at the metal contact

interface. However, for thermocapillary purification and other niche applications it is advantageous to create a rectifying Schottky barrier to adjust the extrinsic CNT properties such that it behaves intrinsically, in the “OFF” state, in ambient conditions. It was shown that this can be done with higher work function metals like Ti contacts [50,60]. Our hypothesis is that depending on the metal’s work function it can supply mobile carriers to induce carrier diffusion the semiconducting nanotube which compensates for local shifts in the fermi energy level from extrinsic doping. Figure 4.21 shows the data from the AFM topology map, MIM capacitance map, and a MIM2 voltage sweep in the center of a CNT diode 5um away from its Ti contacts. The rectifying nature of the contact metal is apparent, notice in figure 4.21 that the MIM2 response to the voltage sweep is completely symmetric around 0V bias, unlike in figure 4.17, where linecuts reveal asymmetric dispersion on as-grown nanotubes coinciding with the presence of doped semiconducting and semi-metallic NTs. In figure 4.21, most of the NT identified as metallic in the MIM map show weak or no MIM2 signal, whereas the semiconducting NTs show very strong MIM2 response, which agrees with the observations made in figure 4.17. The metallic nanotubes are marked by an “M” and a red arrow at the top of figure 4.21; only 10 out of 28 or 36% of the total NTs show metallic behavior which is very close to the theoretical ratio of 33%. Here we have shown direct evidence of the rectifying abilities of metal contacts on CNTs.

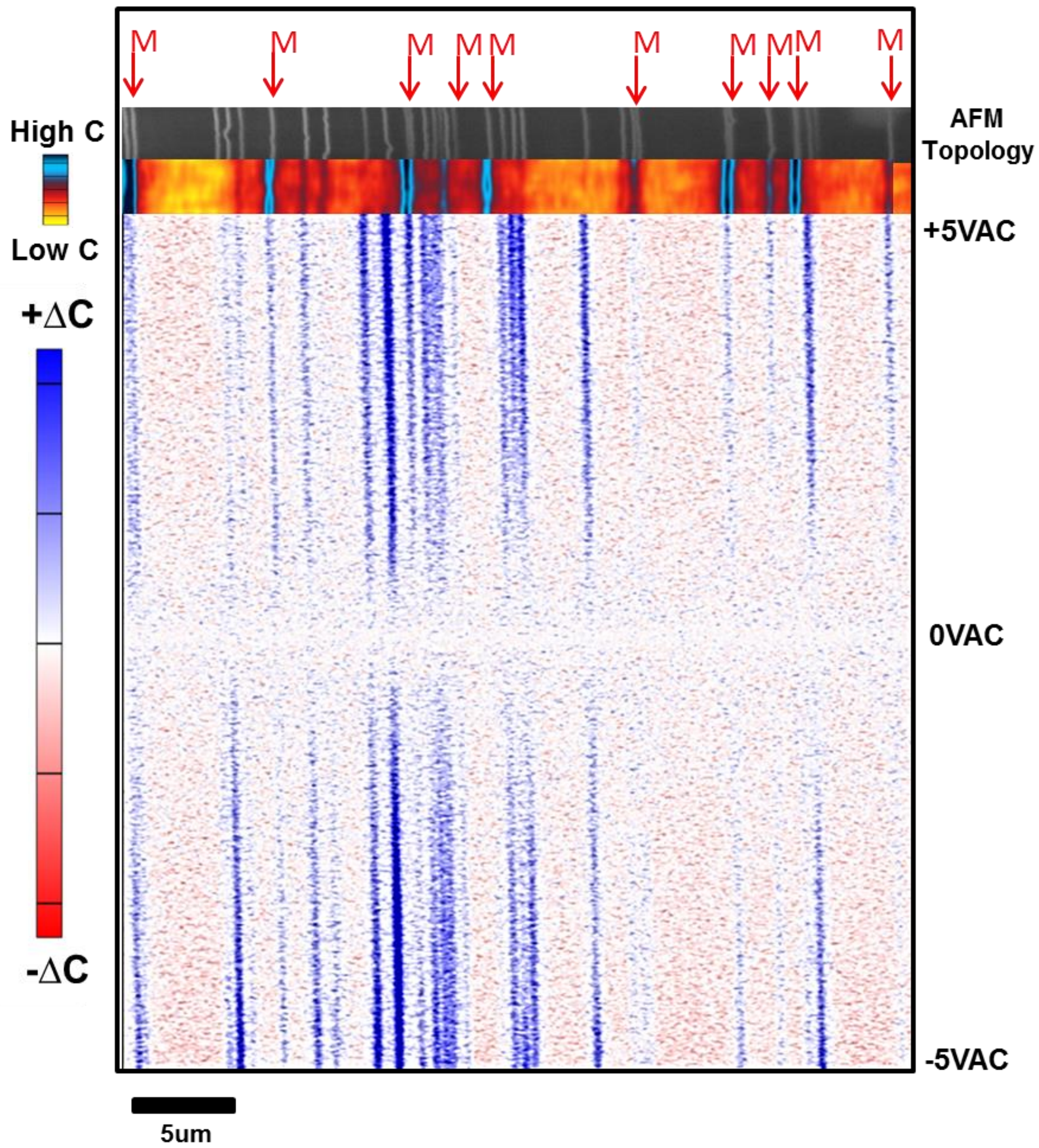

Figure 4.21: MIM2 voltage sweep for CNT diode with Ti contacts. At the top at arrow for NTs identified at metallic, the upper most map is the AFM topology map (greyscale), the MIM map is just below the AFM, and at the bottom is the MIM2 voltage sweep with tip bias as the y-axis. All the data maps are aligned to allow for direct comparison.

4.7 Conclusion

Using the near-field reflective microwave imaging we demonstrate that one can determine the electronic character of SWNTs and directly observe quantum phenomena at the nanoscale. The ability to correlate simultaneously free carrier density via MIM, band dispersion dynamics via MIM2, along with morphology via AFM topography, provides important insight into SWNT physics and electronic behavior. We have demonstrated this technique can be utilized as a non-destructive probe of “as-grown” CVD samples probing SWNT metallicity unambiguously at the nanoscale, thus, making it a promising tool for growth and process optimization. In particular, it can enable rapid analysis of nanotube enrichment strategies without the need of costly processing after growth, a long standing need for the SWNT research community. In this study, the scan probe configuration naturally resembles that of a metal-oxide-semiconductor (MOS) capacitor used in field effect transistors, this implies that the signal response is sensitive to the CNT’s electronic response in a device geometry. In this chapter, there have been many examples of CNT diodes being directly probed using direct contact MIM, the effects of the metal contact type on electronic behavior have been directly observed. An advantage that this method offers is the ability to directly probe CNT during transistor operation since the tip acts like a localize MOS gate electrode, the contacts of the CNT diode can be biased to form a pseudo-transistor operation in situ with the MIM measurement. Continuing the study of intratubular CNT interfaces and sCNT-metal interfaces using MIM is important for understanding electrical transport properties in low dimensional materials. Future improvements of the technique, including the full quantification of quantum capacitance and improvement in spatial resolution, could allow for the direct measurement of quantum phenomena such as the DOS, bandbending, and electron-electron screening effects. We believe that with continued

effort this method has promise for the direct analysis electrical transport properties of CNT devices with nanometer resolution.

4.8 Methods

Preparation of horizontally aligned Carbon Nanotube Samples for MIM-AFM imaging

SCNT samples were grown aligned on Quartz using conventional Chemical Vapor Deposition using Fe catalyst particles (see Appendix A). Next, a 3.5nm layer of MgO was sputtered, at a rate of ~0.1A/s, via E-beam deposition on the entire sample. The samples then underwent a 15min thermal anneal on a hotplate at 400°C to improve thin film uniformity. The samples were stored in a dry environment in-between MIM imaging. The removal of the dielectric thin film is done by submerging the samples in 20% aqueous HCl heated to 60°C for 10min.

Description of MIM imaging system and analysis

MIM and MIM^2 images were obtained using an Asylum Research MFP-3D microscope modified with a PrimeNano microwave reflectivity probe head. The out signal of the MIM electronics was used as an input into a Zurich HF2LI Lock-in amplifier to obtain MIM^2 data. The data underwent some basic flattening and smoothing schemes to obtain images. The color scale of the images was offset by the signal on the quartz substrate such that they represented a normalized comparison for all data collected. To obtain relative capacitance values (arbitrary units) for nanotube statistics a sum of Gaussian deconvolution scheme was implemented to remove signal overlap of dense nanotube samples.

Preparation of CNT Diode Samples for Thermal Capillary Trench Formation

As-grown aligned CNT samples had two terminal 30nm thick Ti contacts with a 10um channel width deposited on them via E-beam deposition. A 35nm thermal resist layer was then sublimated on the samples via thermal deposition. A 250W pulsed bias was applied across the two terminals for 25 mins in vacuum to create the trenches. The samples were stored in a dry environment until used for MIM-AFM imaging. The thermal resist layer was removed by thoroughly rinsing the sample in acetone and DI water.

4.9 References

1 Iijima, Sumio. "Helical microtubules of graphitic carbon." nature 354.6348 (1991): 56.

2 Iijima, Sumio, and Toshinari Ichihashi. "Single-shell carbon nanotubes of 1-nm diameter." Nature 363.6430 (1993): 603-605.

3 Iijima, S. "Growth of Carbon Nanotubes." Mat Sci Eng B-Solid 1993, 19, 172-180.

4 Rutherglen, C.; Jain, D.; Burke, P. "Nanotube electronics for radiofrequency applications." Nature nanotechnology 2009, 4, 811-819.

5 Avouris, P. "Carbon nanotube electronics and optoelectronics." MRS Bull 2004, 29, 403-410.

6 Avouris, P.; Martel, R.; Derycke, V.; Appenzeller, J. "Carbon nanotube transistors and logic circuits." Physica B 2002, 323, 6-14.

7 Kocabas, C.; Hur, S. H.; Gaur, A.; Meitl, M. A.; Shim, M.; Rogers, J. A. "Guided growth of large-scale, horizontally aligned arrays of single-walled carbon nanotubes and their use in thin-film transistors." Small 2005, 1, 1110-1116.

8 Kocabas, C.; Kim, H. S.; Banks, T.; Rogers, J. A.; Pesetski, A. A.; Baumgardner, J. E.; Krishnaswamy, S. V.; Zhang, H. "Radio frequency analog electronics based on carbon nanotube transistors." Proceedings of the National Academy of Sciences of the United States of America 2008, 105, 1405-1409.

9 Lan, Y.; Wang, Y.; Ren, Z. F. Physics and applications of aligned carbon nanotubes. Advances in Physics 2011, 60, 553-678.

10 Cao, Q.; Han, S. J.; Tulevski, G. S.; Franklin, A. D.; Haensch, W. "Evaluation of Field-Effect Mobility and Contact Resistance of Transistors That Use Solution-Processed Single-Walled Carbon Nanotubes." ACS Nano 2012, 6, 6471-6477.

11 Cao, Q.; Han, S. J. "Single-walled carbon nanotubes for high-performance electronics." Nanoscale 2013, 5, 8852-8863.

12 He, M.; Jiang, H.; Liu, B.; Fedotov, P. V.; Chernov, A. I.; Obraztsova, E. D.; Cavalca, F.; Wagner, J. B.; Hansen, T. W.; Anoshkin, I. V.; Obraztsova, E. A.; Belkin, A. V.; Sairanen, E.; Nasibulin, A. G.; Lehtonen, J.; Kauppinen, E. I. "Chiral-Selective Growth of Single-Walled Carbon Nanotubes on Lattice-Mismatched Epitaxial Cobalt Nanoparticles." Sci Rep-Uk 2013, 3.

13 Zhang, H.; Wu, B.; Hu, W.; Liu, Y. "Separation and/or selective enrichment of single-walled carbon nanotubes based on their electronic properties." Chemical Society reviews 2011, 40, 1324-1336.

14 Li, Y.; Cui, R.; Ding, L.; Liu, Y.; Zhou, W.; Zhang, Y.; Jin, Z.; Peng, F.; Liu, J. "How Catalysts Affect the Growth of Single-Walled Carbon Nanotubes on Substrates." Advanced Materials 2010, 22, 1508-1515.

15 Ding, L.; Tselev, A.; Wang, J. Y.; Yuan, D. N.; Chu, H. B.; McNicholas, T. P.; Li, Y.; Liu, J. "Selective Growth of Well-Aligned Semiconducting Single-Walled Carbon Nanotubes." Nano letters 2009, 9, 800-805.

16 Du, F.; Rogers, J. A. "Aligned arrays of single walled carbon nanotubes for transparent electronics." Micro- and Nanotechnology Sensors, Systems, and Applications V 2013, 8725.

17 Ho, X. N.; Ye, L. N.; Rotkin, S. V.; Cao, Q.; Unarunotai, S.; Salamat, S.; Alam, M. A.; Rogers, J. A. "Scaling Properties in Transistors That Use Aligned Arrays of Single-Walled Carbon Nanotubes." Nano letters 2010, 10, 499-503.

18 Rouhi, N.; Jain, D.; Burke, P. J. "Radio Frequency Nanoelectronics Based on Carbon Nanotubes." 2012 Ieee 12th Topical Meeting on Silicon Monolithic Integrated Circuits in Rf Systems (Sirf) 2012, 195-198.

19 Rouhi, N.; Jain, D.; Burke, P. J. "High-Performance Semiconducting Nanotube Inks: Progress and Prospects." Acs Nano 2011, 5, 8471-8487.

20 Rouhi, N.; Jain, D.; Zand, K.; Burke, P. J. "Fundamental Limits on the Mobility of Nanotube-Based Semiconducting Inks." Advanced Materials 2011, 23, 94.

21 Zhou, W. W.; Rutherglen, C.; Burke, P. J. "Wafer Scale Synthesis of Dense Aligned Arrays of Single-Walled Carbon Nanotubes." Nano Res 2008, 1, 158-165.

22 Imtiaz, A.; Wallis, T. M.; Kabos, P. "Near-Field Scanning Microwave Microscopy." IEEE Microw Mag 2014, 15, 52-64.

23 Wu, S. J.; Kienberger, F.; Tanbakuchi, H. "Scanning Microwave Microscopy: Advances in Quantitative Capacitance and Carrier Density Measurements at the Nanometer Scale." Wor Sci Ser Nano 2013, 7, 481-512.

24 Tselev, A.; Anlage, S. M.; Christen, H. M.; Moreland, R. L.; Talanov, V. V.; Schwartz, A. R. "Near-field microwave microscope with improved sensitivity and spatial resolution." Review of Scientific Instruments 2003, 74, 3167-3170.

25 Lai, K.; Kundhikanjana, W.; Kelly, M.; Shen, Z. X. "Modeling and characterization of a cantilever-based near-field scanning microwave impedance microscope." Review of Scientific Instruments 2008, 79.

26 Lai, K.; Peng, H.; Kundhikanjana, W.; Schoen, D. T.; Xie, C.; Meister, S.; Cui, Y.; Kelly, M. A.; Shen, Z.-X. "Nanoscale Electronic Inhomogeneity in In2Se3 Nanoribbons Revealed by Microwave Impedance Microscopy." Nano letters 2009, 9, 1265-1269.

27 Bonnell, D. A.; Basov, D. N.; Bode, M.; Diebold, U.; Kalinin, S. V.; Madhavan, V.; Novotny, L.; Salmeron, M.; Schwarz, U. D.; Weiss, P. S. "Imaging physical phenomena with local probes: From electrons to photons." Rev Mod Phys 2012, 84.

28 Bonnell, D. A.; Dravid, V. P.; Weiss, P. S.; Ginger, D.; Jackson, K.; Eigler, D.; Craighead, H.; Isaacs, E. "Enabling and Investigative Tools: Measuring Methods, Instruments, and Metrology." Nanotechnology Research Directions for Societal Needs in 2020: Retrospective and Outlook 2011, 71-107.

29 McCarty, G. S.; Donhauser, Z. J.; Mantooth, B. A.; Weiss, P. S. "2D dopant profiling at high spatial resolution using a tunable microwave frequency AC scanning tunneling microscope." Abstr Pap Am Chem S 2000, 220, U212-U212.

30 Stranick, S. J.; Weiss, P. S. "A Versatile Microwave-Frequency-Compatible Scanning Tunneling Microscope." Rev Sci Instrum 1993, 64, 1232-1234.

31 Yang, Y. L.; Lai, K. J.; Tang, Q. C.; Kundhikanjana, W.; Kelly, M.; Shen, Z. X.; Li, X. X. A "Shielded Cantilever-Tip Microwave Probe for Micro/Nano Surface Imaging of Conductive Properties." Proc IEEE Micr Elect 2011, 79-82.

32 Lai, K.; Kundhikanjana, W.; Peng, H.; Cui, Y.; Kelly, M. A.; Shen, Z. X. "Tapping mode microwave impedance microscopy." Review of Scientific Instruments 2009, 80.

33 Lai, K.; Kundhikanjana, W.; Kelly, M. A.; Shen, Z. X. "Calibration of shielded microwave probes using bulk dielectrics." Applied Physics Letters 2008, 93.

34 Lai, K.; Ji, M. B.; Leindecker, N.; Kelly, M. A.; Shen, Z. X. "Atomic-force-microscope-compatible near-field scanning microwave microscope with separated excitation and sensing probes." Review of Scientific Instruments 2007, 78.

35 Anlage, S. M.; Vlahacos, C. P.; Dutta, S.; Wellstood, F. E. "Scanning microwave microscopy of active superconducting microwave devices." IEEE T Appl Supercon 1997, 7, 3686-3689.

36 Schmidt, J.; Rapoport, D. H.; Behme, G.; Frohlich, H. J. "Microwave-mixing scanning capacitance microscopy of pn junctions." J Appl Phys 1999, 86, 7094-7099.

37 Cao, Q.; Xia, M. G.; Kocabas, C.; Shim, M.; Rogers, J. A.; Rotkin, S. V. "Gate capacitance coupling of singled-walled carbon nanotube thin-film transistors." Applied Physics Letters 2007, 90.

38 Tselev, A.; Anlage, S. M.; Ma, Z. K.; Melngailis, J. "Broadband dielectric microwave microscopy on micron length scales." Review of Scientific Instruments 2007, 78.

39 Kundhikanjana, W.; Lai, K. J.; Wang, H. L.; Dai, H. J.; Kelly, M. A.; Shen, Z. X. "Hierarchy of Electronic Properties of Chemically Derived and Pristine Graphene Probed by Microwave Imaging." Nano letters 2009, 9, 3762-3765.

40 Lai, K. J.; Peng, H. L.; Kundhikanjana, W.; Schoen, D. T.; Xie, C.; Meister, S.; Cui, Y.; Kelly, M. A.; Shen, Z. X. "Nanoscale Electronic Inhomogeneity in In2Se3 Nanoribbons Revealed by Microwave Impedance Microscopy." Nano letters 2009, 9, 1265-1269.

41 Yang, Y.; Lai, K.; Tang, Q.; Kundhikanjana, W.; Kelly, M. A.; Zhang, K.; Shen, Z.-x.; Li, X. "Batch-fabricated cantilever probes with electrical shielding for nanoscale dielectric and conductivity imaging." J Micromech Microeng 2012, 22.

42 Rotkin, S. V.; Subramoney, S.: "Applied physics of carbon nanotubes : fundamentals of theory, optics and transport devices"; Springer: Berlin ; New York, 2005.

43 Ilani, S.; Donev, L. A. K.; Kindermann, M.; McEuen, P. L. "Measurement of the quantum capacitance of interacting electrons in carbon nanotubes." Nature Physics 2006, 2, 687-691.

44 Bulashevich, K. A.; Rotkin, S. V. "Nanotube devices: A microscopic model." Jetp Lett 2002, 75, 205-209.

45 Luryi, S. "Quantum Capacitance Devices." Applied Physics Letters 1988, 52, 501-503.

46 Wong, H. S. P.; Akinwande, D. "Carbon Nanotube and Graphene Device Physics." Carbon Nanotube and Graphene Device Physics 2011, 1-251.

47 Burke, P. J.; Li, S. D.; Yu, Z. "Quantitative Theory of Nanowire and Nanotube Antenna Performance." IEEE Trans Nanotechnol 2006, 5, 314-334.

48 Burke, P. J. "Luttinger Liquid Theory as a Model of the Gigahertz Electrical Properties of Carbon Nanotubes." IEEE Trans Nanotechnol 2002, 1, 129-144.

49 Jin, S. H.; Dunham, S. N.; Song, J. Z.; Xie, X.; Kim, J. H.; Lu, C. F.; Islam, A.; Du, F.; Kim, J.; Felts, J.; Li, Y. H.; Xiong, F.; Wahab, M. A.; Menon, M.; Cho, E.; Grosse, K. L.; Lee, D. J.; Chung, H. U.; Pop, E.; Alam, M. A.; King, W. P.; Huang, Y. G.; Rogers, J. A. "Using nanoscale thermocapillary flows to create arrays of purely semiconducting single-walled carbon nanotubes." Nature nanotechnology 2013, 8, 347-355.

50 Xie, X.; Wahab, M. A.; Li, Y. H.; Islam, A. E.; Tomic, B.; Huang, J. Y.; Burns, B.; Seabron, E.; Dunham, S. N.; Du, F.; et al. "Direct Current Injection and Thermocapillary Flow for Purification of Aligned Arrays of Single-Walled Carbon Nanotubes." J Appl Phys 2015, 117 (13), 134303.

51 Dresselhaus, M. S.; Dresselhaus, G.; Saito, R.; Jorio, A. "Raman spectroscopy of carbon nanotubes." Phys Rep 2005, 409, 47-99.

52 Dresselhaus, M. S.; Dresselhaus, G.; Jorio, A.; Souza, A. G.; Pimenta, M. A.; Saito, R. “Single nanotube Raman spectroscopy.” Accounts Chem Res 2002, 35, 1070-1078.

53 Jorio, A.; Saito, R.; Hafner, J. H.; Lieber, C. M.; Souza, A. G.; Pimenta, M. A.; Matinaga, F. M.; Dantas, M. S. S.; Hunter, M.; McClure, T.; Dresselhaus, G.; Dresselhaus, M. S. “Resonant Raman scattering of isolated single wall carbon nanotubes: Structural (n,m) determination and resonant window.” Electronic Properties of Molecular Nanostructures 2001, 591, 298-302.

54 Weisman, R. Bruce, and Sergei M. Bachilo. "Dependence of optical transition energies on structure for single-walled carbon nanotubes in aqueous suspension: an empirical Kataura plot." Nano Letters 3.9 (2003): 1235-1238.

55 Kataura, H., et al. "Optical properties of single-wall carbon nanotubes." Synthetic metals 103.1-3 (1999): 2555-2558.

56 Maruyama, Shigeo. “Kataura-Plot for Resonant Raman.” University of Tokyo: Department of Mechanical Engineering. April 15, 2009. http://www.photon.t.u-tokyo.ac.jp/~maruyama/kataura/kataura.html

57 Derycke, V.; Martel, R.; Appenzeller, J.; Avouris, P. “Controlling doping and carrier injection in carbon nanotube transistors.” Applied Physics Letters 2002, 80, 2773-2775.

58 Rochefort, A.; Avouris, P. “Electron interference effects on the conductance of doped carbon nanotubes.” Journal of Physical Chemistry A 2000, 104, 9807-9811.

59 Wu, S. J.; Kienberger, F.; Tanbakuchi, H., Scanning Microwave Microscopy: Advances in Quantitative Capacitance and Carrier Density Measurements at the Nanometer Scale. Scanning Probe Microscopy for Energy Research, Book Series: World Scientific Series in Nanoscience and Nanotechnology 2013, Volume: 7, 481-512

60 Xie, Xu, et al. "Microwave purification of large-area horizontally aligned arrays of single-walled carbon nanotubes." Nature communications 5 (2014): 5332.

61 Kundhikanjana, Worasom, et al. "Unexpected surface implanted layer in static random access memory devices observed by microwave impedance microscope." Semiconductor Science and Technology 28.2 (2013): 025010.

62 Berweger, Samuel, et al. "Microwave near-field imaging of two-dimensional semiconductors." Nano Letters 15.2 (2015): 1122-1127.

63 Odom, T. W.; Huang, J. L.; Kim, P.; Lieber, C. M. “Atomic structure and electronic properties of single-walled carbon nanotubes.” Nature 1998, 391, 62-64.

64 Zhang, Z.; Lieber, C. M. “Nanotube Structure and Electronic-Properties Probed by Scanning-Tunneling-Microscopy.” Applied Physics Letters 1993, 62, 2792-2794.

65 Wildoer, J. W. G.; Venema, L. C.; Rinzler, A. G.; Smalley, R. E.; Dekker, C. “Electronic structure of atomically resolved carbon nanotubes.” Nature 1998, 391, 59-62.

66 Donhauser, Z. J.; McCarty, G. S.; Bumm, L. A.; Weiss, P. S. “High resolution dopant profiling using a tunable AC scanning tunneling microscope.” AIP Conf Proc 2001, 550, 641-646.

67 Ferreira, M. S.; Dargam, T. G.; Muniz, R. B.; Latge, A. “Local electronic properties of carbon nanotube heterojunctions.” Physical Review B 2000, 62, 16040-16045.

68 Odintsov, A. A. “Schottky barriers in carbon nanotube heterojunctions.” Physical Review Letters 2000, 85, 150-153.

69 Ashcroft, N. W., and N. D. Mermin. "Solid State Physics, Chapter: 17 and 29." Pacific Grove: Brooks/Cole (1976).

70 “Work function of single-walled and multiwalled carbon nanotubes: First-principles study”, W. S. Su,1 T. C. Leung, and C. T. Chan, 2007

CHAPTER 5

TAPPING AND FORCE CURVE SCAN PROBE METHODS FOR 100% CLEAN MICROWAVE REFLECTIVITY MAPPING OF CARBON NANOTUBES

5.1 Introduction/Motivation

In previous chapters, nanoscale electronic characterization using Microwave Impedance Microscopy (MIM) was done using a contact mode scan probe geometry, where the tip is in direct contact with the sample surface [1]. There are benefits to operating in contact mode, most notably a high sensitivity to surface capacitance, however, a major limitation using contact mode comes from variation in the stray capacitance background. The stray capacitance background is the result of geometric capacitive coupling to the entire probe including the tip apex, tip cone, and cantilever [2,3,4,5,6]. Although, the probe is shielded to minimize the MIM's sensitivity to capacitance coupling everywhere except the tip, the overall geometric capacitance contribution to the measured tip-sample capacitance still has a substantial impact on the sensitivity and SNR of the desired signal, the electronic or quantum capacitance under the tip apex [7,8].

The relative contribution of the geometric capacitance can be controlled in the contact mode experimental geometry. It was previously shown in chapter 4 that increasing the relative permittivity of the tip-sample dielectric medium, which is typically air, by depositing a thin metal oxide layer on the sample's surface vastly improves the MIM's sensitivity to surface capacitance [7]. For the contact mode MIM mapping of carbon nanotubes, the deposited dielectric layer has an added advantage of keeping the CNTs from moving during the tip scan, which enables high resolution AFM topology mapping in the contact mode geometry. This

allows for the detection of structurally driven electronic properties by simultaneously recording both the MIM capacitance and AFM topology data.

For our previous experiments using contact mode MIM to characterize CNTs, we typically used metal oxide layers with high dielectric constants such as MgO and Al_2O_3. An unavoidable issue with using a MgO layer, which easily washes off after characterization, is it absorbs water from the ambient humidity which can degrade the surface conformity after several hours. Also, once the MgO is washed away some residue remains on the surface which can negatively impact the quality of future oxide layers. For Al_2O_3, the dielectric layer is very stable, however, it cannot be removed making further device patterning after characterization impossible. In addition, it is shown that during atomic layer deposition, a build-up of Al_2O_3 nanoparticles form along the backbone of the CNT due to differences in surface energy between the graphene backbone of the nanotube and the substrate [8,9,10,11]. The roughness of the dielectric layer, regardless of the metal oxide type, can affect the SNR of the measured capacitance signal. The presence of a thin (<5nm), high permittivity dielectric medium makes the MIM observable is more sensitive to quantum capacitance, but the geometric component is still present in the signal enabling changes in surface topology and/or dielectric thickness to affect the measured signal. Since any spatial change in dielectric constant or oxide thickness will notably alter the contribution of geometric capacitance such that topology coupling can act as a source of noise in the stray geometric capacitance background [4,5,6,7]. The effects of topology roughness on the measured signal can be seen in figure 5.1b, where a linecut of the AFM topology and MIM capacitance of a semiconducting nanotube shows variation in MIM signal with changing topology. We know from previous measurements of CNT topology, that the ~0.25nm roughness seen in the topology data from figure 5.1 originates from the roughness in the deposited metal

oxide layer. Notice that the MIM capacitance is slightly higher on the taller side of a semiconducting CNT, where we expect zero contrast in quantum capacitance, implying that the observed correlation between MIM and topology in figure 5.1b wouldn't be present without the influence of the geometric capacitance. We propose that this source of noise can be eliminated by increasing the permittivity of the tip-sample dielectric medium without depositing a metal oxide layer.

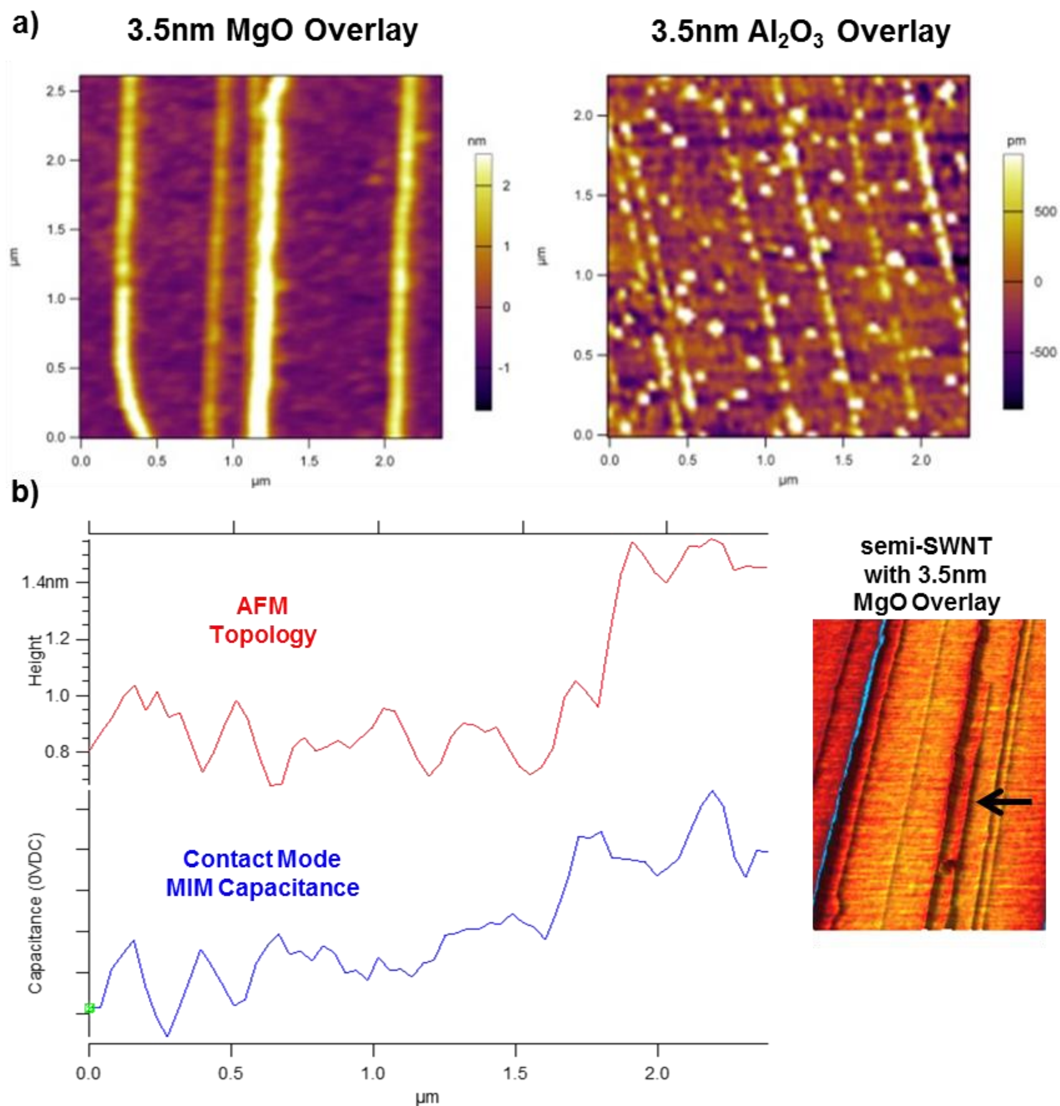

Figure 5.1: (a) AFM images of an aligned CNT sample coated with a 3.5nm MgO and Al_2O_3 layer. (b) MIM-AFM response data for a semiconducting Single Walled CNT with a MgO overlayer.

Many device applications, such as transistors and sensors, require high purity CNT of a single electronic type. One method of obtaining high purity CNTs is to separate them based on their diameter using ultra-centrifuge purification (refer to Chapter 1). The resulting CNT samples is composed of short segments of CNTs of mostly one electronic type dissolved in solution [12]. The aqueous CNTs are dispersed in a random network on a substrate as seen in figure 5.2a after the purification. Many of the NT segments are coated with a residual thin surfactant layer from the purification process, which can make the CNT appear larger than they are supposed to be in AFM topology images.

To verify the homogeneity in electrical properties after purification, characterization methods, such as Raman Spectroscopy, are used to measure the averaged optical response of the sample [13]. Although these methods can provide information for the average composition of CNT electronic type, we must use an electronic characterization method with nanoscale resolution, such as MIM, to identify the electronic character of individual CNT segments that will affect the device performance. Characterizing the CNT segments using contact mode MIM requires the deposition of a metal oxide layer as previously discussed. The AFM topology image of CNTs segments on quartz, after being processed using ultra-centrifuge purification and coated with a 3.5nm layer of Al_2O_3, is shown in figure 5.2b. Notice that the formation of metal oxide nanoparticles, as previously discussed, can greatly diminish the accuracy and resolution of the topology data making individual CNT segment identification more difficult.

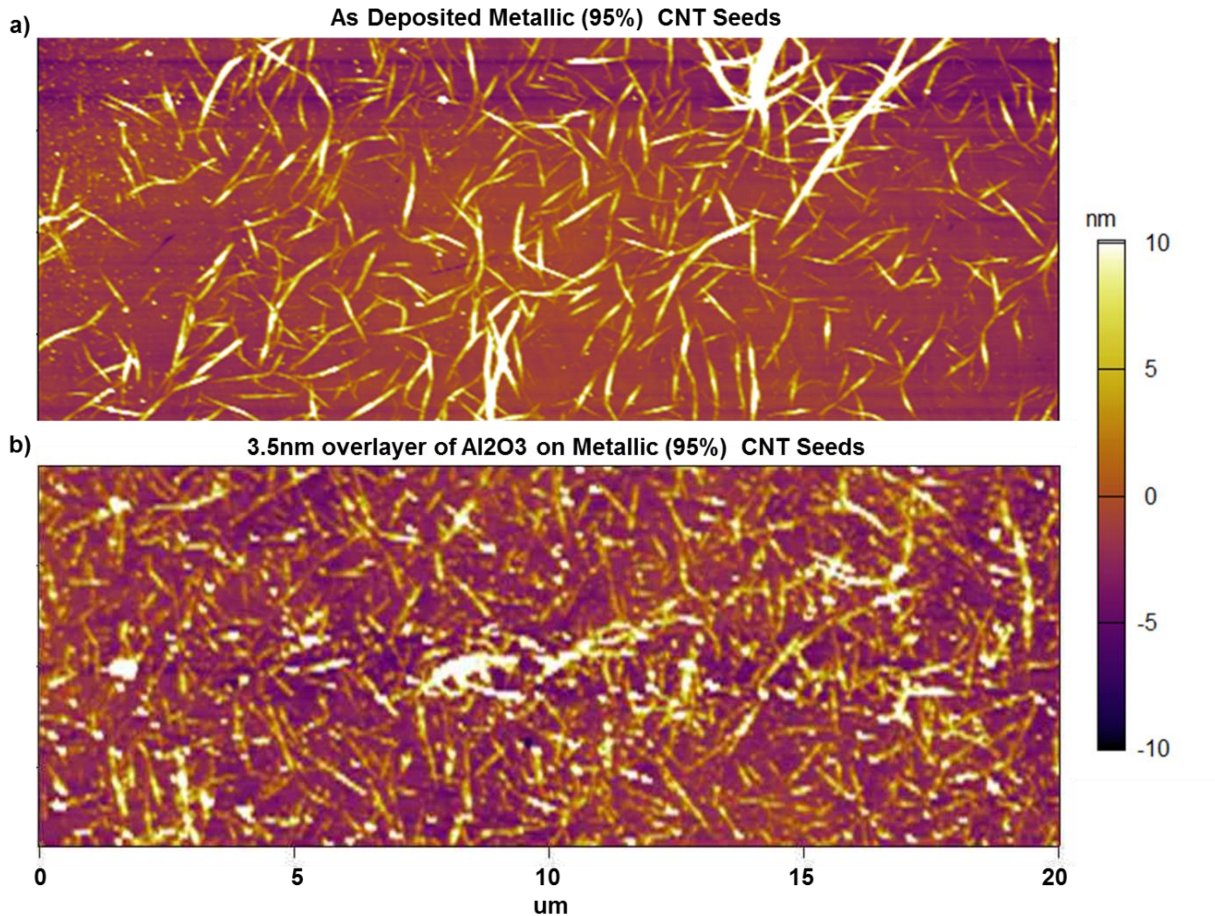

Figure 5.2: AFM image of sample made of ~95% metallic CNT segments deposited on quartz before (a) and after coating with a thin layer of alumina (b).

The contact mode MIM-AFM results after coating a metallic CNT segments with 3.5nm of Al_2O_3 is seen in figure 5.3. Mapping the electrical properties of individual CNT segments using MIM was greatly hindered by the roughness of the dielectric layer. The metal oxide nanoparticles and the surfactant layer both add topology roughness on the order of the CNT diameters. In the MIM image both the metallic CNT seeds and the alumina nanoparticles appear as high capacitance which diminishes the image quality. The presence of the metal oxide layer introduces issues with topology noise from surface roughness and the formation of nanoparticles which can greatly hinder the ability to obtain high quality capacitance data. In addition, the

coating of a dielectric layer, in some cases, will ruin the sample preventing further processing and characterization analysis.

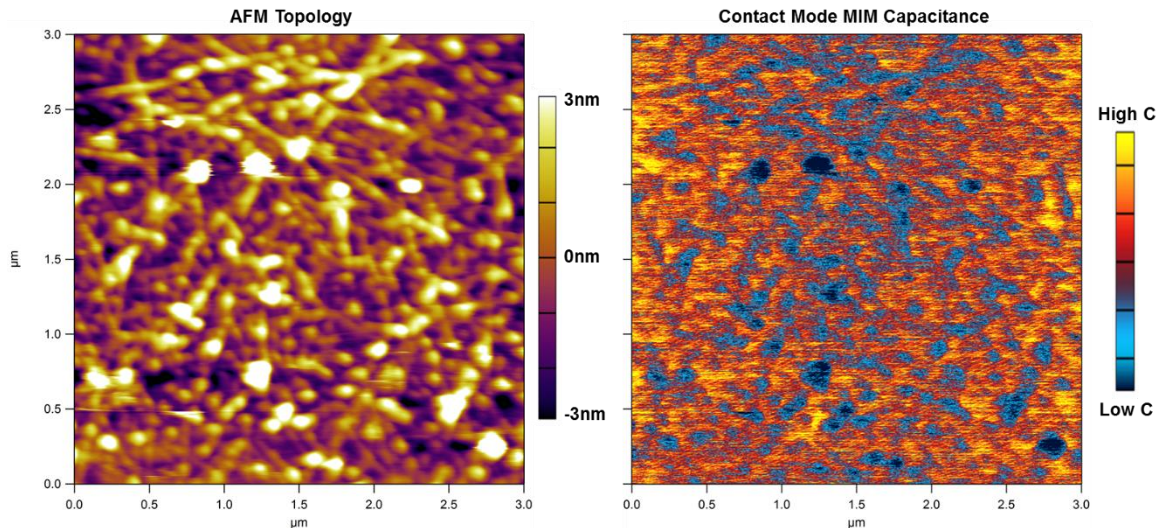

Figure 5.3: An AFM (left) and MIM Capacitance (right) image of a sample made of metallic CNT segments deposited on quartz and coated with alumina.

How do we modify our MIM imaging methodology so that we can measure quantum or electronic capacitance on the sample surface without needing to deposit a dielectric layer? Solving this problem will make the MIM-AFM characterization process 100% clean and more compatible for process characterization in an industrial setting. For our purposes, we need to develop a method to operate a non-contact scanning geometry, so that we don't drag the NTs and can acquire high resolution topology data. We know that we can achieve high sensitivity to quantum capacitance by controlling the dielectric constant in the space between the tip and sample. Most bulk materials either have a native oxide layer or behaves like the dielectric medium itself when its physical dimensions are larger of the microwave near-field penetration depth. For bulk sample geometries, contact mode MIM is the ideal preferred to achieve the highest SNR and sensitivity to electronic capacitance. However, for nanoscale materials, the geometric capacitance dominates the signal whenever an air gap is present between the tip and

sample. For low dimensional sample geometries, the near-field extends deeper than the sample surface resulting in an effective dielectric constant equal to the average permittivity of the air gap and substrate. This implies that we need to control the dielectric constant of medium between the tip and sample to characterize low dimensional materials using MIM. Considered the case when the tip is very close to the sample surface, we expect an ultra-thin (<2nm) layer of water, native to the sample surface, to form a water meniscus bridge with the tip apex [14,15,16,17]. This is a common phenomenon that occurs with scan probe microscopy; SEM images of the water meniscus on an AFM tip can be seen in figure 5.4 [14,15,16,17]. Water adhesion and capillary action are the driving forces behind the water meniscus [15,16]. These forces are known to have a notable effect on tip-cantilever dynamics in under certain experimental conditions, this will be an important consideration for the experimental design and analysis [15]. The native water layer has a dielectric constant of ~80 and present on most surfaces in ambient humidity conditions (h>10%) [16]. Hence, the water meniscus bridge is the ideal dielectric medium to use for quantum capacitance detection without the need of a metal oxide deposition.

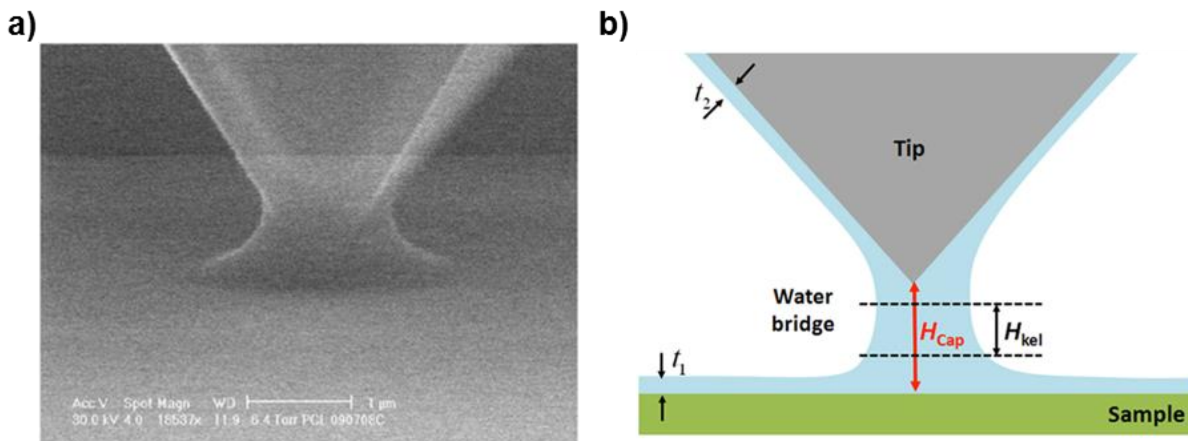

Figure 5.4: (a) SEM image of the water meniscus formation at the tip-sample interface under low humidity, near-vacuum. (b) An illustration of the physical model for the water meniscus formation. [14]

In this chapter, we explore the use of intermittent-contact scan probe geometries to take advantage of the native water layer as the dielectric medium for the mapping of quantum capacitance. We will present experimental and simulation data that illustrates the importance of the water meniscus formation for the detection of quantum capacitance using MIM-AFM. First, we attempted tapping mode MIM to explore how the forces that affect the tip-cantilever dynamics would affect the measured capacitance signal. We show that under ideal experimental conditions, we can tap close enough to the surface to directly take advantage of the water layer to obtain quality tapping mode MIM-AFM images. However, the short-range forces can create noise and instability when tapping very close to the surface, so we sought to improve the stability of the tip-cantilever dynamics. Force Curve mapping AFM takes advantage of well controlled, slow and stable, tip movements to measure nanoscale forces. This presents an opportunity to directly detect the water meniscus formation to map quantum capacitance without noise contributions from short-range forces (tapping mode) and dielectric surface roughness (contact mode). Here we present data that shows a notable improvement in sensitivity and SNR when measuring MIM capacitance in parallel with a force curve map. Our results prove that high resolution capacitance maps of carbon nanotubes can be acquired with MIM using only the native water layer.

5.2 Tapping MIM-AFM Analysis

The MIM signal is sensitive to the tip-nanotube capacitance modeled as the geometric capacitance and quantum capacitance in series, with the substrate capacitance, which acts as a uniform background, in parallel [2,5,7]. The geometric capacitance is sensitive to the physical geometry of the tip and nanotube including separation distance, size of the nanotube, and

permittivity of the medium [6,7]. Since the quantum capacitance contains all the information for a carbon nanotube, the goal is to minimize the relative contribution of the geometric capacitance by using the thin water meniscus layer. When the tip is very close to the sample surface a water meniscus forms which keeps the tip's apex inside the water layer, in quasi-contact with the surface. When the permittivity of the dielectric medium is large, $\varepsilon_{water} = 80$, and the separation distance (Z) is very small, the desired quantum capacitance will dominate the measured capacitance (C_{meas}) signal. The equation for the measured capacitance when the tip is in the water meniscus layer is given by equation 5.3.

$$C_{meas} = C_{sub} + \frac{C_Q * C_g(\varepsilon, Z)}{C_Q + C_g(\varepsilon, Z)} \qquad (5.1)$$

$$C_{meas}\,|water = C_{sub} + \frac{C_Q * C_g(\varepsilon_{water}, Z \to 0)}{C_Q + C_g(\varepsilon_{water}, Z \to 0)} \qquad (5.2)$$

$$C_Q \ll C_{geo}(\varepsilon_{water}, Z \approx 0) \rightarrow C_{meas}(x, y)|water \sim C_Q(x, y) \qquad (5.3)$$

In tapping mode MIM the tip oscillates at the resonant frequency determined by the tip-cantilever geometry and physical characteristics [18,19]. The distance between the tip and sample surface is modulated with a precision piezo electric feedback loop allowing for nanometer control [18,19]. When the tip interacts with the surface it is sensitive to the Van der Waals forces allowing it to track topology [18,19]. When the tip is very close to the surface the Van der Waals forces and capillary forces, from the water meniscus, creates a net attractive force on the tip. If the tip continues to get closer the repulsive Van der Waals forces will begin to dominate the interaction implying direct contact with the surface. It has been shown throughout literature that operating the tip in the repulsive force regime yield more accurate topology data [19,20]. The tip oscillation is also sensitive to the coulomb forces, which are stronger at low tip-surface separation. Figure 5.5 shows an illustration of the different tapping regimes and the

important capacitance contributions which affect our measured signal. It is important to understand that any tip-sample forces that effects the dynamics of the tip oscillation or tip-surface separation will be detected in the stray geometric capacitance contribution to the MIM data.

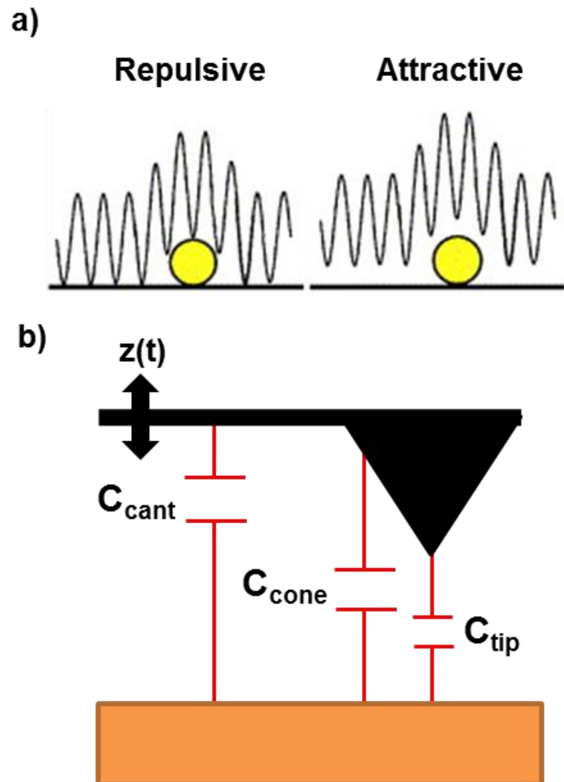

Figure 5.5: (a) Simple illustration of the tip oscillation for tapping mode in the repulsive and attractive regimes [20]. (b) Geometric model for the capacitance contributions to the measured signal.

The capacitance contributions from the tip apex, cone, and cantilever are functions of tip-sample separation, z(t) (equation 5.4) [3,4,5,6]. The z-position of the tip-cantilever geometry has a constant z-offset (Δz) and an oscillation amplitude (A) [18,21]. The oscillation frequency will have several resonant components dominated by the free air resonance (equation 5.5) [18,21]. To ensure that the tip apex is operating in the water meniscus layer for the entire tip oscillation period, the tapping is done at a low z-offset and low amplitude [15,17,22]. In this tapping

condition, the measured average capacitance is dominated by the quantum capacitance (equation 5.6). The remaining geometric components of the measured signal can be added together as stray capacitance, which the most common source of noise and topology coupling. It has been shown that all short-range forces interact with the tip, $F_{probe-sample}$, including the capillary and coulomb forces, influence the tip's oscillation dynamics causing non-resonant oscillations and unstable shifts in tapping phase (equation 5.7) [6,15,21]. These forces are coupled to the measured stray capacitance by changing tapping dynamics and will be the primary contributor to noise in the measured capacitance data (equation 5.8).

$$C_{meas} = C_{tip}\left(\varepsilon_{tip}, z_{tip}\right) + C_{cone}(\varepsilon_{cone}, z_{cone}) + C_{cant}(\varepsilon_{cant}, z_{cant}) \tag{5.4}$$

$$z(t) = \Delta z + \sum_{\omega} A(\omega t + \theta) \tag{5.5}$$

$$z_{tip}^{max}|^{LA} = dz + A^{max} < z_{water} \rightarrow C_{tip} \approx C_Q \tag{5.6}$$

$$A(\omega t + \theta) \equiv f(F_{probe-sample}) \tag{5.7}$$

$$C_{meas}(x, y) = C_Q(x, y) + C_{stray}\left(\varepsilon_{air}, z\left(F_{ps}(x, y), \omega\right)\right) \tag{5.8}$$

In figure 5.6a, the phase lag between the drive frequency and tapping frequency is shown as a function of z-offset and tapping amplitude. When lightly tapping, the z-offset is nearly the same as oscillation amplitude, the attractive force regime dominates, which dampens the tapping amplitude [15,19,20]. The repulsive force regime dominates when separation distance low enough to ensure direct contact during a significant part of the tapping oscillation period [15,19,20]. According to literature, the attractive and repulsive regimes begin to show instability with tapping with a very low amplitude and z-offset, where the separation distance is on the order of the water meniscus formation [15,20,23]. In figure 5.6ab, signatures of this instability are evident from the large discontinuities seen in the tapping phase and amplitude data [23]. In figure 5.6c, phase space maps are plotted for low amplitude tapping at various tip-surface

separation distances; the repulsive and attractive regimes are represented regions of white and grey accordingly. Notice that when the tapping amplitude gets smaller regions of instability get closer together, implying that maintaining stable operation with a low tapping amplitude may be difficult the achieve [23].

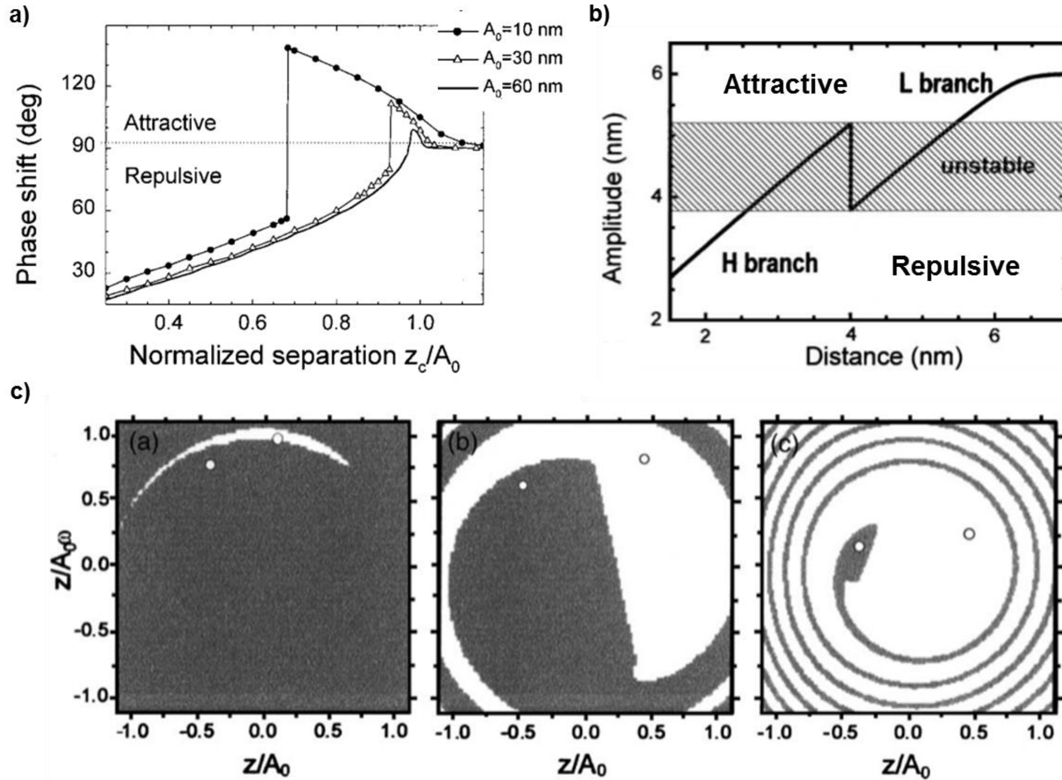

Figure 5.6: Simulation data from literature showing the instability in low amplitude tapping operation [23]. (a) Tapping phase shift vs oscillation amplitude (x-axis) showing the amplitude discontinuity. (b) Tapping oscillation amplitude vs tip offset (x-axis) showing the amplitude discontinuity. (c) Phase space maps at various tip offsets of 16nm (left), 14.5nm (middle), and 7.5nm (right), showing the discontinuity between the attractive mode (grey) and the repulsive mode (white).

For the purposes of our experiments using low amplitude tapping MIM, the measured capacitance is the signal response of the microwave reflection averaged over the entire oscillation period. Therefore, we prefer to use a low enough amplitude to ensure the tips stays in the water meniscus layer for most of the tapping oscillation period. In figure 5.7 an aligned CNT

sample coated with thin alumina layer is mapped with contact mode MIM and low amplitude tapping MIM to directly compare the capacitance data for consistency. The contact mode MIM easily reveals the metallic CNTs with nearly tip limited resolution, whereas the resolution of the tapping MIM data was diminished by capacitance noise. Despite this the general contrast trend of the tapping MIM data is consistent with that of the contact MIM implying that accurate electronic mapping of CNTs using low amplitude tapping MIM is possible.

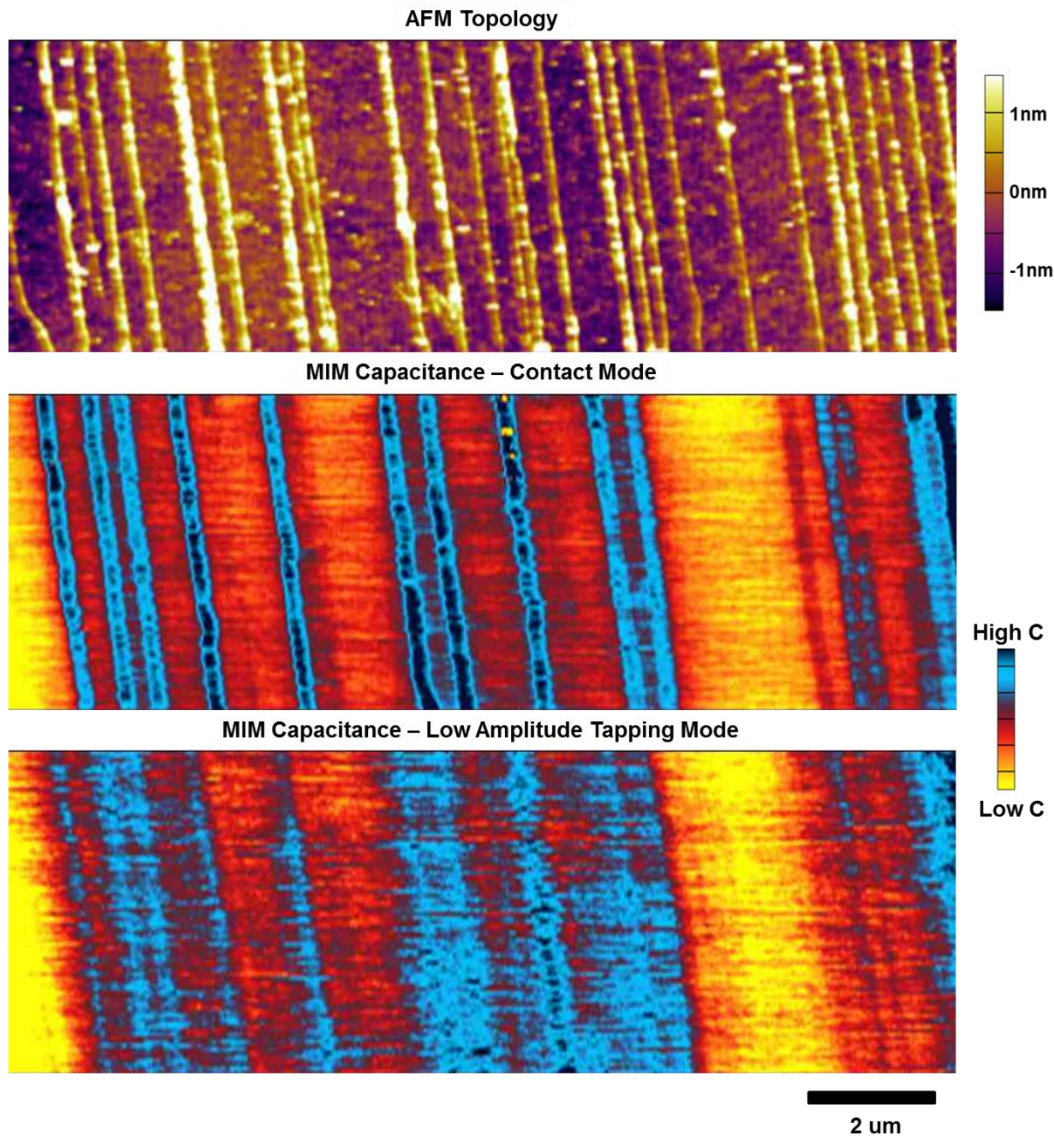

Figure 5.7: AFM image of an aligned CNT array (top) and the corresponding MIM data for contact operation (middle) and repulsive low amplitude tapping operation (bottom).

Figure 5.8 shows a low amplitude MIM-AFM scan of an as-grown (uncoated), aligned CNT array. The AFM topology, AFM phase, and MIM capacitance data is shown for direct comparison. The image was taken using a very low tapping amplitude (6nm) to ensure that the tip was operating in the water meniscus layer for the majority of the oscillation period. In the attractive mode of operation, identified by the higher phase and slightly inflated AFM topology, the MIM capacitance map shows an area of improved SNR and resolution. When the tip hits a piece of debris, the tapping dynamics change from the attractive to repulsive force regime, indicated by a sudden phase shift and improved spatial resolution. The debris could have caused tip contamination or initiated a natural shift to a more stable tapping force regime. The tapping phase itself doesn't have a notable impact on the measured SNR, as seen by subtle phase shift while operating in attractive mode. Notice that not every piece of dirt or nanoparticle causes a phase shift and not all phase shift indicate a change in stable tapping operation. We believe that the SNR of tapping MIM is optimal when operating in an attractive force regime with a tapping amplitude low enough to remain in the water meniscus layer. It can be concluded from our data that careful control of the tip-cantilever oscillation dynamics is needed for the stable operation of low amplitude tapping MIM-AFM. This experiment proves under ideal experimental conditions it is possible to map the electronic properties of CNTs, without a dielectric layer, using very low amplitude tapping MIM-AFM in the water meniscus layer.

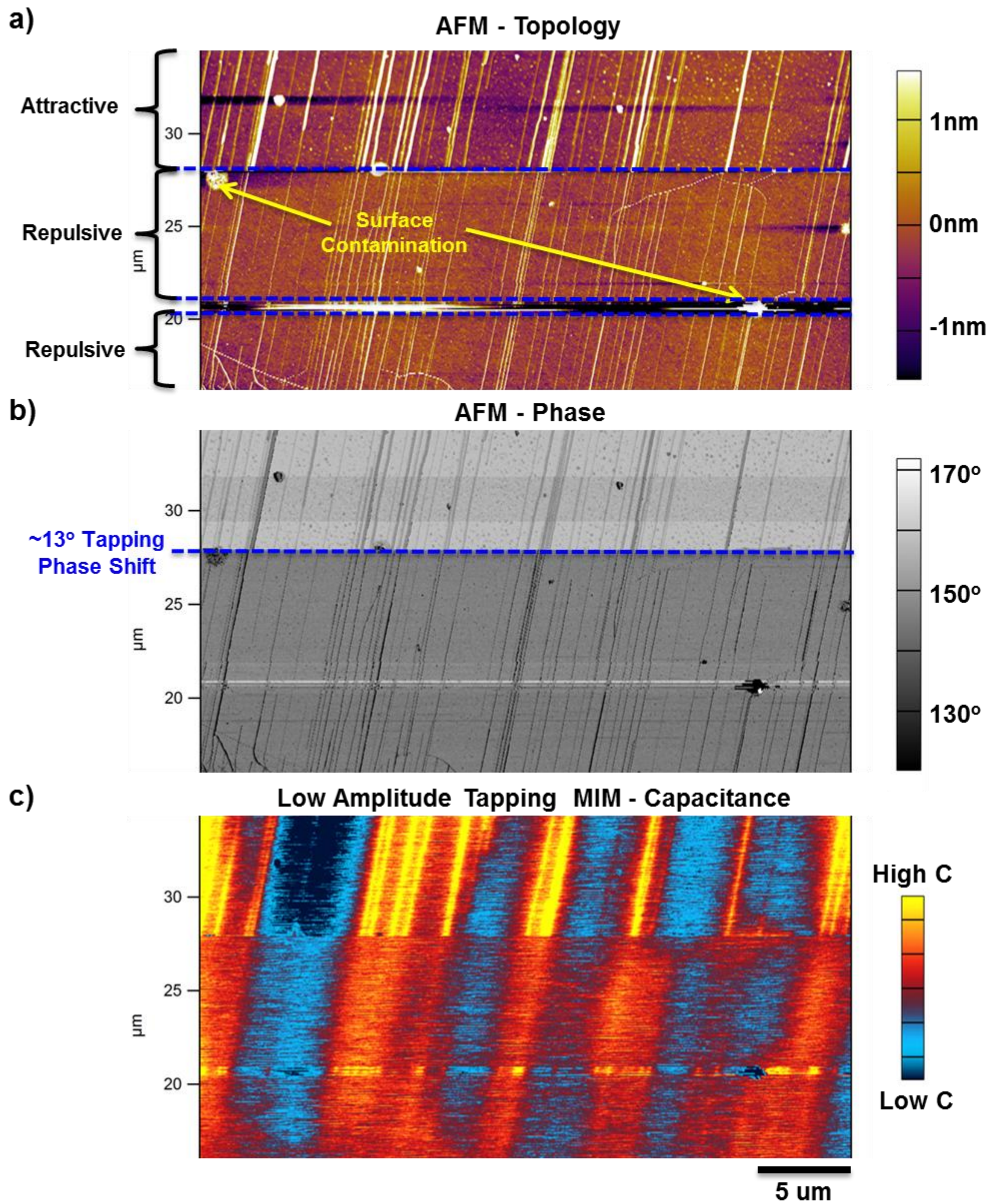

Figure 5.8: Direct comparison of the AFM topology, AFM Phase, and MIM capacitance data for a low amplitude (A=6nm) tapping scan on an aligned CNT array. The tapping phase shift after contact with the sample debris (yellow arrows) is highlighted by the horizontal blue line.

Next, we explored using larger, more stable tapping amplitudes in conjunction with a lock-in amplifier to detect the spatial changes in surface capacitance. We used the lock-in amplifier to detect the change in capacitance with respect to tip-surface separation, dC/dZ. This eliminated the restriction of operating the water layer using very low amplitudes, which allows for a more stable tapping condition. The results of the lock-in signal compared to low amplitude, repulsive regime tapping MIM in the is shown in figure 5.9. Our results suggest that there's an opportunity to exploit capacitance derivative detection (dC/dZ) for CNT electronic mapping.

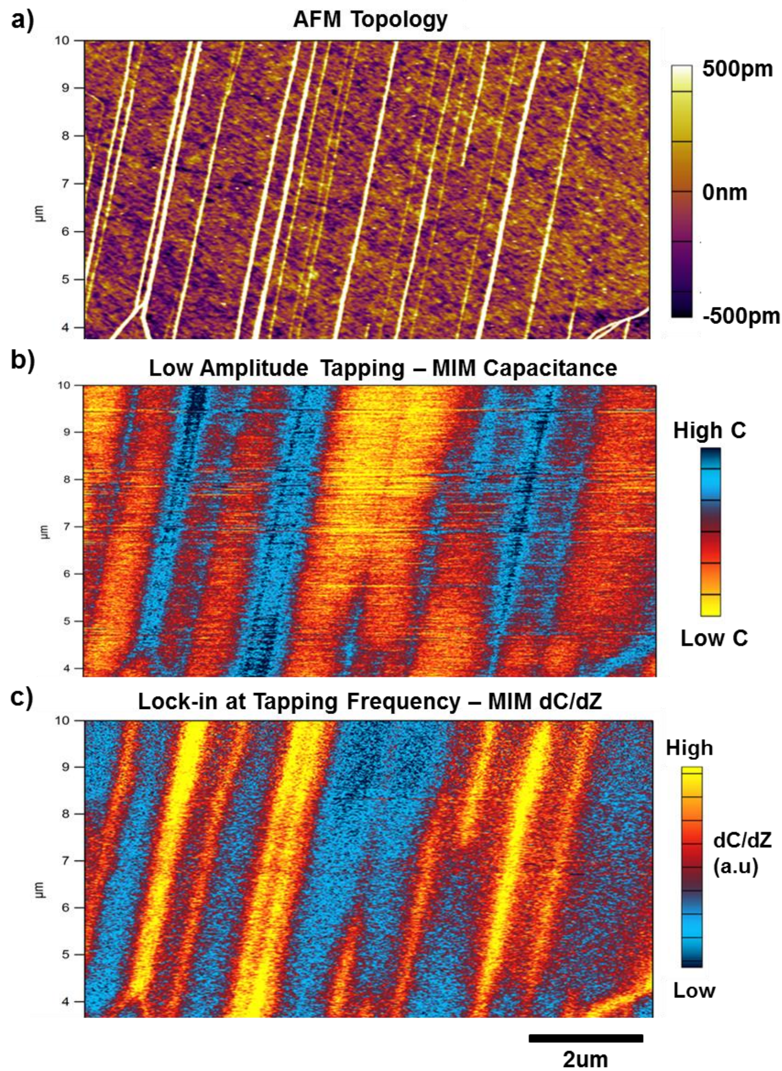

Figure 5.9: Direct comparison of the AFM topology, low amplitude (A=6nm) tapping MIM capacitance, and lock-in tapping (A=20nm) MIM dC/dZ on an aligned CNT sample.

For capacitance derivative detection, the SNR is maximized for larger tapping amplitudes, which maximizes capacitance swing between the geometric baseline, in air, and the quantum capacitance, in contact. In addition, frequency filters, phase sensitive detection, and signal averaging allows for high resolution mapping of the capacitance derivative (dC/dV) using a lock-in amplifier as seen in figure 5.10. Two ultra-centrifuge purified CNT samples, one with primarily metallic CNT segments and the other with semiconducting segments, are characterized using capacitance derivative mapping. The effects of short-range forces interacting on the tip are revealed by directly correlating of the AFM tapping phase data with the amplitude and phase of the MIM differential capacitance data. Images of the semiconducting NT samples shows contrast driven by geometric capacitance coupling to the tapping amplitude and phase, which generates contrast in the differential capacitance map contrary to the expected quantum capacitance response. Metallic CNTs generate contrast from both the quantum and geometric components of the capacitance, unlike the semiconducting NTs, resulting a higher SNR from the differential capacitance data. The influence of stray geometric capacitance coupling is inherent with dC/dZ detection, since they it is a strong function of tip-sample separation and cantilever dynamics. The contribution of geometric capacitance to the measured signal is amplified by the lock-in detection and cannot be separated from the desired observable. This implies that although high resolution capacitance mapping is possible using differential capacitance MIM, there is no way to separate the geometric artifacts from the quantum capacitance contrast, which diminishes the reliability and accuracy of the measured data.

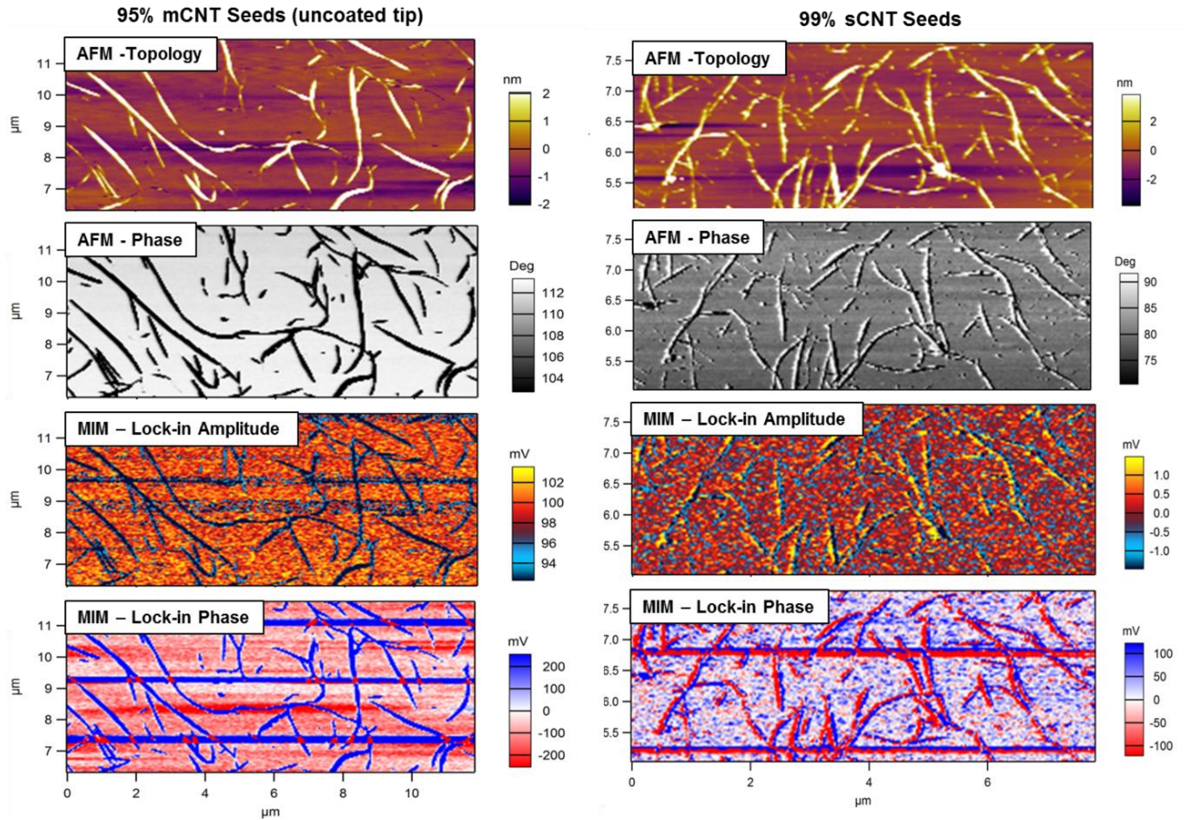

Figure 5.10: Direct comparison of AFM topology, AFM phase, MIM differential capacitance amplitude and phase images of a metallic (left) and semiconducting (right) nanotube sample.

5.3 Force Curve MIM-AFM Analysis

The results from chapter section 5.2 suggests that we must maximize sensitivity to quantum capacitance without the hindering influence of stray geometric capacitance to acquire high quality data. Here we explore the use of force curve mapping to directly detect the influence of the water meniscus layer and simultaneously record the capacitance using MIM. An illustration of the proposed scan probe geometry is shown in figure 5.11. The tip does not oscillate rather it measures a force curve, where the tip moves at a constant slow speed towards the sample (extend) until it detects or touches the surface, it then slowly returns to its initial non-contact tip-sample separation height (retract) [24]. The force curve and the MIM response (MIM-FC) is recorded at every pixel point to create a map of force curve data [24]. When the tip is far

from the sample, illustrated in the red square, the tip-sample medium is air, however, when the tip gets close to the sample surface a water meniscus will form between the tip apex and the ambient water layer, illustrated in the blue square (figure 5.11).

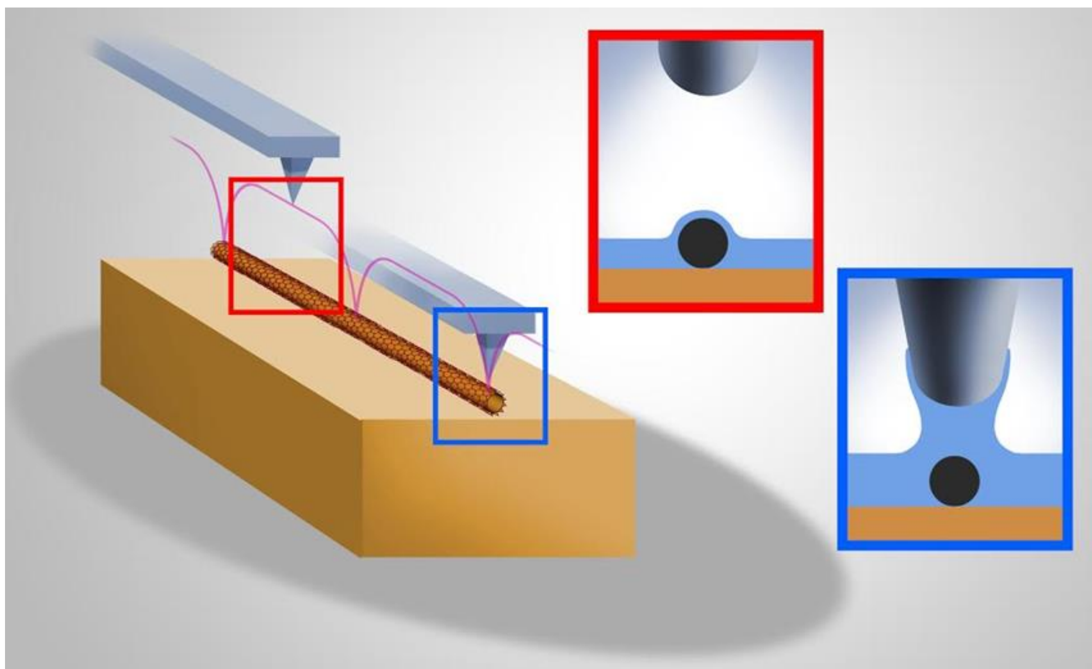

Figure 5.11: An illustration showing the experimental geometry for a MIM-FC scan on a CNT sample. The red box shows the tip at the top of the scan and the blue box shows the water meniscus at the bottom of the force curve.

Force curve mapping allows for careful control and precise signal detection with respect to the tip-sample separation distance. According to figure 5.5 and equation 5.8, the stray capacitance background, caused by geometric capacitance coupling to the entire probe, is a function of tip-sample separation and cantilever dynamics [3,4,5,6,15,18,21]. The advantage of force curve mapping is that the forces interacting with the tip are detected by changes in the tip-cantilever deflection as a function of tip-sample separation, allowing for stable the measurement of the stray capacitance background in real-time [2,4,5,6]. When the tip is in air the capacitance is dominated by the geometric contributions; the geometric capacitance at the tip apex will have the biggest contribution since it is the closest to the sample. The force curve and capacitance

curve as a function of tip-sample separation is present in the data from figure 5.12b. We used MATLAB to simulate the expected logarithmic trend from the stray capacitance response; it directly agrees with experimental C-Z curve obtained from a MIM-FC on highly doped bulk Silicon [3]. As the tip approaches the sample the attractive Van der Waals forces and the capillary forces from the water meniscus causes the tip to "snap-down" to the surface, it is detected as a rapid change in measured deflection curve without a change in the probe z-offset [6,25]. The sudden change in the signal comes from both a change in tip-sample separation and permittivity of the dielectric medium from the water meniscus. Notice in figure 5.12b that the discontinuity in both the capacitance and deflection data occurs at the "snap-down" before the tip is in full contact with the sample surface, implying that the permittivity of the water layer may play a larger role in capacitance detection than the tip-sample separation distance. The probe force is increased until the deflection inverts implying full contact. According to figure 5.12b, the tip's geometric capacitance contribution shouldn't change much in this part of the force curve, only the effects from cantilever bending is evident in the data after full contact.

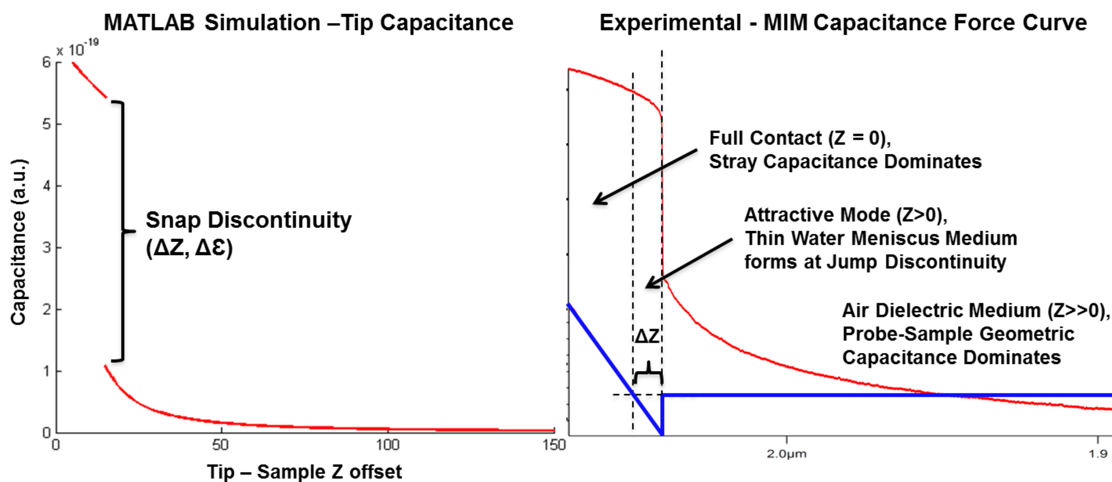

Figure 5.12: (a) MATLAB simulation of tip capacitance and (b) MIM capacitance experimental data as a function of z-offset for a force curve on doped silicon; Δz represent the maximum change in tip separation during snap discontinuity. The deflection force curve response is shown in blue.

Once the tip begins to retract, the capillary forces from the water meniscus rapidly weaken causing a “snap-off” to occur at a higher tip-sample separation than the discontinuity during “snap-down” [15]. To decouple the relative contributions of the separation jump (Δz) and the dielectric medium change (ΔƐ) during “snap-off” (or down), we recorded the MIM-FC response for a doped Silicon sample in ambient air and fully immersed in DI water. Figure 5.13 shows that the water meniscus formation, which only occurs for force curves preformed in air, plays a big role in the signal discontinuity by not only driving the capillary forces that induces the snap effect and subsequent change in tip-sample separation (Δz), but also by rapidly increasing changing the permittivity of the dielectric medium during the snap effect. We calculated the capacitance signal’s sensitivity to the snap discontinuity (ΔC/ΔZ) in water and air to test to relative contributions of rapidly changing tip-sample separation and dielectric medium to the signal discontinuity. We found that the capacitance response is more than double using an air medium compared to water medium, which implies that the rapid change in the permittivity of the dielectric medium during the water meniscus induced snap discontinuity is essential for maximizing sensitivity and SNR.

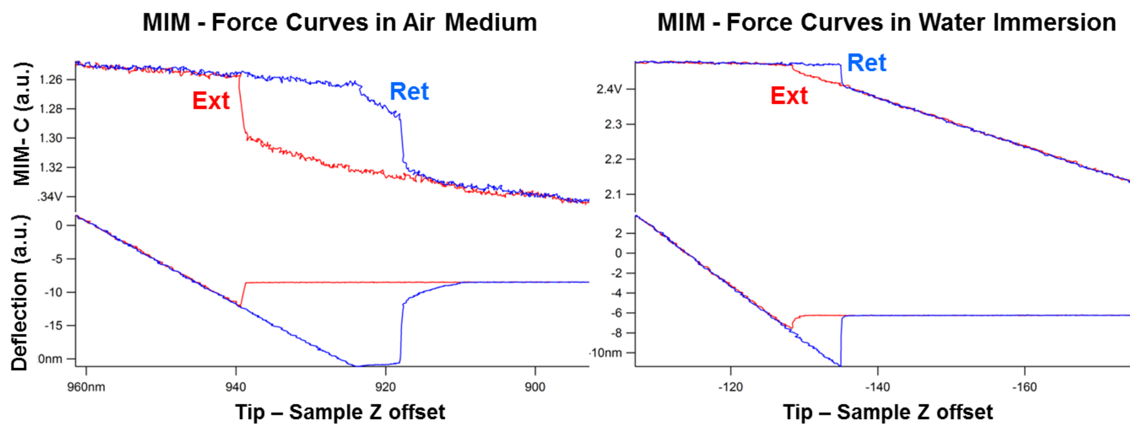

Figure 5.13: MIM – Force Curve capacitance (top) and deflection (bottom) data on doped silicon in ambient (left) and water immersion (right) experimental conditions.

When the snap discontinuity occurs, the change in the measured capacitance signal can be modeled as the difference between the tip capacitance using a water medium and an air medium plus a subtle change in the stray geometric capacitance from the change in tip-sample separation. The contribution of the geometric capacitance, dependent on the probe-sample geometry, to the observed signal can be measured and predicted. Since a force curve is acquired at every pixel point, the stray capacitance contribution can more normalized by subtracting the trends from the geometric capacitance data from the desired signal at every pixel point. This approach is effective for normalizing the background signal, making the observable contrast equal to the difference between measured capacitance before and after the jump discontinuity (equation 5.12). Using this method, we believe that the observable contrast is only sensitive to spatial changes in the quantum capacitance (equation 5.13).

$$C_{meas} = C_{tip}\left(\varepsilon_{tip}, z_{tip}\right) + C_{stray}\left(\varepsilon_{stray} = 1, z_{stray}\right) \qquad (5.9)$$

$$z_{tip} \rightarrow dz \approx 0 \,\{snap\} \qquad (5.10)$$

$$z_{stray} \rightarrow z_{stray} - \Delta z_{stray} \,\{snap\} \qquad (5.11)$$

$$\Delta C_{meas}\{snap\} = C_{tip}|^{water} - C_{tip}|^{air} + \Delta C_{stray} \qquad (5.12)$$

$$\Delta C_{meas}(x, y) = C_Q(x, y) + C_{stray}\{\text{constant}\} \qquad (5.13)$$

Figure 5.14 shows deflection and microwave reflectivity data from a single point on an MIM-FC map of a metallic single walled carbon nanotube. The tip movement during the force curve is illustrated in the figure 5.14a. Both the out-of-phase, capacitance (MIM-C), and the in-phase, surface conductivity (MIM-R), components of the microwave reflectivity signal is shown throughout the force curve period in figure 5.14b. The capacitance channel has a high SNR and flat signal response over the force curve period. Notice that the resistive channel is sensitive to a

slightly different electrical response, this will be analyzed in greater detail later in the chapter. A typical MIM-FC response of a metallic NT is shown in greater detail in figure 5.14c. The flatness of the stray capacitance response is due to the weak geometric coupling between the tip and the CNT-quartz sample geometry. The effects of quantum capacitance dominate between the Air-WM transition that occur during the snap discontinuities in the extension and retraction deflection data. During tip retraction, the capacitance response doesn't change until "snap-off", even though the tip is no longer in direct contact with the surface. This observation reaffirms the importance of the water meniscus dielectric medium to electrostatically couple the tip to the surface without the need of hard contact.

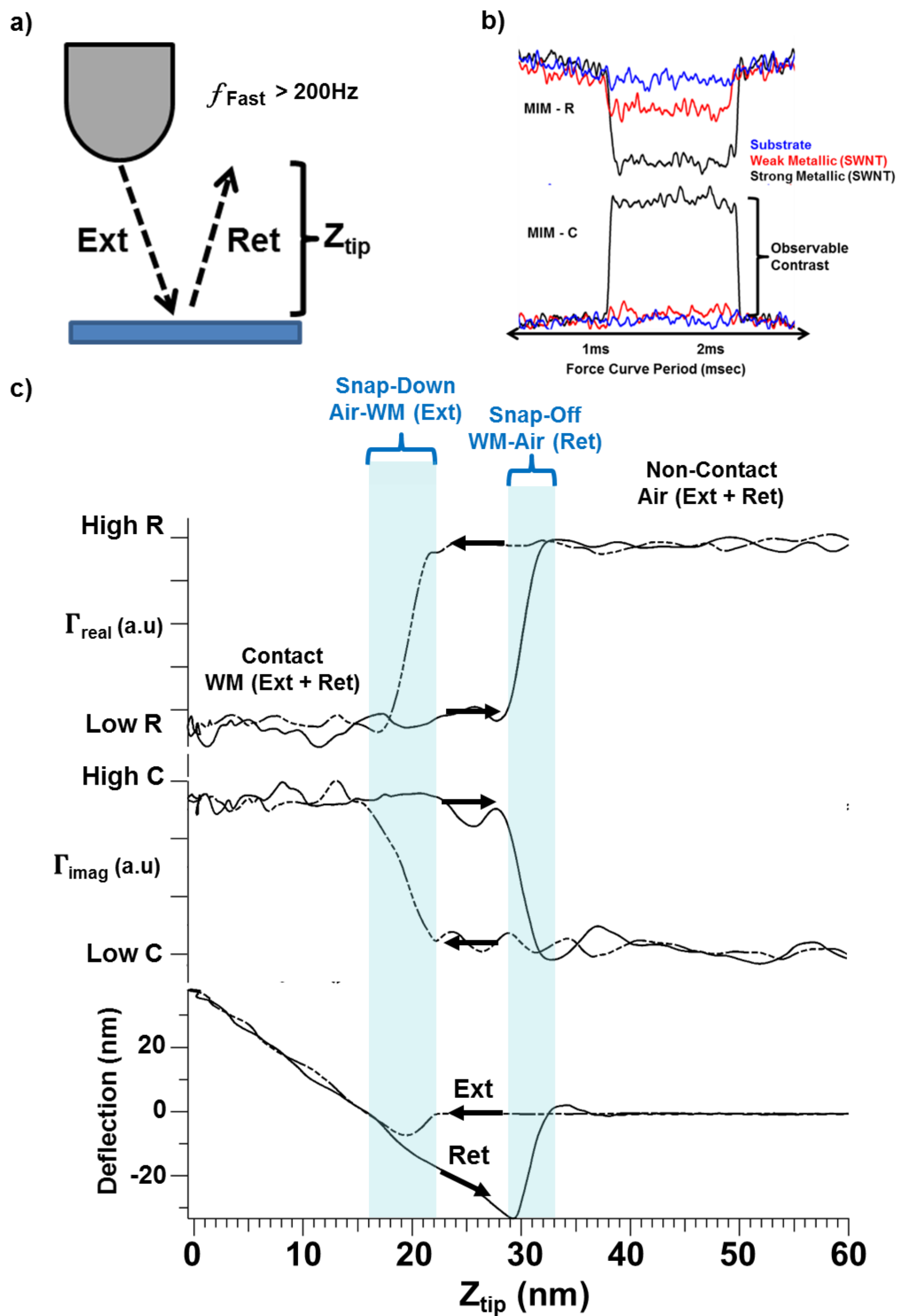

Figure 5.14: (a) A simple illustration of the tip movement during a force curve. (b) Typical MIM conductance (upper, MIM-R) and capacitance (lower, MIM-C) data from a single force curve on the substrate (blue), a weak metallic SWNT (red), and a strong metallic SWNT (blue). (c) A plot of the microwave reflection force curve response during the extension (Ext) and retraction (Ret) of the tip, the air-water meniscus transition is highlighted in blue.

The water meniscus layer thickness and the subsequent jump in tip-sample separation is correlated to the relative humidity. In literature, it was shown that lower humidity significantly lowers the magnitude of the jump discontinuity and the native water layer thickness [16,25]. Thus, ambient humidity is important experimental parameter for force curve mapping. Since the snap height of the jump discontinuity affects the measured capacitance data, large spatial variation in hydrophobicity and surface adhesion can create artifacts in the data. In tapping mode, it would make the most sense to operate with a higher humidity so that a higher, more stable, tapping amplitude can be used while remaining in the thicker native water layer. For force curves mapping keeping the ambient humidity low, $< 20\%$, minimizes the height of the snap discontinuity. This ensures that the measured capacitance is dominated by the change in medium's permittivity, rather than short-range forces, such as the capillary force, which affects to the stray geometric capacitance (equation 5.12). To achieve this experimental condition, we flowed N_2 gas through the AFM chamber, this stabilized the ambient conditions with less than 20% relative humidity.

The force curve mapping must be done quick enough to avoid drift and other imaging artifacts to create high quality MIM-AFM images. Temperature and humidity fluctuations are a primary contributor to noise when doing force curve mapping. Thermal drift not only causes the arbitrary MIM reflectivity signal to fluctuate, but also causes the piezo motor control to drift with time. As the ambient temperature fluctuates so does the local relative humidity which effects the snap down height. During long scan times, these fluctuations compile which negatively impacts image quality and resolution. These effects can be mitigated in the short term, < 1 hour, by flowing dry N_2 gas in the AFM chamber. However, each force curve must move slow enough to maintain a high degree of separation control and data averaging. If the force curve map takes a

few tenths of a second to record a force curve, then a high-resolution image (256 x 256 pixel) will take several hours to complete, which leads to major issues with image quality. The tradeoff is to operate with a lower pixel density and smaller images to lower the scan time, the results of this approach on a CNT sample, ~95% metallic NT segments on quartz, is shown in figure 5.15. Notice that the true resolution of the technique cannot be realized using slow force curves. To overcome this issue, we utilized a newly developed scan probe technique capable of acquiring force curves with at a much faster rate. Asylum Instruments Cypher AFM can be equipped with Fast Force Curve mapping, capable of mapping at speeds >200Hz; MIM-FFC enables the acquisition of high resolution capacitance maps in a reasonable time.

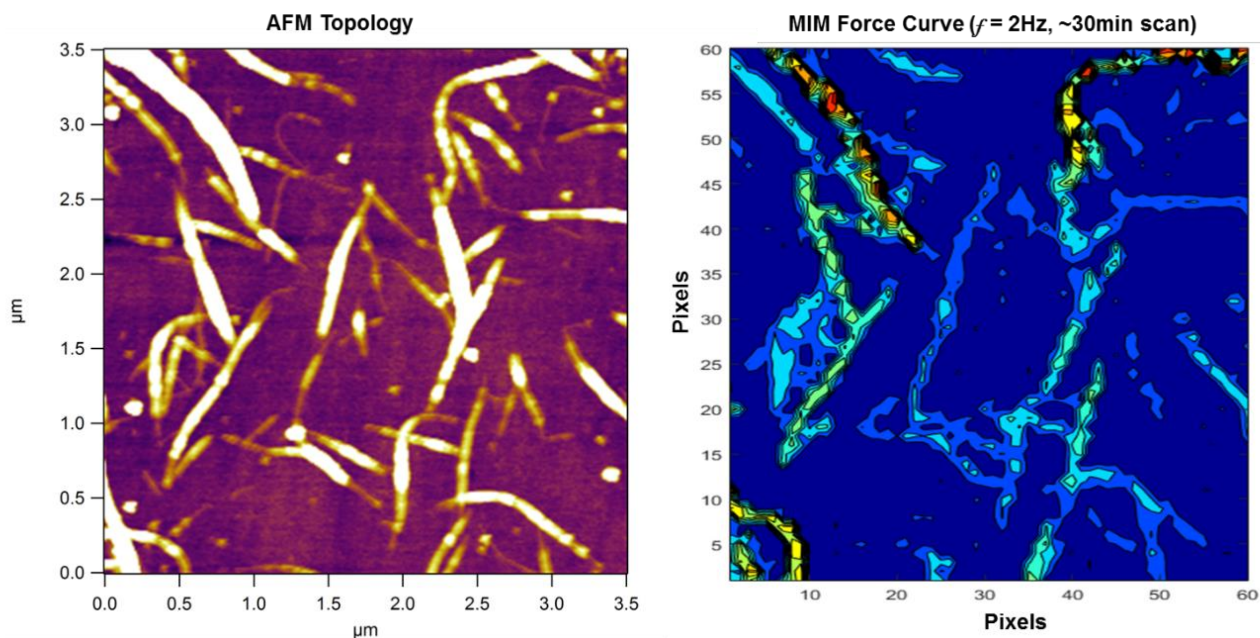

Figure 5.15: AFM topology image (left), 256 x 256 pixel, and MIM force curve map (right), 60 x 60 pixel, on a ~95% metallic CNT sample at low pixel density.

A proof of concept experiment was performed on aligned CNTs to ensure that the MIM-FFC response is accurate and consistent. We preformed MIM-FFC capacitance mapping on a bare aligned CNT array, after which the sample was coated with a 3.5nm layer of alumina and

characterized using contact mode MIM-AFM. The capacitance response of the nanotube array agrees for both characterization methods. This implies that MIM-FFC can accurately and consistently measure the electronic properties of individual CNTs. The advantage of MIM-FFC for mapping quantum capacitance on CNTs is very evident from the images presented in figure 5.16. There is a clear improvement in the SNR and resolution of the capacitance signal and a noticeable increase in sensitivity to quantum capacitance. The enhanced resolution of the MIM-FFC is limited by the width of the water meniscus, where quantum capacitance is strongly coupled, instead of the full width of the tip apex. We believe that these improvements are attributed to the very high dielectric constant of water, which significantly suppresses the contribution of geometric tip-nanotube capacitance while maximizing the overall capacitance coupling to the tip apex where the water meniscus formed.

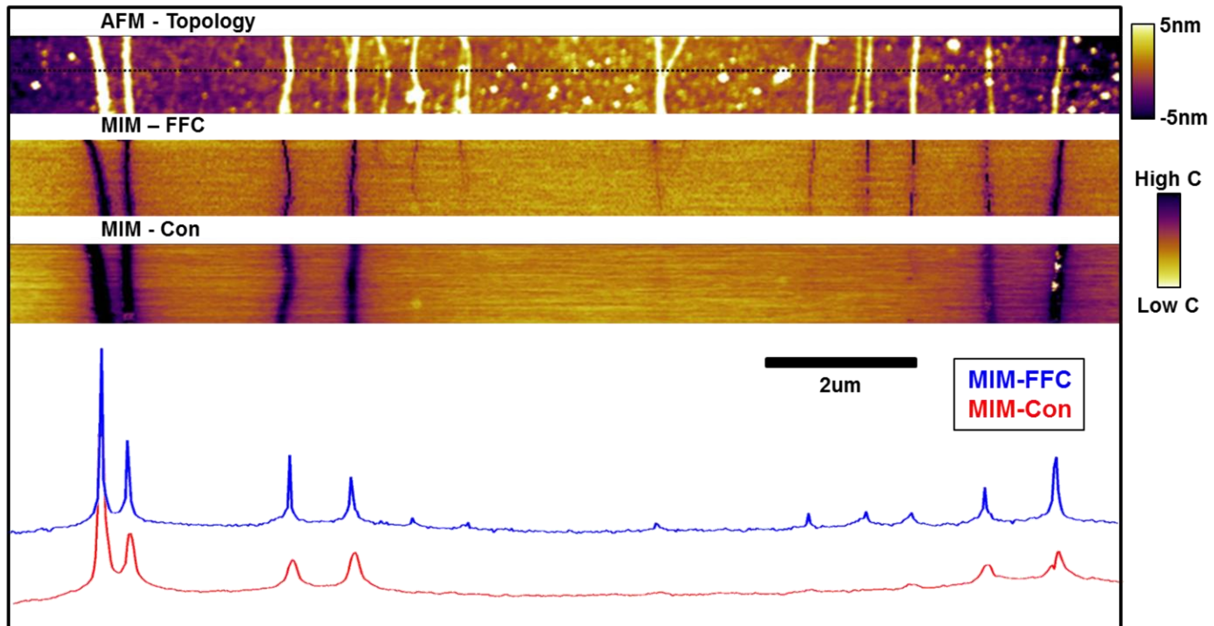

Figure 5.16: Direct comparison of the AFM topology (top), MIM – Fast Force Curve (middle), and MIM – Contact Mode images. The lower part shows MIM-FFC (blue) and MIM-Contact (red) linecuts aligned to the horizontal black line in the AFM image.

Short Carbon Nanotube segments, used in ultra-centrifuge purification, have been particularly difficult to characterize with contact mode MIM-AFM due to the limitations imposed by the metal oxide layer deposition. The immediate impact of MIM-FFC on the characterization of CNT segments can be seen in figure 5.17. The AFM topology, force curve adhesion, and MIM-FFC capacitance and conductance maps of an as-deposited (95%) metallic NT segment sample is shown for direct comparison. The adhesion, which is strongly correlated to the separation height at the snap discontinuity, and the topology data shows no apparent cross talk with the measured MIM-FFC data. Almost all the observable metallic seeds in the AFM topology data show contrast in the capacitance data as expected, however, the nature of the contrast is notably different in the conductance data. For contact mode MIM mapping of CNTs, the real part of the microwave reflectivity has a lower SNR compared to the imaginary reflectivity because of the insulating metal oxide layer. In this case of force curve mapping, the water meniscus doesn't behave like an insulating barrier, rather it creates a conduction path allowing the tip to directly interact with nanotube. This presents an opportunity to simultaneously acquire high quality capacitance and conductivity maps of as-grown CNTs.

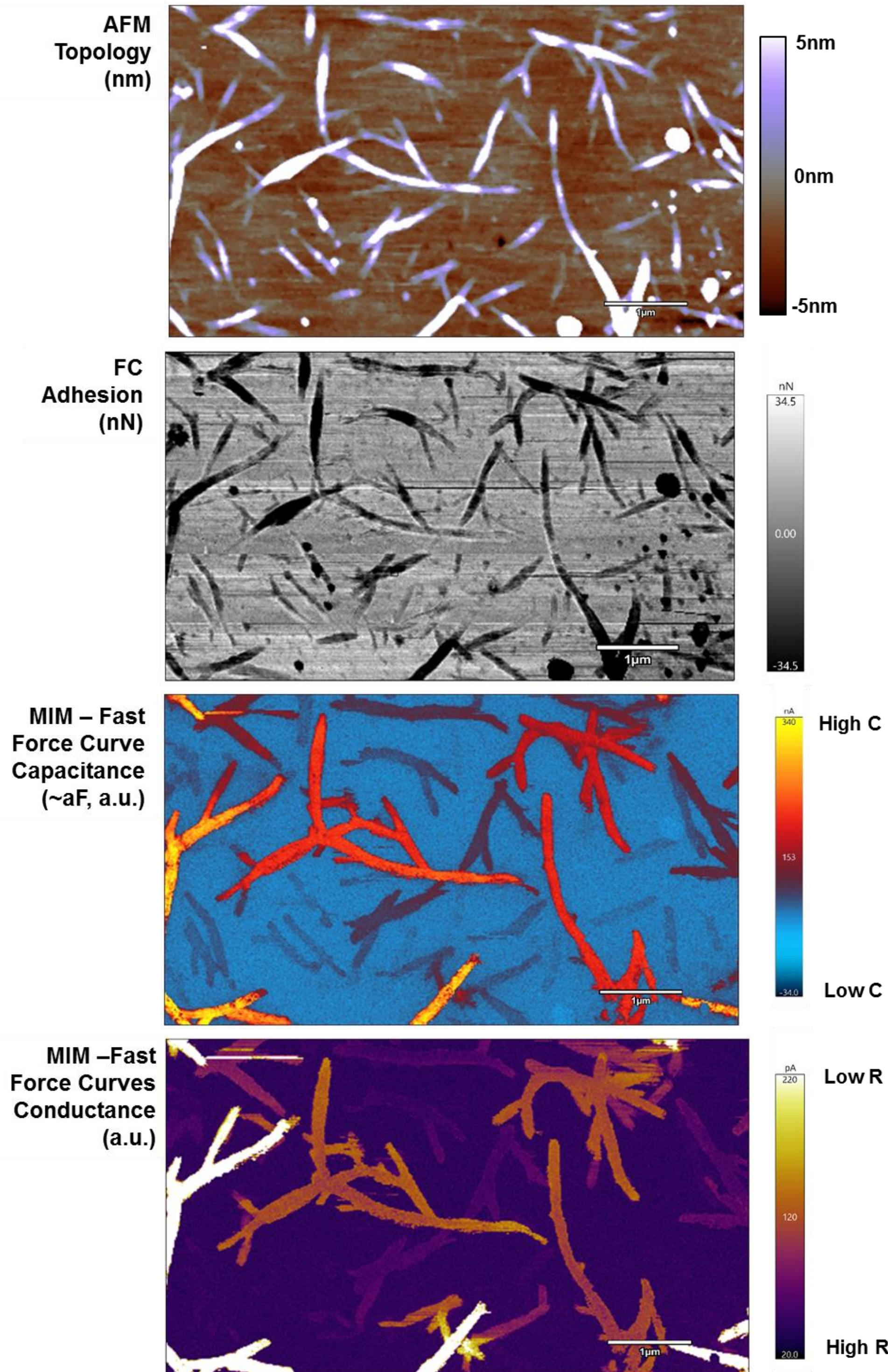

Figure 5.17: Images of CNT sample, made of ~95% metallic NT segments deposited on quartz, spatially mapped with AFM topology (upper-left), FC adhesion (upper-right), MIM-FFC capacitance (lower-left) and resistance (lower-right) data.

The conductance part of the measured data originates from the real part of the reflectivity and is sensitive to the microwave power leakage out of the tip. The microwave power leakage is close to zero if there is no path to ground, however, microwaves will propagate and radiate along metal transmission lines depending on their effective open circuit impedance. Power transfer from a resistive source to an open-circuit load is govern by equation 5.14 [26].

$$P_{load} = V_{OC}^2 \frac{R_{load}}{(R_{load}+R_{source})^2} \qquad (5.14)$$

When directly coupled to a microwave source, such as the coaxial tip, carbon nanotubes can act as low efficiency antennas that have a higher resistive impedance with increasing length [27,28]. As the impedance of the CNT transmission line impedance increases with nanotube length, the power transfer to the CNT load is improved according to equation 5.15.

$$if\ R_{tip} = R_{source} \gg R_{CNT} = R_{load} \rightarrow P_{load} \sim R_{CNT}(L_{CNT}) \qquad (5.15)$$

We believe that the short metallic NT segments can couple to each other creating long networks which behave like open circuit transmission lines, in which case, all the segments with a network will collectively interact with the tip. The conductance channel is influenced by long range coupling through conduction paths in the CNT network. In contrast, the capacitance channel is most sensitive to localize quantum capacitance coupling through the water meniscus under the tip apex. In figure 5.18, the conductance map for a metal CNT seed network is shown as a color map overlaid on a 3D topology map. The colormap is made with narrow data bins to show distinct signal levels in the MIM conductance data. Notice that the background signal near NT segment is more uniform, with a sharper substrate-nanotube contrast, in the resistive signal than the capacitance signal. Despite the improved background capacitance signal when using MIM-FFC, longer range capacitance coupling to nearby NTs can still make the local background signal appear falsely high. We hypothesize that strong contrast in the MIM-R maps requires the

tip to be in direct contact with a dissipative load such as a CNT segment or NT network. This explains why we observe a sharper contrast and more uniform substrate response in MIM-R maps compared to MIM-C maps. We also noticed that the signal is unusually uniform on segments within the same NT network. Standalone, short single walled NT segments, identified by white arrows, don't show any contrast in MIM-R, despite showing distinct contrast in the MIM-C map. Whereas, the NT seeds in the most expansive CNT network shows a large uniform contrast in the MIM-R map regardless of their length, diameter, or MIM-C response. It appears that the MIM-R signal is sensitive to the collective interaction of a NT segments within a network, which supports our hypothesis. There are many examples seen in figures 5.17 and 5.18 where there is a distinct difference between a NT segment's signal response in the MIM-R and MIM-C data maps, which are recorded independently of each other. This unique sensitivity may have potential applications for mapping conduction paths in nanoscale materials and should be explore in greater detail for future work.

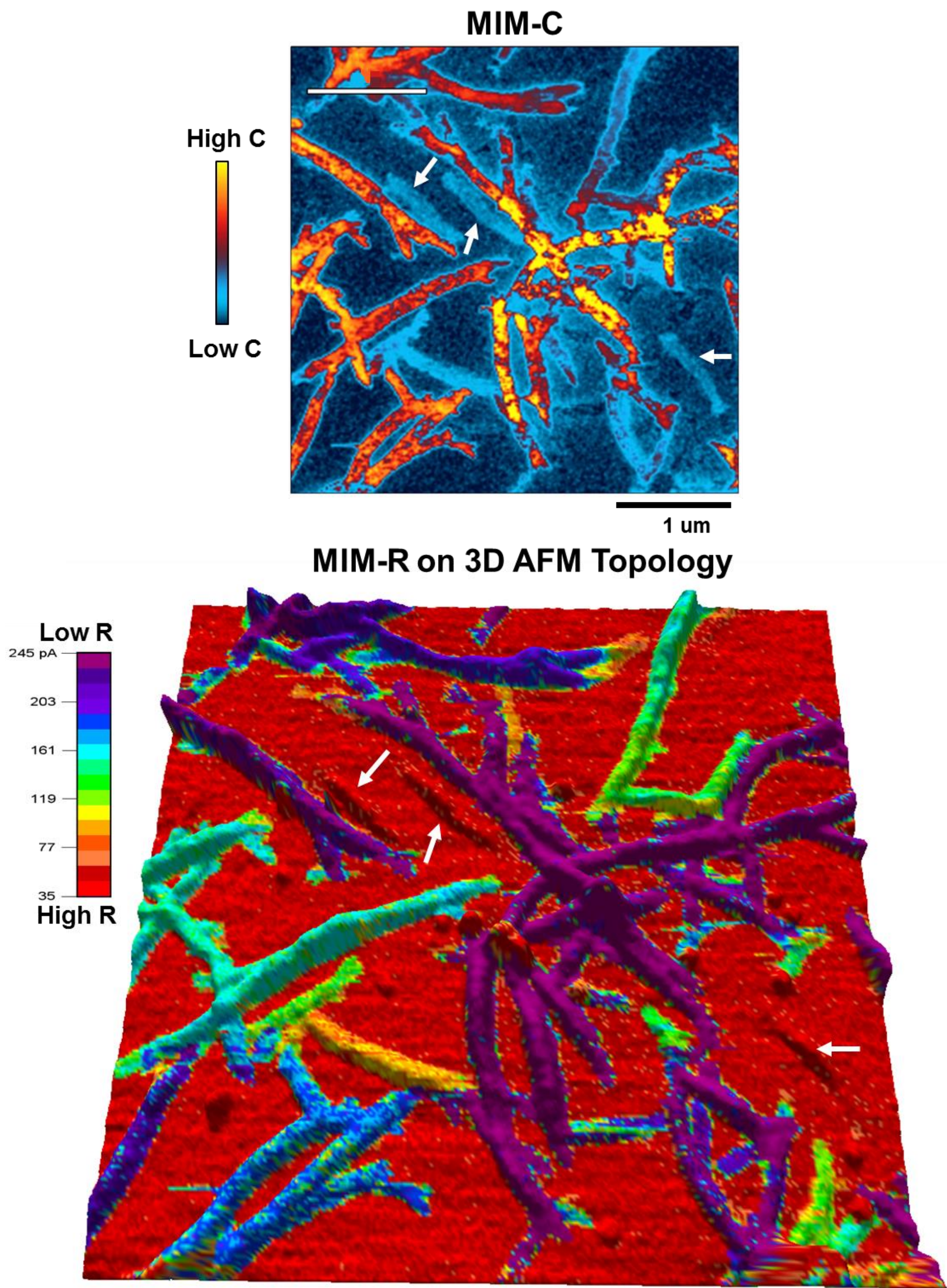

Figure 5.18: MIM conductance data color-mapped onto a 3-dimensional topology contour. The 2-dimension MIM capacitance map is shown in the upper left. White arrows are used to identify some ultra-short SWNT segments that show conflicting contrast in MIM-R and MIM-C.

5.4 Conclusion

There are several takeaways from this work that provides insight on how to map the quantum capacitance of CNTs *via* MIM-AFM at a high resolution with any sample preparation. We know that controlled the permittivity of the dielectric medium between tip and sample is essential to maximize the sensitivity and SNR. Here we prove that the native water layer from ambient humidity, is an ideal dielectric medium since it's a naturally occurring conformal thin layer with a high permittivity. Contact mode MIM of CNTs using a thin metal oxide layer is a reliable but limited MIM-AFM methodology, mostly due to the metal oxide deposition which can add contaminates that ruin image quality and prevents further device processing after characterization. It was shown that low amplitude tapping MIM-AFM has promise for high SNR capacitance mapping, but is limited by instabilities in the tapping dynamics. We can map the differential capacitance during tapping MIM using a lock-in amplifier providing insight into how the tapping mode cantilever dynamics affects the measured capacitance. We show that differential capacitance mapping is suffers sensitivity topology which appear as image artifacts. MIM-FFCs clearly showed the most potential for obtaining high quality MIM images of CNTs without any sample prep, making the technique 100% clean in ambient conditions. From the MIM-FFC data, we provide direct evidence of the important role that the water meniscus plays in measuring quantum capacitance. Humidity control, tip quality, and sample cleanliness have a large impact on the SNR of MIM-FFC capacitance and conductance maps. Under ideal operating conditions, the newly developed Fast Force Curve mapping, capable of >200Hz force curve acquisition, can provide the best SNR, highest resolution, least tip ware, and great suppression of stray capacitance and drift compared to both contact mode and tapping mode operation. In addition, MIM-FFC has the advantage of directly coupling to the sample surface which

maximizes it's the sensitivity to the real part of the microwave reflectivity, enabling the acquisition of high quality MIM conductivity maps. We show that the MIM-FFC technique can measure the topology, capacitance, and conductance simultaneously with high sensitivity and a stable background signal without the need for sample preparation, making it a very promising method for CNT metrology and electronic property mapping at the nanoscale.

5.5 Methods

Carbon Nanotube Segments

The segment samples that were used in this work were purchased from NanoIntegris Inc. The segments purified using an ultra-centrifuge separation which produced highly enriched segments of mostly one electronic type and narrow diameter distribution. NanoIntegris uses Raman Spectroscopy on aqueous samples to estimate an average purity for the segment samples. The samples were obtained with the carbon nanotubes already dissolved in the surfactant solution. We used a pipet to put 1-2 drops of the solution on a clean quartz substrate. The sample was then dried until the liquid surfactant was gone. The residue from the surfactant was then rinse off using warm water then baked on a hot plate for several minutes at 180°C to drive off additional water and surfactants.

Tapping Mode Operation Considerations

The stability of the tapping dynamics can be directly measured using a lock-in amplifier to detect the deflection signal in during a tapping scan. The lock-in amplifier detects dC/dZ which is sensitive to the stray capacitance since it's a function of z (tip-surface separation). The presence of the stray capacitance background isn't a strong noise source if it stable and doesn't

change spatially. Figure 5.19 shows a spectrograph of the deflection and capacitance signal for both hard tapping (repulsive) and light tapping (attractive) operation. The noise floor of the stray capacitance at low frequencies is much higher and the resonant capacitance frequency is shifted for the hard tapping case, which coincides with a noise in the deflection spectra. Based on our results, we believe tapping mode scanning at very low tip separation in an attractive force regime is beneficial for minimizing the geometric noise coupling, despite being an unstable tapping operation.

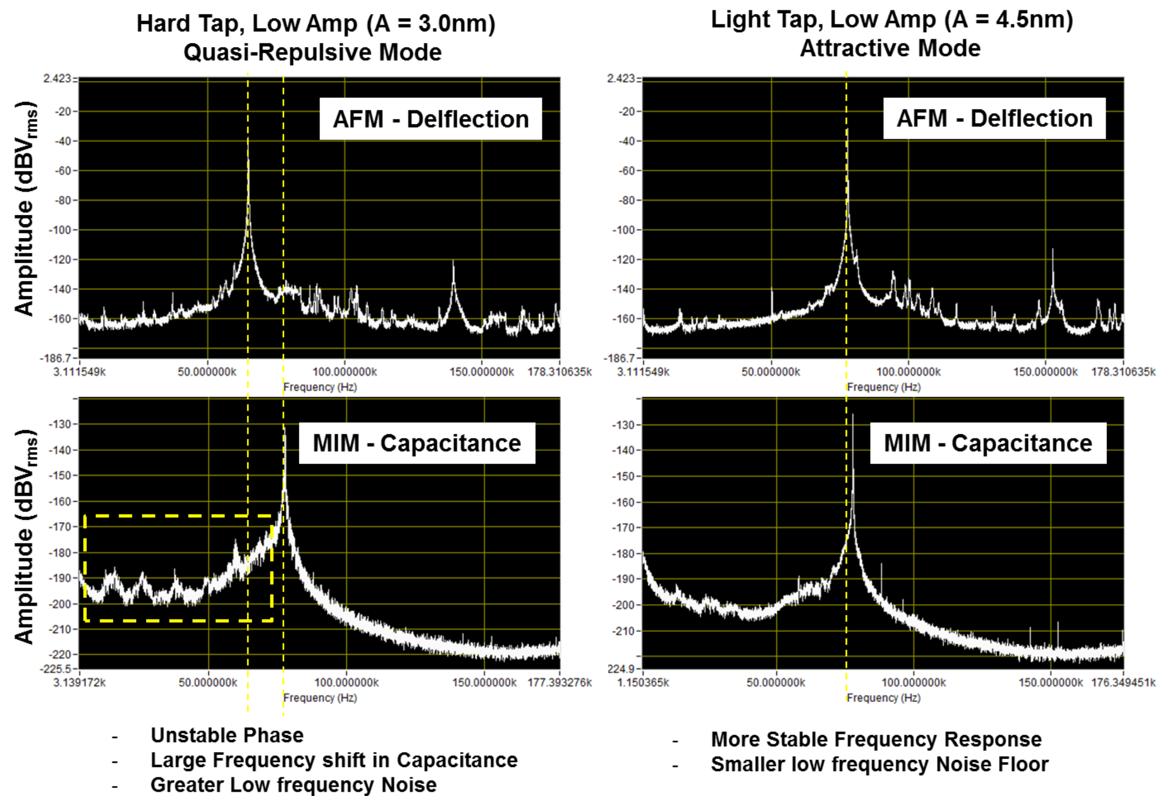

Figure 5.19: Spectrograph of the deflection (top) and MIM capacitance lock-in signal (bottom) from 3kHz to 177kHz during a low amplitude scan on Al_2O_3, in the repulsive (left) and attractive (right) tapping regime. The instabilities and noise in the signal are highlighted using yellow markers.

Force Curve Operation Considerations

The formation of the water meniscus is nearly instantaneous and nonlinear, it can cause snap downs to occur after the initial jump discontinuity and/or non-ideal meniscus shapes. Also, other forces can affect the tip movement and capacitance coupling in ways that are difficult to model or predict. If the tip is pressed hard, when in direct contact, the tip undergoes some elastic deformation, which may also cause the shape of the water meniscus to change in unexpected ways. Any combination of these effects can greatly diminish the reliability of the measured capacitance and force data. Examples of unusable MIM-FFC data is shown in figure 5.20, notice that the jumps in capacitance don't necessarily coincide with the "snap-down" effect. This has been shown to cause false positives in CNT identification data as shown in figure 5.21. We believe the cause of these false positives is related the adhesion forces irregular discontinuities in the signal. Some experimentally methods to mitigate issues with irregular jumps discontinuities is using a smaller diameter tip which has less surface adhesion implying a smaller jump discontinuity, pressing with low force when in full contact, and operating on a clean sample. Another approach is to create an algorithm to filter the force data so that it only plots the capacitance jumps that coincide with the formation of water meniscus under the tip, denoted by the initial "snap" discontinuity.

Bad Force Curves → False Positives

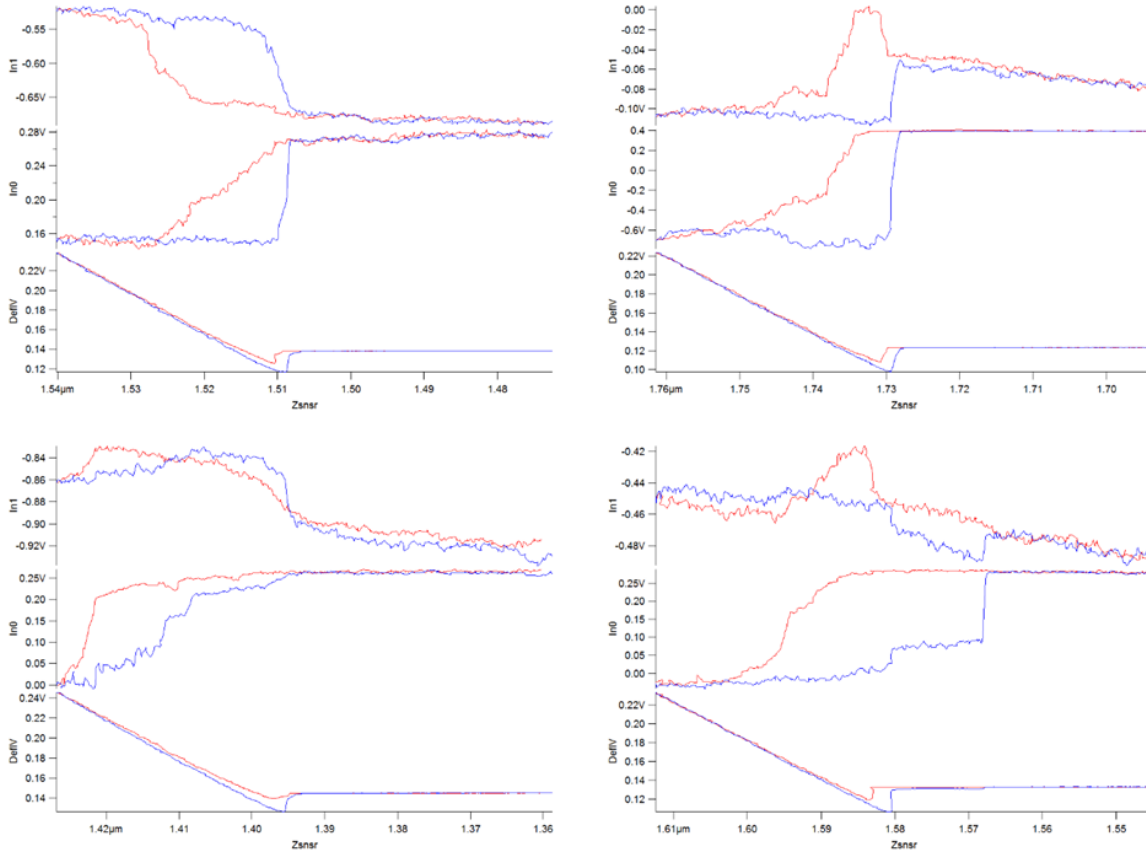

Okay Force Curves

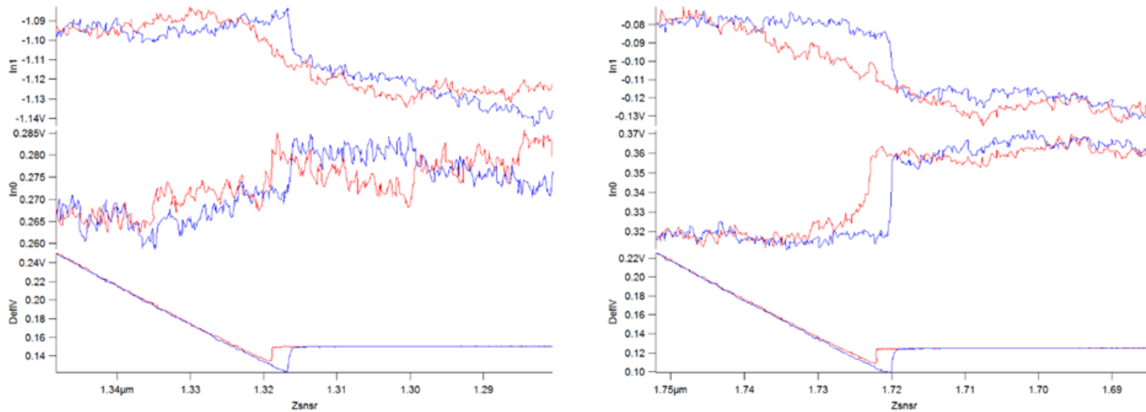

Figure 5.20: Force Curve data plots of MIM-C (top), MIM-R (middle), and tip-cantilever deflection (bottom) as a function of tip-sample separation (x-axis). Examples of unusable and okay force curve data are labeled.

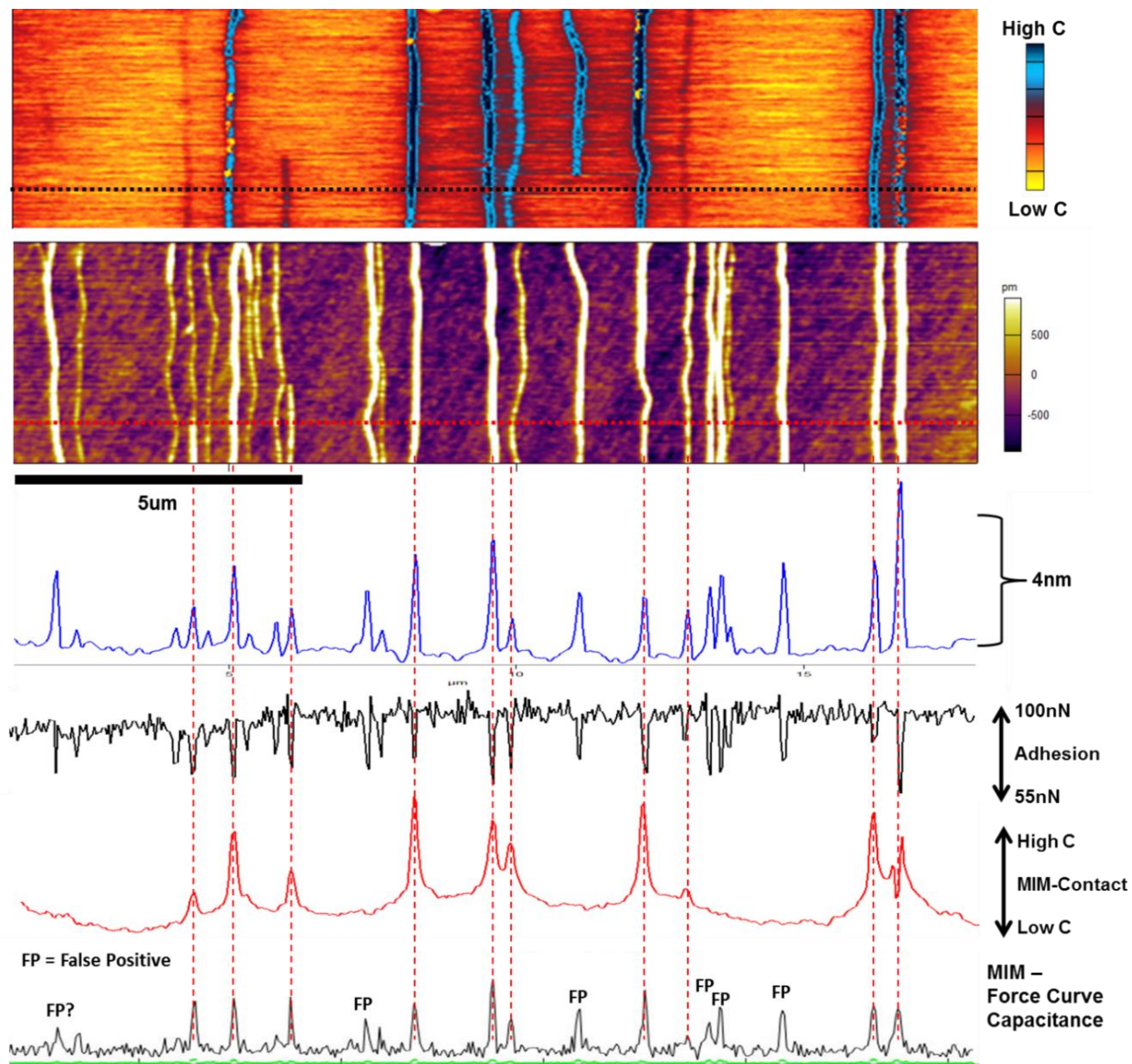

Figure 5.21: The images are a direct comparison of MIM-contact mode capacitance (upper) and AFM topology (lower) maps on aligned CNTs. The lower data set are linecuts of the topology, adhesion, MIM-contact, and MIM-FC data aligned to the horizontal line in the images. The metallic nanotubes are labeled by vertical red lines and the MIM-FC false positives are identified with a "FP" label.

Theory and MATLAB Simulation of Measured Force Curve Capacitance

First, we define our constants for the physical model; the permittivity of free space, ε_p, and the dielectric constant for water, $\varepsilon_{wat} = 80$, and air, $\varepsilon_{air} = 1$. The geometric capacitance is a function of the dielectric constant and the tip geometry describe by the width of the apex, R = 250nm, and pitch of the cone, $X=45^o$. The geometric capacitance is plotted as a function of tip-

sample separation, H, where the snap down occurs at $H = H_{wat}$. Once the snap discontinuity occurs, the tip sample separation is such that $H \rightarrow T_{wat} \approx 2nm$, the thickness of the water meniscus layer under the tip in the attractive regime. The functions for the geometric capacitance with both water and air mediums are shown below:

$$C_{air} = 2\varepsilon_{air}\varepsilon_p * \ln\left(1 + \frac{R}{H}(1 - \sin(X))\right) \quad (5.16)$$

$$C_{wat} = 2\varepsilon_{wat}\varepsilon_p * \ln\left(1 + \frac{R}{T_{wat}}(1 - \sin(X))\right) \quad (5.17)$$

The geometric and quantum capacitance form the measured capacitance, C_{meas}, according to the equations below. The estimated quantum capacitance of a metallic NT, C_q = 0.01*1e-18 (~aF), is used to show how the contribution of the geometric capacitance affects C_{meas} as a function of with tip separation, H.

$$if\ H > H_{wat}:\ \ C_{meas} = \frac{1}{C_{air}(H)^{-1} + C_q^{-1}} \quad (5.18)$$

$$if\ H \leq H_{wat}:\ \ C_{meas} = \frac{1}{C_{wat}^{-1} + C_q^{-1}} \quad (5.19)$$

5.6 References

1 Refer to Chapter 4 for more information

2 Estevez, Ivan, et al. "Specific methodology for capacitance imaging by atomic force microscopy: A breakthrough towards an elimination of parasitic effects." Applied Physics Letters 104.8 (2014): 083108.

3 Fumagalli, L., et al. "Nanoscale capacitance imaging with attofarad resolution using ac current sensing atomic force microscopy." Nanotechnology 17.18 (2006): 4581.

4 Oliver, Rachel A. "Advances in AFM for the electrical characterization of semiconductors." Reports on Progress in Physics 71.7 (2008): 076501.

5 Karbassi, A., et al. "Quantitative scanning near-field microwave microscopy for thin film dielectric constant measurement." Review of scientific instruments 79.9 (2008): 094706.

6 Hudlet, S., et al. "Evaluation of the capacitive force between an atomic force microscopy tip and a metallic surface." The European Physical Journal B-Condensed Matter and Complex Systems 2.1 (1998): 5-10.

7 Seabron, Eric, et al. "Scanning probe microwave reflectivity of aligned single-walled carbon nanotubes: Imaging of electronic structure and quantum behavior at the nanoscale." ACS nano 10.1 (2015): 360-368.

8 Wang, Xinran, Scott M. Tabakman, and Hongjie Dai. "Atomic layer deposition of metal oxides on pristine and functionalized graphene." Journal of the American Chemical Society 130.26 (2008): 8152-8153.

9 Oh, Il-Kwon, et al. "Nucleation and growth of the HfO2 dielectric layer for graphene-based devices." Chemistry of Materials 27.17 (2015): 5868-5877.

10 Han, Wei-Qiang, and A. Zettl. "Coating single-walled carbon nanotubes with tin oxide." Nano Letters 3.5 (2003): 681-683.

11 Gavrilov, Sergei Aleksandrovich, et al. "Ultrathin Metal Oxides Layer on A Carbon Nanotube Oriented Arrays Surface Formation Process Development and Study for Supercapacitors Electrode Specific Capacity Increasing." Biomedical and Pharmacology Journal 8.2 (2015): 731-739.

12 Tanaka, Takeshi, et al. "Simple and scalable gel-based separation of metallic and semiconducting carbon nanotubes." Nano Letters 9.4 (2009): 1497-1500.

13 Dresselhaus, Mildred S., et al. "Perspectives on carbon nanotubes and graphene Raman spectroscopy." Nano letters 10.3 (2010): 751-758.

14 Van Honschoten, Joost W., Nataliya Brunets, and Niels R. Tas. "Capillarity at the nanoscale." Chemical Society Reviews 39.3 (2010): 1096-1114

15 Zitzler, Lothar, Stephan Herminghaus, and Frieder Mugele. "Capillary forces in tapping mode atomic force microscopy." Physical Review B 66.15 (2002): 155436.

16 Rozhok, Sergey, et al. "AFM study of water meniscus formation between an AFM tip and NaCl substrate." The Journal of Physical Chemistry B 108.23 (2004): 7814-7819.

17 Santos, Sergio, and Albert Verdaguer. "Imaging Water Thin Films in Ambient Conditions Using Atomic Force Microscopy." Materials 9.3 (2016): 182.

18 Sarioglu, Ali Fatih, and Olav Solgaard. "Time-resolved tapping-mode atomic force microscopy." Scanning Probe Microscopy in Nanoscience and Nanotechnology, 2 (2011): Chapter 1: 3-37.

19 Hoffmann, Peter M., et al. "Direct measurement of interatomic force gradients using an ultra-low-amplitude atomic force microscope." Proceedings of the Royal Society of London A: Mathematical, Physical and Engineering Sciences. Vol. 457. No. 2009. The Royal Society, 2001.

20 Chen, Liwei, Xuechun Yu, and Dan Wang. "Cantilever dynamics and quality factor control in AC mode AFM height measurements." Ultramicroscopy107.4 (2007): 275-280.

21 Crittenden, S., Arvind Raman, and R. Reifenberger. "Probing attractive forces at the nanoscale using higher-harmonic dynamic force microscopy." Physical Review B 72.23 (2005): 235422.

22 Lai, Chia-Yun, Sergio Santos, and Matteo Chiesa. "Systematic multidimensional quantification of nanoscale systems from bimodal atomic force microscopy data." ACS nano 10.6 (2016): 6265-6272.

23 Garcia, Ricardo, and Alvaro San Paulo. "Attractive and repulsive tip-sample interaction regimes in tapping-mode atomic force microscopy." Physical Review B 60.7 (1999): 4961.

24 Cappella, Brunero, and Giovanni Dietler. "Force-distance curves by atomic force microscopy." Surface science reports 34.1-3 (1999): 15-3104.

25 Yang, Liu, et al. "Nanoscopic characterization of the water vapor-salt interfacial layer reveals a unique biphasic adsorption process." Scientific Reports 6 (2016).

26 McLaughlin, James C., and Kenneth L. Kaiser. "" Deglorifying" the maximum power transfer theorem and factors in impedance selection." IEEE Transactions on Education 50.3 (2007): 251-255.

27 Hanson, George W. "Fundamental transmitting properties of carbon nanotube antennas." IEEE Transactions on antennas and propagation 53.11 (2005): 3426-3435.

28 Burke, Peter J., Shengdong Li, and Zhen Yu. "Quantitative theory of nanowire and nanotube antenna performance." IEEE transactions on nanotechnology 5.4 (2006): 314-334.

CHAPTER 6

SUMMARY AND FUTURE WORK

6.1 Summary of Work

From this work, we show the significance of scan probe based electronic characterization to better understand nanoscale electronic materials for next generation transistors. We used atomic force microscopy to detect morphological phenomena such as grain boundaries in MoS2, corrugations in GaAs nanowires, and the diameter distribution of Carbon Nanotubes. For the GaAs nanowires and Carbon Nanotubes electronic and topology maps were acquired simultaneously to reveal detailed structurally dependent electrical phenomenon. Both GaAs nanowires and Carbon nanotubes are leading candidates for semiconductors in next generation transistors, which is the motivation behind exploring electrical characterization techniques capable of nanoscale resolution.

To better understand the morphologically driven defects along the GaAs nanowire, we sought to map the dopant distribution in the corrugated regions. First, we characterized the morphology using electron microscopy to obtain high resolution images of the poorly understood regions. Microwave impedance microscopy (MIM) and tip voltage modulated MIM was used to directly map the free carrier distribution and the doping distribution respectively. We also used Infrared Scanning Near-field Optical Microscopy (SNOM-IR) to directly map the free carrier distribution, which agreed with our MIM results. Dual-Pass Electrical Force Microscopy was used as a non-contact control image to further validate our observations by ensuring that the topology signal had no significant contribution to the observed contrast. The image results depict a non-uniform doping distribution composed of repeated areas of high and low dopant impurity

concentration in the corrugated region of the nanowire. Our hypothesis and observations agrees with Density Function Theory calculations. This was used to create a physical model for the spatial band dispersion along the nanowire growth axis. The complementary information provided by these electrical scan probe techniques and the physical model provide valuable insight into in situ impurity incorporation during the Vapor-Liquid-Solid epitaxial growth of nanowires, during the MOCVD process.

For Carbon Nanotubes, a major barrier for transistor device applications is the difficulty to create quality (few defects), high purity (>99% semiconducting), uniform arrays of nanotubes. In this work, we showed the effectiveness of thermocapillary purification and introduced some approaches for achieving carbon nanotube arrays suitable for devices. Measuring and optimizing the quality of CNT arrays at an industrial scale requires a metrology technique capable of identifying a carbon nanotube's electronic character (semiconducting, semi-metallic, or metallic) at the nanoscale. Hence, a major focus for this work is the development of novel methods to map the properties of an individual nanotube in an array. We believe that the electronic character of a carbon nanotube can be revealed by measuring the nanotube's quantum capacitance, which is a directly related to the density of states. We present theoretical and experimental evidence that maximizing the permittivity of the dielectric medium between the tip and carbon nanotube sample is essential for optimal sensitivity to quantum capacitance. For the purposes of exploring interesting nanoscale phenomena, a thin metal oxide layer such as MgO or Al_2O_3 can be used. We showed that Microwave Impedance Microscopy, under the ideal experimental conditions, can spatially map the quantum capacitance of the nanotube revealing their electronic character with high resolution. With the thin metal oxide coating on the nanotubes, a tip voltage modulation can be used to map band dispersion with MIM. The sweeping the voltage shifts the

local fermi energy level revealing information correlated the nanotubes 1-dimensional density of states. By fixing the modulated voltage amplitude, 2D spatial mapping reveals areas of band-bending near intratubular heterojunctions and metal interfaces. We believe this may be experimental evidence of long-range electron-electron screening in a 1-dimensionally quantum confined material.

For industrial processes, the deposition of a metal oxide layer on the CNTs has some limitations. To resolve the issues related to metal oxide deposition, we proposed using the native water layer that exist on surfaces in ambient humidity conditions as the high permittivity dielectric medium. The native water layer has a high dielectric constant, it naturally occurs as a thin film, and is 100% clean implying that no special sample preparation is needed. The tip must be close enough to the sample that a water meniscus forms between the sample surface and tip apex. We explored two experimental geometries to control the tip's interaction with the native water layer: tapping AFM and force curve mapping. Low amplitude tapping MIM-AFM can produce quality images when operating in the attractive force regime, but instabilities in the bending dynamics during tapping make it difficult to maintain a good signal to noise ratio. We measured the differential capacitance signal using lock-in tapping MIM-AFM. Although we observed contrast similar to low amplitude tapping MIM-AFM, there were clear indications of cross-talk between the tapping phase/amplitude and the observed MIM signal. Finally, Force Curve MIM was shown to have all the benefits of intermittent contact like tapping MIM, but in a much more controlled way. We found that the formation of the water meniscus, noted by a sudden change in cantilever deflection, coincides perfectly with a change in observed capacitance which supports our hypothesis regarding the importance of the dielectric medium. We utilized a high speed experimental setup denoted as Fast Force Curve MIM to improve the

sensitivity and resolution capacitance map. We verified that MIM-FFC is capable of producing images of similar or higher quality than MIM using a metal oxide layer, by doing a direct comparison images taken on the same sample using the same tip. We also show that MIM-FFC enables the measurement of the resistive part of the microwave reflectivity with high SNR, which would be limited by an insulating metal oxide layer. Here we successfully present MIM-FFC as a promising, completely non-destructive, CNT metrology technique that is compatible with an industrial laboratory setting.

6.2 Future Work

Microwave Impedance Microscopy is a great compliment to other characterization techniques in an industrial laboratory setting. For example, the use of MIM-FFC on carbon nanotubes shows how imaging can be done on as-grown samples without special sample preparation. MIM doesn’t require a conduction path or ground plane, making it more versatile than other capacitance and conductance scan probe techniques. Our work has made great strides toward understanding the experimental geometries needed to obtain high quality MIM data. However, before wide spread industrial applications can be realized there are some experimental issues that need to be mitigated.

First, there needs to be improvement in MIM probe reliability and resolution. The tips work using an RF coaxial that is connected to the probe’s conductive cantilever. The probe is shielded all the way to the tip to achieve optimum sensitivity to the surface. Creating these tips is a long, complicated process with lots of opportunity for error. Even small defects such as bubbles in the shielding layer or residue on the probe contact pad can cause parasitic capacitances along the RF pathway, which diminishes the SNR. We found that the current

process used by manufactures can create a large distribution in tip quality on a wafer. This is a problem when comparing data sets taken from different tips, since the SNR of the data can vary greatly from tip to tip. As mentioned in Appendix B, one can improve the SNR by dull the tip to create a broader tip apex at the expense of resolution. We found that Fast Force Curve MIM operation has the benefit of less tip ware and improved SNR, which mitigates some of these issues. However, to fully achieve industrial level reliability and precision, the process to make MIM probes must be improved to create sharper tips with more reliable quality.

In most applications MIM can only produce qualitative maps for capacitance and conductance contrast. Researchers have been working towards making MIM a quantitative technique capable of providing information regarding the material's specific dielectric constant, free carrier concentration, and dopant impurity levels. The primary limitation towards achieving quantitative results is the arbitrarily varying background signal and constantly changing tip geometry. Fast Force Curve MIM is a major step towards mitigating those issues by normalizing the background signal at every pixel point and minimizing tip ware. However, water meniscus layer, which is essential for MIM-FFC, is affected by the local humidity and hydrophobicity of the tip and sample. In our experiments, the humidity was not well controlled and the tip/sample adhesion properties were not accounted for. We believe that keeping the humidity as low as possible or by working fully immersed in DI water will improve the uniformity of the tip's hydrodynamic response. However, there hasn't been much work done that measures how the local humidity affects the stability of tapping AFM. New technology such as environmental humidity chambers and water immersion may improve tapping MIM-AFM. A good capacitance standard specific for Fast Force Curve MIM may allow one make quantitative MIM results more

feasible. We highly encourage the exploration of better controlled experimental setups for Fast Force Curve MIM to obtain quantitative electronic data.

In this work, we showed the versatility of contact mode MIM for probing a semiconductor's response to an applied tip voltage. In this variant of MIM, which we called Modulated MIM (MIM2), the perturbation gave addition information regarding the material's electronic structure. MIM is a great technique for measuring an electronic materials response to perturbations because the probe signal, the microwave reflection coefficient, is generally is not directly affected the perturbation. The first application of this would be experiments that study charge carrier transport in a transistor during operation. The MIM signal can image through the oxide layer on transistors and diodes to map quantum capacitance without affecting the conduction path. Using a low temperature, vacuum pressure MIM experimental setup, it may be possible to measure elusive quantum phenomena such as superconductivity and ballistic transport at the nanoscale. Second, we encourage the exploration of other methods for sample perturbation to reveal different electronic structure. For example, MIM mapping combined with a time resolved laser perturbation will give photovoltage information related to the optical density of states and absorption spectrum of the material.

We believe that this work is a completed framework describing different approaches to spatially map the electronic properties of nanoscale materials with ultra-high resolution. Specifically, we present methods to characterize both bulk semiconductor and 1-dimensional carbon nanotube in a completely non-destructive way making it possible to use these methods in conjunction with an industrial process. We also believe this work is also a completed framework for understanding subtle, previously unexplored, growth phenomena in carbon nanotubes and

how it would affect the wafer scale quality for transistor applications. This work is a major step toward creating versatile and practical methods for nanoscale electronic material metrology.

APPENDIX A

PROCEDURE FOR CHEMICAL VAPOR DEPOSITION GROWTH OF CARBON NANOTUBES

Images of aligned carbon nanotubes after CVD growth can be seen in chapter 1.

Overview of CVD growth of Carbon Nanotubes

- General Procedures:
  - Clean Substrate
  - Deposit Catalyst lines (Typically a Metal Thin Film)
  - Clean Sample
  - Preform CVD growth
  - Characterize using SEM and MIM-AFM
- Growth Considerations:
  - Catalyst Deposition Method (0.5 - 1nm thin ebeam deposited thin film is the current convention used, needs to be optimized)
  - Catalyst Type, Fe and Cu works well… Grain Size Matters!!
  - Growth Precursor Gases, Ar and He typically Used, Water Vapor may offer enriched growth.
  - Gas Flow Rate (gfr), 30sccms is typical
  - Carbon Source, Ethanol works well
  - Growth Temperature, 950degress C works well
  - Growth Time, a 30min growth time is more than enough, cycling the growth has also shown promise for high density growth in literature.

Practical Notes:

- The CNT growth show be aligned close to parallel to the length of the CVD gas tube furnace.
- The growth temperature is the highest and most stable at the center of the CVD chamber.
- Environmental humidity can worsen yield. Therefore, the humidifiers in the room should be dumped regularly.
- Too many samples in the chamber at once lowers the overall density of the tubes. No more than 2 samples at a time to ensure maximum yield.

Sample and Quartz Substrate Cleaning

1. Cut Sample with Diamond Scribe then break into proper piece if necessary (use the scribe to add simple cross at the center of each sample to help determine orientation)
2. Rinse Sample in Acetone then IPA water (or DI water)
3. Dry by Nitrogen
4. Bake at 110°C Degrees for 5-10min
5. Store in proper storage

Detailed Procedures for CVD growth of Aligned CNTs

1. Attach sample to Silicon piece and load into CVD tube
2. Anneal for 1hr at 950 ^{o}C
3. Cool down to 100 - 150 ^{o}C using fan
4. Seal CVD tube on both ends
5. Turn on first 5 Manual gas valves at bottom

6. Set purge temperature, 925 ^{o}C
7. Turn on H2 purge for 3 min (Check for gas flow by turning on ethanol bubbler for a few seconds and look for spinning)
8. Shut furnace to commence heating until stable
9. Turn off H2 purge then turn on H2 growth (30 gfr) and Ar growth (30gfr) carrier gases and wait until gfr is stable
10. Turn on ethanol (precursor) bubbler and flow for 30min at 925C (If you hear cracking noises or see water vapor O2 leaking can cause explosion! Turn off all gases except Ar, turn off furnace and step away from the CVD setup)
11. Turn off Ethanol bubbler and H2 growth gasses, but leave on Ar to commence cooling to 100 - 150 ^{o}C
12. Turn off Ar growth gas and unhook CVD tube

APPENDIX B

PROCEDURES FOR MICROWAVE IMPEDANCE MICROSCOPY IMAGING

General Procedures:

1. Load the MIM tip into the tip holder and secure into the AFM
2. Preform MIM calibration on calibration sample
3. Use AC mode to find target area on the sample
4. Use MIM-AFM scan in contact mode to acquire high resolution image
5. Post process the data (3D overlays look very nice...)

Calibration Notes:

- Disabling slow scan over Al2O3 dots makes calibration easier
- Always record and save the phase offset and Al2O3 dots image to figure out which pathway the C-signal is in and which direction is high Capacitance. (Note: the capacitance can be in either I or Q signal pathway and high capacitance can be negative or positive changes in voltage.)
- Note the S/N ratio by taking a line cut of the Al2O3 dots. Signal > ~±20mV is necessary for high quality images… If the S/N is too low than it indicates either that there is an issue with the tip loading or the tip may be too sharp.
- The MIM tip acts as a RF antenna, thus there is an inverse tradeoff between tip sharpness and sensitivity; tips that are too sharp have low S/N and great resolution, whereas tips that are too dull have poor resolution and very high S/N. The tip can be dulled purposely according to the dimensions of the sample and desired sensitivity/contrast of the scan. (Note: tips will dull as the scan progresses according the relative hardness of the sample.)

- During calibration the signal in the resistive channel will never be completely nullified.

Calibration Procedures:

1. Load MIM tip into the AFM
2. Input calibration sample in AFM
3. Preform frequency sweep (set # of points to 81) then auto null. Ensure that the dip is lower -20dB, if not then there is a problem with the MIM tip loading.

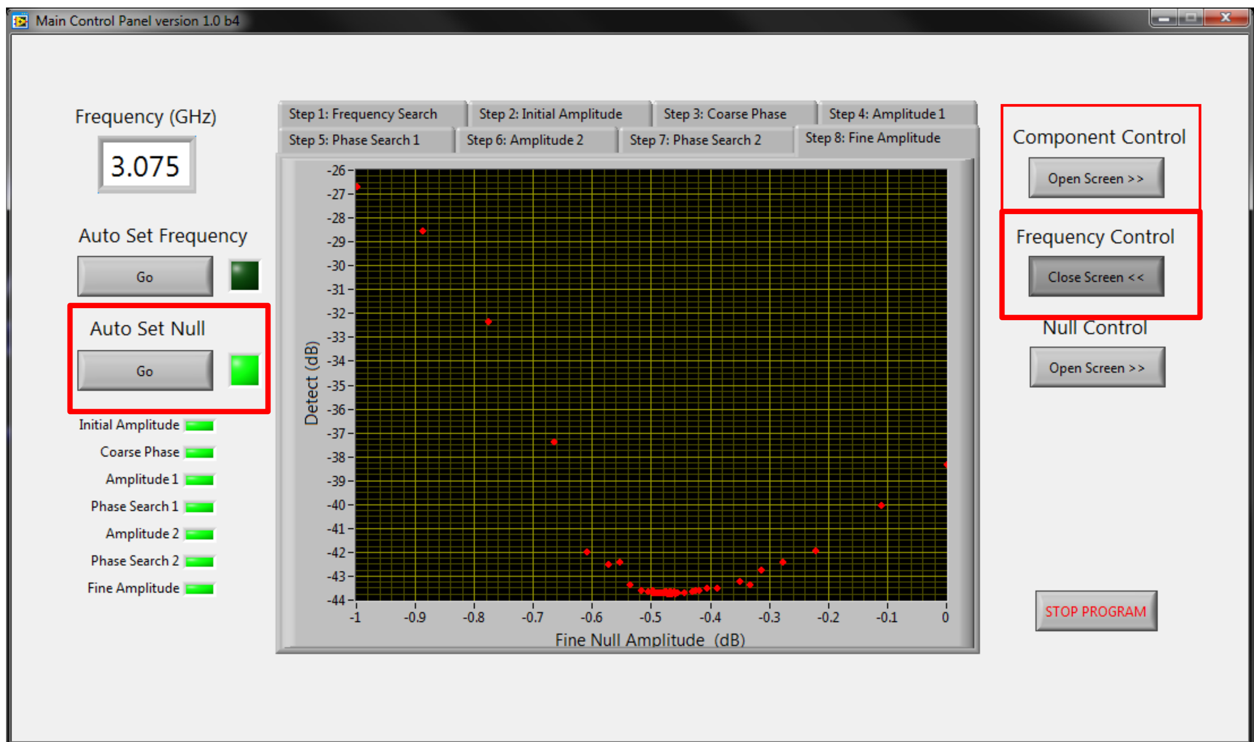

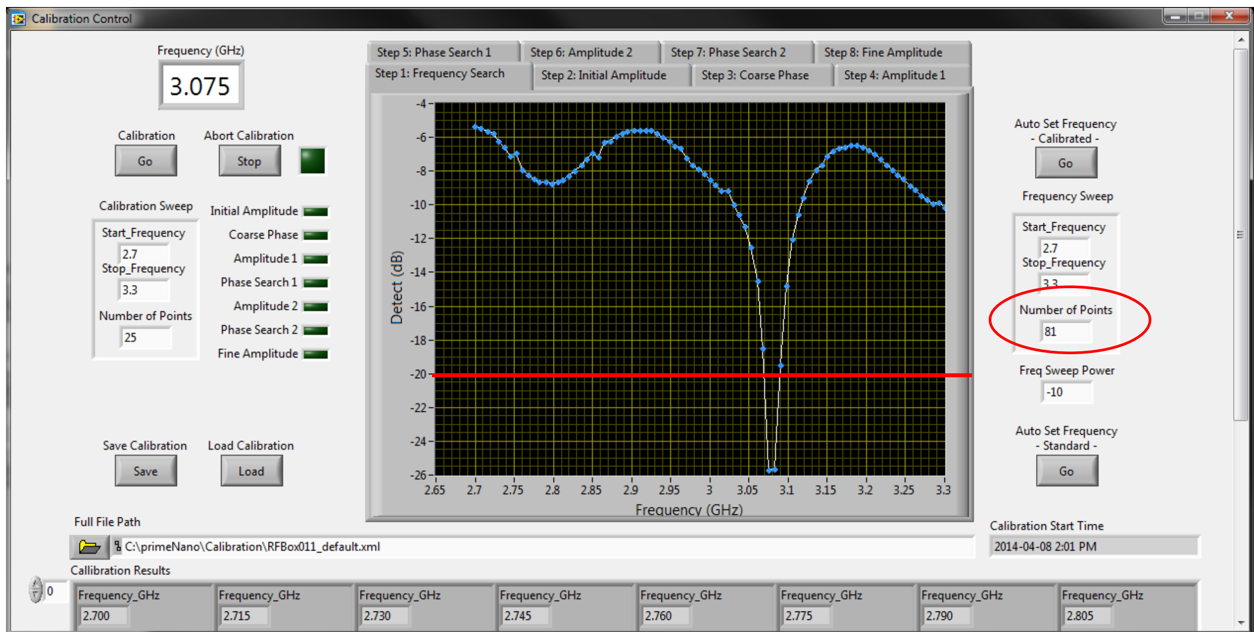

4. Start MFP3D

5. Pick the “Peak” option on the pop-up menu, then close the menu

6. Select the “MIM_contact_mode” experiment file on the desktop (this file has all the general settings for MIM preloaded)

7. Align the Laser on the middle of the tip and zero the deflection

8. Find clean area on the calibration sample and start tip approach

9. Start scan (disabling the slow scan option may help with calibration)

10. Adjust the “demod phase” offset until all the signal is in the capacitance channel in the “component control menu”

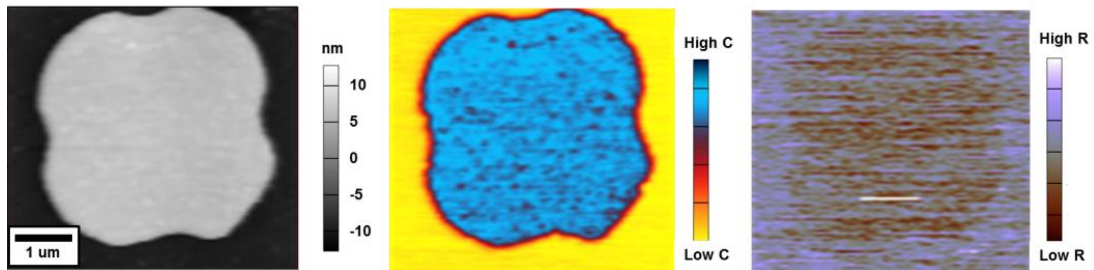

11. Check the S/N level, if it is too low then the tip may be too sharp

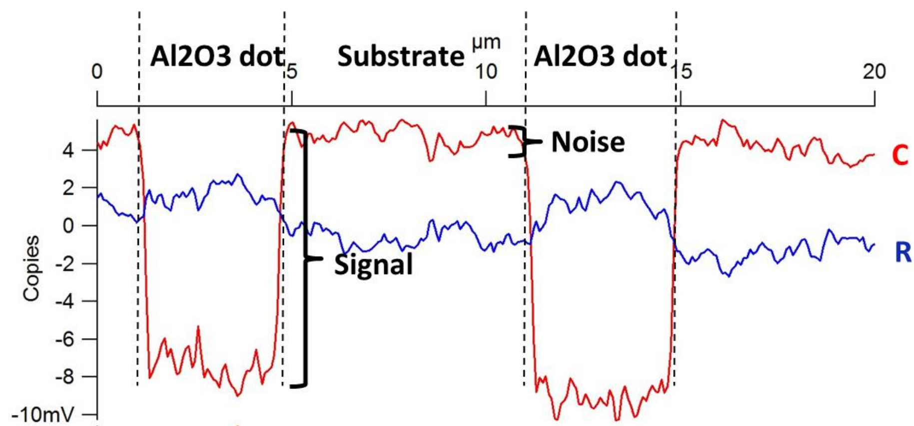

12. If the S/N is too low then disable slow scan over the Al2O3 dots, slowly increase the set point until ~0.5V; as the tip broadens the S/N increases. Once the desired S/N is obtained then withdraw and auto null. Repeat steps 8-11.

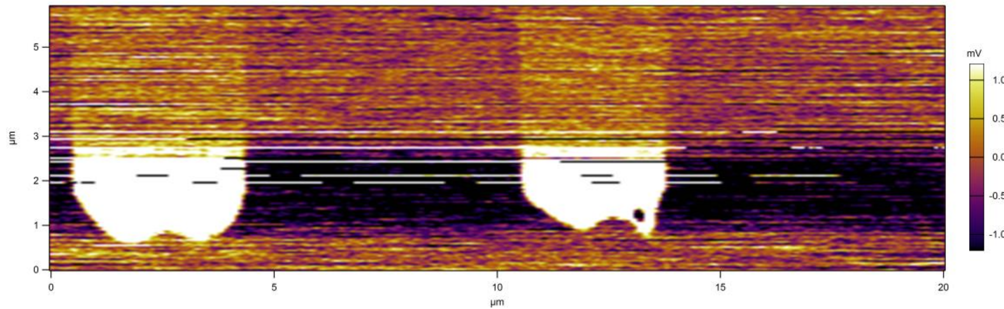

13. Save image

Image Acquisition Notes:

- Scanning at 45degrees can eliminate some tip affects which may improve resolution
- The MIM signal will drift as the scan persists which is why flattening the image is important. If the I or Q voltages drifts >3V, then consider using the "auto null" in-between scans.
- Note that the smallest feature size is ~20nm so adjust the pixel size accordingly
- When picking a new place on the sample after switching to AC mode may have to redo a slow tip approach and auto tune.
- Increasing the "power set" on the component control panel will increase the sample volume which may also improve S/N. It can also cause hysteresis is set too high so avoid going above -3dB if possible

Image Acquisition Procedures:

1. Put the desired sample into the AFM

2. Find the desired area on the sample

3. Switch to AC mode

4. Auto Tune @ 1V, put the set point at 950mV. Typical piezo frequency is between 50-100kHz.

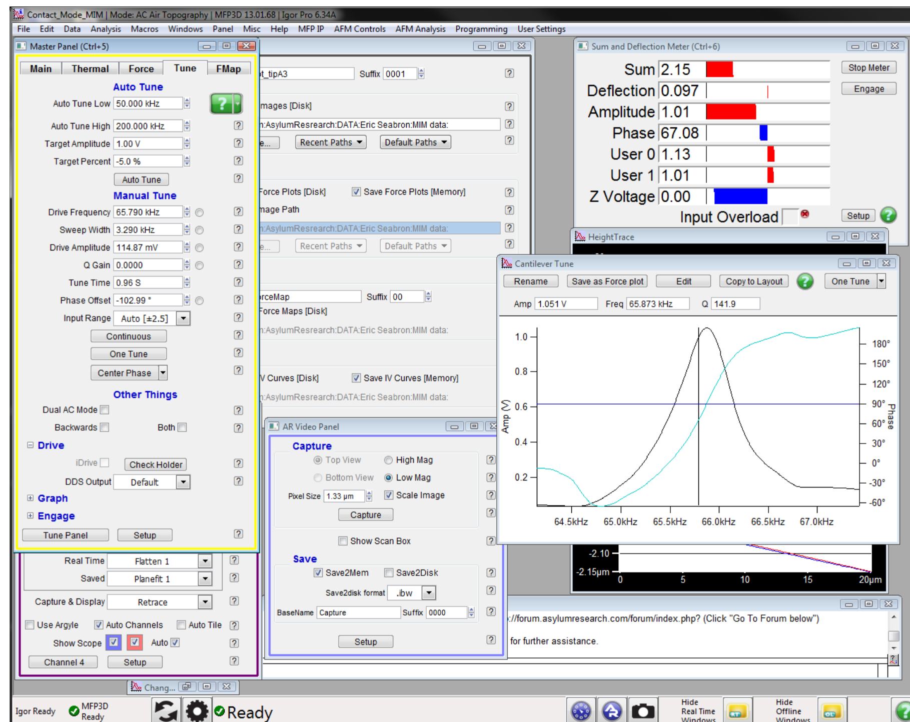

5. Start the slow tip approach (Note: the idea is not to obtain a high quality image, rather to find the ideal part of the sample without damaging the tip)

6. Once the desired area is found, click withdraw tip and switch back to contact mode. Ensure that the set point ~250mV. Engage the sample, auto null, then acquire MIM image.

7. Repeat steps 3-6 in order to image other parts of the sample.